

**A Finite Element Based Dynamic Modeling Method
for Design Analysis of Flexible Multibody Systems**

A Dissertation
Presented to
The Academic Faculty

By

Chih-Hsing Liu

In Partial Fulfillment of the Requirements for the Degree of
Doctor of Philosophy in Mechanical Engineering

Georgia Institute of Technology

May 2010

A Finite Element Based Dynamic Modeling Method for Design Analysis of Flexible Multibody Systems

Approved by:

Dr. Kok-Meng Lee, Advisor
School of Mechanical Engineering
Georgia Institute of Technology

Dr. Shreyes Melkote
School of Mechanical Engineering
Georgia Institute of Technology

Dr. Suresh Sitaraman
School of Mechanical Engineering
Georgia Institute of Technology

Dr. Yang Wang
School of Civil and Environmental Engineering
Georgia Institute of Technology

Dr. Bruce Webster
Department of Poultry Science
University of Georgia

Date Approved: March 29, 2010

ACKNOWLEDGEMENTS

I wish to express my sincere gratitude to those who support me throughout my thesis research. The list goes first to my advisor, Dr. Kok-Meng Lee. His insightful advice provides me the possibility to accomplish this thesis. Most importantly, he has fully demonstrated his professional and enthusiastic attitude toward the research. I also wish to express my appreciation to my thesis committee members, Professors Shreyes Melkote, Suresh Sitaraman, Yang Wang, and Bruce Webster for serving on my thesis committee and providing valuable suggestions.

I deeply appreciate the support from Dr. Wayne Whiteman and the School of Mechanical Engineering for providing me the opportunity to serve as a graduate teaching assistant in the undergraduate course, ME3057 Experimental Methods, and the guidance offered by Dr. Suresh Sitaraman during my teaching practicum in the graduate course, ME6124 Finite Element Method. I also like to take this opportunity to thank Professors Massimo Ruzzene and Jeff Jagoda for their support when I was in the School of Aerospace Engineering.

Finally, thanks my family and all friends in my life!

This research is funded by the US Poultry and Egg Association, Georgia Food Processing Advisory Council (FoodPAC), and Georgia Food Industry Partnership (FIP).

TABLE OF CONTENTS

ACKNOWLEDGEMENTS	iii
LIST OF TABLES	viii
LIST OF FIGURES	x
LIST OF SYMBOLS	xv
LIST OF ABBREVIATIONS	xix
SUMMARY	xx
CHAPTER 1 INTRODUCTION	1
1.1 Motivation and Background	1
1.2 Review of Prior and Related Work	3
1.2.1 Compliant Mechanisms	4
1.2.2 Explicit Dynamic Finite Element Method	6
1.2.3 Damping Identification	8
1.2.4 Topology Optimization	9
1.3 Research Objectives	13
1.4 Outline of the Thesis	16
CHAPTER 2 DYNAMIC MODELING METHOD	19
2.1 Introduction	19
2.2 Overview of the Application Problem	21
2.3 Explicit Dynamic Finite Element Method	24
2.3.1 Explicit Time Integration	26
2.3.2 Critical Time Step and Numerical Stability	27
2.3.3 Formulations of Critical Time Step for Different Elements	31

2.3.4 Effect of Element Size and Shape.....	32
2.3.5 Effect of Characteristic Length and Material Properties	33
2.3.6 Contact Model.....	35
2.3.7 Colomb Friction.....	37
2.4 Modal Analysis.....	38
2.4.1 Basic Formulation.....	38
2.4.2 Illustrative Example in Analyzing a Portal Frame Structure	39
2.5 Viscous Damping Model	48
2.5.1 Proportional Damping Effect.....	48
2.5.2 A Computational/Experimental Coupled Damping Identification Method .	51
2.5.3 Illustrative Example: Light-Damped Compliant Beam with Tip Mass	52
2.6 Topology Optimization.....	58
2.6.1 Basic Formulation.....	58
2.6.2 Topology Optimization of a Short Cantilever Beam	59
2.6.3 Characterizing Ligament Locations of a Biological Structure	61
2.7 Summary	65
CHAPTER 3 DYNAMIC MODELING OF THE COMPLIANT FINGER	67
3.1 Introduction	67
3.2 Modal Analysis.....	68
3.3 Finger-Modeling Comparison: Time Step Consideration	71
3.4 Damping Modeling and Identification	75
3.4.1 Damping Coefficients of the High-Damped Compliant Fingers	77
3.4.2 Damping Properties v.s. Finger Lengths.....	82

3.5 Contact between Rotating Finger and Elliptical Object.....	84
3.5.1 Dynamic Modeling and Experimental Results	85
3.5.2 Parameter Effect.....	89
3.6 Twist Deformation of Compliant Finger	99
3.7 Summary	103
CHAPTER 4 GRASPING DYNAMIC ANALYSIS OF ELLIPSOIDAL OBJECTS....	104
4.1 Introduction	104
4.2 Grasping Dynamic Analysis of a Football	104
4.3 Effects of Operating Parameters.....	112
4.4 Grasping and Flipping Dynamic Analysis of an Ellipsoid.....	117
4.5 Summary	123
CHAPTER 5 GRASPING DYNAMIC ANALYSIS OF LIVE OBJECTS.....	124
5.1 Introduction	124
5.2 Geometry Modeling and Optimization.....	125
5.2.1 Geometry Modeling for Body-Grasping and Leg-Gripping.....	125
5.2.2 Geometry Modeling for Shackle-Rotating/Inverting.....	129
5.2.3 Topology Optimization of the Shackle Mechanism.....	130
5.3 Operating Parameters	135
5.4 Simulation Results.....	141
5.4.1 Body-Grasping and Leg-Gripping	141
5.4.2 Shackle-Rotating/Inverting	149
5.5 Summary	156
CHAPTER 6 CONCLUSIONS AND FUTURE WORK.....	158

6.1 Conclusions	158
6.2 Future Work.....	161
APPENDIX A GENERAL ELEMENT TYPES FOR EXPLICIT DYNAMIC FINITE ELEMENT ANALYSIS.....	162
APPENDIX B SOME ENGINEERING EXAMPLES GOVERNED BY THE WEAK FORM FORMULATION.....	165
APPENDIX C NATURAL FREQUENCIES AND MODE SHAPES OF THE PORTAL FRAME STRUCTURE	167
APPENDIX D TRADITIONAL DAMPING IDENTIFICATION METHODS	174
D.1 Log Decrement Method (Time Domain).....	174
D.2 Half-Power Bandwidth Method (Frequency Domain).....	177
APPENDIX E DUNKERLEY’S METHOD	181
APPENDIX F CAD MODEL OF THE LIVE OBJECT	183
REFERENCES	184

LIST OF TABLES

Table 2-1 Critical time step formulations	31
Table 2-2 Effects of element size and shape on the critical time step	32
Table 2-3 Effects of parameters on time step calculation.....	33
Table 2-4 Finite element modeling of the portal frame structure	41
Table 2-5 Comparison of natural frequencies obtained by FEM and experiment.....	42
Table 2-6 Comparison of missing-screw effect on natural frequencies	45
Table 2-7 Transfer function of the SDOF model for the tip response.....	54
Table 2-8 Simulation parameters for the compliant beam.....	55
Table 2-9 Finite element modeling of the compliant beam	55
Table 2-10 Damping identification results	56
Table 2-11 Simulation parameters of the short cantilever beam	60
Table 3-1 Geometry and material properties of the rubber finger	68
Table 3-2 Finger modeling comparison.....	72
Table 3-3 Damping identification of compliant fingers	81
Table 3-4 Geometry modeling.....	85
Table 3-5 Material and finite element modeling.....	86
Table 3-6 Boundary conditions.....	86
Table 3-7 Parameter effect of the contact between the rotating finger and object	89
Table 3-8 Equipment for the torsion test	100
Table 4-1 Finger set configuration.....	106
Table 4-2 Material and finite element modeling of the football grasping analysis	108
Table 4-3 Boundary conditions.....	108
Table 4-4 Design analysis for conveyor (pallet) speed and timing	113
Table 4-5 Boundary conditions for grasping dynamic analysis.....	119
Table 4-6 Boundary conditions for flipping dynamic analysis.....	121
Table 5-1 Geometry model of the live object (chicken).....	127
Table 5-2 FE model and force-displacement relationship of each limb	129
Table 5-3 Geometry model for shackle-rotating/inverting.....	130
Table 5-4 Design analysis cases for different operating parameters	138

Table 5-5 Material and FE model for body-grasping and leg-gripping.....	139
Table 5-6 Boundary conditions.....	140
Table 5-7 Material and FE model for shackle-rotating/inverting.....	150
Table 5-8 Parameters for shackle-rotating/inverting simulation	151
Table A-1 General element types for explicit dynamic FEA	162
Table B-1 Some engineering examples governed by the weak form formulation	166

LIST OF FIGURES

Figure 1-1 Automated grasping by the robotic hand with multiple compliant fingers.....	3
Figure 1-2 Illustrative examples of compliant mechanisms	4
Figure 1-3 Flex-Foot [www.ossur.com]	5
Figure 1-4 Compliant mechanisms in MEMS applications.....	6
Figure 1-5 Applications of explicit dynamic finite element analysis	8
Figure 1-6 Classification of structural optimization.....	10
Figure 1-7 Applications of topology optimization.....	13
Figure 2-1 Comparison of two FEA based parameter-evaluation procedures.....	19
Figure 2-2 Procedure of the dynamic modeling method	20
Figure 2-3 Automated live-bird transfer system.....	23
Figure 2-4 Illustrative scheme for dynamic FEA involving deformable contact	24
Figure 2-5 Illustration examples for different element size and shape effect.....	32
Figure 2-6 Effects of characteristic length and material properties on critical time step .	34
Figure 2-7 Contact between two deformable bodies	35
Figure 2-8 Portal frame structure and its first three mode shapes	40
Figure 2-9 Finite element modeling for the portal frame structure	41
Figure 2-10 Comparison of experiment and FEM modal analysis (assembled model)....	41
Figure 2-11 Comparison of significantly changed first four mode shapes.....	43
Figure 2-12 Analysis cases on missing-screw effect	44
Figure 2-13 Missing-screw effect on natural frequencies and mode shapes	47
Figure 2-14 Illustration of proportional damping effect for single DOF system.....	50
Figure 2-15 A computational/experimental coupled damping identification procedure ..	51
Figure 2-16 Experiment of the light-damped beam [Yoo <i>et. al.</i> , 2003]	54
Figure 2-17 Dynamic response under different damping coefficients.....	56
Figure 2-18 Comparison of simulation and experimental data of the free vibration.....	57
Figure 2-19 Snapshots of the compliant beam under free vibration.....	57
Figure 2-20 Compliance minimization process of the cantilever beam	60
Figure 2-21 Topology optimization for the short cantilever beam.....	61
Figure 2-22 Analysis example in biological structure	62

Figure 2-23 Compliance minimization process	63
Figure 2-24 Topology optimization for ligament locations.....	64
Figure 2-25 Ligament layout	64
Figure 3-1 CAD model of the compliant finger (4.5-inch).....	68
Figure 3-2 Finite element model of the 8-inch compliant finger.....	69
Figure 3-3 First ten mode shapes of the 8-inch compliant finger	70
Figure 3-4 Modeling comparison of a 4.5-inch compliant finger.....	72
Figure 3-5 Tip responses of different analysis cases	73
Figure 3-6 Maximum equivalent stresses of different analysis cases.....	73
Figure 3-7 Displacement and stress contour of the detailed finger model	74
Figure 3-8 Experimental setup for the measurement of free vibration response.....	76
Figure 3-9 Experimental results for free vibration response of compliant fingers.....	77
Figure 3-10 Dynamic simulation of free vibration response of compliant fingers.....	78
Figure 3-11 Dynamic response of 3-inch finger under different damping coefficients ...	79
Figure 3-12 Dynamic response of 4.5-inch finger under different damping coefficients	79
Figure 3-13 Dynamic response of 6-inch finger under different damping coefficients ...	80
Figure 3-14 Dynamic response of 8-inch finger under different damping coefficients ...	80
Figure 3-15 Comparison of simulation and experimental results.....	81
Figure 3-16 Damping ratios versus finger lengths.....	83
Figure 3-17 Damping coefficients/critical damping coefficients versus finger lengths ...	83
Figure 3-18 Experimental setup for the rotating finger/fixed elliptical object contact.....	84
Figure 3-19 Finite element model for contact simulation.....	85
Figure 3-20 Simulation and experimental results of finger-contact deformation.....	87
Figure 3-21 Reaction force from contact between rotating finger and elliptical object ...	88
Figure 3-22 Contact location at the elliptical object.....	88
Figure 3-23 Effect of finger damping coefficient on maximum finger stress	91
Figure 3-24 Effect of finger damping coefficient on maximum object stress	92
Figure 3-25 Effect of finger damping coefficient on reaction force.....	92
Figure 3-26 Dynamic response for $\alpha = 1$ case ($\zeta = 0.02$).....	93
Figure 3-27 Dynamic response for $\alpha = 7.5$ case ($\zeta = 0.15$).....	93
Figure 3-28 Dynamic response for $\alpha = 180$ case ($\zeta = 3.6$).....	94

Figure 3-29 Dynamic response for $\alpha=600$ case ($\zeta=12$).....	94
Figure 3-30 Initial and final contact instants for $\alpha=7.5, 180$ and 600 cases.....	95
Figure 3-31 Effect of finger elastic modulus on maximum finger stress	96
Figure 3-32 Effect of finger elastic modulus on maximum object stress	96
Figure 3-33 Effect of finger elastic modulus on reaction force	97
Figure 3-34 Effect of object elastic modulus on maximum finger stress	97
Figure 3-35 Effect of object elastic modulus on maximum object stress	98
Figure 3-36 Effect of object elastic modulus on reaction force.....	98
Figure 3-37 Finite element model for finger-twist simulation.....	99
Figure 3-38 Experimental setup of finger-twist test	100
Figure 3-39 Comparison of simulation and experimental results of the twist angle	101
Figure 3-40 Dynamic responses of the loading points.....	102
Figure 3-41 Twist angle versus time.....	102
Figure 4-1 Finite element (half symmetric) model for football grasping	107
Figure 4-2 Experiment of football grasping [Yin, 2003].....	109
Figure 4-3 Football y-axis trajectory	111
Figure 4-4 Relative X-displacement between the football and pallet.....	111
Figure 4-5 Dynamic response from simulation	112
Figure 4-6 X-direction response of the football.....	114
Figure 4-7 Y-direction response of the football.....	114
Figure 4-8 Maximum equivalent stress on football	115
Figure 4-9 Dynamic response under the optimal operating parameters (case 2).....	115
Figure 4-10 Contact location between the fingers and football (Case 2)	116
Figure 4-11 Finger-tip response (y-axis)	116
Figure 4-12 Top view of the transfer system for the grasping/flipping analysis	117
Figure 4-13 Grasping dynamic analysis results	119
Figure 4-14 Symmetry expansion of grasping dynamic analysis result	120
Figure 4-15 Finger tip response (y-axis).....	120
Figure 4-16 Y-axis deformation and stress contour of the compliant fingers	120
Figure 4-17 Flipping dynamic analysis result.....	122
Figure 4-18 Trajectory of the ellipsoid object and drum center	122

Figure 5-1 Geometry modeling of the live object (chicken).....	126
Figure 5-2 Live object (chicken) model and simplified skeleton	126
Figure 5-3 Analysis of the force-displacement relationship of each limb	128
Figure 5-4 Geometry modeling for shackle-rotating/inverting.....	130
Figure 5-5 Topology optimization of the shackle-body (half model).....	132
Figure 5-6 Topology optimization of the gripper (compliant part)	133
Figure 5-7 Optimal shackle concept design.....	134
Figure 5-8 FE model for body-grasping and leg-gripping.....	135
Figure 5-9 Trajectory of the input operating parameters	137
Figure 5-10 Comparison of the dynamic responses for different cases.....	142
Figure 5-11 Trajectory of the live object under different cases.....	143
Figure 5-12 Dynamic response under the optimal operating parameters (Case 4).....	145
Figure 5-13 Trajectories of the output parameters (optimal case).....	146
Figure 5-14 Finger-tip response.....	146
Figure 5-15 Simulation result when maximum finger-stress happened (t=0.97s).....	147
Figure 5-16 Simulation result of the body-grasping (t=0.7s)	148
Figure 5-17 Simulation result of the leg-gripping (t=1.1s).....	148
Figure 5-18 Schemes of the live-bird transfer system	149
Figure 5-19 FE model for shackle-rotating/inverting	150
Figure 5-20 Resultant displacement (m) of chicken and shackle	152
Figure 5-21 Dynamic analysis results of the shackle-rotating process.....	152
Figure 5-22 Dynamic analysis results of the shackle-inverting process.....	153
Figure 5-23 Simulation snapshots by Lagrange dynamics [Wang, 2009]	154
Figure 5-24 Comparison of the body-center response (shackle-rotating)	155
Figure 5-25 Comparison of the body-center response (shackle-inverting)	155
Figure A-1 General element types for explicit dynamic FEA	164
Figure C-1 Simulation models for the study of missing-screw effect	167
Figure C-2 Natural frequencies and mode shapes (modes 1-5).....	168
Figure C-3 Natural frequencies and mode shapes (modes 6-10).....	169
Figure C-4 Natural frequencies and mode shapes (modes 11-15).....	170
Figure C-5 Natural frequencies and mode shapes (modes 16-20).....	171

Figure C-6 Natural frequencies and mode shapes (modes 21-25).....	172
Figure C-7 Natural frequencies and mode shapes (modes 26-30).....	173
Figure D-1 Underdamped free vibration response.....	175
Figure D-2 Damping ratio effect on free vibration response in time domain.....	176
Figure D-3 FRF magnitude vs. frequency: half-power bandwidth method.....	179
Figure D-4 Damping ratio effect in frequency domain response	180
Figure F-1 Engineering drawing of the live object (chicken).....	183

LIST OF SYMBOLS

Upper case	Definition
A	Area
$A_{e\max}$	Area for largest side of element
B	Bulk modulus
C	Damping matrix
D_s	Magnification factor
E	Elastic modulus
E_{finger}	Elastic modulus of finger
E_{ijkl}	Elastic tensor
E_{object}	Elastic modulus of object
F	Force load
$F_{reaction}$	Reaction force
H	Frequency response function
I	Moment of inertia
J	Polar moment of inertia
J_n	Joint n
K	Stiffness matrix
L	Length
L_e	Element length
M	Mass matrix
N	Interpolation function matrix
Q	Quality factor
R_x	Orientation angle about x axis
R_y	Orientation angle about y axis
S	Surface
T	Period

U	Degree of freedom
V	Volume
$V_{conveyor}$	Conveyor speed
$V_{conveyor\ x}$	X component conveyor speed
$V_{conveyor\ y}$	Y component conveyor speed
V_e	Volume of element
X	Global nodal degree of freedom

Lower case

Definition

c	Damping coefficient
c_{cr}	Critical damping coefficient
c_d	Exponential decay coefficient
c_w	Wave propagation speed
d	Diameter
f_f	Friction force
f_n	Normal (interface) force
g_n	Gap function
h_f	Finger height (placed on drum)
k	Stiffness
k_n	Penalty (interface) stiffness
m	Mass
p	Concentrated load
p_0	Excitation force
r	Frequency ratio
r_{drum}	Drum radius
r_{ext}	External load
s_f	Scale factor

t	Time
u	Displacement
v	Velocity
v_r	Relative velocity
x	Peak of amplitude

Greek

Definition

Γ	Boundary
Δt	Time step
Δt_{num}	Numerical time step
Ω	Computational domain
α	Mass proportional damping coefficient
β	Stiffness proportional damping coefficient
δ	Log decrement
δu	Virtual displacement
$\delta \varepsilon$	Strain corresponding to virtual displacement
ε	Strain
ε_{ij}	Strain tensor
ε_v	Volumetric strain
$\dot{\varepsilon}$	Strain rate
μ	Friction coefficient
μ_d	Dynamic coefficient of friction
μ_s	Static coefficient of friction
ν	Poisson ratio
θ	Angle
θ_b	Bird orientation
$\theta_{conveyor}$	Conveyor angle
θ_f	Finger angle

$\theta_{shackle}$	Shackle angle
ρ	Density
σ	Stress
σ_{finger}	Finger stress
σ_h	Hydrostatic stress
σ_{object}	Object stress
ω	Frequency
ω_1	Fundamental natural frequency
ω_d	Damped frequency
ω_{drum}	Angular velocity of the drum
ω_{max}	Maximum natural frequency
ω_n	Natural frequency
ω_x	Angular velocity about x axis
ω_y	Angular velocity about y axis
ω_z	Angular velocity about z axis
ζ	Damping ratio

LIST OF ABBREVIATIONS

1D	One dimensional
2D	Two dimensional
3D	Three dimensional
APDL	ANSYS parametric design language
CAD	Computer aided design
CAE	Computer aided engineering
CFL	Courant-Friedrichs-Lewy
CT	Computed tomography
DOF	Degree of freedom
ESO	Evolutionary structural optimization
F/T	Force/Torque
FE	Finite element
FEA	Finite element analysis
FEM	Finite element method
FFT	Fast Fourier transform
FRF	Frequency response function
MDTO	Multi-domain topology optimization
MEMS	Micro-electro-mechanical systems
OC	Optimal criteria
PDE	Partial differential equation
SBES	Simulation-based engineering science
SCP	Sequential convex programming
SDOF	Single degree of freedom
SHM	Structural health monitoring
TFT-LCD	Thin film transistor liquid crystal display

SUMMARY

This thesis develops a finite element based dynamic modeling method for design and analysis of compliant mechanisms which transfer input force, displacement and energy through elastic deformations. Most published analyses have largely based on quasi-static and lump-parameter models neglecting the effects of damping, torsion, complex geometry, and nonlinearity of deformable contacts. For applications such as handling of objects by the robotic hands with multiple high-damped compliant fingers, there is a need for a dynamic model capable of analyzing the flexible multibody system.

This research begins with the formulation of the explicit dynamic finite element method (FEM) which takes into account the effects of damping, complex geometry and contact nonlinearity. The numerical stability is considered by evaluating the critical time step in terms of material properties and mesh quality. A general framework incorporating explicit dynamic FEM, topology optimization, modal analysis, and damping identification has been developed. Unlike previous studies commonly focusing on geometry optimization, this research considers both geometric and operating parameters for evaluation where the dynamic performance and trajectory of the multibody motion are particularly interested. The dynamic response and contact behavior of the rotating fingers acting on the fixed and moving objects are validated by comparing against published experimental results.

The effectiveness of the dynamic modeling method, which relaxes the quasi-static assumption, has been demonstrated in the analyses of developing an automated transfer system involved grasping and handling objects by the compliant robotic hands. This FEM based dynamic model offers a more realistic simulation and a better understanding of the

multibody motion for improving future design. It is expected that the method presented here can be applied to a spectrum of engineering applications where flexible multibody dynamics plays a significant role.

CHAPTER 1

INTRODUCTION

1.1 Motivation and Background

Flexible multibody systems involve rigid and compliant mechanisms which transfer input force, displacement and energy to another point through elastic deformations. The flexible parts are usually monolithic (single-piece), joint-less structures with certain advantages over rigid mechanisms. For example, a robotic hand with compliant fingers has many advantages such as lightweight, reducing wear, and the capability to accommodate a limited range of varying size and shape of objects. In addition, they are cheaper to manufacture than the jointed rigid mechanisms. However, for applications such as grasping geometrically poorly defined objects by compliant robotic hands, they are difficult to analyze because of the interdisciplinary nature.

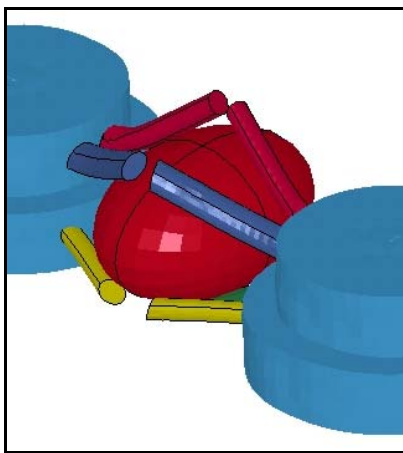
Simulation-based engineering science (SBES) [Oden *et al.*, 2006] could play a significant role in many applications ranging from microelectronic devices to automobiles and aircrafts. Finite element method (FEM), also known as finite element analysis (FEA), is one of the most popular numerical methods for engineering applications. It is a numerical technique for finding approximate solutions to partial differential equations (PDEs) as well as integral equations to simulate physical phenomena by converting the computational domain from continuum to discrete. Today, most of the commercial FEM packages have the capability for handling complex

geometries and boundary conditions. Computer simulation is an essential scientific methodology to advance research in nearly all engineering and science branches.

This thesis is motivated by the interest to reduce the number of design configurations and live chickens needed during the development of an innovative automated live-bird transfer system [Lee *et al.*, 2009] for food processing and poultry industry. For high speed automated transfer of live objects, robotic hands with highly damped compliant fingers (Figure 1-1) are used to handle live chickens on a moving conveyor. A critical requirement is that the design must need to accommodate different sizes/shapes of the objects to avoid potential damage. Grasping, in the literature of manufacturing and robotics, has received considerable attention in the context of fixture and manipulation. Most of these studies assume that the size, shape and location of the object are known, upon which, finger positions that ensure force closure grasp are designated. As compared to the rigid body dynamics, live objects are more difficult to analyze not only because of their varying sizes, shapes and weights but also they have natural reflexes and active reactions. In addition, the exact contact location is usually unknown.

For developing an automated transfer system, Lee *et al.* [1999] use slender rubber fingers to singulate and grasp live chickens by its body on conveyors. Joni [2000] performed a two dimensional (2D) quasi-static FEA to analyze the contact behavior between compliant fingers and the live object. Lee and Yin [2001] presented a method for designing a dynamic grasper for handling live objects. Yin [2003] studied the dynamic effect of high speed grasping of live birds. Yin *et al.* [2004] presented the computational models for predicting the deflection shapes of a non-uniform flexible finger. Lan [2005]

performed an analytical contact model to predict the contact force and deflected shape of the compliant fingers by a generalized shooting method. Previous studies primarily focus on the analysis of a compliant finger (modeled as a 2D beam) and its contact on a chicken (modeled as an ellipse or ellipsoid). These models are limited to the in-plane bending problem and the twist and out of plane bending deformation can not be considered. Other assumptions commonly made are that the dynamics is quasi-static and the damping effect of the rubber finger is negligible. It is desired to develop a more detailed 3D chicken model as a compliant mechanism in order to more realistically predict both the body-grasping and the leg-shackling processes. For such an application, a systematic dynamic modeling method will reduce costly trial-and-error designs, which can be regarded as the SBES in poultry industry.



(a) Grasping object scheme



(b) Automated grasping application [Lee, 2003]

Figure 1-1 Automated grasping by the robotic hand with multiple compliant fingers

1.2 Review of Prior and Related Work

The section begins with a review of compliant mechanisms. Related studies of explicit dynamic FEA and damping identification are then discussed. Finally, some

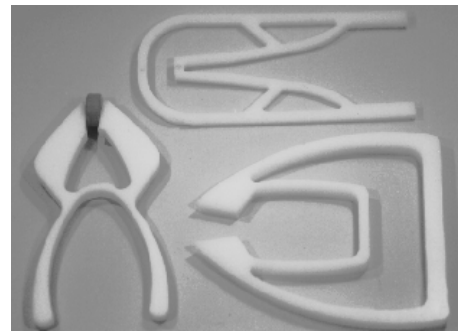
studies of topology optimization are reviewed.

1.2.1 Compliant Mechanisms

Compliant mechanisms are widely used in engineering applications as well as in our daily life. These include common compliant devices such as binder clip, paper clip, backpack latch, lid eyelash curler, and nail clipper in Figure 1-2a, as well as the compliant gripper in Figure 1-2b. Compliant mechanisms are also used in medical applications because of its light weight and compliance. For example, Figure 1-3 shows the prosthesis “Flex-Foot” for sprinting, which greatly improves the sport performance of an amputee.



(a) Common compliant devices
[Howell, 2001]



(b) Compliant gripper
[www.seas.upenn.edu/~gksuresh]

Figure 1-2 Illustrative examples of compliant mechanisms

In literature of compliant mechanisms, kinematics and structural optimization are the two major approaches [Shuib *et al.*, 2007] for the synthesis of compliant mechanisms.

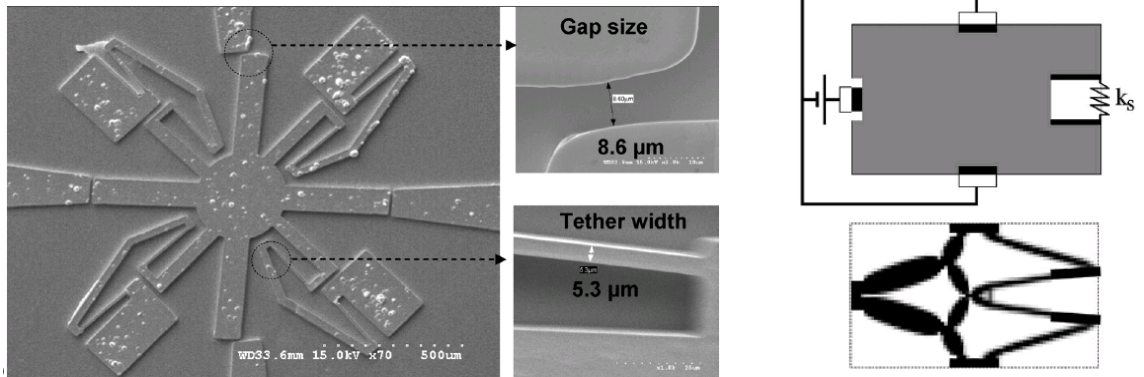
In the kinematic based approach, the pseudo-rigid-body model [Howell *et al.*, 1996; Midha *et al.*, 2000; Howell, 2001] is a popular method to analyze compliant mechanisms. In this method, the flexible member is treated a rigid link attached at a compliant pin joint with specified stiffness to derive a force-deflection relationship. The key factor for the

pseudo-rigid-body model is to decide where to place the pin joint and what value to assign for the spring constant. Applications based on pseudo-rigid-body model include the constant-force compression mechanism [Boyle *et al.*, 2003], actuator design [Wang, 2005], flapping mechanism [Khatait *et al.*, 2006], and an in-plane rotary bistable micromechanism in MEMS application [Luharuka and Hesketh, 2007] as shown in Figure 1-4a (which consists of four identical bistable mechanisms arranged in a cyclic symmetry manner about a central proof mass).



Figure 1-3 Flex-Foot [www.ossur.com]

Topology optimization is a general design method to optimize compliant mechanisms. Unlike kinematic based approach which begins with known link mechanisms, topology optimization begins with an initial design domain with specified loading and constraint boundary conditions. It focuses on determining the optimal topology synthesis for compliant mechanisms. Numerous applications are based on topology optimization such as micro actuator as shown in Figure 1-4b [Sigmund, 2001], the actuator with constant output force [Pedersen *et al.*, 2006], compliant grippers [Mankame and Ananthasuresh, 2004; Lu and Kota, 2006; Hull and Canfield, 2006], and MEMS mechanisms [Maute and Frangopol, 2003; Jang *et al.*, 2008].



(a) In-plane rotary bistable micromechanism
[Luharuka and Hesketh, 2007]

(b) Micro gripping mechanism
[Sigmund, 2001]

Figure 1-4 Compliant mechanisms in MEMS applications

Other approaches such as assumed mode method [Chen, 2001], shooting method [Lan and Lee, 2006; Banerjee *et al.*, 2009] and FEM [Zettl *et al.*, 2005; Dede and Hulbert, 2008] are also used to analyze compliant mechanisms. It is noted that the most attractive feature of FEM is the capability for handling complex geometries and boundary conditions. Most algorithms for topology optimization are also based on FEM.

1.2.2 Explicit Dynamic Finite Element Method

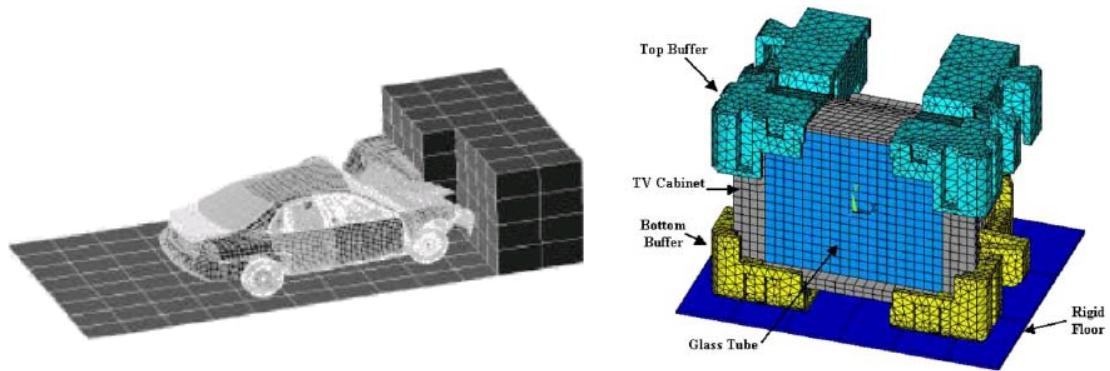
The name “finite element” was first used by Clough [1960]. Since its inception, the literature on FEM (or FEA in other words) and its applications have grown exponentially. The time integration procedure of a dynamic FEA can be classified into two categories; implicit and explicit methods. Implicit methods require a lot more computational effort to solve for the solution to a system of equations in each time step as compared to explicit methods which do not require the inversion of the stiffness matrix. However, unlike implicit methods that are stable for linear and many nonlinear problems, explicit methods are only stable when time steps are smaller than the critical time step size, which is

known as the Courant-Friedrichs-Lewy (CFL) condition [Mullen and Belytschko, 1983; Cook *et al.*, 2001]. Relative studies about the critical time step for stability considerations of explicit methods can be found in Belytschko *et al.* [1979], Hughes *et al.* [1979], Flanagan and Belytschko [1984], Ling and Cherukuri [2002], and Koterias and Lehoucq [2007].

General-purpose FEA computer programs such as NASTRAN and ANSYS emerged in late 1960s and early 1970s are based on the implicit method. In the late 1970s, DYNA3D (now known as LS-DYNA) is based on the explicit method.

Dynamic FEA has contributed to numerous applications especially in analyzing vehicle structures to avoid potential threats to equipment and human life. Figure 1-5a [Cheng *et al.*, 2001] shows a front impact simulation at a speed 40 mph to a stationary barrier of an automobile. Other example applications include impact and penetration analysis of fuselage-like structure [Knight *et al.*, 2000], impact simulation of a low profile concrete work zone barrier [Consolazio *et al.*, 2003], bird-strike simulation of aeronautic structures [Hanssen *et al.*, 2006], and crash and safety assessment for paratransit buses [Kwasniewski *et al.*, 2009].

Applications of dynamic FEA can also be found in handling and developing electronic devices to improve product reliability. For instance, the drop and shock impact analyses of TFT-LCD [Pan and Chen, 2007] and a 29" TV with buffer protection as shown in Figure 1-5b [Low *et al.*, 2004]. Dynamic FEA can reduce significantly number of physical prototype tests as well as the cost and time during product design. However, many applications of dynamic FEA neglect the damping effect which could be significant especially for problems involving highly damped flexible mechanisms.



(a) Car crash [Cheng *et al.*, 2001] (b) TV drop impact [Low *et al.*, 2004]

Figure 1-5 Applications of explicit dynamic finite element analysis

1.2.3 Damping Identification

Damping dissipates energy and causes vibration to decay with time. The consideration of damping is important for an accurate prediction of system dynamics which requires the time or frequency domain experiment to obtain the damping parameters. For example, steel poles and tubular towers [Pagnini and Solari, 2001] are pulled and released by a cable attached to the column shaft, and the free vibration information is measured by accelerometers. Another example is a wire cable [Zhu and Meguid, 2007] fixed at one end, and an impulse point load is applied transversely at the other end. The free vibration of the cable is captured using a high-speed digital camera, and the measurements are retrieved from the motion images. For both examples, the dynamic responses are measured in time domain, and the damping ratios are obtained using the log decrement technique. In frequency domain, for example, the frequency response function (FRF) of a gearbox [Drew and Stone, 2002] can be obtained under swept-sine excitation and laser vibrometer measurement. Then the damping ratios are

obtained by the circle-fit and half-power bandwidth method. For the purpose of simulating the damped behavior, the proportional (Rayleigh) damping technique (that defines damping as mass and stiffness proportional) is often used [Low *et al.*, 2004; Zhu and Meguid, 2007] in the dynamic analysis.

1.2.4 Topology Optimization

In literature, structural optimization problems can be divided into three categories; size, shape, and topology. Size and shape involve actual dimensions defining the entities of the object. Topology is the connectivity and associativity of the object entities. It defines the relational information between object entities, and neither geometry nor topology alone can completely define the objects.

Figure 1-6 illustrates the use of structural optimization to design a short cantilever beam under a force load at the middle of its free end. For size optimization, the dimension (width, height, or length) is progressively modified to minimize the deflection or stress under the force load. Shape optimization finds the best shape subject to certain loading condition or to avoid stress concentration in engineering consideration; for example, minimum bending moment design. In topology optimization, the connectivity of the structure (such as adding a hole) is considered which finds the best use of material in a structure while considering stiffness. It is worth to point out that the optimization process is similar to natural evolution of biological objects.

In general, structural optimization typically changes some design variables to maximize or minimize an objective function while satisfying a specified set of constraints. Generally, the objective function of topology optimization can be divided into two major categories; minimizing structural compliance (or maximizing static stiffness in other

words), and maximizing the natural frequency of a structure.

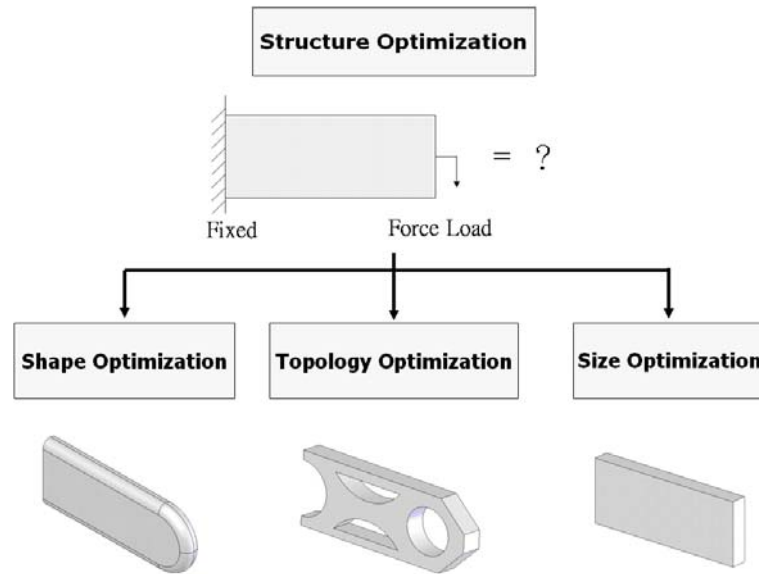


Figure 1-6 Classification of structural optimization

In the category of structural static stiffness topology optimization, some related algorithms have been developed. For example, the homogenization method [Bendsøe and Kikuchi, 1988] and the optimal criteria (OC) [Rozvany, 1989] provide the general formulations for optimal design of linearly elastic structures, which avoid the drawback of traditional FE based structural optimization approach that requires some kind of re-mesh in the analysis domain.

Other approaches have also been presented such as simulated bone remodeling method [Weinans *et al.*, 1992; Mullender *et al.*, 1994], SKO method [Baumgartner *et al.*, 1992], sequential convex programming (SCP) [Fleury, 1993], and sequential linear programming [Young and Chuang, 1994]. The SKO (soft kill option) algorithm solved the structural optimization problem by varying the Young's modulus according to a

calculated stress distribution; while the basic idea of the bubble method [Eschenauer *et al.*, 1994] is the iterative positioning of new holes (so-called “bubbles”) into the present structure.

The basic concept of an evolutionary structural optimization (ESO) approach [Xie and Steven, 1993, 1994, 1997] is based on removing material that is not needed leading to the optimum residual shape. A fully stressed design approach [Hinton and Sienz, 1995] is based on the ESO algorithm, and the optimal design is obtained by a gradual removal of low stressed elements. By applying this evolutionary procedure, an optimal topology of a structure can be found from an initial block domain. The procedure incorporates automatic mesh generation, finite element analysis and the fully stressed design algorithm.

Similar to the concept of the bubble method, in the level set method [Wang *et al.*, 2003], the structure under optimization is represented by a moving boundary embedded in a scalar function (the level set function) of a higher dimensionality. The level set model can also be referred to as implicit moving boundary (IMB) models and they can easily represent complex boundaries that can form holes, split into multiple pieces, or merge with others to form a single one.

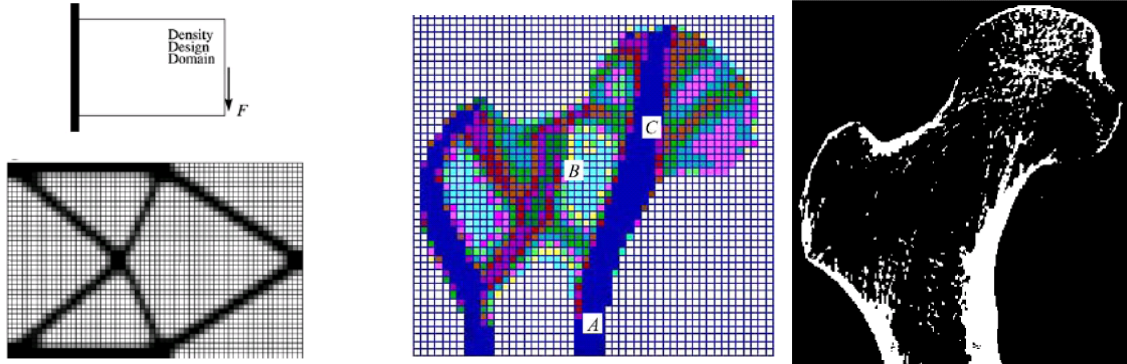
A new algorithm of Sequential Approximate Optimization (SAO) is proposed for the multidomain topology optimization (MDTO) [Ma *et al.*, 2006] to allow for multiple materials or composite materials in the various sub-domains of the structure. In traditional structural topology optimization, the material properties of continuum finite elements of fixed form and coupling are varied to find the optimal topology that satisfies the design problem.

In the topology optimization by penalty (TOP) method [Bruns, 2007], the design space search is dependent on the coupling, and the goal of the topology optimization by penalty (TOP) method is to determine the optimal finite element coupling constraints. Figure 1-7a shows a classical example in the field of static stiffness topology optimization.

In the category of natural frequency topology optimization (sometimes it is referred to as dynamic stiffness topology optimization), the frequency of a structure can be shifted towards to a desired value by the optimization algorithms. The design domain is discretized using a finite element mesh and the eigenvalue problem is solved. Some related algorithms are developed for this application such as eigenvalue homogenization method [Diaz and Kikuchi, 1992], frequency ESO [Xie and Steven, 1994, 1997], multidiscipline topology optimization which the compliances, displacements and natural frequencies are treated as constraints [Yang, 1997], and MDTO [Ma *et al.*, 2006].

Topology optimization has a wide spectrum of applications; to name a few, the design of compliant mechanisms (described in previous review of compliant mechanisms), automobile components [Chiandussi *et al.*, 2004], magnetic field [Yoo and Hong, 2004], heat transfer problems [Li *et al.*, 2004; Bruns, 2007], aerospace structures [Luo *et al.*, 2006]; cellular structures [Seepersad, *et al.*, 2008], periodic structures [El-Sabbagh *et al.*, 2008; Nomura *et al.*, 2009], and bone remodeling problems in biomechanics [Harrigan and Halmilton, 1994; Machado and Trabuco, 2004; Zhu *et al.*, 2005 ; Kim *et al.*, 2008; Jang and Kim, 2008]. It is believed that the morphology of bone is affected by its mechanical load, and that has self-optimizing capability. This phenomenon is well known as the Wolff's law [Wolff, 1986] of bone remodeling. Figure

1-7b shows an example with the simulation result and the computed tomography (CT) image.



(a) Optimal design of the cantilever beam [Bruns, 2007]

(b) Bone remodeling: simulation vs. CT image [Zhu et al., 2005]

Figure 1-7 Applications of topology optimization

1.3 Research Objectives

This thesis investigates the explicit dynamic FEA based method for modeling the dynamics of a flexible multibody system with large deformation and contact nonlinearity without neglecting the damping effect. Although existing methods are available, there remain some challenges in dynamic modeling:

- (a) There is a need for a method to estimate the damping coefficient for investigating its effect on high-damped continuum structures.
- (b) In order to solve the dynamic problems more realistically, there is a need to examine the commonly used quasi-static and lump-parameter assumptions by using the explicit dynamic FEA that allows for more detailed geometries.
- (c) Dynamic FEM has been computationally expensive, where the time step is a compromise between numerical stability and computation time. As will be

illustrated, the critical time step plays an important role especially for complex geometries in the flexible multibody systems.

- (d) For industrial automation applications, there is a need to evaluate both the operating parameters (such as speed and corresponding timing) for improving the dynamic performance of the multibody motion, and the geometric parameters (such as size and shape under stress, strain, or displacement constraints) for optimizing the strength-to-weight ratios.

To address the above challenges, this thesis research has been organized into three tasks:

1. To develop a general FEA based dynamic modeling method capable of analyzing a flexible multibody system with large deformation, contact nonlinearity, damping effect, and three dimensional complex geometries.
2. To develop and evaluate a damping modeling and identification method for analyzing high-damped continuum structures.
3. To investigate the dynamic performance and trajectory of the flexible multibody system by evaluating both geometric and operating parameters.

With respect to these objectives, this thesis research offers the followings:

- (1) The generalized FEA based dynamic modeling method which includes both geometric and operating parameters for evaluation has been developed for analyzing a flexible multibody dynamic system involving large deformation, complex geometries, contact nonlinearity, and damping effect.

- (2) The effects of material properties (elastic modulus, density, and Poisson ratio) and mesh quality (characteristic length) on the critical time step for explicit dynamic FEA have been investigated. The critical time step plays an important role especially for complex geometries in the flexible multibody dynamic systems. Among the material properties, the critical time step is sensitive to elastic modulus and density, and relatively insensitive to Poisson ratio. Smaller elastic modulus and larger density can lead to larger critical time step. The characteristic length is a function of element sizes and shapes, and is linearly proportional to the critical time step. Thus, mesh quality must be carefully considered and well planned.
- (3) A technique that couples the computational and experimental methods in identifying the damping coefficient of a flexible member has been illustrated. Unlike traditional damping identification methods such as log decrement method (time domain) and half-power bandwidth method (frequency domain), which estimate the damping ratios for lump-parameter models, and are only valid for light-damped cases, the advantage of this coupled method is the capability to obtain the damping coefficient of a high-damped continuum structure. The proportional damping assumption is used in the dynamic model. For mechanisms vibrate at lower modes, the proportional damping model can be reduced to a single mass proportional term since the stiffness proportional term is insignificant at lower-mode/frequency applications. Based on this method, the critical damping coefficient can be obtained numerically, and the damping coefficient can be estimated by the aid of experimental data.
- (4) A general numerical technique to analyze a flexible multibody system involved a robotic hand with multiple high-damped compliant fingers is proposed. Several

numerical cases of grasping ellipsoidal and live objects are simulated offering a better understanding of the multibody motion for improving future designs.

1.4 Outline of the Thesis

The remainder of this thesis is organized as follows:

In Chapter 2, a FEA based dynamic modeling method with a coupled computational/experimental technique for damping identification is introduced. It begins with the review of the theoretical formulation of the explicit dynamic FEM. The critical time step can be interpreted in terms of element sizes, shapes and material properties. The corresponding effects of these parameters are discussed. The contact model based on the penalty method, the viscous damping model based on proportional damping assumption, and the Coulomb friction model for the sliding contact are introduced. A modal analysis for obtaining natural frequencies and mode shapes is introduced with an illustrative example and compared against the modal testing result. A damping modeling and identification method is presented and the damped response of a compliant beam is analyzed to demonstrate the practical use of the proposed method. Finally, the formulation of topology optimization is introduced with illustrative examples; a cantilever beam design, and locating ligaments of a biological structure.

In Chapter 3, the analysis of the high-damped compliant finger is discussed in detail to illustrate the practical use of the dynamic modeling method and to verify the numerical model. In the modal analysis, it shows the compliant finger primarily vibrates at its first mode, and the mass proportional damping assumption is valid in this application. Four different finger-modeling cases (with different element types and sizes) based on the time

step considerations are discussed. The damping coefficients are obtained by the computational/experimental coupled identification technique. After the damped behavior of the high-damped compliant finger is realistically modeled, the simulated contact response between the rotating finger and the fixed elliptical object are compared against experimental data, which shows excellent agreement. The simulated twist deformation is also compared against the experiment. Once verified the dynamic model, these compliant fingers are applied in the grasping application in Chapter 4.

In Chapter 4, the dynamic modeling method is applied to evaluate the grasping capability of the robotic hand with multiple high-damped compliant fingers. Two engineering applications are simulated involving the grasping and handling of a football and an ellipsoid. For the first case, the simulated dynamic response of the football passing through the compliant hand is compared against the experimental result. Several design analysis cases under different operating parameters are presented to investigate the sensitivity of the conveyor speed and timing parameters on the trajectory of the multibody system. The second case simulates grasping and flipping dynamics of the ellipsoid.

In Chapter 5, the dynamics of grasping an object is analyzed to demonstrate practical applications of the proposed method. Unlike Chapter 4 used an ellipsoid to represent the live object, a more detailed chicken model is developed without neglecting its legs and head. The automated transfer processes involved body-grasping, leg-gripping, and shackle-rotating/inverting are simulated to investigate the dynamic performance and the trajectory of the multibody motion. The optimal operating parameters for controlling the automated system are investigated, and the topology optimization is applied to obtain

an optimal shackle design.

Finally, the conclusions of this thesis are summarized in Chapter 6. Several aspects of potential future work are addressed to increase the applicability of the dynamic modeling method discussed in this thesis, and also to facilitate the design and analysis of flexible multibody systems.

CHAPTER 2

DYNAMIC MODELING METHOD

2.1 Introduction

In the interest to develop a general method for analyzing the design of a flexible multibody system, the FEA based evaluation problem is divided into two parts; geometric and operating parameter-evaluation as compared in Figure 2-1. The first part (Figure 2-1a) evaluates geometric parameters under stress, strain or displacement constraints. As a new FEA application for industrial automation, the second part (Figure 2-1b) evaluates operating parameters under trajectory constraints. The FEA based dynamic modeling method includes both geometric and operating parameters for evaluation, where the dynamic performance and trajectory of the multibody motion are particularly interested.

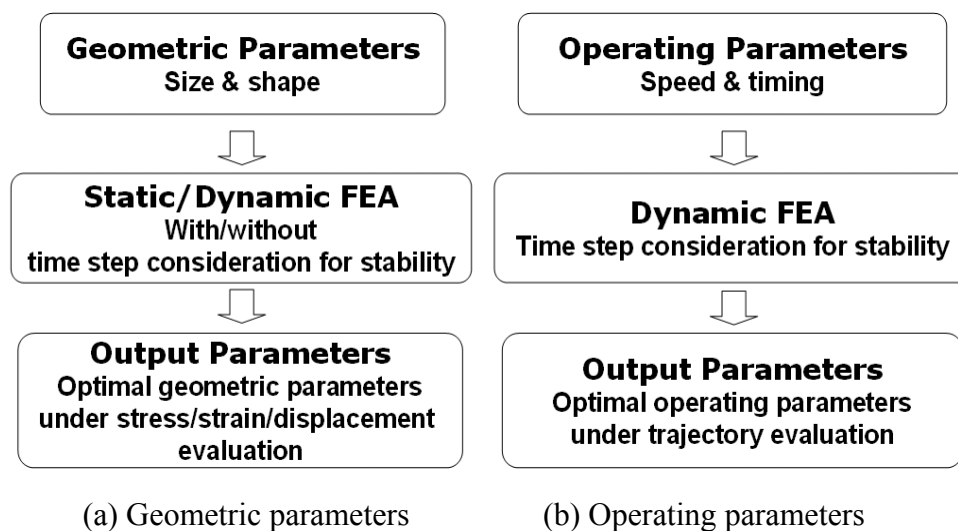


Figure 2-1 Comparison of two FEA based parameter-evaluation procedures

Figure 2-2 illustrates the procedure to analyze the dynamic performance of a flexible multibody system. This approach begins with the geometry model built using a general CAD (or CAE) package, and solves by the explicit dynamic FEA. The time step size for this method is a compromise between numerical stability and computation time. The dynamic modeling method is a framework incorporating explicit dynamic FEA, topology optimization, modal analysis, and damping modeling/identification. The dynamic response is evaluated iteratively until the input parameters meet the design requirement leading to a set of optimum parameters of the flexible multibody system.

The general-purpose numerical packages ANSYS, LS-DYNA, and LS-Prepost are used for pre-processing, solution, and post-processing respectively in this thesis. The finite element models are numerically programmed by the ANSYS Parametric Design Language (APDL) and LS-DYNA code. The general element types for explicit dynamic FEA are listed in Appendix A. The computation from the commercial FEA packages are experimentally validated against published data wherever applicable.

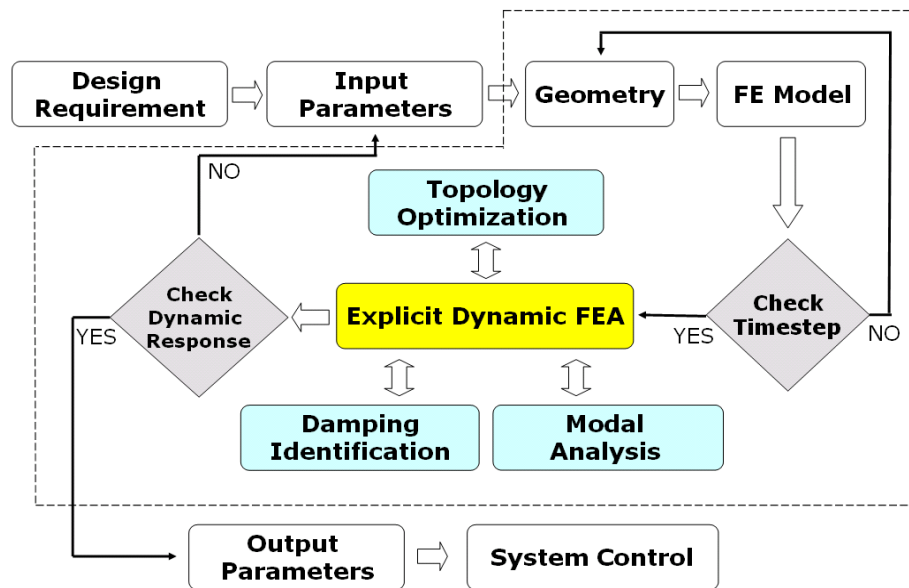


Figure 2-2 Procedure of the dynamic modeling method

The following sections provide an overview of the application problem (the development of the live-bird transfer system), and the formulations of the FEM modeling method for solving it. This overview begins with the methods to determine the numerical stability and the critical time step for explicit dynamic FEA. The contact model based on the penalty method, and the Coulomb friction model for the sliding contact will be introduced. The modal analysis will be examined by comparing FEA results against experiment [Zhu *et al.*, 2009; Guo *et al.*, 2009]. This analysis also offers information on the natural frequencies and mode shapes which are utilized to identify any failure at a screw connection. A coupled computational/experimental damping identification technique will be developed. Unlike the traditional damping identification methods (such as log decrement method in time domain and half-power bandwidth method in frequency domain) which are only valid for oscillatory responses, the method introduced here is capable of analyzing highly damped continuum structures. Finally, the formulation of topology optimization will be explained with two illustrative examples; a cantilever beam design, and locating ligaments of a biological structure.

2.2 Overview of the Application Problem

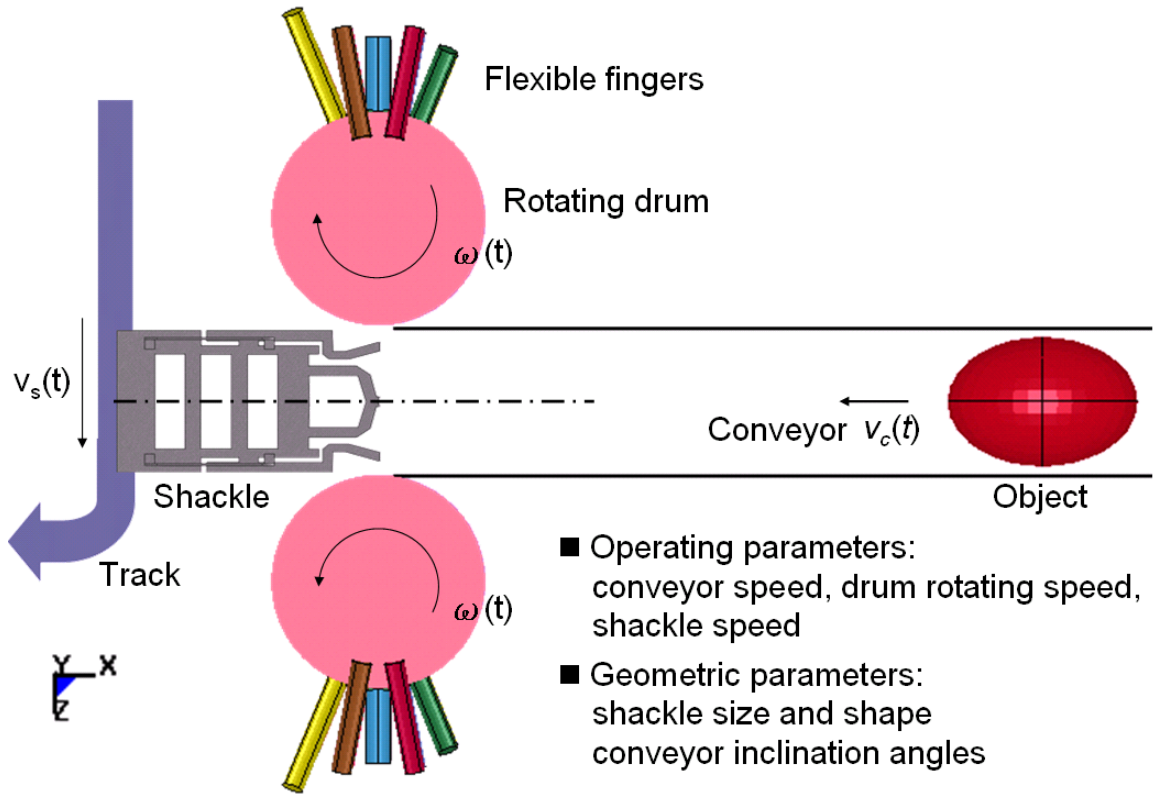
The modeling procedure is illustrated in Figure 2-2 in the context of practical application where live objects are transferred from conveyors to subsequent processing lines. In the poultry industry, the task requires workers to grasp live chickens by one or both legs and insert both legs into a shackle on the moving conveyor line typically running at speeds of 180 shackles per minute. The repetitive task is usually laborious, unpleasant and sometimes hazardous. Thus, the process of live birds handling is an ideal

candidate for automation [Lee, 1999]. The development of the live-bird transfer system [Lee *et al.*, 2009] has been chosen as an immediate application in this thesis research.

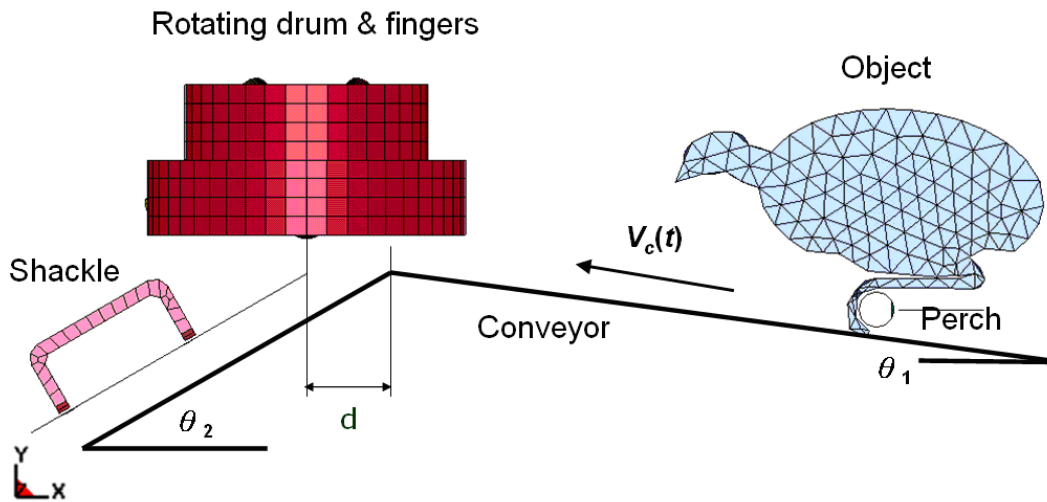
Figure 2-3a shows the plan view of the automated live-bird transfer system. The X-Z plane is symmetric about the centerline of the shackle. Figure 2-3b shows the sectional view at the symmetric plane. The handling operation consists of body-grasping, leg-gripping, and shackle-rotating/inverting processes. A typical cycle of the system starts with a conveyor moving at a velocity $v_c(t)$ which transports singulated chickens towards a pair of robotic hands rotating at an angular velocity $\omega(t)$. While the body of a live chicken is grasped by the compliant fingers, both of its legs are guided into a pair of grippers on the inclined shackle mechanism moved on a separate track. Once both legs of the chicken are gripped, the shackle mechanism rotates the leg-gripped chicken about the Y-axis at an angular velocity $\omega_y(t)$ out of the grasping area for inverting its body at an angular velocity $\omega_z(t)$. This is followed by locating the head of the inverted bird for subsequent electrical stunning to render it insensitive to pain for neck cutting.

A critical requirement [Lee, 1999] in the design of a live-bird transfer system is to ensure that live objects are handled without damage or stress and meet the production throughput requirement at a reasonable cost. The corresponding parameters (involved in the design analysis of the live-bird transfer system) include the following:

- *Input (operating) parameters:* Conveyor speed, drum speed, and corresponding timing specifications.
- *Geometric parameters:* Shackle shape/size, conveyor inclination, and relative distance of each component.
- *Output parameters:* Trajectory, deformation, stress, and contact locations between compliant fingers and object.



(a) Plan view



(b) Sectional view at the symmetric plane

Figure 2-3 Automated live-bird transfer system

The objectives are to analyze the design under different parameters, to predict the trajectory of the flexible multibody system, and to design an optimal shackle mechanism for a given cycle time.

2.3 Explicit Dynamic Finite Element Method

FEM simulates physical phenomena by converting a continuum into a discrete domain (nodes and elements) as shown in Figure 2-4. For a dynamic problem, the equation of motion can be derived from the work balance among the contributions of external load, inertial effect, viscosity, and strain energy.

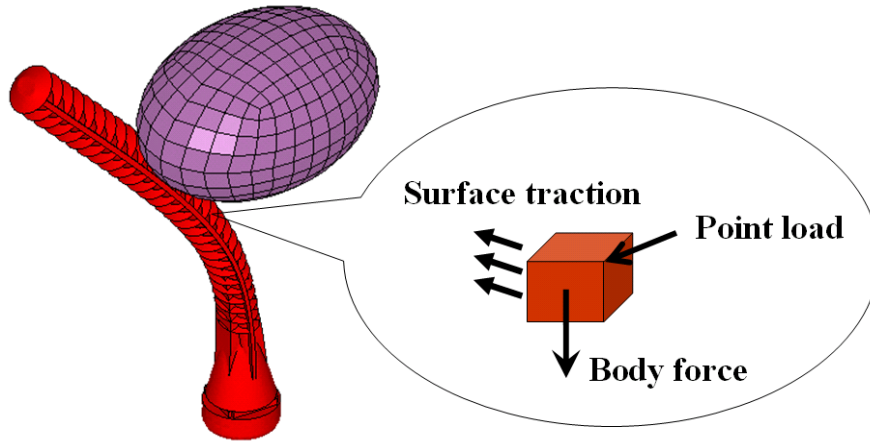


Figure 2-4 Illustrative scheme for dynamic FEA involving deformable contact

For a single element subjected to body force, surface traction, and point load, the work balance of the element (with density ρ , viscous damping coefficient c , volume V , and surface S) is given by Equation (2-1):

$$\int \{\delta u\}^T \{f\} dV + \int \{\delta u\}^T \{t\} dS + \sum_{i=1}^n \{\delta u\}_i^T \{p\}_i = \int (\{\delta u\}^T \rho \{\ddot{u}\} + \{\delta u\}^T c \{\dot{u}\} + \{\delta \varepsilon\}^T \{\sigma\}) dV \quad (2-1)$$

In Equation (2-1), the first, second and third terms on the left hand side denote the work done by the body force $\{f\}$, surface traction $\{t\}$ and the concentrated load $\{p\}$ respectively; the first, second and third terms on the right hand side denote the work done by inertial effect, viscosity, and strain energy respectively; the notation $\{\}$ represents a vector; $\{\delta u\}$ is the virtual displacement; $\{\delta \varepsilon\}$ is the corresponding strain to the virtual displacement; and $\{u\}$ is the displacement which is function of space and time.

In FE formulation, the displacement $\{u\}$ over an element can be represented by the interpolating functions and nodal degree-of-freedom (DOF) as in Equation (2-2):

$$\{u\} = [N]\{x\} \quad (2-2)$$

where the space-dependent interpolation (or shape) function matrix $[N]$ can be determined according to the element types; and $\{x\}$ is the nodal DOF dependent on time only. With the aid of interpolation functions, strain and stress are giving by Equation (2-3a) and (2-3b) respectively.

$$\{\varepsilon\} = [B]\{x\}; \quad \{\sigma\} = [E]\{\varepsilon\} = [E][B]\{x\} \quad (2-3a,b)$$

where $[B]$ is a strain-displacement matrix (space derivative of the interpolation function matrix $[N]$); and $[E]$ is a stress-strain matrix. With Equations (2-2) and (2-3a,b), Equation (2-1) can be rewritten as Equation (2-4) in terms of element mass, damping, and stiffness matrices as well as the external load, which are denoted by $[m]$, $[c]$, $[k]$ and $\{r_{ext}\}$ respectively in Equation (2-4a~d):

$$[m]\{\ddot{x}\} + [c]\{\dot{x}\} + [k]\{x\} = \{r_{ext}\} \quad (2-4)$$

$$[m] = \int \rho [N]^T [N] dV \quad (2-4a)$$

$$[c] = \int c [N]^T [N] dV \quad (2-4b)$$

$$[k] = \int [B]^T [E] [B] dV \quad (2-4c)$$

$$\{r_{ext}\} = \int [N]^T [f] dV + \int [N]^T \{t\} dS + \sum_{i=1}^n \{p\}_i \quad (2-4d)$$

By assembling the above element matrices, the equation of motion for the whole domain being analyzed is given by Equation (2-5):

$$[M]\{\ddot{X}\} + [C]\{\dot{X}\} + [K]\{X\} = \{F\} \quad (2-5)$$

where $[M]$, $[C]$, and $[K]$ are the global mass, damping, and stiffness matrices respectively; and $\{X\}$ and $\{F\}$ are the global nodal DOF and load vectors respectively. In this thesis, the numerical packages ANSYS will be used to create the discrete domain $\{X\}$, and LS-DYNA (which is an explicit time integration solver) will be used to solve the equation of motion.

2.3.1 Explicit Time Integration

The time integration of the dynamic equation can be broadly divided into explicit and implicit methods; their forms are given respectively in Equations (2-6a) and (2-6b).

$$U_{n+1}|_{exp} = f(U_n, \dot{U}_n, \ddot{U}_n, U_{n-1}, \dots) \quad (2-6a)$$

$$U_{n+1}|_{imp} = f(U_n, \dot{U}_{n+1}, \ddot{U}_{n+1}, \dots) \quad (2-6b)$$

where the subscript n denotes the time at $t=n\Delta t$, and Δt is the time step.

For *explicit methods*, the unknown quantities for the next time instant $(n+1)\Delta t$ is a function of known quantities for the current time $n\Delta t$ or previous time $(n-1)\Delta t$. So the displacement for the next time instant can be solved directly from the information at the current or previous time instants. For *implicit methods*, the unknown quantities for the next time instant $(n+1)\Delta t$ appear in both sides of the equation, and the solution needs to

be solved simultaneously from a system of equations. Thus, implicit methods require more computation than explicit methods within each time step. However, unlike implicit methods that are stable for linear and many nonlinear problems, explicit methods are only stable when the time step is smaller than a critical value. If the time step is too large, the method is numerically unstable. On the other hand, computation could become expensive if time step is smaller than necessary. The procedure of the explicit time integration (based on the central difference scheme) can be found in [Hallquist, 1998]. The following practical considerations will be discussed in the following sections; critical time step and numerical stability; element size and shape effect; characteristic length and material properties effect.

The explicit method, where unknowns in the next time step are solved directly from the information at current (or previous) time instant, is employed for the time integration of Equation (2-5). The explicit method requires significantly less computation within each time step than the implicit method. However, it is only stable when the time step Δt satisfies Equation (2-7) for the numerical stability [Mullen and Belytschko, 1983; Cook *et al.*, 2001], where ω_{max} is the highest natural frequency.

$$\Delta t \leq \frac{2}{\omega_{max}} \quad (2-7)$$

2.3.2 Critical Time Step and Numerical Stability

The critical time step depends on the material properties, and element size and shape. As an illustration, consider a classical 1D finite element formulation of an undamped free vibrating rod. The eigenvalue problem can be written as Equation (2-8):

$$\det(K - \omega^2 M) = 0 \quad (2-8)$$

where K and M are the stiffness and mass matrices. The stiffness matrix can be derived from the weak form formulation in Equation (2-9):

$$0 = \int_{x_a}^{x_b} w(x) \left[-\frac{d}{dx} \left(a(x) \frac{du(x)}{dx} \right) + c(x)u(x) \right] - f(x) dx \quad (2-9)$$

where $u(x)$ is the unknown function; $w(x)$ is the weight function; (x_a, x_b) is the domain of an element; and $a(x)$, $c(x)$, and $f(x)$ are the known quantities. The physical interpretation of these functions can be found in Appendix B. By multiplying the second order governing differential equation with the weight function, then integrating (using integration by parts) over a element from x_a to x_b , the weak form Galerkin finite element model is given by Equation (2-10):

$$0 = \int_{x_a}^{x_b} \left[a(x) \frac{dw(x)}{dx} \frac{du(x)}{dx} + c(x)w(x)u - w(x)f(x) \right] dx - w(x_a)Q_1 - w(x_b)Q_2 \quad (2-10)$$

where $Q_1 = \left(-a(x) \frac{du}{dx} \right) \Big|_{x_a}$; $Q_2 = \left(a(x) \frac{du}{dx} \right) \Big|_{x_b}$ (2-11)

The polynomial approximation of the solution over each finite element can be written with the aid of the Lagrange interpolation function ψ_j^e :

$$u = \sum_{j=1}^n u_j^e \psi_j^e(x) \quad (2-12)$$

Substituting Equation (2-12) into Equation (2-9) yields:

$$0 = \sum_{j=1}^n K_{ij}^e u_j^e - f_i^e - Q_i^e \quad (i=1, 2, \dots, n) \quad (2-13)$$

where e denotes element, and

$$K_{ij}^e = \int_{x_a}^{x_b} \left(a_e \frac{d\psi_i^e}{dx} \frac{d\psi_j^e}{dx} + c_e \psi_i^e \psi_j^e \right) dx \quad (2-14)$$

$$f_i^e = \int_{x_a}^{x_b} f_e \psi_i^e dx \quad (2-15)$$

For structural mechanics application, K_{ij}^e is the stiffness matrix, and f_i^e is the force vector in global coordinate system x . Equation (2-14) and (2-15) can be transferred into the local coordinate system \bar{x} in Equation (2-16) and (2-17):

$$K_{ij}^e = \int_0^{L_e} \left(a_e \frac{d\psi_i^e}{d\bar{x}} \frac{d\psi_j^e}{d\bar{x}} + c_e \psi_i^e \psi_j^e \right) d\bar{x} \quad (2-16)$$

$$f_i^e = \int_0^{L_e} f_e \psi_i^e d\bar{x} \quad (2-17)$$

$$\text{where } x = x_a + \bar{x} \ ; \ dx = d\bar{x} \ ; \ \frac{d\psi_i^e}{dx} = \frac{d\psi_i^e}{d\bar{x}} \quad (2-18)$$

By substituting the linear Lagrange interpolation functions in Equation (2-19) into Equation (2-16) and (2-17), K_{ij}^e and f_i^e can be obtained in the matrix form as Equation (2-20) and (2-21):

$$\psi_1^e(\bar{x}) = 1 - \frac{\bar{x}}{L_e} \ ; \ \psi_2^e(\bar{x}) = \frac{\bar{x}}{L_e} \quad (2-19)$$

$$[K_e] = \frac{a_e}{L_e} \begin{pmatrix} 1 & -1 \\ -1 & 1 \end{pmatrix} + \frac{c_e L_e}{6} \begin{pmatrix} 2 & 1 \\ 1 & 2 \end{pmatrix} \quad (2-20)$$

$$\{f_i^e\} = \frac{f_e L_e}{2} \begin{Bmatrix} 1 \\ 1 \end{Bmatrix} \quad (2-21)$$

where L_e is the element length.

For axial deformation of structural mechanics application with uniform cross section and homogeneous material properties, $a_e = EA$, $c_e = 0$ (Appendix B), which yields the stiffness matrix in Equation (2-22):

$$[K_e] = \frac{AE}{L_e} \begin{pmatrix} 1 & -1 \\ -1 & 1 \end{pmatrix} \quad (2-22)$$

where A is cross sectional area; E is elastic modulus; and ρ is density.

For the mass matrix in Equation (2-8), it can be approximated by using lumped masses at the two nodes, which yields Equation (2-23):

$$[M_e] = \frac{\rho AL_e}{2} \begin{bmatrix} 1 & 0 \\ 0 & 1 \end{bmatrix} \quad (2-23)$$

From above, the eigenvalue problem in Equation (2-8) can be written in the matrix form as in Equation (2-24):

$$\det \left(\frac{AE}{L_e} \begin{bmatrix} 1 & -1 \\ -1 & 1 \end{bmatrix} - \omega^2 \frac{\rho AL_e}{2} \begin{bmatrix} 1 & 0 \\ 0 & 1 \end{bmatrix} \right) = 0 \quad (2-24)$$

The above implies:

$$\omega_{\max} = \frac{2}{L_e} \sqrt{\frac{E}{\rho}} = \frac{2c_w}{L_e} \quad (2-25)$$

where c_w is the wave propagation speed; and L_e is the characteristic length (equal to element length for 1D problem). From the criteria given by Equation (2-7), the conditionally stable time step (also known as the CFL condition) can be obtained by substituting (2-25) into (2-7), which yields Equation (2-26):

$$\Delta t \leq \Delta t|_{critical} = \frac{L_e}{c_w} \quad (2-26)$$

The physical interpretation of Equation (2-26) is that the time step must be small enough so the wave would not propagate across more than one element within each time step.

As elements deform, the time step must be calculated at each time instant for each element, (Δt_i , $i=1 \sim n$, n is element number). For stability consideration, the numerical time step given in Equation (2-27) must be smaller than the critical time step, which is the smallest value in the global analysis domain.

$$\Delta t_{num} = a \times \min\{\Delta t_1, \Delta t_2, \dots, \Delta t_n\} \quad (2-27)$$

where a is a scale factor between 0~1, and it is set as 0.9 in this thesis.

2.3.3 Formulations of Critical Time Step for Different Elements

The discussion on time step calculation for different element types (beam, triangular and quadrangular shell, and tetrahedral and hexahedral solid elements) can be found in [Hallquist, 1998], upon which the formulations are organized in Table 2-1 for ease of comparison, where L_i is the length of the sides defining the shell elements; Q is a function of the bulk viscosity coefficients C_0 and C_1 ; $\dot{\varepsilon}$ is the strain rate; V_e is the volume of the element; and A_{emax} is the area for the largest side of the element.

Table 2-1 Critical time step formulations

Element Type	Critical Time Step (Δt)	Characteristic Length (L_e)	Wave Propagation Speed (c_w)
Beam	$\Delta t = \frac{L_e}{c_w}$	$L_e = \text{element length}$	$c_w = \sqrt{\frac{E}{\rho}}$
Quadrangular Shell	$\Delta t = \frac{L_e}{c_w}$	$L_e = \frac{A}{\max(L_1, L_2, L_3, L_4)}$	$c_w = \sqrt{\frac{E}{\rho(1-\nu^2)}}$
Triangular Shell	$\Delta t = \frac{L_e}{c_w}$	$L_e = \frac{2A}{\max(L_1, L_2, L_3)}$	$c_w = \sqrt{\frac{E}{\rho(1-\nu^2)}}$
Hexahedral Solid	$\Delta t = \frac{L_e}{[Q + \sqrt{(Q^2 + c_w^2)}]}$ $Q = C_1 c_w + C_0 L_e \dot{\varepsilon}_{kk} , \dot{\varepsilon}_{kk} < 0$ $= 0, \dot{\varepsilon}_{kk} \geq 0$	$L_e = \frac{V_e}{A_{e\max}}$	$c_w = \sqrt{\frac{E(1-\nu)}{\rho(1+\nu)(1-2\nu)}}$
Tetrahedral Solid	$\Delta t = \frac{L_e}{[Q + \sqrt{(Q^2 + c_w^2)}]}$ $Q = C_1 c_w + C_0 L_e \dot{\varepsilon}_{kk} , \dot{\varepsilon}_{kk} < 0$ $= 0, \dot{\varepsilon}_{kk} \geq 0$	$L_e = \text{minimum altitude}$	$c_w = \sqrt{\frac{E(1-\nu)}{\rho(1+\nu)(1-2\nu)}}$

As summarized in Table 2-1, the critical time step is a function of the element size and shape as well as the material properties (elastic modulus, density and Poisson ratio). The corresponding effects of these parameters and illustrative examples are discussed in following sections.

2.3.4 Effect of Element Size and Shape

Figure 2-5 shows three different elements (a triangular, and two different-size quadrangular shell elements). The corresponding critical time step calculations (based on the formulations listed in Table 2-1) are given in Table 2-2.

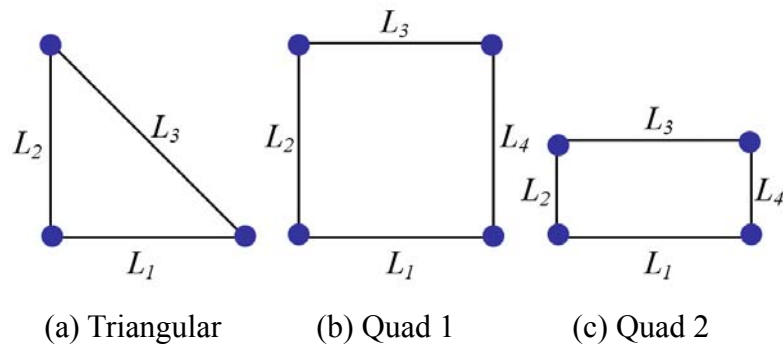


Figure 2-5 Illustration examples for different element size and shape effect

Table 2-2 Effects of element size and shape on the critical time step

Shell Element	L_1, L_2 (m)	L_e (m)	C_w (m/s)	Δt (μ s)	# Steps to 1ms
Triangular	0.01, 0.01	0.0071	5355.3	1.32	758
Quad 1	0.01, 0.01	0.01	5355.3	1.87	535
Quad 2	0.01, 0.005	0.005	5355.3	0.93	1070

(Material: AL6061, elastic modulus: 69GPa, density: 2700 kg/m³, Poisson ratio: 0.33)

Considering only the effect of time step, Table 2-2 tabulates the number of steps needed to solve a 1-millisecond dynamic problem for each element in terms of element

dimensions L_i , wave propagation speed C_w , characteristic length L_e and critical time step Δt . As compared in Table 2-2, Quad 1 requires the smallest number of steps; twice of that for Quad 2, and 1.4 of that for the triangular element for the same L_1 and L_2 . These time-step calculations suggest that the uniform mesh with regular quadrangular (or hexahedral solid) elements need less-computation. In addition, Equation (2-27) shows that the critical time step is dominated by the smallest element in the global analysis domain. Thus, a well-planned mesh with regular quadrangular and hexahedral elements is highly preferred for the explicit dynamic FEA.

2.3.5 Effect of Characteristic Length and Material Properties

Figure 2-6 shows the effect for characteristic length and material properties (elastic modulus, density, and Poisson ratio) on the critical time step calculation for the quadrangular shell element (the formulations are listed in Table 2-1). When studying the effect of a parameter, the values of all other parameters remain unchanged as listed in Table 2-3. For example, the density effect curve is computed for the range from 100 kg/m³ to 5000 kg/m³ while other properties are keep at $E=70\text{GPa}$, $\nu=0.3$, and $L_e=0.01\text{m}$.

Table 2-3 Effects of parameters on time step calculation

Item effect to time step	E (GPa)	ρ(kg/m³)	L_e (mm)	ν
Elastic modulus curve	10 to 500	2700	10	0.3
Density curve	70	100 to 5000	10	0.3
Char. length curve	70	2700	1 to 25	0.3
Poisson ratio curve	70	2700	10	0 to 0.5

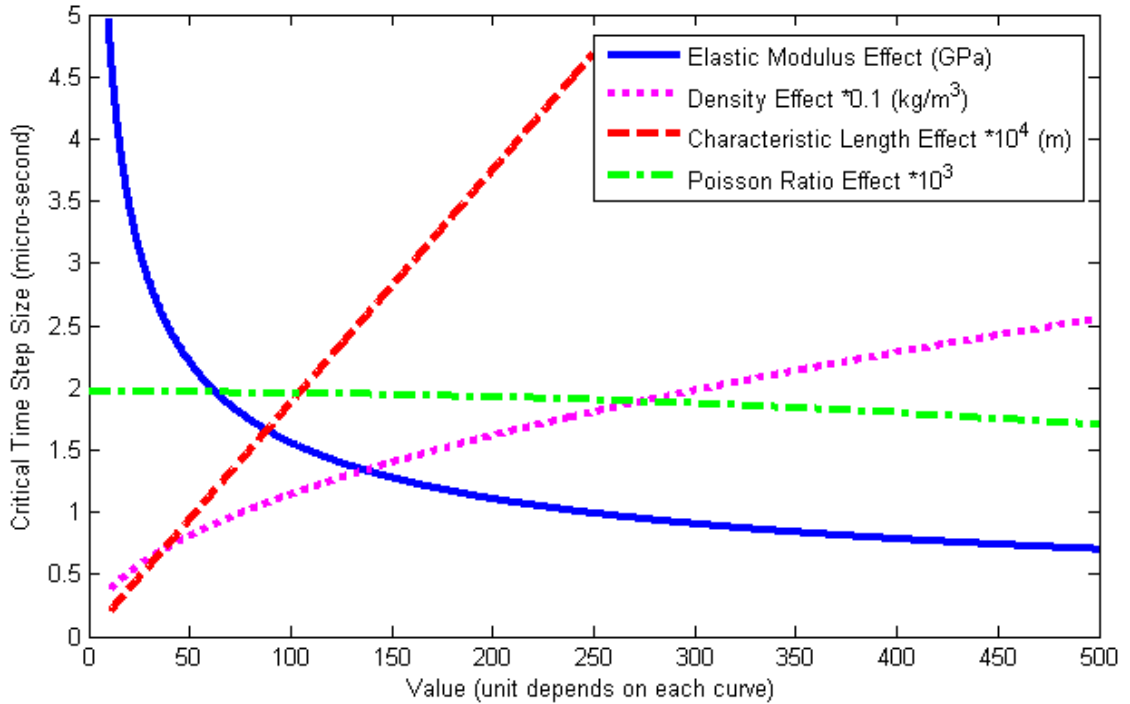


Figure 2-6 Effects of characteristic length and material properties on critical time step

Some observations drawn from Figure 2-6 are discussed below:

1. Among the material properties, the critical time step is most sensitive to small elastic modulus but relatively insensitive to Poisson ratio. A larger density can lead to a larger critical time step.
2. The characteristic length, which is linearly proportional to critical time step, implies that mesh quality must be carefully considered and well planned. Provided that mesh density satisfies the accuracy requirement, smaller elements should be avoided since it is computationally expensive.
3. Since a smaller elastic modulus results in a larger critical time step, it implies soft materials can have larger mesh density compared to stiff materials.
4. Since larger density can lead to larger critical time step. An effective way to increase the critical time step is to scale the mass of few smallest elements to effectively

increase their density. As long as the increased mass is very small as compared to the overall mass, and not in a critical region, its effect on the global dynamics can be neglected.

2.3.6 Contact Model

For dynamic problems involving deformable contacts, the problem is treated as the interaction between two (or more) bodies. The load vector $\{F\}$ in Equation (2-5) includes contact forces at the interface. The penalty method [Hallquist, 1998], which checks each node for penetration through the contact interface, will be applied in formulating the contact problem.

Physically, contact can be interpreted as a constraint that the two bodies (Ω_A and Ω_B , bounded by the boundaries Γ_A and Γ_B respectively) can not penetrate into each other as illustrated in Figure 2-7, where $\mathbf{x}_A(X, t)$ and $\mathbf{x}_B(X, t)$ represent the deformed coordinate of an arbitrary particle on the bodies; and X is the original un-deformed coordinate of a particle A and B respectively at time t .

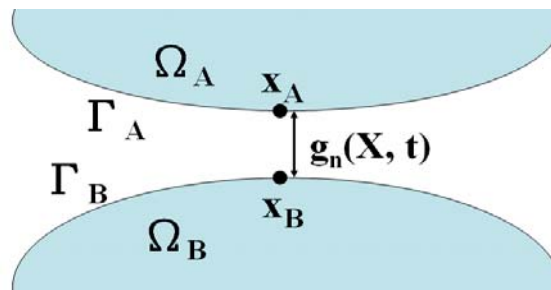


Figure 2-7 Contact between two deformable bodies

Mathematically,

$$\Omega_A \cap \Omega_B = \emptyset \quad (2-28)$$

Although the contact constraint in Equation (2-28) can be easily understood, it is inconvenient to handle numerically. Thus, the contact problem is formulated as a displacement constraint on the discretized nodes. The distance between two particles on Γ_A and Γ_B can be expressed as a gap function $g_n(X, t)$, which obeys the rules in Equation (2-29):

$$\begin{aligned}
 g_n(X, t) &> 0, \text{ when two points are not in contact} \\
 &= 0, \text{ when two points are at contact} \\
 &< 0, \text{ penetration occurs}
 \end{aligned}
 \tag{2-29}$$

The first two conditions in Equation (2-29) state that the distance between the two points at the same contact should be zero when the two bodies are in contact; or greater than zero when they depart. The last condition in Equation (2-29) is physically invalid since the two bodies can not move into each other. However, small penetration is necessary numerically and assumed in the penalty method as follows [Hallquist, 1998]:

$$f_n = -k_n g_n \tag{2-30}$$

$$\text{where } k_n = \frac{s_f B A^2}{V} \text{ for solid element} \tag{2-30a}$$

$$k_n = \frac{s_f B A}{\max(\text{shell_diagonal})} \text{ for shell element} \tag{2-30b}$$

In Equation (2-30), the normal interface force f_n is proportional to g_n in terms of the penalty (interface) stiffness k_n ; in which B is the bulk modulus (function of elastic modulus and Poisson ratio); A and V are the area and volume (of the element) in contact; and s_f is a scale factor (the suggest value is 1).

The bulk modulus is defined as hydrostatic stress divided by volumetric strain. The

volumetric strain is the ratio of change to the original volume. For an isotropic material, the volumetric strain can be expressed in terms of stress (by the aid of generalized Hook's law) given by Equation (2-31):

$$\varepsilon_v = \frac{dV}{V} = \varepsilon_x + \varepsilon_y + \varepsilon_z = \frac{1-2\nu}{E}(\sigma_x + \sigma_y + \sigma_z) \quad (2-31)$$

The hydrostatic stress is defined as the average normal stress given by Equation (2-32):

$$\sigma_h = \frac{\sigma_x + \sigma_y + \sigma_z}{3} \quad (2-32)$$

Finally, bulk modulus can be obtained in Equation (2-33):

$$B = \frac{\sigma_h}{\varepsilon_v} = \frac{E}{3(1-2\nu)} \quad (2-33)$$

which yields the bulk modulus to be a function in terms of elastic modulus and Poisson ratio. One observation from the volumetric strain equation is that a perfectly incompressible material would have a Poisson ratio of exactly 0.5, which makes a zero volumetric strain.

In applying this penalty method, each slave node is checked for penetration through the master surface. If the slave node does not penetrate, nothing is done. If it does penetrate, an interface force is applied between the slave node and its contact point. The magnitude of this force is proportional to the amount of penetration. This penalty approach may be thought of as the addition of a normal interface spring between contact locations. Once the normal contact force is obtained, the friction force is then given by the product of the normal force and the friction coefficient.

2.3.7 Colomb Friction

Coulomb friction (dry friction) resists relative lateral motion of two solid surfaces in

contact. The dry friction effect also refers to Coulomb damping or dry friction damping. The friction force can be solved based on Coulomb formulation given by equation (2-34):

$$f_f = \mu f_n \quad (2-34)$$

In Equation (2-34), f_f is the friction force; f_n is the normal force; and the friction coefficient μ for the contact surface is given by Equation (2-35):

$$\mu = \mu_d + (\mu_s - \mu_d) e^{-c_d * |v_r|} \quad (2-35)$$

where μ_s is the static coefficient of friction; μ_d is the dynamic coefficient of friction; c_d is the exponential decay coefficient (the presume value is 0); and v_r is the relative velocity (between the slave node and the master segment) of the surface in contact.

2.4 Modal Analysis

Modal analysis is a commonly used method to determine the natural frequencies and mode shapes of a structure, which are important parameters for a structure under dynamic loading conditions. In addition, these modal parameters are also expected to be used for crack detection in structural health monitoring (SHM). In this section, the basic formulation of modal analysis will be introduced and followed by an illustrative example in analyzing a portal frame structure. Results of numerical simulation will be compared against the published experimental data [Zhu *et al.*, 2009; Guo *et al.*, 2009]. The effect of the failure at screw connection on the natural frequencies and mode shapes will also be investigated.

2.4.1 Basic Formulation

The undamped dynamic system is formulated to solve for the free vibration response.

In classical modal analysis, the damping and external loading terms in Equation (2-5) are set to zero reducing the equation of motion to Equation (2-36):

$$[M]\{\ddot{X}\} + [K]\{X\} = 0 \quad (2-36)$$

Assuming that the displacements have the form:

$$\{X\} = \{\phi\}e^{i\omega t} \quad (2-37)$$

Substituting Equation (2-37) into Equation (2-36), the eigenvalue equation can be obtained in Equation (2-38):

$$([K] - \omega^2[M])\{\phi\} = 0 \quad (2-38)$$

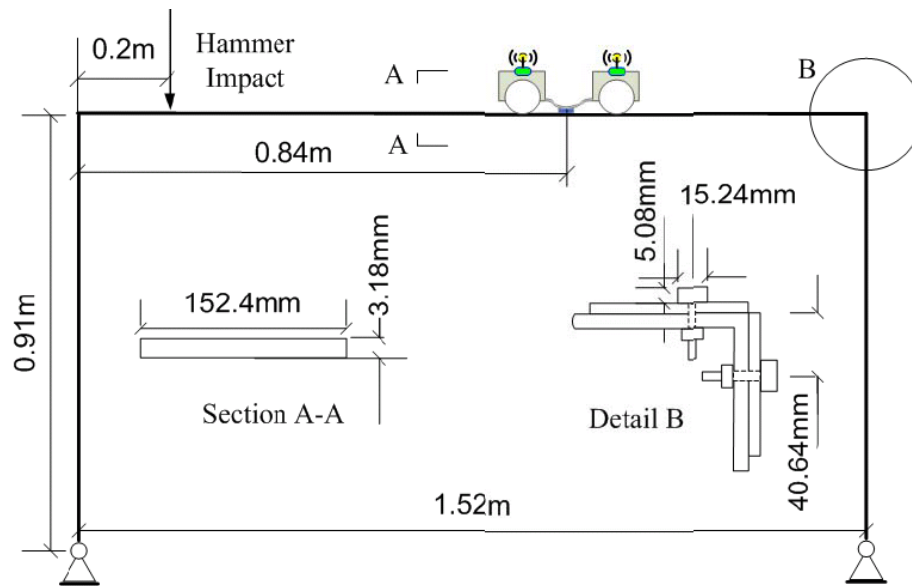
Many numerical methods are available to solve Equation (2-38) such as Block Lanczos method, Subspace method, and Householder method, which are also referred to mode extraction methods. In this thesis, ANSYS that uses the Block Lanczos method is applied for the mode extraction.

2.4.2 Illustrative Example in Analyzing a Portal Frame Structure

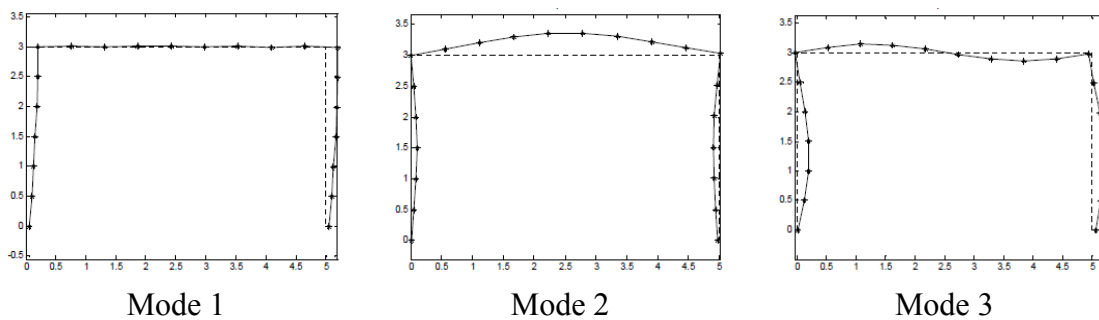
Consider the steel portal frame structure given in Figure 2-8a since the published experimental data [Zhu *et al.*, 2009; Guo *et al.*, 2009] are available for comparison. The interest here is to solve for the natural frequencies and mode shapes of the structure. In this experiment, a hammer impact is applied on the steel frame and the dynamic response is measured by accelerometers both fixed and in a wireless mobile car. Then the time domain response can be transferred into frequency domain by the fast Fourier transform (FFT). The experimentally obtained mode shapes are given in Figure 2-8b.

Two FE models as shown in Figure 2-9 and Table 2-4 are considered; single part and assembled models. The commonly used simplified single part model neglects the assembled screws and assumes the portal frame structure as a perfectly combined single

component while the assembled model considers the screw modeling by coupling the DOF at the connection interface. As in Figure 2-9b, the horizontal and vertical plates are connected by the L-shape brackets and fixed by totally 16 screws. The comparison of natural frequencies obtained by FEM and experiment are shown in Figure 2-10 and Table 2-5.



(a) Portal frame structure [Guo *et al.*, 2009]



(b) First three mode shapes by modal testing [Zhu *et al.*, 2009]

Figure 2-8 Portal frame structure and its first three mode shapes

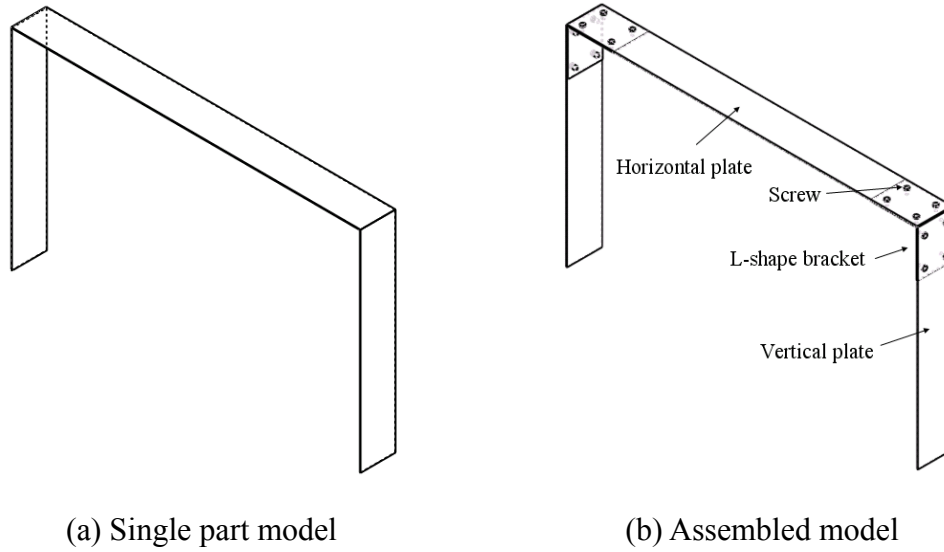


Figure 2-9 Finite element modeling for the portal frame structure

Table 2-4 Finite element modeling of the portal frame structure

FE Model	Screw Modeling	Element Type	Element#	Node#
Single Part Model	No	SHELL93	5392	16883
Assembled Model	Yes	SHELL93	6736	21215

($E=210$ GPa, $\nu=0.28$, $\rho=7700$ kg/m³)

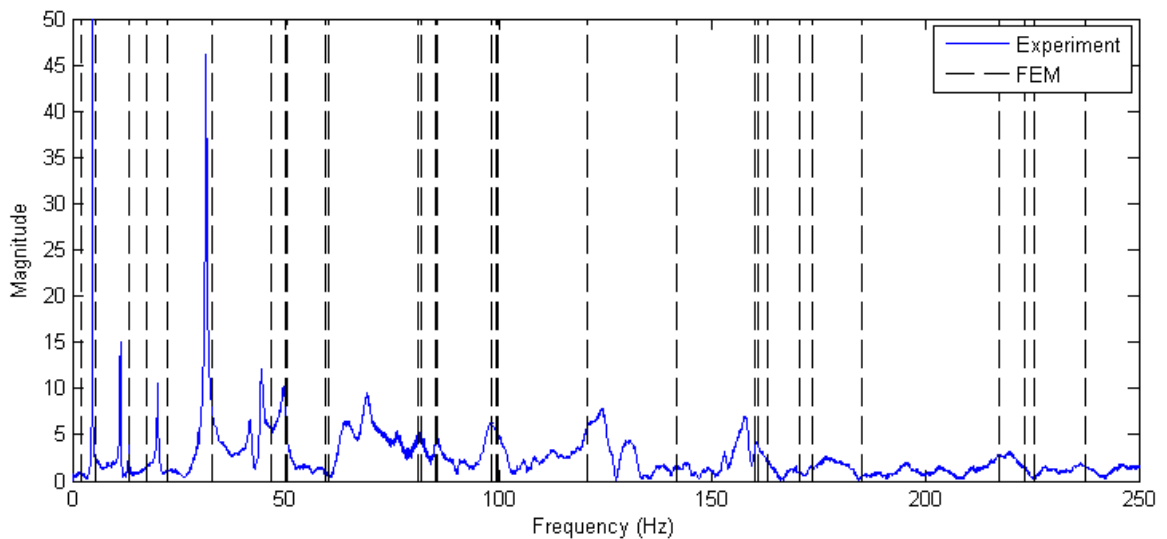


Figure 2-10 Comparison of experiment and FEM modal analysis (assembled model)

Table 2-5 Comparison of natural frequencies obtained by FEM and experiment

Mode	Assembled Model Freq. (Hz)	Single Part Model		Experiment	
		Freq. (Hz)	Difference (%)	Freq. (Hz)	Difference (%)
1	2.1	2.3	10.23	2	-5.32
2	5.5	5.2	-4.45	4.7	-13.95
3	13.4	13.8	3.11	11.2	-16.57
4	17.2	17.2	-0.01	-	-
5	22.3	21.6	-3.11	20.1	-9.84
6	32.8	34.0	3.83	31.3	-4.46
7	46.6	45.4	-2.41	44.3	-4.85
8	49.9	49.1	-1.68	49.5	-0.83
9	50.5	52.4	3.78	-	-
10	59.2	62.9	6.23	-	-
11	59.9	67.5	12.70	-	-
12	81.1	78.8	-2.84	81.3	0.21
13	82.0	79.2	-3.41	-	-
14	85.3	87.1	2.09	85.4	0.11
15	85.5	91.8	7.37	-	-
16	98.4	103.3	4.96	98.2	-0.20
17	99.3	103.5	4.15	-	-
18	99.8	107.7	7.90	-	-
19	120.8	129.9	7.55	124.2	2.82
20	141.6	139.2	-1.74	141.6	-0.01
21	160.0	161.5	0.96	160.5	0.34
22	160.9	162.3	0.85	-	-
23	163.1	162.9	-0.12	-	-
24	170.3	176.3	3.52	169.4	-0.53
25	173.3	185.2	6.89	173.1	-0.12
26	185.1	189.9	2.58	185.9	0.41
27	217.2	222.8	2.60	217.1	-0.04
28	223.1	239.6	7.41	222.8	-0.13
29	225.4	251.2	11.46	-	-
30	237.4	252.3	6.26	237	-0.17

From the experimental result [Guo *et al.*, 2009] and FEM simulation, the natural frequencies of the assembled model are closer to the experiment when that of the single part model. The difference between simulation and experiment may result from the material properties of the steel frame used in the simulation, and the accuracy of the accelerometer in time domain measurement. Some mode shapes of the single part model are different comparing to the assembled model. Figure 2-11 shows the first four significantly changed mode shapes. The first 30 mode shapes of the assembled model are summarized in Appendix C. The numerical modal analysis offers additional information such as out of plane mode shapes, torsion (mode 9) and out of plane bending (mode 11), generally difficult to obtain experimentally.

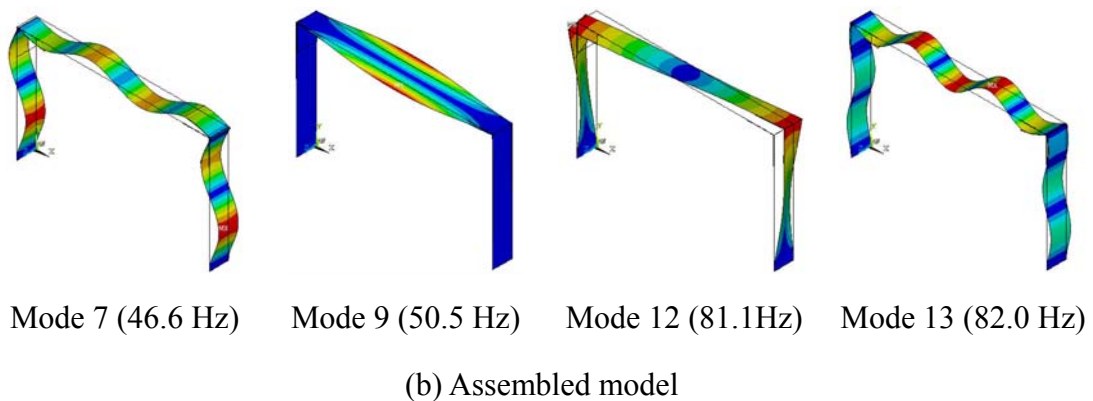
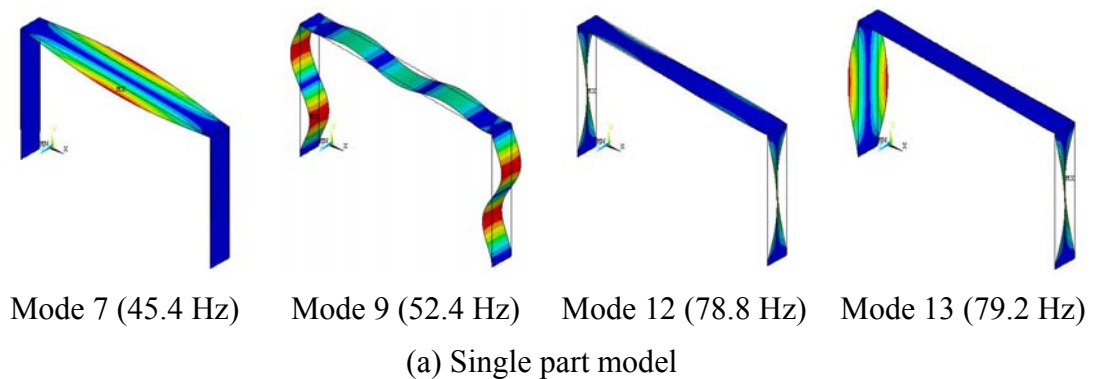


Figure 2-11 Comparison of significantly changed first four mode shapes

Measuring natural frequencies and mode shapes can be used to detect cracks in structural health monitoring. In order to study the effect of failure at the bolt connection on the modal parameters, two cases (missing 1 and 2 screws respectively as shown in Figure 2-12) are analyzed. The first 30 natural frequencies (solved by FEM modal analysis) are summarized in Table 2-6, and the corresponding mode shapes are given in Appendix C.

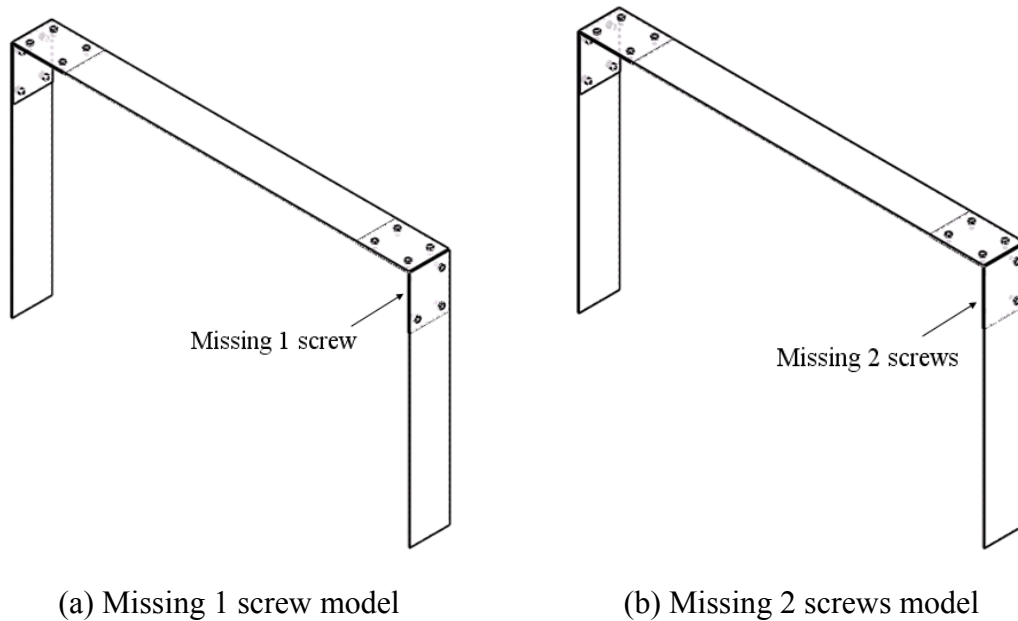


Figure 2-12 Analysis cases on missing-screw effect

Table 2-6 Comparison of missing-screw effect on natural frequencies

Mode	Assembled Model Freq. (Hz)	Missing 1 Screw Model		Missing 2 Screws Model	
		Freq. (Hz)	Difference (%)	Freq. (Hz)	Difference (%)
1	2.1	2.1	-0.15	2.1	-0.31
2	5.5	5.4	-0.30	5.4	-0.61
3	13.4	13.4	-0.08	13.4	-0.25
4	17.2	17.2	-0.06	17.1	-0.51
5	22.3	22.2	-0.21	22.1	-0.71
6	32.8	32.7	-0.25	32.6	-0.55
7	46.6	46.4	-0.31	46.0	-1.12
8	49.9	49.7	-0.38	49.2	-1.53
9	50.5	50.5	-0.03	50.4	-0.05
10	59.2	59.1	-0.19	58.6	-1.14
11	59.9	59.9	-0.03	59.7	-0.27
12	81.1	78.6	-3.11	68.7	-15.34
13	82.0	81.4	-0.69	81.1	-1.01
14	85.3	82.2	-3.70	81.5	-4.44
15	85.5	85.5	0.00	85.5	-0.01
16	98.4	97.1	-1.32	94.8	-3.70
17	99.3	99.1	-0.28	99.0	-0.34
18	99.8	99.8	-0.01	99.5	-0.22
19	120.8	120.7	-0.11	120.1	-0.55
20	141.6	130.4	-7.93	123.8	-12.61
21	160.0	143.0	-10.62	141.6	-11.48
22	160.9	160.8	-0.09	154.2	-4.18
23	163.1	161.9	-0.70	161.6	-0.89
24	170.3	169.2	-0.67	164.5	-3.38
25	173.3	172.7	-0.34	172.4	-0.51
26	185.1	184.6	-0.29	176.4	-4.75
27	217.2	196.8	-9.38	188.6	-13.15
28	223.1	217.2	-2.66	199.5	-10.56
29	225.4	224.1	-0.58	216.8	-3.80
30	237.4	225.7	-4.95	224.9	-5.29

(Corresponding mode shapes are given in Appendix C)

For the ease of comparison, some mode shapes (mode 12, 20, 21, and 27) where natural frequencies are significantly changed are summarized in Figure 2-13 and discussed as follows:

1. The natural frequencies and mode shapes remain the same at lower modes while higher modes are changed when there is a failure at the screw connection. The natural frequencies are decreased for missing-screw models since missing screws reduce the stiffness of the structure.
2. The first significant change occurs at mode 12. The natural frequency decreases 3.11% for the missing 1 screw model, while the missing 2 screws model is 15.34%. The mode shapes are also changed as shown in Figure 2-13.
3. The largest change in natural frequency for the missing 1 screw model occurs at mode 21 (-10.62%), while the missing 2 screws model is mode 12 (-15.34%).
4. From Table 2-6, the natural frequencies change more sharply in the missing 2 screws model than that in the missing 1 screw model implying a larger crack.

The above simulation shows that modal analysis can be applied for the structural health monitoring.

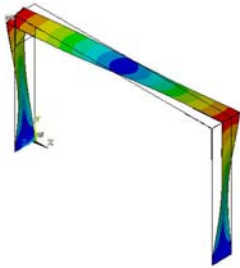
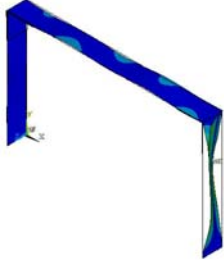
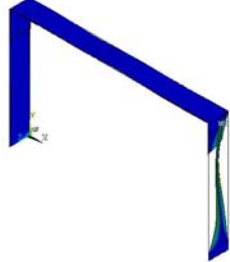
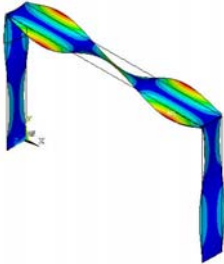
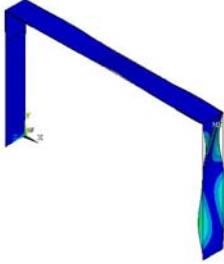
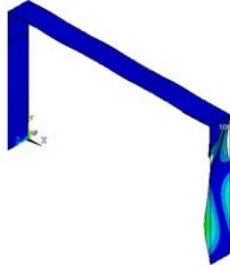
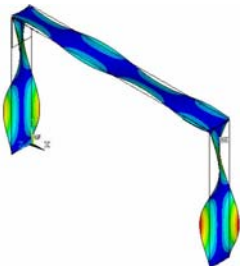
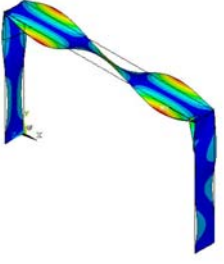
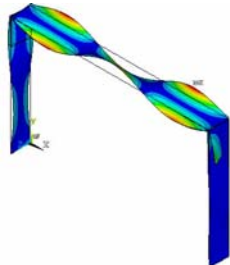
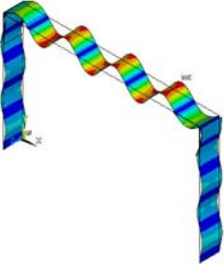
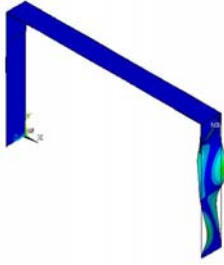
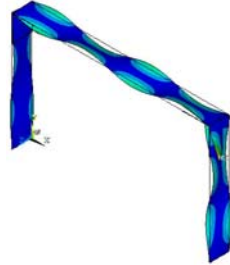
12	 81.1Hz	 78.6 Hz Difference: -3.11%	 68.7 Hz Difference: -15.34%
20	 141.6 Hz	 130.4 Hz Difference: -7.93%	 123.8 Hz Difference: -12.61%
21	 160.0 Hz	 143.0 Hz Difference: -10.62%	 141.6 Hz Difference: -11.48%
27	 217.2 Hz	 196.8 Hz Difference: -9.38%	 188.6 Hz Difference: -13.15%
Mode	Assembled Model	Missing 1 Screw Model	Missing 2 Screws Model

Figure 2-13 Missing-screw effect on natural frequencies and mode shapes

2.5 Viscous Damping Model

Damping dissipates energy reducing the oscillatory amplitude of a vibrating structure. The damping effect may result from the looseness of joints, internal atomic or molecular interaction, fluid-structure interaction, friction between components, and many other complex causes. The most popular assumption in modeling the damping effect is that the damping force is proportional to the velocity.

Unlike static problems where consider only the stiffness term in Equation (2-5), the effects of inertia and damping terms must be taken into account when solving dynamic problems. Given the geometry and material properties, the mass and stiffness matrices can be formulated based on the element types; and the proportional damping (also known as Rayleigh damping) defined in Equation (2-39) is applied to model the damping matrix in Equation (2-5).

$$[C] = \alpha[M] + \beta[K] \quad (2-39)$$

where α and β are the mass and stiffness proportional damping coefficients respectively.

With the damping matrix defined by Equation (2-39), the only problem left is to determine the two scalar parameters, α and β , experimentally. As will be discussed, the β term can be neglected for mechanisms operated at low frequencies (modes), and α can be identified from a coupled computational/experimental technique.

2.5.1 Proportional Damping Effect

To illustrate the proportional damping effect, we consider free vibration of a single DOF system (with mass m , stiffness k , and viscous damping coefficient c), which can be written in terms of natural frequency and damping ratio in Equation (2-40), where natural

frequency ω_n , critical damping coefficient c_{cr} , and damping ratio ζ are defined in Equation (2-41), (2-42), and (2-43) respectively.

$$\ddot{u} + 2\zeta\omega_n\dot{u} + \omega_n^2u = 0 \quad (2-40)$$

$$\omega_n = \sqrt{(k/m)} \quad (2-41)$$

$$c_{cr} = 2m\omega \quad (2-42)$$

$$\zeta = c/c_{cr} \quad (2-43)$$

The proportional damping is defined as a linear combination of the mass and stiffness given in Equation (2-39). In scalar form, it reduces to Equation (2-44):

$$c = \alpha m + \beta k \quad (2-44)$$

Substituting Equation (2-44) into Equation (2-43) yields the damping-frequency relation given in Equation (2-45), which makes the damping ratio frequency dependent.

$$\zeta = \frac{1}{2} \left(\frac{\alpha}{\omega_n} + \beta \omega_n \right) \quad (2-45)$$

Based on above equation, the proportional damping effects can be plotted in Figure 2-14, which shows damping ratio as a function of natural frequency. The minimum damping ratio occurs at $d\zeta/d\omega_n=0$. As shown in Figure 2-14, the mass proportional damping term damps the lowest modes most heavily and thus dominates in low frequency (mode) applications. The opposite effect can be observed for the stiffness proportional damping term which damps highest mode. Thus for the mechanisms vibrate at lower modes, the proportional damping assumption can be reduced to a single mass proportional term.

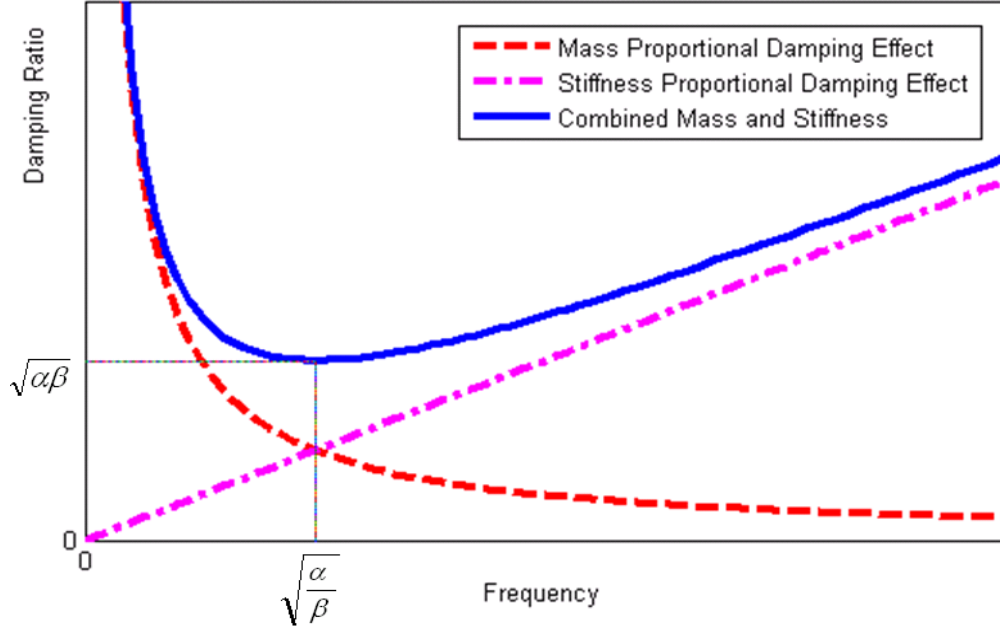


Figure 2-14 Illustration of proportional damping effect for single DOF system

Illustrative Example

The effect can be illustrated numerically by selecting the design spectrum between ω_1 and ω_2 (with their corresponding damping ratios ζ_1 and ζ_2). The mass and stiffness proportional damping coefficients α and β can be obtained as in Equation (2-46) and (2-47) by solving the simultaneous equations of Equation (2-45).

$$\alpha = 2\omega_1\omega_2 \frac{\zeta_1\omega_2 - \zeta_2\omega_1}{\omega_2^2 - \omega_1^2} \tag{2-46}$$

$$\beta = 2 \frac{\zeta_2\omega_2 - \zeta_1\omega_1}{\omega_2^2 - \omega_1^2} \tag{2-47}$$

To illustrate the low frequency applications, assume that $\omega_1 = 2\pi(10)$, $\omega_2 = 2\pi(20)$, and $\zeta_1 = \zeta_2 = 0.1$. From Equation (2-46) and (2-47), the proportional damping coefficients are $\alpha = 8.38$ (1/s) and $\beta = 0.001$ (s) showing the relatively insignificant effect of stiffness proportional damping term for structures vibrates at lower modes.

2.5.2 A Computational/Experimental Coupled Damping Identification Method

Unlike general damping identification methods estimate damping ratios for lump-parameter models, a computational/experimental coupled damping identification method is incorporated into the dynamic model which focuses on obtaining damping coefficients for continuum structures. The coupled method introduced here combines the explicit dynamic FEA, proportional damping assumption, traditional damping identification method (log decrement or half-power bandwidth as in Appendix D), and dynamic response experiment. This technique resolves the limitation of traditional damping identification methods that are only applicable for light-damped cases (as discussed in Appendix D). This identification procedure capable of analyzing high-damped (even for overdamped cases) continuum structures estimates the proportional damping coefficients (particularly for the mass proportional damping term α for structures vibrate at lower modes) for the dynamic FEA. The detailed procedure is illustrated in Figure 2-15.

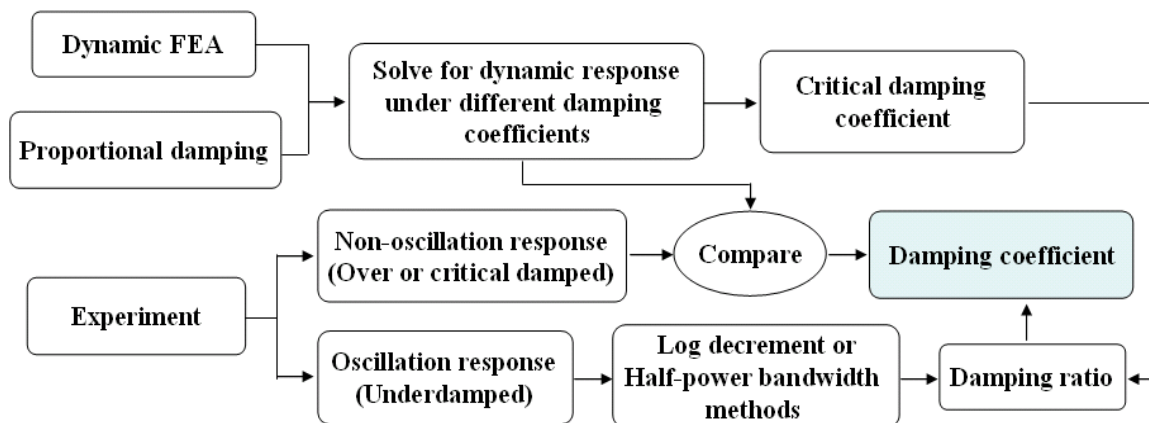


Figure 2-15 A computational/experimental coupled damping identification procedure

Discussions of Figure 2-15 are given below:

1. This method begins with searching for the critical mass proportional damping coefficient (α_{cr}) between oscillation and non-oscillation responses by numerically solving Equation (2-5). This result corresponds to numerically obtain the critical damping of a continuum structure.
2. For the search of the critical mass proportional damping coefficient, the log decrement method can be applied to analyze the damping ratio right after an initial guess value of α . Then a reasonable α_{cr} can be calculated.
3. For underdamped case, the damping coefficient can be obtained from multiplying the numerically obtained α_{cr} and damping ratio (which can be estimated experimentally by log decrement or half-power bandwidth method).
4. For an overdamped structure, the time domain dynamic response to an impulse load will be measured to provide a basis to search for the damping coefficient by comparing the solution to Equation (2-5) based on “trial damping coefficients” against experimental data until a match is found.
5. The computational/experimental obtained damping coefficient can be used for the further dynamic FEA to investigate the dynamic response of the flexible multibody systems.

2.5.3 Illustrative Example: Light-Damped Compliant Beam with Tip Mass

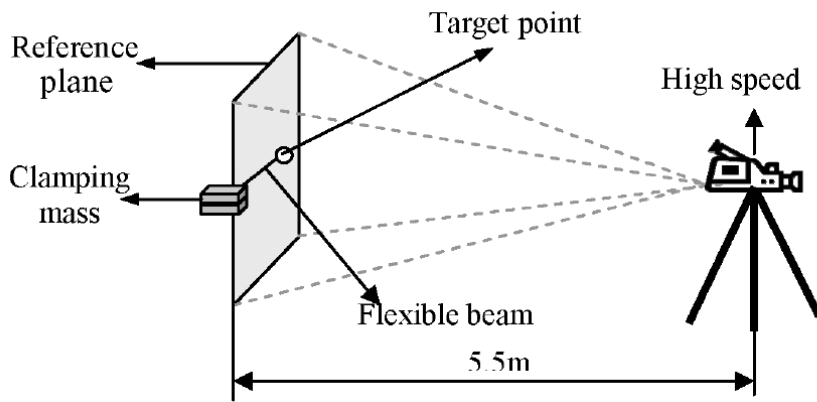
To illustrate the damping modeling and identification method, this section shows an example which simulates the free vibration response of a compliant cantilever beam. As shown in Figure 2-16a [Yoo *et al.*, 2003], a steel beam is clamped at the base with a tip mass at its free end. An initial load is applied at the tip and a high speed camera is used to

measure the dynamic response at the tip point. The experimental tip response is shown in Figure 2-16b.

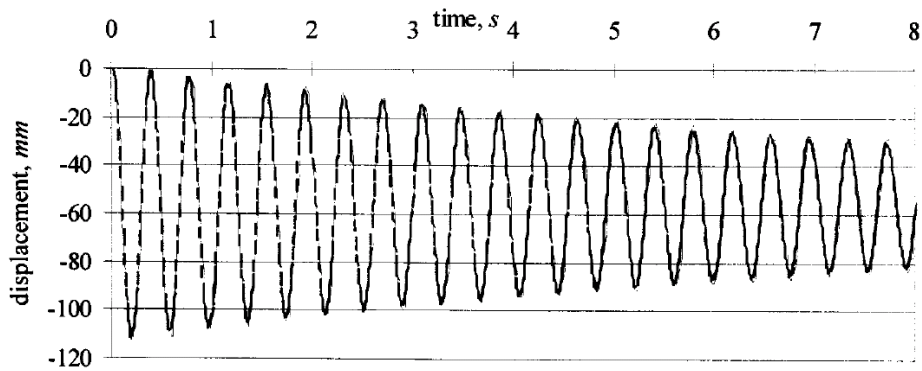
From the experimental response, the damping ratio is found to be 0.0055 by using the log decrement method described in Appendix D, and natural frequency is found as 16.33 rad/s. Based on the experimentally obtained damping ratio and natural frequency, the transfer functions for the tip responses (damped and undamped) are summarized in Table 2-7. The SDOF model is limited to offer the behavior of the end point, and cannot be used to calculate any stress-strain relation along the beam.

A more detailed dynamic model based on FEM is performed to simulate the dynamic response of the compliant beam. The simulation parameters and the finite element model are summarized in Table 2-8 and Table 2-9 respectively, where the corresponding element types are defined in Appendix A.

The mass proportional damping is used in the dynamic model since the compliant beam vibrates at its first mode. The dynamic response (measured from the tip) under different mass proportional damping coefficients (an initial guess and the critical damped) can be seen in Figure 2-17. The critical mass proportional damping coefficient is found as 30 s^{-1} (by using the log decrement method to analyze the damped response with the initial guess value). Based on the above numerically obtained critical damping coefficient and experimentally obtained damping ratio, the mass proportional damping coefficient α can be solved as 0.165 s^{-1} (which can be used in the dynamic FE model). The corresponding damping identification results are summarized in Table 2-10.



(a) Experimental setup



(b) Experimental tip response

Figure 2-16 Experiment of the light-damped beam [Yoo *et. al.*, 2003]

Table 2-7 Transfer function of the SDOF model for the tip response

SDOF Model	Transfer function: $\frac{(s + 2\zeta\omega_n)x(0) + \dot{x}(0)}{s^2 + 2\zeta\omega_n s + \omega_n^2}$
Damped response	$\frac{55.5s + 9.969}{s^2 + 0.1796s + 266.7}$
Undamped response	$\frac{55.5s}{s^2 + 266.7}$

Table 2-8 Simulation parameters for the compliant beam

Simulation Parameters	Values
Length L	0.4 m
Diameter d	0.6 mm
Density ρ	7957 kg/m ³
Young's Modulus E	209 GPa
Mass m	0.9 g
End-point Mass M	0.015 g
Impact Loading	0.003 N
Impact Loading Time	0.2 s
Total Simulation Time	4.0 s

Table 2-9 Finite element modeling of the compliant beam

Part#	Part Name	Element Type	Element#	Node#
1	Compliant Beam	Beam 161	100	101
2	End-point Mass	Mass 166	1	-
sum	-	-	101	101

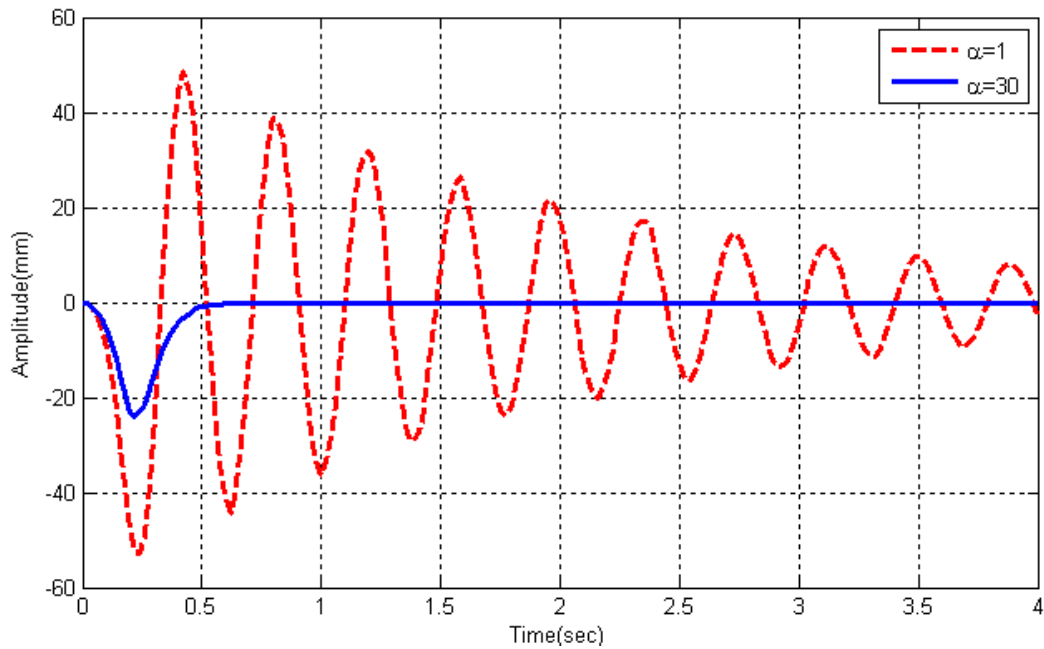


Figure 2-17 Dynamic response under different damping coefficients

Table 2-10 Damping identification results

Parameters	Values
Damping Ratio ζ	0.0055
Damped Frequency ω_d	16.33 rad/s
Natural Frequency ω_n	16.33 rad/s
Critical Mass Proportional Damping Coefficient α_{cr}	30 1/s
Mass Proportional Damping Coefficient α	0.165 1/s

After the damping coefficient is obtained, the FEA simulated tip response is compared against the previous described SDOF model and experimental result as shown in Figure 2-18, which shows excellent agreement. Figure 2-19 shows the snapshots of the vibrating beam at some specific time.

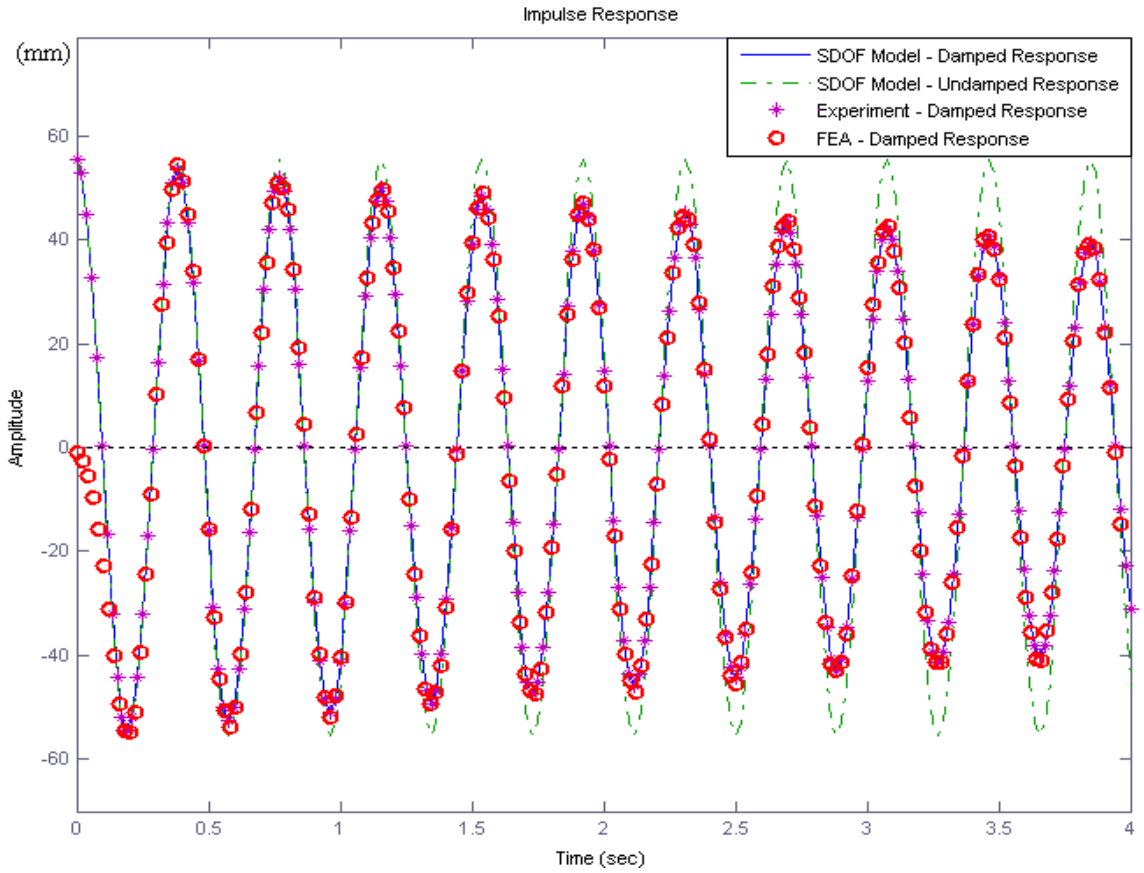


Figure 2-18 Comparison of simulation and experimental data of the free vibration

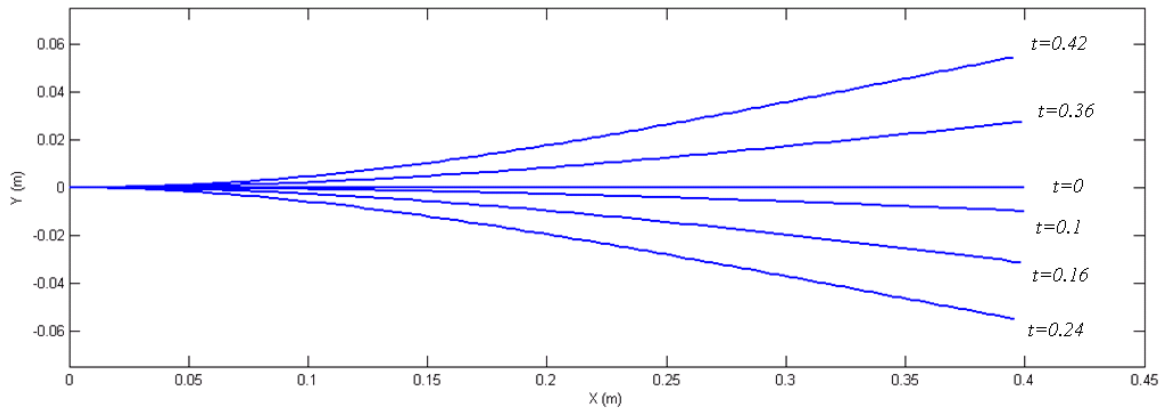


Figure 2-19 Snapshots of the compliant beam under free vibration

The Dunkerley's method described in Appendix E is also used to estimate the fundamental natural frequency of an Euler-Bernoulli beam with a tip mass. Based on the Dunkerley's method, the fundamental natural frequency of the compliant beam with the tip mass can be obtained as $\omega_1=16.33$ rad/s; which is the same as the previous simulation and experimental results.

Although the compliant beam simulates the plane motion, the dynamic model can be extended to simulate 3D responses involving contact deformation and will be discussed in subsequent chapters for analyzing high-damped compliant fingers.

2.6 Topology Optimization

Given the maximum loading conditions, which can be obtained from the results of a dynamic FEA at a particular time instant, the method of static stiffness topology optimization can be employed to optimize a design. The energy of the structural compliance is chosen as the objective function to be minimized subject to the constraint of a specified percentage of volume reduction. Minimizing the structural compliance is equivalent to maximizing the structural static stiffness. The basic formulation of topology optimization along with illustrative examples will be examined in the following subsections.

2.6.1 Basic Formulation

The formulation of static stiffness topology optimization, which can be found in [Vogel, 1997] is briefly described here. The optimal criteria use the pseudo-density $\rho(x)$ to each element as a design variable which varies from 0 to 1. For a given domain Ω , the optimal choice of the elasticity tensor $E_{ijkl}(x)$ takes the form:

$$E_{ijkl}(x) = \rho(x)\bar{E}_{ijkl} \quad (2-48)$$

where \bar{E}_{ijkl} is the elastic tensor. The indicator function $\rho(x)$ for the part $\Omega^* \subseteq \Omega$ satisfies the following:

$$\rho(x) = 0 \quad \text{if } x \notin \Omega^*; \quad \rho(x) = 1 \quad \text{if } x \in \Omega^* \quad (2-49)$$

where $\rho(x)$ approaching 0 implies that the element can be removed from the structure; on the other hand, $\rho(x)$ closer to 1 suggests that the element should be kept in the structure.

To obtain the optimal solution, we minimize the load linear form:

$$\text{Minimize:} \quad l(u) = \int_{\Omega} f u dx + \int_{\Gamma_t} t u ds \quad (2-50)$$

which subjects to the following two constraints

$$\text{Constraint (1):} \quad a(u, v) = l(v), \forall v \in U \quad (2-51)$$

$$\text{Constraint (2):} \quad \int_{\Omega} \rho(x) dx \leq Vol \quad (2-52)$$

Equations (2-51) and (2-52) are the weak form formulation and volume constraint respectively; where the strain energy bilinear form $a(u, v)$ is defined as:

$$a(u, v) = \int_{\Omega} \sum_{i,j,k,l=1}^3 E_{ijkl} \varepsilon_{ij}(u) \varepsilon_{kl}(v) dx, \quad \text{where} \quad \varepsilon_{ij} = \frac{1}{2} \left(\frac{\partial u_i}{\partial x_j} + \frac{\partial u_j}{\partial x_i} \right) \quad (2-53)$$

The first constraint implies the topology optimization is based on the finite element formulation, and the above topology optimization problem can be solved using optimal criteria (OC) and sequential convex programming (SCP) in ANSYS.

2.6.2 Topology Optimization of a Short Cantilever Beam

To validate the topology optimization technique in ANSYS, a classical example of a short cantilever beam is considered in this section. As shown in Figure 1-6, the left side

of the beam is fixed, and a vertical load is applied at the middle of its free end. The dimension and material properties used in this simulation is given in Table 2-11. The analysis domain is meshed by 8-node 2D structural element (PLANE82 in ANSYS) with totally 11501 nodes and 3750 elements. The static stiffness topology optimization with the OC approach is used to find the optimum material distribution in this design space. The volume reduction constraint is set as 70%. The topology optimization process is converged after 24 iterations and the compliance minimization process can be seen in Figure 2-20, where the x-axis is the iteration number; and y-axis is the compliance.

Table 2-11 Simulation parameters of the short cantilever beam

Parameters	Values
Beam dimension	150× 100 ×1 (mm)
Force load	3 KN
Elastic modulus	207 GPa
Poisson's ratio	0.3

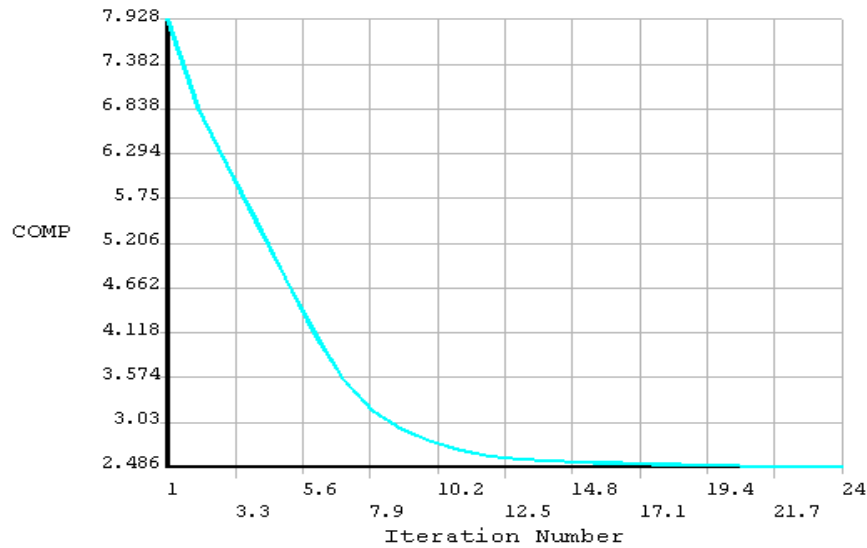


Figure 2-20 Compliance minimization process of the cantilever beam

The simulation result for design of the cantilever beam is given in Figure 2-21a. Comparing with the results by ESO [Xie and Steven, 1997] and TOP [Bruns, 2007] as shown in Figure 2-21b and Figure 1-7a respectively, the optimal topology of the cantilever beam agrees with the published results.

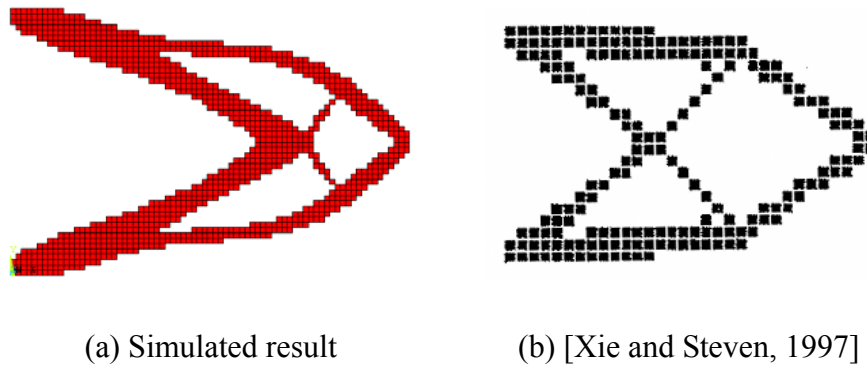


Figure 2-21 Topology optimization for the short cantilever beam

2.6.3 Characterizing Ligament Locations of a Biological Structure

Topology optimization can also be used to characterize the ligament distribution for the wing of chicken (Figure 2-22a). A practical application is the automated deboning process in poultry industry which requires to accurately locate the ligaments for appropriate manipulating the wings for removing the chicken breast meat. From Wolff's law [Wolff, 1986], it is believed that the morphology of bones is subject to mechanical load and self-optimized evolutionally. If loading on a particular bone increases, the bone will remodel itself over time to become stronger to resist that sort of loading. Similarly, we assume that ligaments are the strongest part of the muscle; the growth of the ligament in the muscle strongly depends on the way how it exercised.

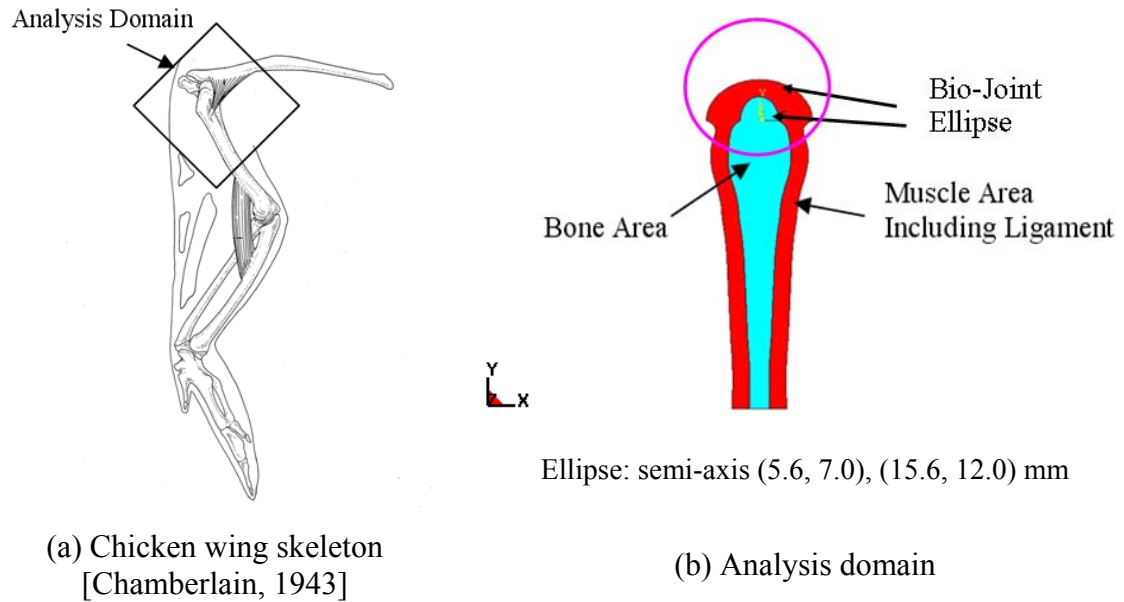


Figure 2-22 Analysis example in biological structure

The analysis domain for this example is shown in Figure 2-22b. The connection area between two bones is modeling as a simplified bio joint based on Lee and Guo [2008]. The geometry (other than ellipse and circle) is modeled using B-Spline curves. The elastic modulus of the soft tissue is 22.1 KPa [Misra *et al*, 2008], and Poisson's ratio is 0.4. The bone area is assumed to be rigid and the muscle area (including ligament) is assumed initially homogeneous. The largest height in this model is 96mm and the width at the bottom line is 16mm. The FE model (muscle area) is meshed by 8-node 2D structural element (PLANE82 in ANSYS) with totally 14512 nodes and 4557 elements. The degree of freedom along the bone area is fixed in x direction since the bone is assumed to be rigid so the muscle cannot penetrate into bone area. The top line in this model (half ellipse curve) is fixed for all degree of freedom because it is connected to another part of bone and is assumed to be fixed. The nodal point force (tension) is applied

in the negative y direction at the bottom line (-1N on each node) since it is the general force loading direction when wing flap.

The static stiffness topology optimization with the OC approach is used to find the optimum material distribution in this design domain. The volume reduction constraint is set as 75%. The optimization process converges after 29 iterations as shown in Figure 2-23. The corresponding optimal topology is given in Figure 2-24. The different colors show the pseudo-density of each element varying from 0 to 1. It is assumed that ligament locations are where the pseudo-density equal to 1. Figure 2-24a is the plot for those elements. Figure 2-24b shows the layout of real ligament (marked with blue spot in the figure), which is similar to the topology optimization result.

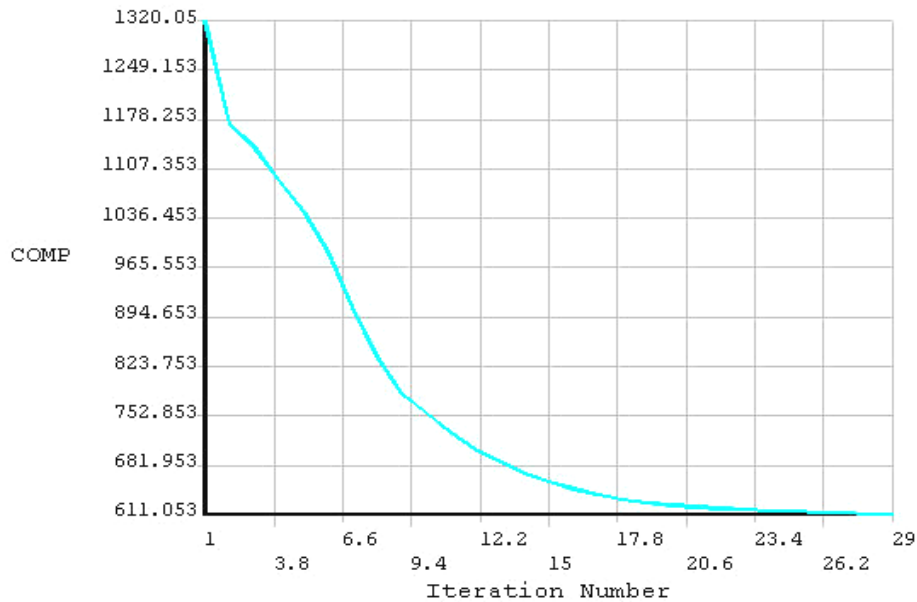


Figure 2-23 Compliance minimization process

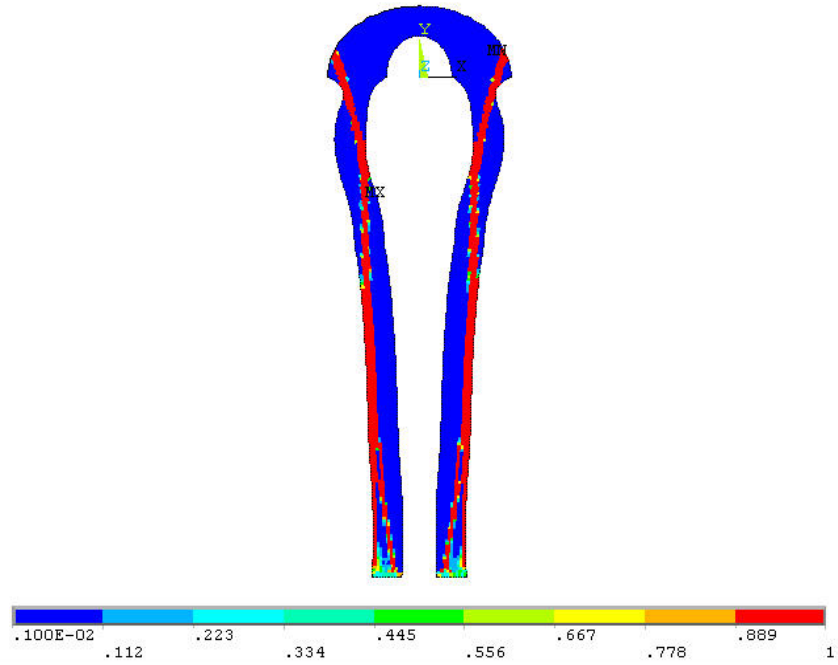


Figure 2-24 Topology optimization for ligament locations



(a) optimization result



(b) real ligaments

Figure 2-25 Ligament layout

2.7 Summary

In this chapter, a FEM based dynamic modeling method is introduced, which is capable to analyze high-damped continuum structures involving large deformation, complex geometries, and contact nonlinearity. The explicit method requires significantly less computation within each time step than implicit method. However, unlike implicit method that is stable for linear and most nonlinear problems, explicit FEM is only stable when its time step is smaller than a critical value (which is called critical time step). If the time step is too large, the explicit method could become numerically unstable. On the other hand, computation would become too expensive if time step is smaller than necessary. The critical time step is a function of element sizes and shapes as well as the material properties. The corresponding effects of these parameters are discussed.

The contact model based on the penalty method and the Coulomb friction model are introduced. The modal analysis for obtaining natural frequencies and mode shapes is discussed along with an illustrative example (a portal frame structure). The effect of the failure at screw connection on natural frequencies and mode shapes are performed.

The viscous damping model is based on the proportional damping assumption. For mechanisms vibrate at lower modes, the proportional damping can be reduced to a single mass proportional term since the stiffness proportional term is insignificant at lower-mode/frequency applications. The computational/experimental coupled damping identification technique is introduced. Unlike traditional damping identification methods such as log decrement method (time domain) and half-power bandwidth method (frequency domain) estimate damping ratios for lump-parameter models, and are only valid for light-damped cases, the advantage of the developed method is the capability to

obtain the damping coefficients for high-damped continuum structures.

Finally, the formulation of topology optimization is introduced with two illustrative examples; topology optimization of a short cantilever beam, and characterization of ligament locations of a biological structure, which extends the Wolff's law of bone remodeling.

This chapter validates the numerical models as well as the effectiveness of general-purpose numerical packages used in this thesis. A general framework incorporating explicit dynamic FEM, topology optimization, modal analysis, and damping identification has been developed. The proposed finite element based dynamic modeling method will be used in the analyses of developing an automated transfer system involved grasping and handling objects by the compliant robotic hands with multiple high-damped rubber fingers. The corresponding design analyses are introduced in the following chapters.

CHAPTER 3

DYNAMIC MODELING OF THE COMPLIANT FINGER

3.1 Introduction

This chapter examines the validity of the formulation by comparing simulated results against experimental data. The dynamic modeling method is applied to analyze the highly damped compliant rubber finger as shown in Figure 3-1. The geometry and material properties (assumed to be homogeneous and linear elastic) of the compliant finger are summarized in Table 3-1.

For the following sections, a modal analysis will first be performed to examine the frequency operating range of the compliant finger and thus the validity of the mass proportional damping assumption. The time step consideration for four different finger-modeling cases (with different element types, sizes, and geometry of the finger) will also be discussed. After the best finger-modeling method is determined, the damping coefficients of these compliant fingers (3, 4.5, 6, and 8-inch in length) will be found by the aid of the computational/experimental coupled damping identification technique. Once the damped behavior of the compliant fingers is realistically modeled, the dynamic model will further be verified against the experimental data involving the contact between the rotating compliant finger and a fixed elliptical object. The twist deformation of the compliant finger will also be simulated and compared against the experiment. Further, these compliant fingers will be applied as the robotic hand in the grasping

application and will be discussed in Chapter 4.

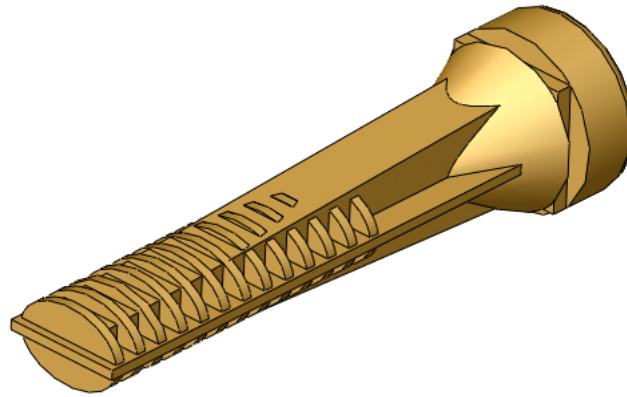


Figure 3-1 CAD model of the compliant finger (4.5-inch)

Table 3-1 Geometry and material properties of the rubber finger

Property	Value
Elliptical cross section	Major/minor semi-axes: 12 / 8.45 (mm)
Finger length	3, 4.5, 6, 8 (inch)
Elastic modulus	6.1 MPa
Poisson ratio	0.49
Density	1000 kg/m ³

3.2 Modal Analysis

A modal analysis is performed numerically using FEM to determine the vibration characteristics (natural frequencies and mode shapes), which are important parameters for a structure under dynamic loading conditions. Specifically, the interest here is to obtain

the mode shapes of the compliant finger. As shown in Figure 3-2, the finite element model of an 8-inch finger is meshed by 10-node tetra element (SOLID92 in ANSYS) with totally 83721 nodes and 53349 elements. The Block Lanczos method is chosen for the mode-extraction.

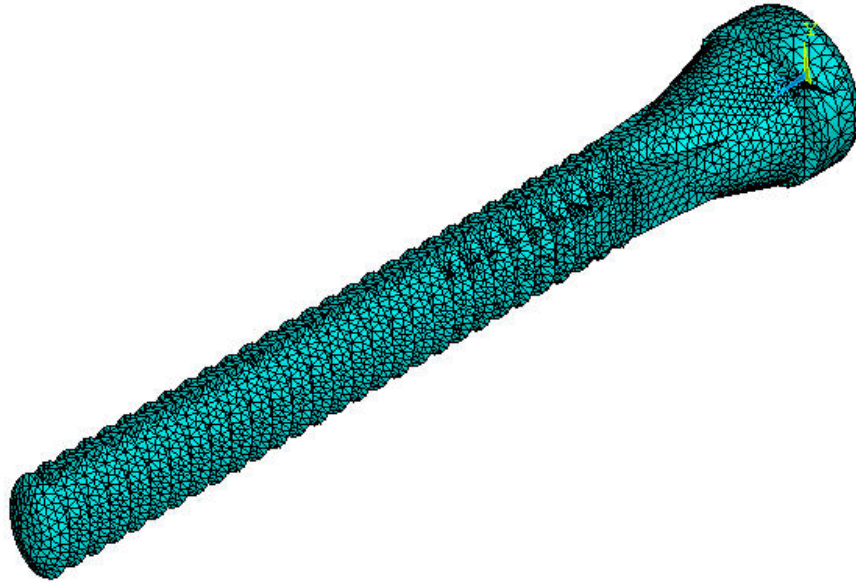


Figure 3-2 Finite element model of the 8-inch compliant finger

The first ten mode shapes and natural frequencies of the 8-inch compliant finger (fixed at one end) are shown in Figure 3-3. These mode shapes describe the expected deformation of the 8-inch finger vibrating at some particular frequencies. Most of these mode shapes correspond to the bending deformation except mode 5 and 10 are due to torsion, and mode 9 is in elongation. Since natural frequency corresponds to the square root of stiffness divided by mass, a lower frequency implies a lower stiffness. Among which, mode 1 is the most common case in our application and is chosen as the target mode for modeling of damping.

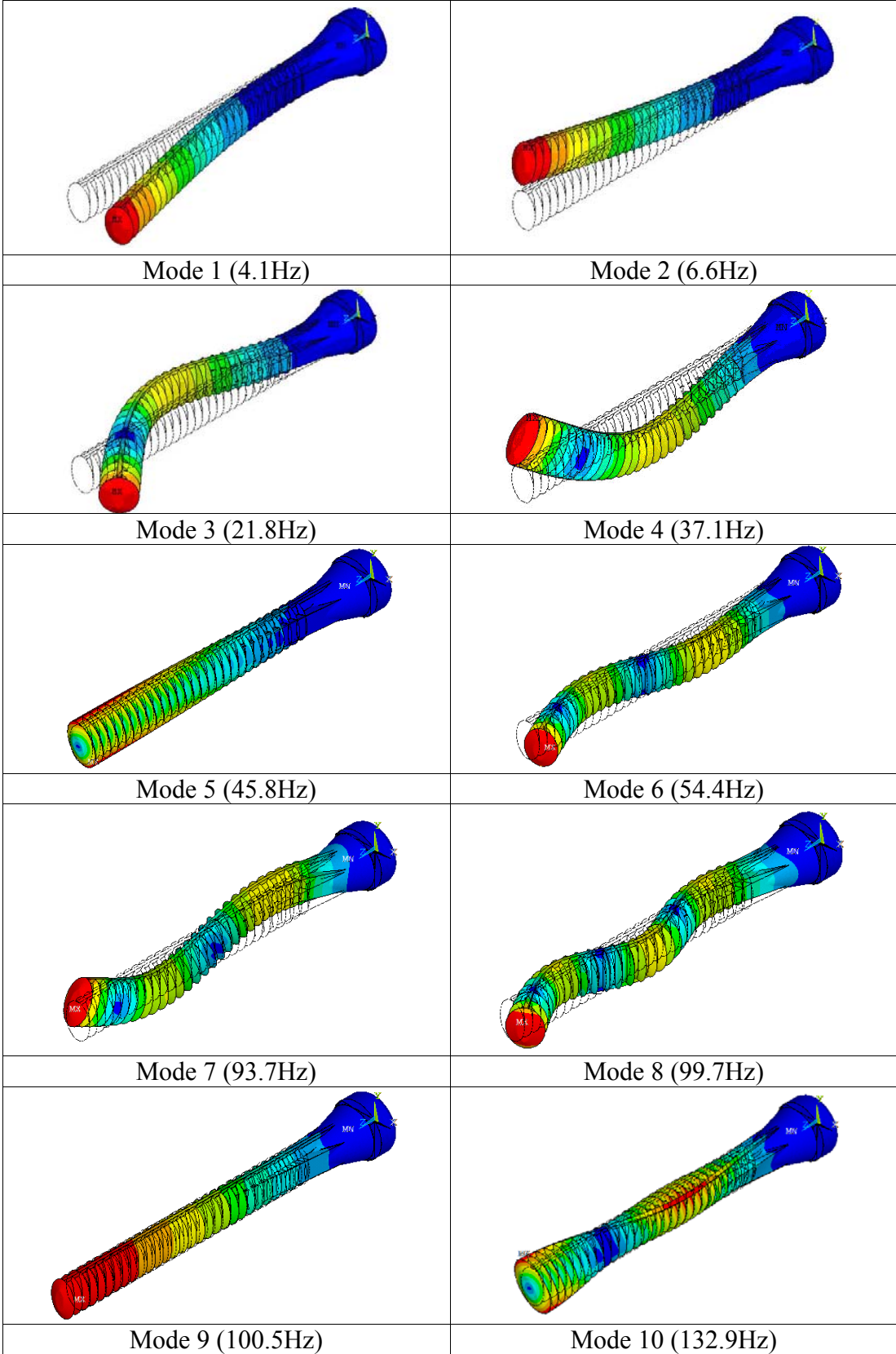


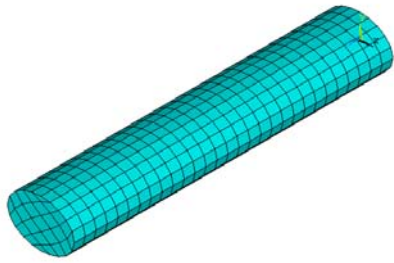
Figure 3-3 First ten mode shapes of the 8-inch compliant finger

3.3 Finger-Modeling Comparison: Time Step Consideration

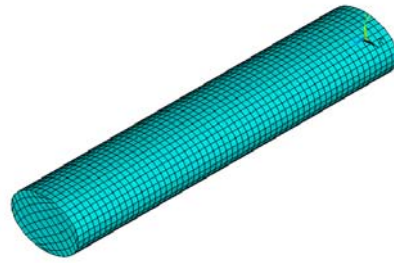
The effect of three different finger approximations (Cases A, B and C) for the consideration of critical time step are numerically examined and compared against the detailed model (Case D). A 4.5-inch compliant finger is chosen for this study. These models are shown in Figure 3-4 and described as follows.

- Case (A): a simplified model with hexa element (average element length 4mm).
- Case (B): a simplified model with refined hexa element (average element length 2mm).
- Case (C): a simplified model with tetra element (average element length 4mm).
- Case (D): a detailed model with tetra element (average element length 2.8mm).

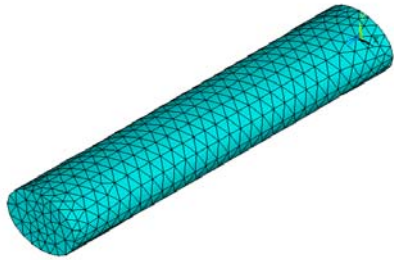
Cases (A), (B) and (C) have the same simplified elliptical cross section but different element sizes and/or shapes. In the dynamic simulation, these fingers are fixed at one end and an impulse load is applied at the other end. The mass proportional damping assumption is applied to these cases with the mass proportional damping coefficient α be set as 180 s^{-1} . For these cases, the node and element numbers, numerical time step, number of steps to solve a 0.2 second dynamic problem, and the relative ratio for the number of steps compared to Case (A) are summarized in Table 3-2. Figure 3-5 is the tip response curves of these cases. Figure 3-6 shows the maximum equivalent stress curves. The displacement and stress contour of the detailed model are given in Figure 3-7.



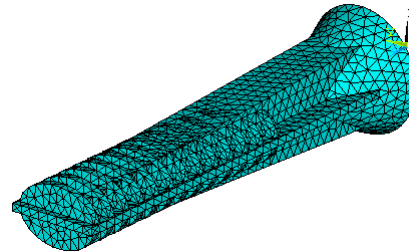
(a) Simplified model with hexa element



(b) Simplified model with refined hexa element



(c) Simplified model with tetra element



(d) Detailed model with tetra element

Figure 3-4 Modeling comparison of a 4.5-inch compliant finger

Table 3-2 Finger modeling comparison

Case	Modeling Types	Average Element Length (mm)	Node & Element #	Numerical Time Step (μ s)	# Steps to 0.2s	# Steps Ratio
(A)	Simplified Model Hexa Element	4	1080 725	4.04	49505	1
(B)	Simplified Model Refined Hexa Element	2	5900 4698	1.43	139860	2.83
(C)	Simplified Model Tetra Element	4	7481 4682	1.26	158730	3.21
(D)	Detailed Model Tetra Element	2.8	36782 23147	0.22	909091	18.36

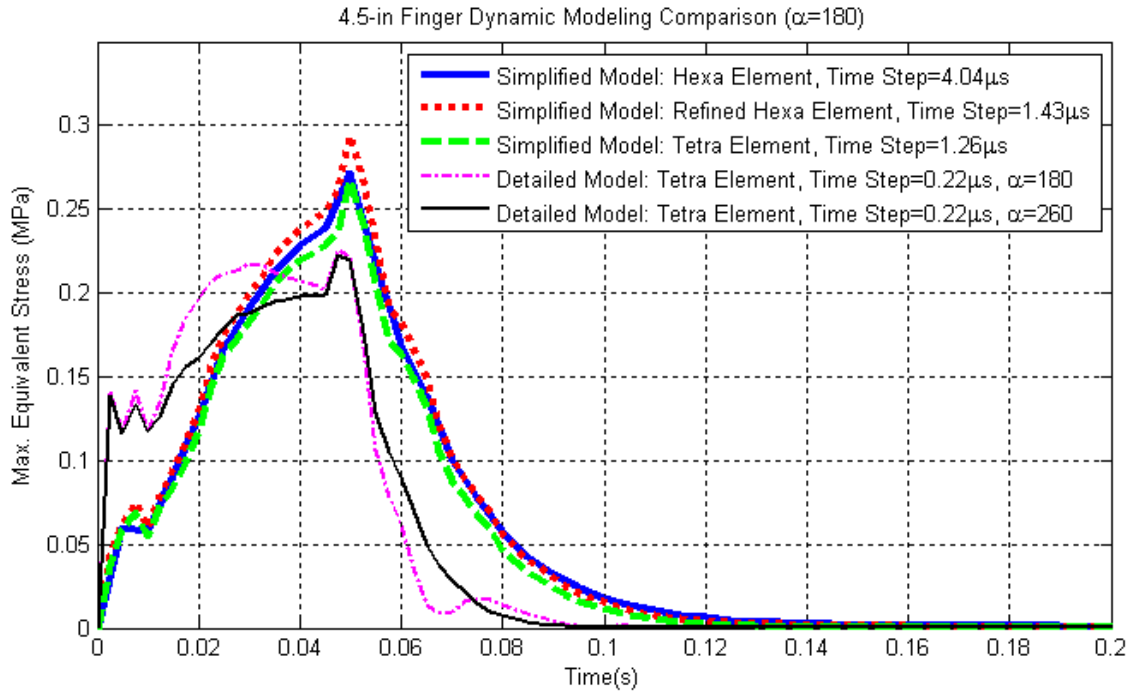


Figure 3-5 Tip responses of different analysis cases

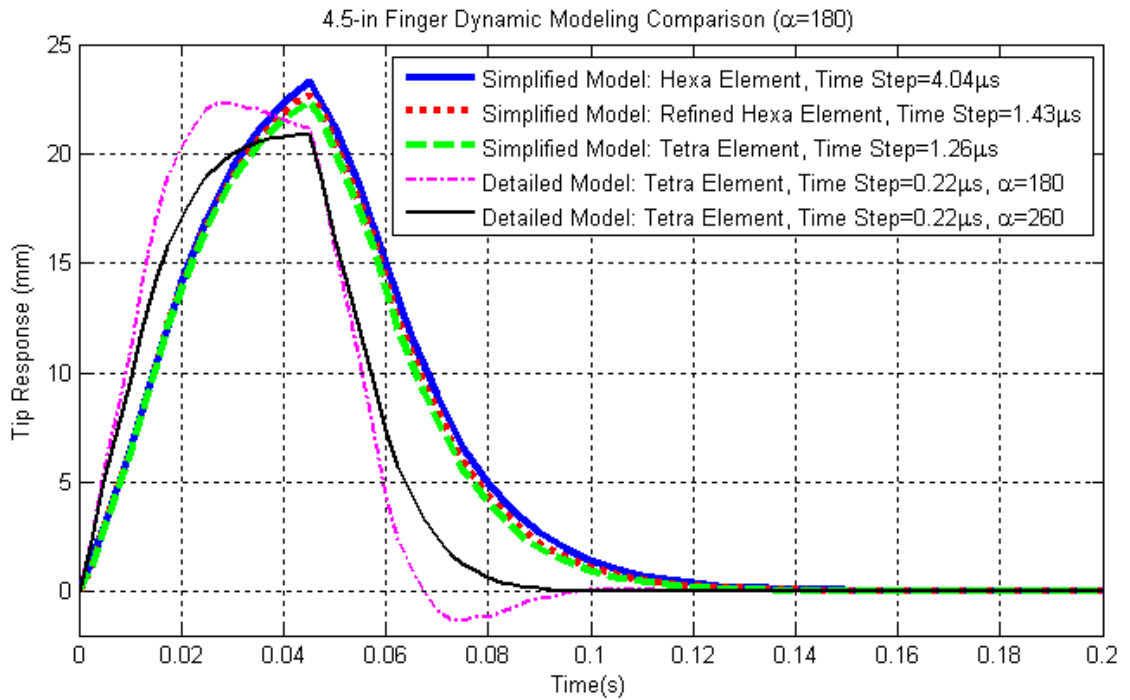
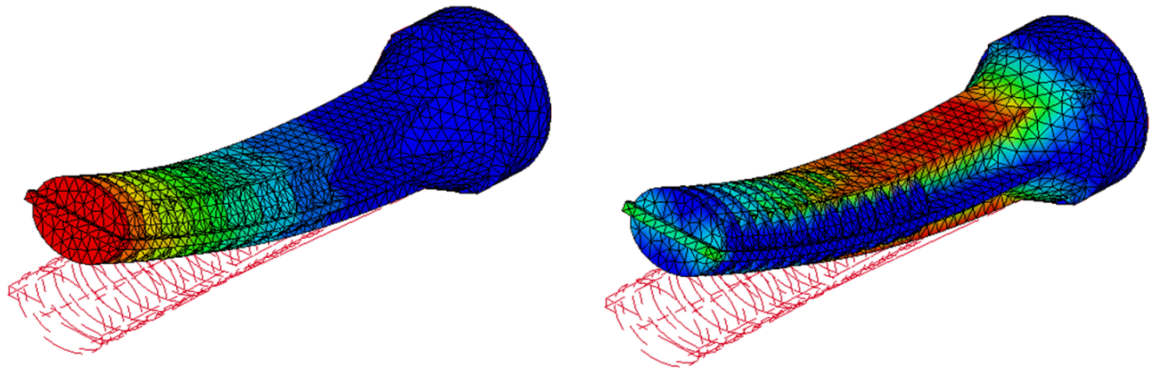


Figure 3-6 Maximum equivalent stresses of different analysis cases



(a) Displacement contour

(b) Stress contour

Figure 3-7 Displacement and stress contour of the detailed finger model

Observations from above simulation results are summarized as follows:

- (1) For the same average element length, tetra elements require a smaller time step than that taken by hexa elements. Case (C) requires 3.21 times more steps in computing a 0.2 second dynamic problem than that in Case (A).
- (2) Although Case (C) that uses tetra elements has a larger average element length than Case (B) that meshed with smaller hexa elements, its time step is smaller due to the mesh with tetra elements.
- (3) The detailed model can not be meshed with hexa elements due to its complex geometry. Small detailed features lead to relatively non-homogeneous element lengths. As the numerical time step is determined by the smallest element in the whole domain, this leads to a large number of steps (around 18.36 times) than Case (A) to solve the same 0.2 second dynamic problem.
- (4) The actual ratio of the computation time is larger than the ratio of number of steps since the matrix size of these cases (that use refined hexa elements and tetra elements)

- are larger than Case (A) due to the larger number of nodes and elements (the matrix size is $3n \times 3n$ in this study, where n is the number of nodes).
- (5) As shown in Figure 3-5, similar tip response curves can be obtained for Cases (A), (B), and (C). The detailed model yields a stiffer response than the simplified models due to the inclusion of the ribs and the fact that it has a larger cross-section close to the fixed end.
 - (6) For the same mass proportional damping coefficient (180 s^{-1}), the simplified models show the overdamped response but the detailed model shows the underdamped response. The relatively larger difference in the mass and stiffness matrices between the detailed and simplified models results in different damping matrix. To obtain similar overdamped responses, the damping coefficient of the detailed model needs to be increased to 260 s^{-1} .
 - (7) As shown in Figure 3-6, similar stress response curves can be obtained for Cases (A), (B), and (C) which show that the stress response of the detailed model is smaller than that of the simplified models.
 - (8) Since the simplified models yield relatively higher deflection and stress responses, it is a reasonable model for a conservative analysis. Among these simplified models, Case (A) has the largest numerical time step (lowest computation) for similar results, and will be applied in the following dynamic simulation.

3.4 Damping Modeling and Identification

The experimental setup for measuring the free vibration responses of the compliant fingers (manufactured by the Waukesha Rubber Company) is shown in Figure 3-8

(similar setup for 3-inch, 4.5-inch, and 8-inch fingers) where the non-contact magnetic sensor measures the tip displacement. In this experiment, the tested finger is clamped at one end, and an impulse load is applied at the other end. The Banner S18MB magnetic sensor measures the magnetic field of a cylindrical permanent magnet (4mm-radius and 1.65mm-height) embedded in the finger's tip. When an impulse load is applied at the finger tip, tip displacements are recorded.

The experimental results are shown in Figure 3-9. Their damping ratios of the underdamped cases (6 and 8-inch fingers) can be determined by the log decrement method from the decaying amplitude as described in Appendix D. As discussed in the computational/experimental coupled damping identification technique in Section 2.5.2, their corresponding damping coefficients (mass proportional) can be obtained from multiplying the experimentally obtained damping ratios and the numerically determined critical damping coefficients. For the overdamped responses (3 and 4.5-inch fingers), as the damping ratio can not be obtained from the log decrement, trial-and-error FEA simulations are performed to determine a match between simulation and experiment.

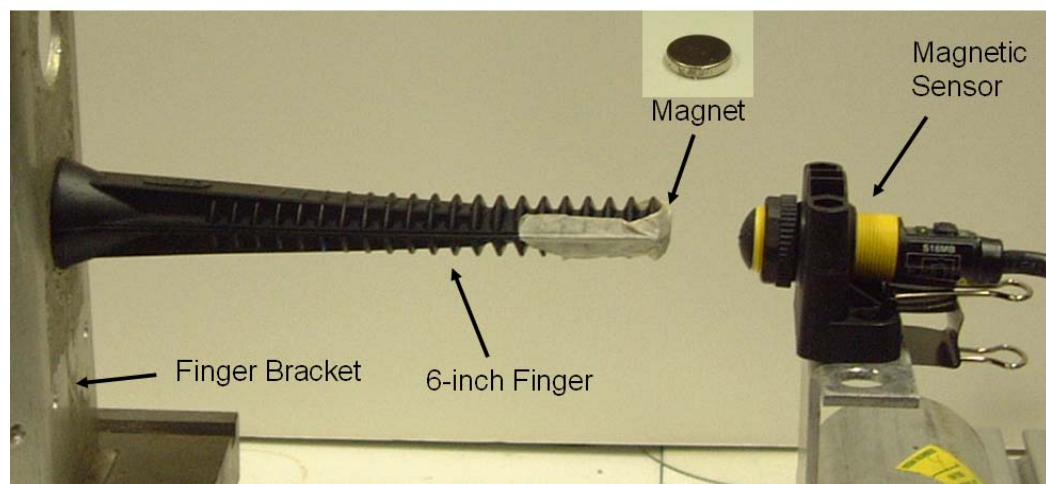
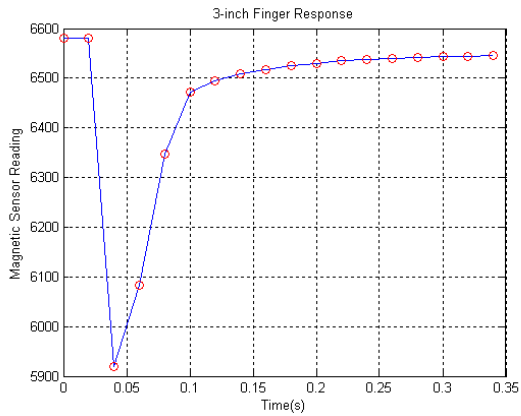
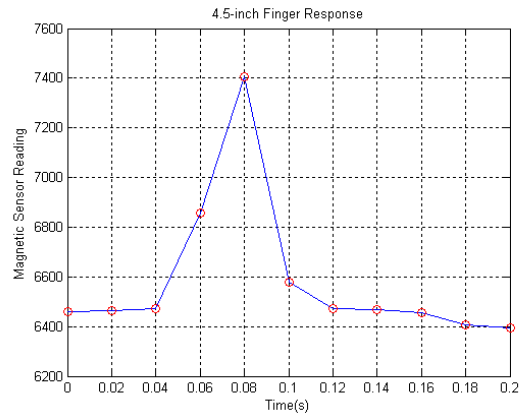


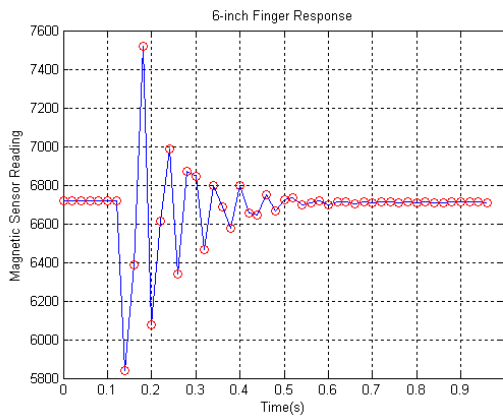
Figure 3-8 Experimental setup for the measurement of free vibration response of the 6-inch compliant finger (similar for 3-inch, 4.5-inch, and 8-inch fingers)



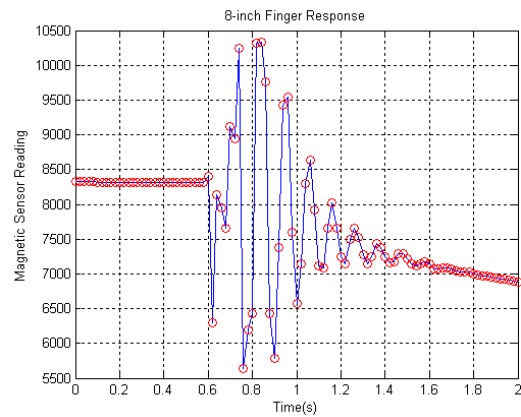
(a) 3-inch: overdamped



(b) 4.5-inch: overdamped



(c) 6-inch: underdamped



(d) 8-inch: underdamped

Figure 3-9 Experimental results for free vibration response of compliant fingers

3.4.1 Damping Coefficients of the High-Damped Compliant Fingers

Using the mass proportional damping assumption (with only the α term) in Equation (2-39) along with the simplified finger models (Figure 3-10), the free vibration responses of the compliant fingers (3, 4.5, 6, and 8-inch in length) are numerically simulated. The critical damping coefficient can be obtained by searching for the critical α value between oscillation and non-oscillation responses. Figure 3-11 shows the dynamic response of the

3-inch finger under different mass proportional damping coefficients. Similar procedure can be performed for fingers of different length. The corresponding results for the 4.5-inch, 6-inch, and 8-inch fingers are shown in Figure 3-12, Figure 3-13, and Figure 3-14 respectively.

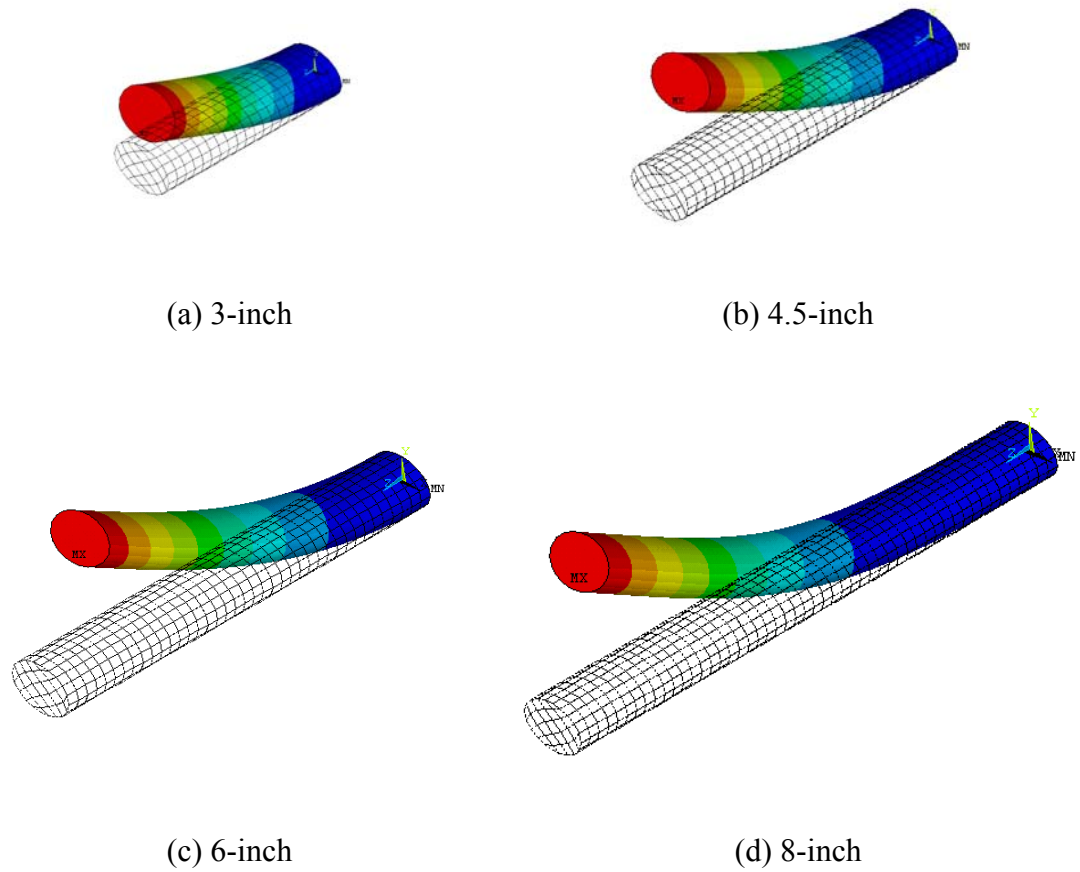


Figure 3-10 Dynamic simulation of free vibration response of compliant fingers

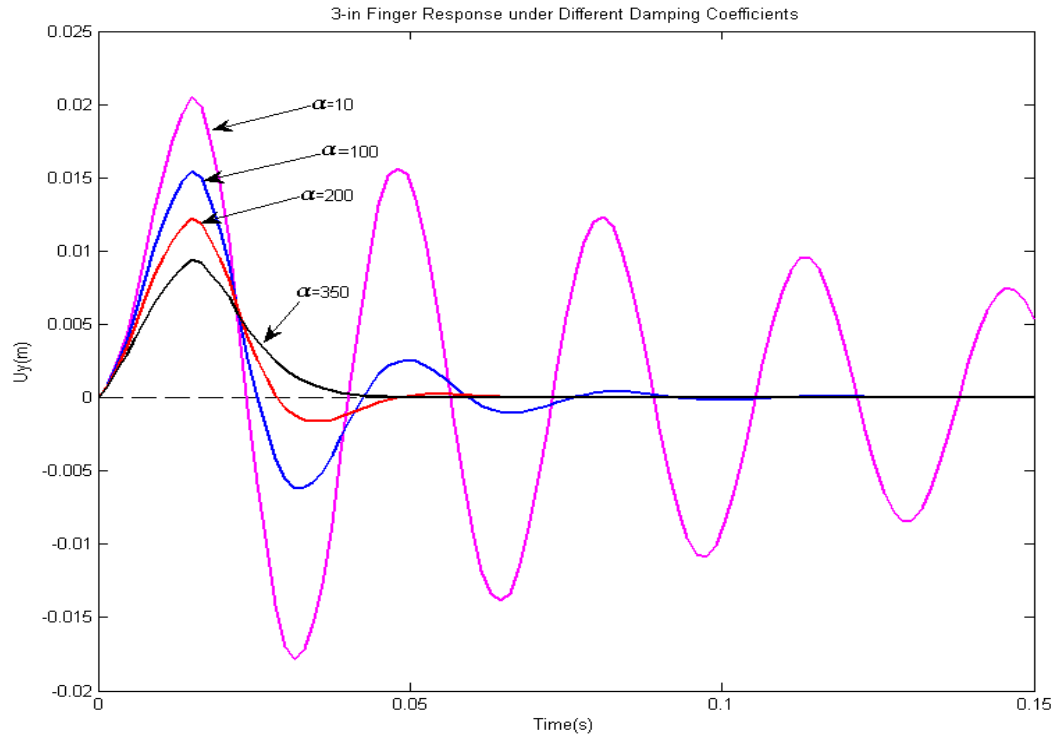


Figure 3-11 Dynamic response of 3-inch finger under different damping coefficients

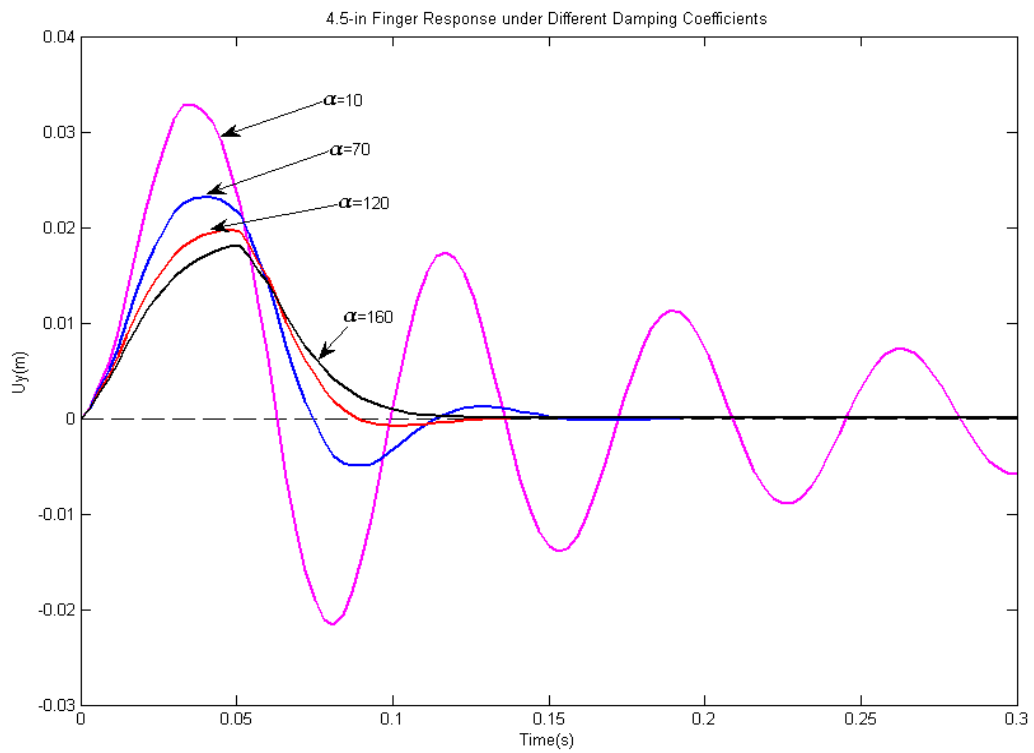


Figure 3-12 Dynamic response of 4.5-inch finger under different damping coefficients

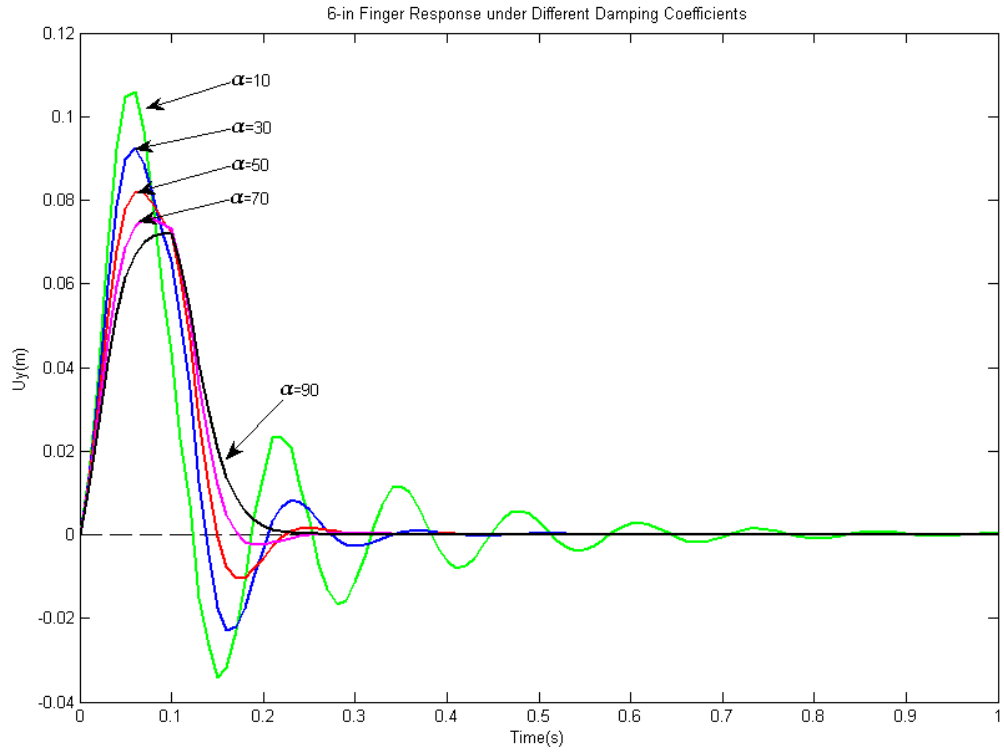


Figure 3-13 Dynamic response of 6-inch finger under different damping coefficients

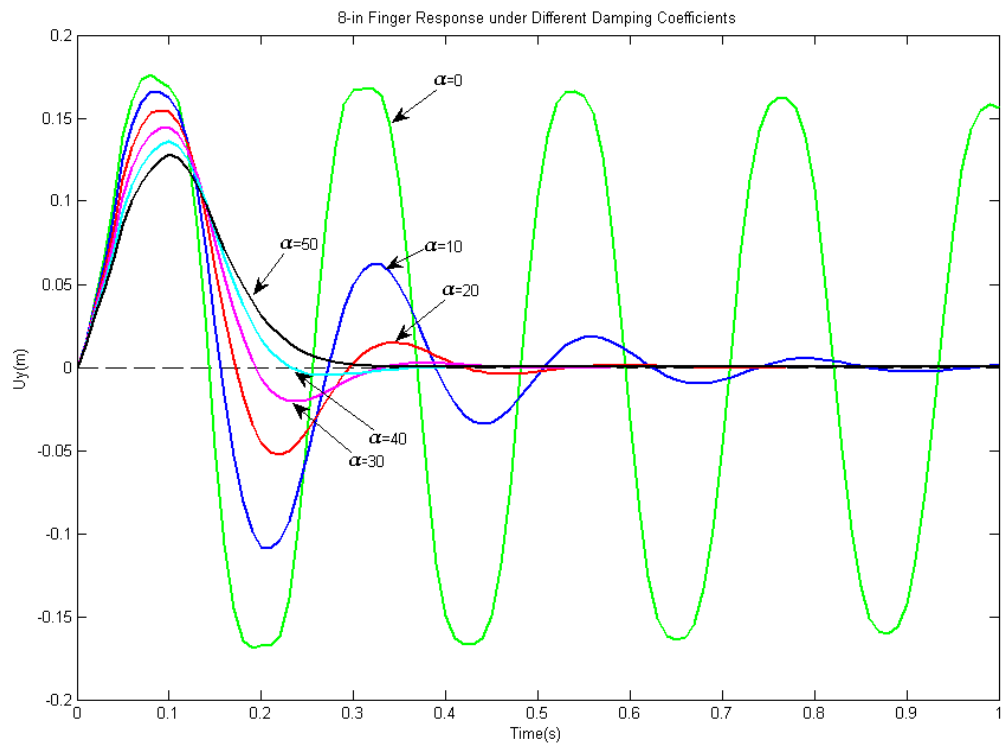


Figure 3-14 Dynamic response of 8-inch finger under different damping coefficients

The numerically obtained critical mass proportional damping coefficients (α_{cr}) are summarized in Table 3-3. The damping ratios (ζ) of 6-inch and 8-inch fingers (underdamped response) are obtained from the experimental response (as shown in Figure 3-9) by log decrement, and their corresponding damping coefficients (α) are calculated by multiplying of ζ and α_{cr} . The damping coefficients of the overdamped 3-inch and 4.5-inch fingers are estimated by comparing simulation and experimental response as shown in Figure 3-15.

Table 3-3 Damping identification of compliant fingers

Finger Length (inch)	Damped Response	α_{cr} (1/s)	ζ	α (1/s)
3	Overdamped	350	1.71	600
4.5	Overdamped	160	1.13	180
6	Underdamped	90	0.17	15
8	Underdamped	50	0.15	7.5

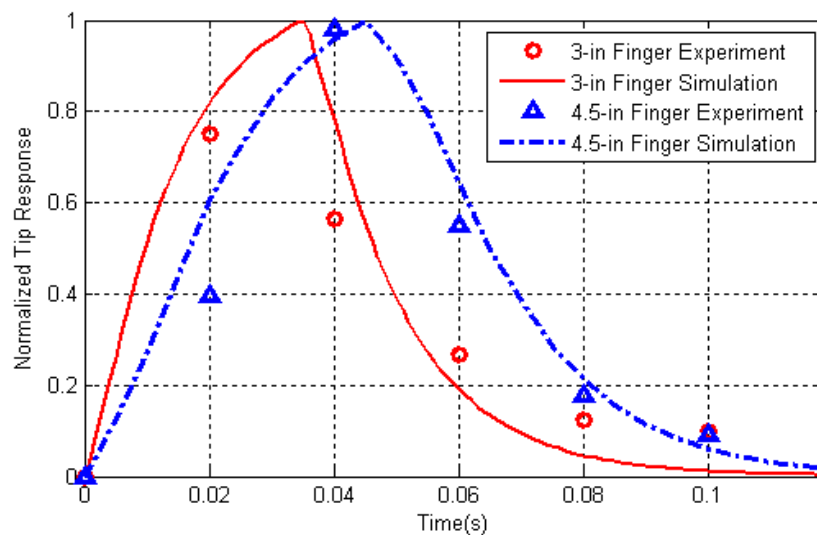


Figure 3-15 Comparison of simulation and experimental results for 3-inch ($\alpha=600$) and 4.5-inch ($\alpha=180$) fingers

3.4.2 Damping Properties v.s. Finger Lengths

Based on the previous damping identification results (Table 3-3), Figure 3-16 and Figure 3-17 plot the damping ratios, damping coefficients, and critical damping coefficients as a function of finger lengths for these specific type of fingers shown in Figure 3-8. The damping ratio (ζ) and mass proportional damping coefficient (α) for a given finger length (x) can be curve-fitted by polynomial functions given in Equation (3-1) and Equation (3-2) respectively:

$$\zeta = \begin{cases} -0.082x^2 + 0.2222x + 1.7857 \\ -0.0083x + 0.2167 \end{cases} \text{ when } \begin{cases} 3 \leq x \leq 6 \\ 6 \leq x \leq 8 \end{cases} \quad (3-1)$$

$$\alpha = \begin{cases} 56.667x^2 - 705x + 2205 \\ -3.75x + 37.5 \end{cases} \text{ when } \begin{cases} 3 \leq x \leq 6 \\ 6 \leq x \leq 8 \end{cases} \quad (3-2)$$

Similarly, the critical mass proportional damping coefficient (α_{cr}) can be curve-fitted by a power function in Equation (3-3):

$$\alpha_{cr} = 3120.4x^{-1.983} \quad \text{when } 3 \leq x \leq 8 \quad (3-3)$$

Based on these approximations, the damping parameters for these particular fingers with different lengths can be estimated.

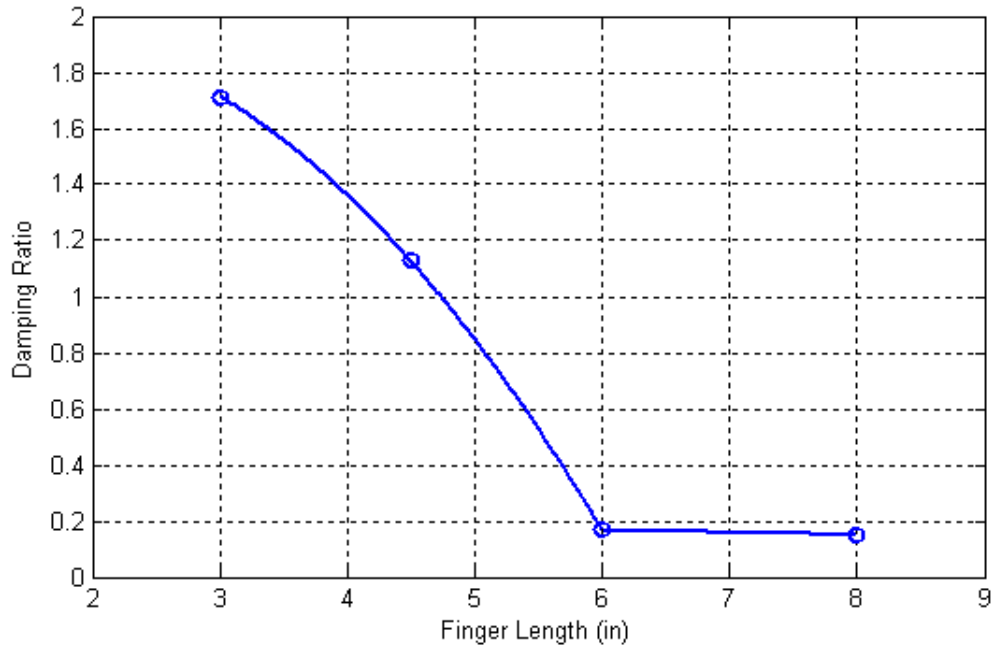


Figure 3-16 Damping ratios versus finger lengths

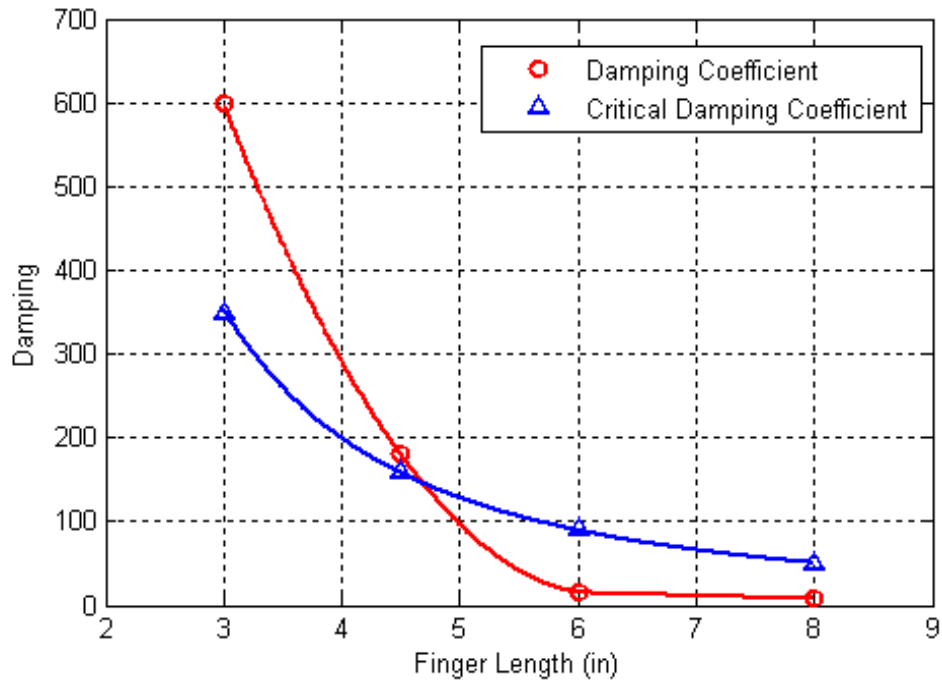


Figure 3-17 Damping coefficients/critical damping coefficients versus finger lengths

3.5 Contact between Rotating Finger and Elliptical Object

To validate the dynamic response of the deformable contact due to the rotating finger acting on the elliptical object, the experimental setup shown in Figure 3-18 is simulated, where published experimental data [Lee *et al.*, 2001] are available for comparison. The compliant finger is mounted on a rotating drum exerting a contact force on the fixed elliptical object (aluminum). A 6-DOF force/torque transducer (mounted between the object and the fixed structure) experimentally measured the reaction force acting on the elliptical object. The geometrical parameters and friction coefficient between rubber finger and aluminum elliptical object are based on the data given in [Lee *et al.*, 2001]. The relative distance between the elliptical object and drum-center is $(x, y) = (101.6 \text{ mm}, 184.15 \text{ mm})$.

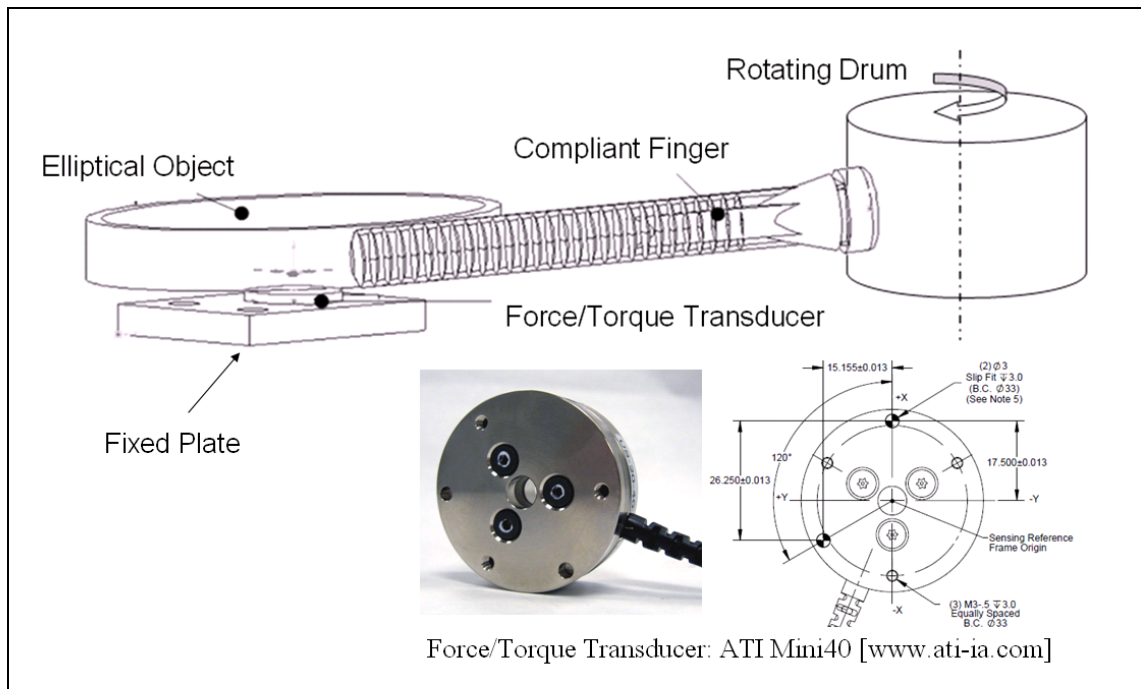


Figure 3-18 Experimental setup for the rotating finger/fixed elliptical object contact

3.5.1 Dynamic Modeling and Experimental Results

The finite element model for the dynamic simulation is given in Figure 3-19. The geometry modeling, material and finite element modeling, and boundary conditions are summarized in Table 3-4, Table 3-5, and Table 3-6 respectively, where element types are defined in Appendix A.

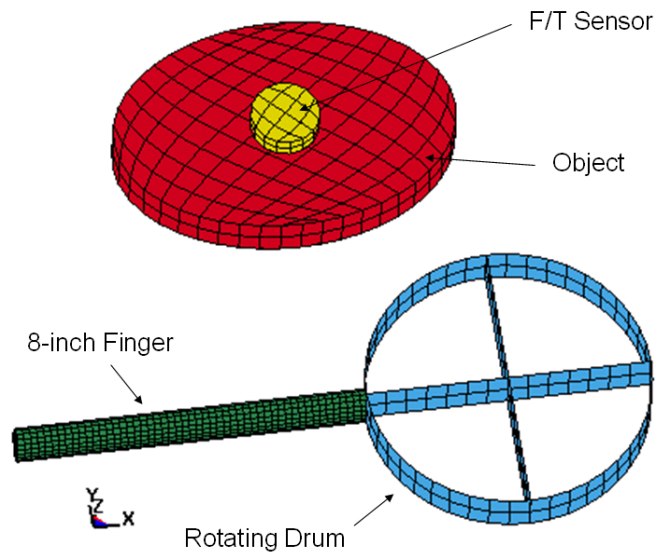


Figure 3-19 Finite element model for contact simulation

Table 3-4 Geometry modeling

Part Name	Cross Section	Cross Section Dimension (mm)	Length/Thickness (mm)
Finger	Ellipse	Semi-axis: 12, 8.45	203.20
Object	Ellipse	Semi-axis: 99.1, 67.3	25.00
Drum	Circle	Radius: 82.55	25.00
F/T sensor	Circle	Radius: 20	12.25

Table 3-5 Material and finite element modeling

Part Name	Material	<i>E</i> (GPa)	<i>v</i>	ρ (kg/m ³)	Element Type	Element#	Node#
Object	AL6061	69	0.33	2700	Solid 164	242	432
Drum	Steel	210	0.28	7700	Shell 163	144	212
Finger	Rubber	0.0061	0.49	1000	Solid 164	1275	1872
F/T sensor	AL6061	69	0.33	2700	Solid 164	32	75
sum	-	-	-	-	-	1693	2591

Table 3-6 Boundary conditions

Parameters	Values
Drum rotation speed (ω_z)	2.095 rad/s (20 rpm)
Friction coefficient	0.6
Damping coefficient of finger (α)	7.5 s ⁻¹
Constraints	Drum axis: fixed UX, UY, UZ, RX, RY F/T sensor top surface: fixed all DOF
Drum rotation angle	360 degree
Simulation time	3 sec

The numerically predicted deformed shapes are compared against snapshots captured at some specific instants given in Figure 3-20. The reaction force measured from the force/torque sensor can be seen in Figure 3-21. Figure 3-22 shows the contact location between finger and object (the reduced object stiffness case will be discussed in the following parameter effect section). These comparisons show excellent agreement between the simulation and experimental results.

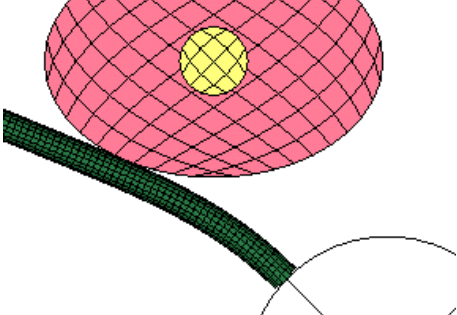
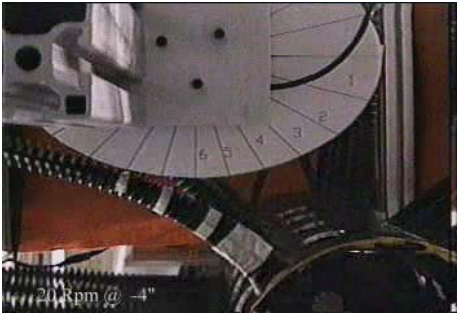
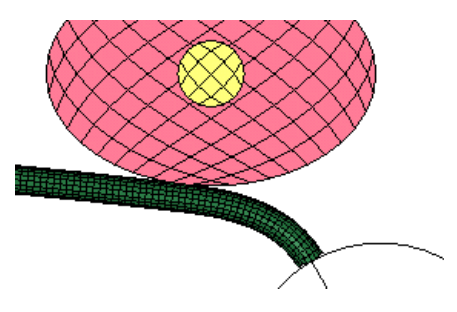
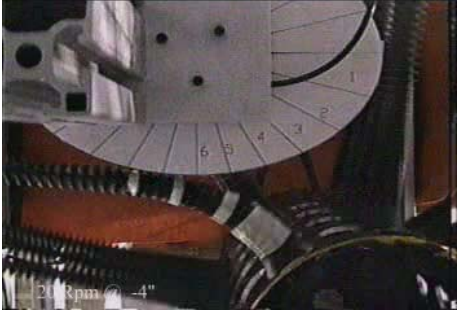
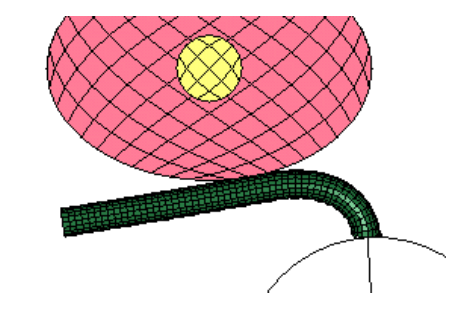
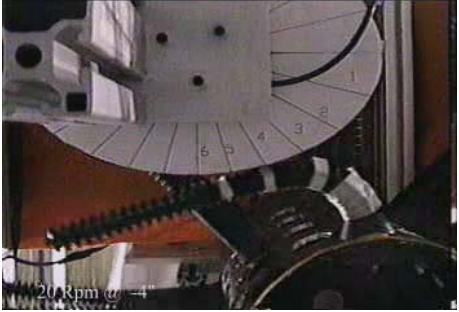
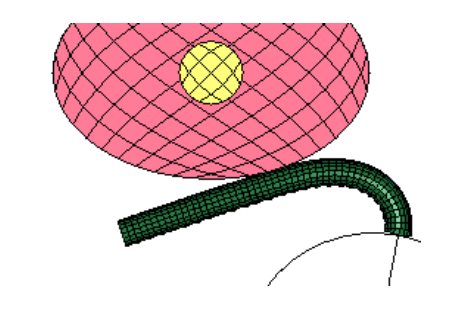
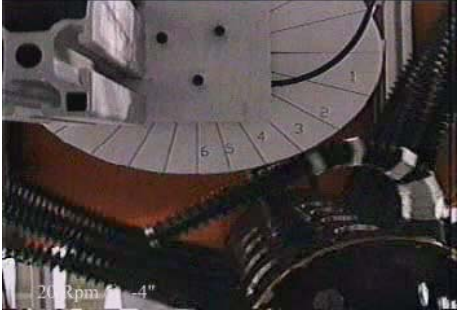
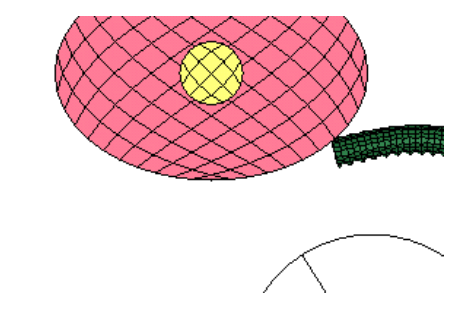
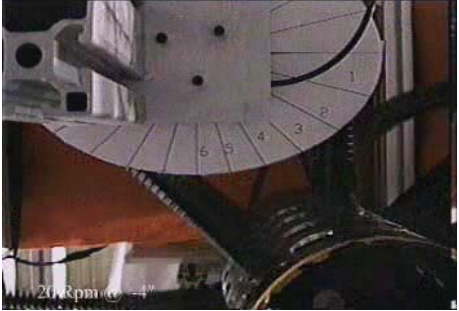
$t=0.37s$		
$t=0.50s$		
$t=0.72s$		
$t=0.84s$		
$t=1.23s$		
time	Simulation	Experiment [Lee <i>et al.</i> , 2001]

Figure 3-20 Simulation and experimental results of finger-contact deformation

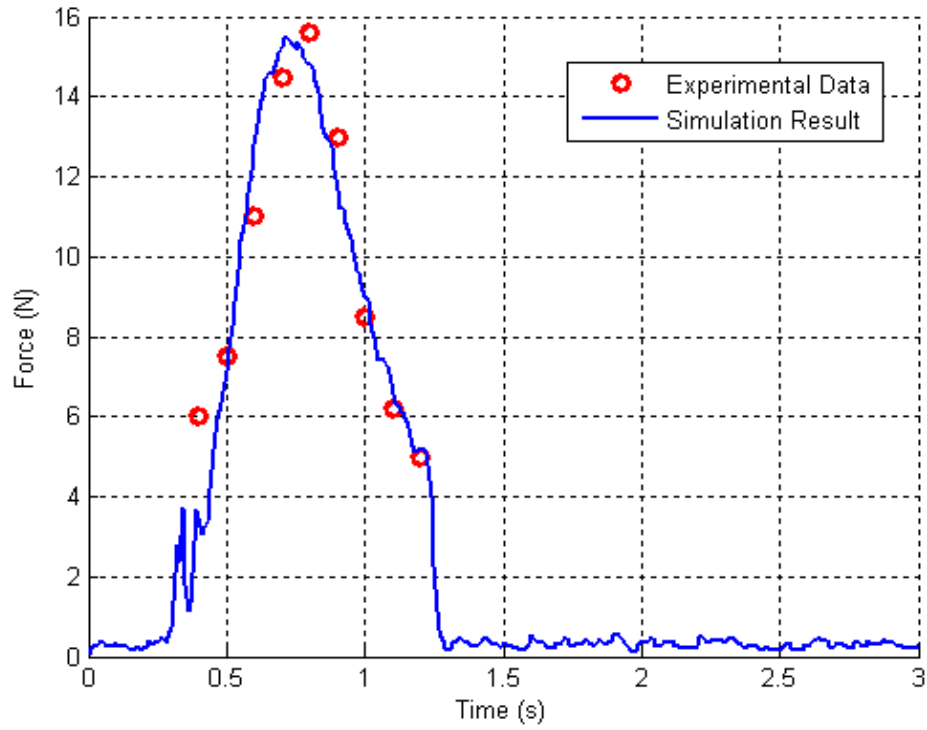


Figure 3-21 Reaction force from contact between rotating finger and elliptical object

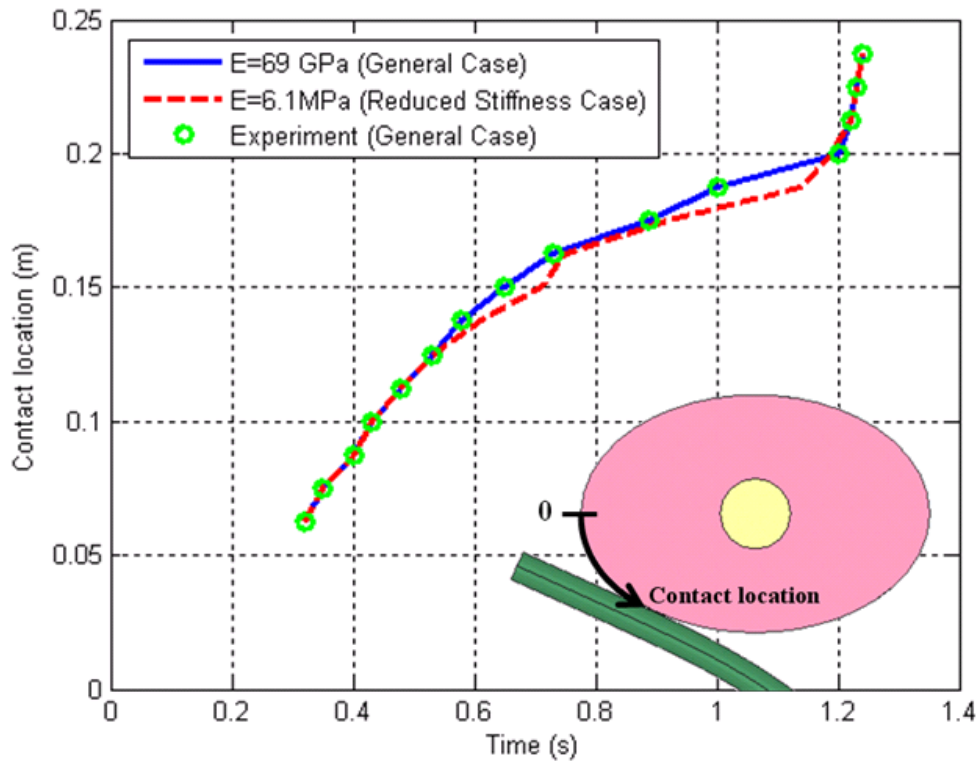


Figure 3-22 Contact location at the elliptical object

3.5.2 Parameter Effect

The objective here is to conduct a parametric study on the contact between the rotating finger and fixed elliptical object. The parameters include the damping coefficient and elastic modulus of the finger, and the elastic modulus of the object. The particular interest is to investigate the effect of these parameters (summarized in Table 3-7) on the maximum stress and reaction force on the object; where E_{finger} and E_{object} are the elastic moduli of the finger and object respectively; σ_{finger} and σ_{object} are the equivalent stresses of the finger and object respectively; and $F_{reaction}$ is reaction force measured from the fixed surface of the force/torque sensor.

Table 3-7 Parameter effect of the contact between the rotating finger and object

Parameter	Value	Max. σ_{finger} (MPa)	Max. σ_{object} (MPa)	Max. $F_{reaction}$ (N)
α (s^{-1})	1, $\zeta=0.02$	1.90	0.89	15.6
	7.5, $\zeta=0.15$	1.90	0.89	15.6
	20, $\zeta=0.4$	1.90	0.93	15.6
	50, $\zeta=1.0$	1.90	0.97	15.4
	180, $\zeta=3.6$	1.95	1.02	15.4
	600, $\zeta=12.0$	2.09	0.21	13.5
E_{finger} (MPa)	4.2	1.29	0.68	10.8
	6.1	1.90	0.89	15.6
E_{object} (MPa)	6.1	1.86	0.04	15.2
	69000	1.90	0.89	15.6

(For general case: $E_{finger} = 6.1MPa$, $E_{object} = 69GPa$, and $\alpha = 7.5 s^{-1}$)

The three parameters being investigated are α , E_{finger} and E_{object} . When the effect of one parameter is studied, the same values (as in the general case) are kept for the other

two. For the effect of the fingers with different damping coefficients, six cases are investigated; $\alpha = 1, 7.5,$ and 20 lead to underdamped responses; $\alpha = 50$ corresponds to critically damped; and $\alpha = 180$ and 600 characterize overdamped responses. The corresponding damping ratios are summarized in Table 3-7. The dynamic responses of the maximum finger stress, maximum object stress, and reaction force are given in Figure 3-23, Figure 3-24, and Figure 3-25 respectively. The maximum finger stress responses are almost the same before time 1.25 second for the underdamped and critical damped cases. At the end of the contact, the finger with lower damping coefficient continues its free vibration. Figure 3-23 shows the oscillating stresses for the lower damping case; while the opposite effect can be observed for the case with higher damping coefficients. The corresponding deformed shapes at some specific time for $\alpha = 1$ and 7.5 cases are shown in Figure 3-26 and Figure 3-27.

For the overdamped cases, the fingers cannot spring back immediately after the drum moves as well as after the contact with the object because of their extra high damping ratios (the damping ratio effect on the free vibration response is shown in Figure D-2 in Appendix D). The corresponding deformed shapes for $\alpha = 180$ and 600 cases are shown in Figure 3-28 and Figure 3-29 respectively. The maximum finger stress (happened at the fixed root location) increases when the damping coefficient increases. The dynamic responses of the $\alpha = 7.5, 180$ and 600 cases are comparing in Figure 3-30 showing that higher damping coefficient decreases the contact duration due to it increases the initial deformation as shown in Figure 3-28 and Figure 3-29, thus changes the contact location.

Table 3-7 and Figure 3-24 show that the maximum object stress (happened at the contact location) increases when damping ratio increases. However, for the case of $\alpha = 600$, the object stress decreases due to the finger deforms initially and does not spring back when the drum rotates. The reaction forces in Figure 3-25 and Table 3-7 are almost the same for these cases, which implies the effect of the damping coefficient is not significant for the calculation the reaction force (except the $\alpha = 600$ case since the finger deforms before the contact). The result is consistent to those reported in [Lee *et al.*, 2001] which have been based on quasi-static assumptions in the calculation of the reaction force for this particular case.

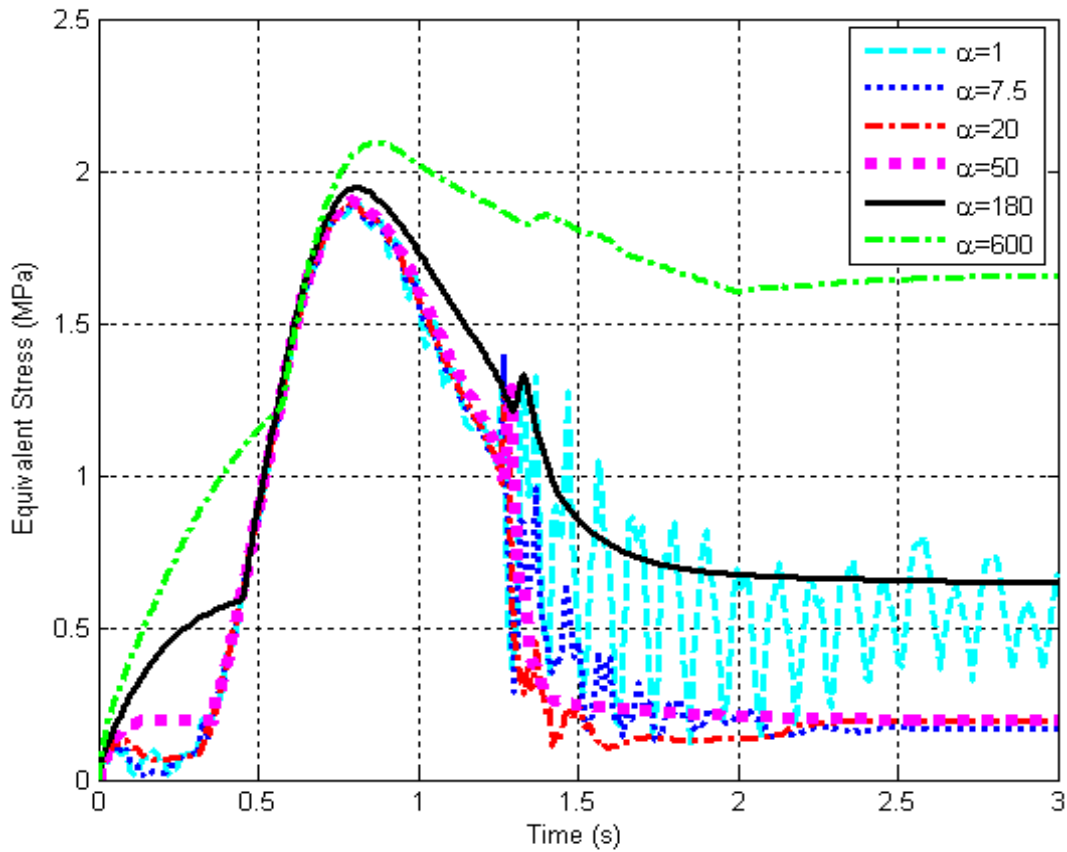


Figure 3-23 Effect of finger damping coefficient on maximum finger stress

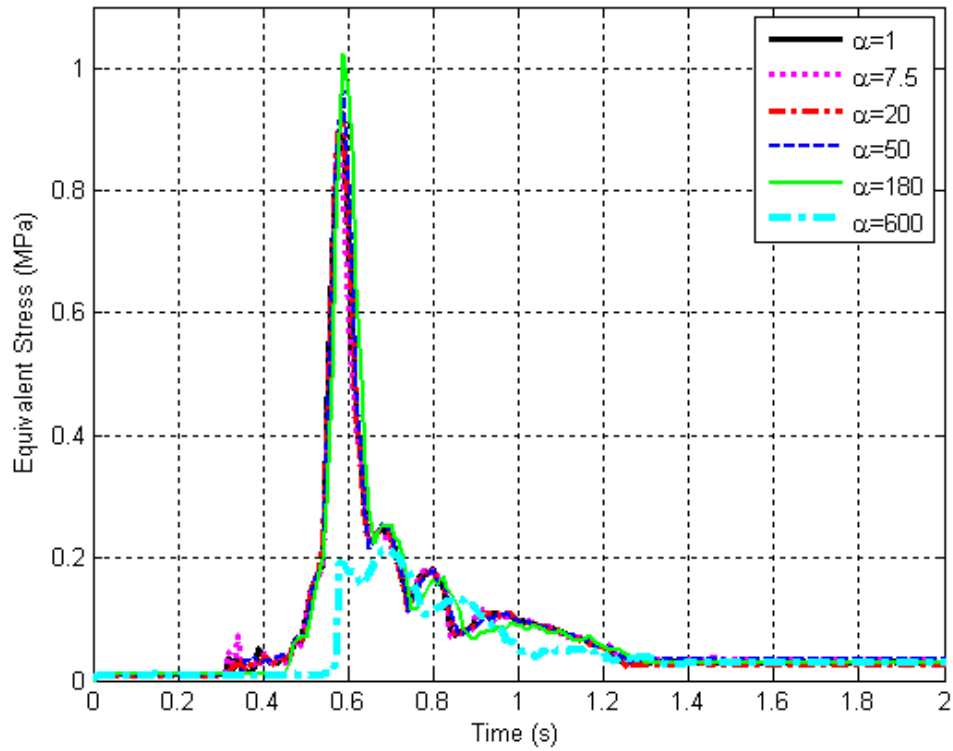


Figure 3-24 Effect of finger damping coefficient on maximum object stress

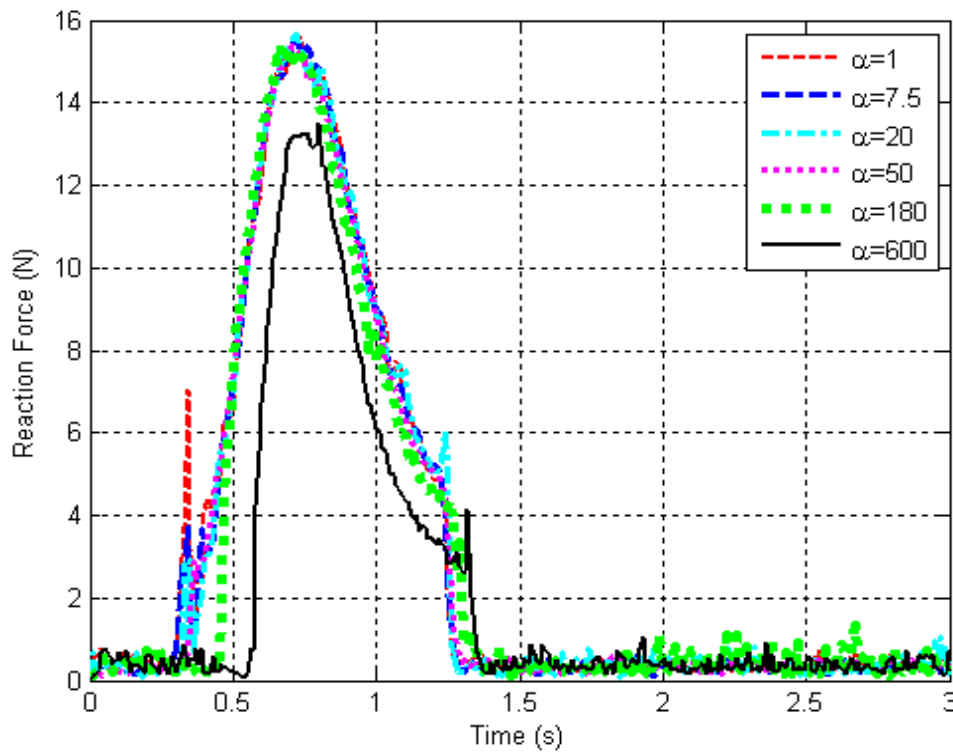


Figure 3-25 Effect of finger damping coefficient on reaction force

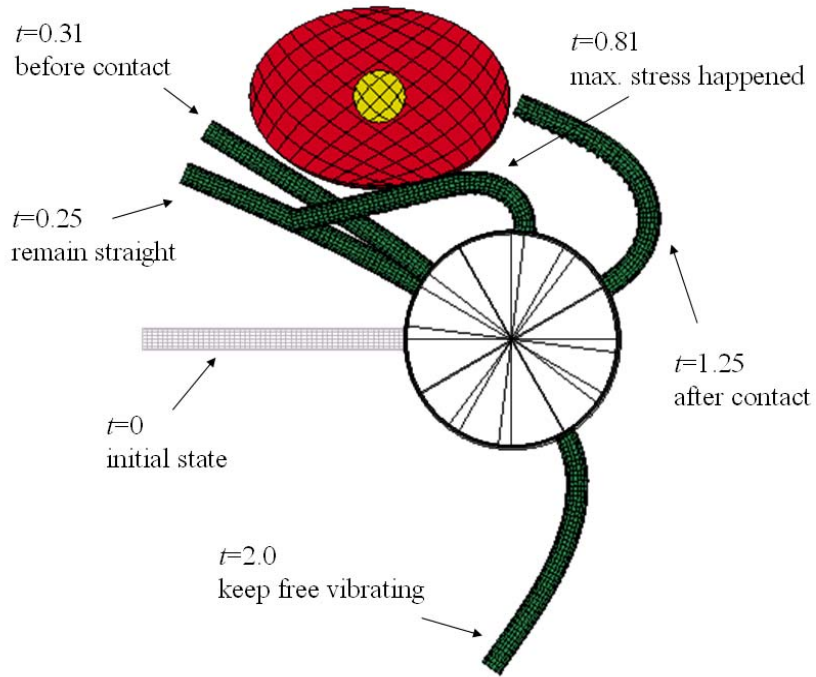


Figure 3-26 Dynamic response for $\alpha=1$ case ($\zeta=0.02$)

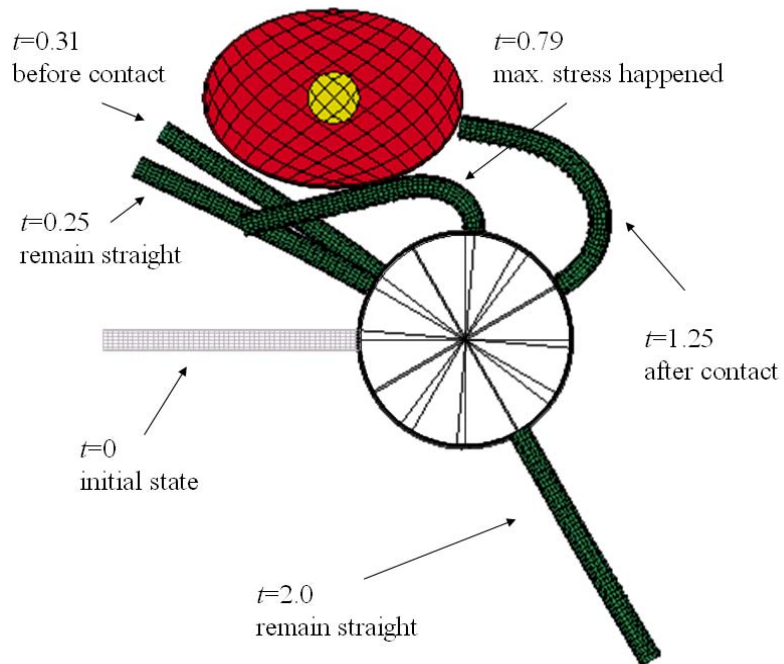


Figure 3-27 Dynamic response for $\alpha=7.5$ case ($\zeta=0.15$)

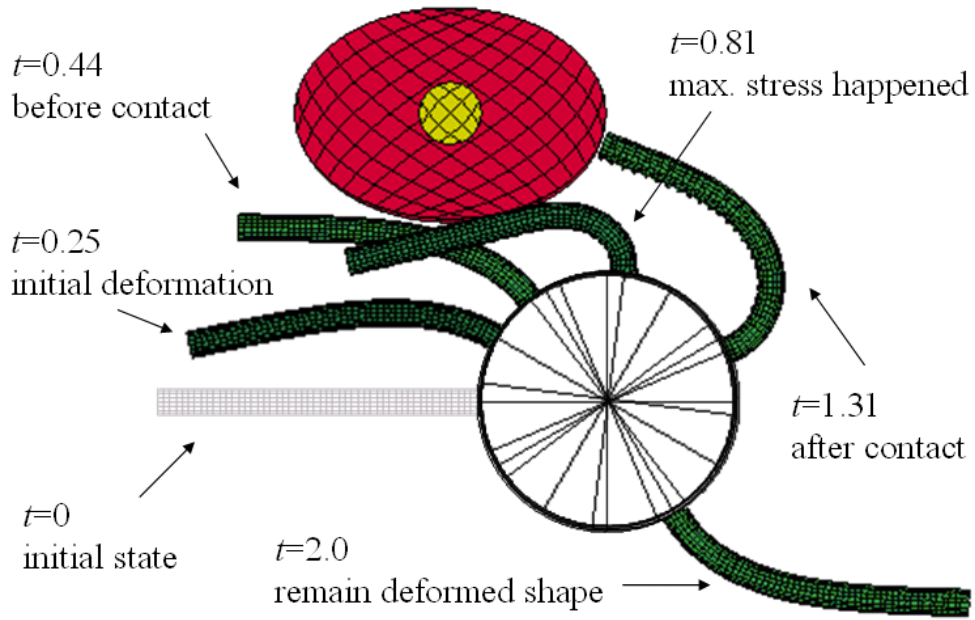


Figure 3-28 Dynamic response for $\alpha=180$ case ($\zeta=3.6$)

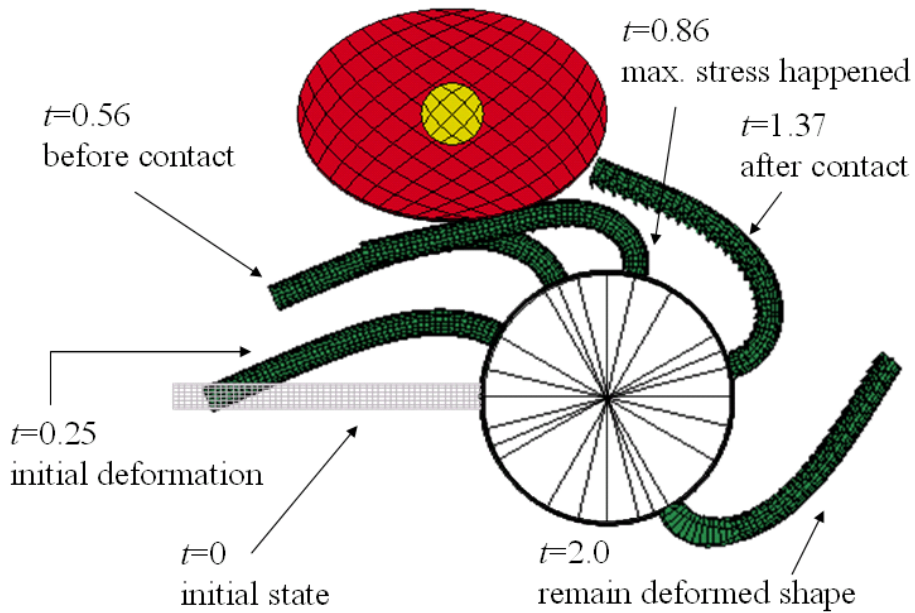


Figure 3-29 Dynamic response for $\alpha=600$ case ($\zeta=12$)

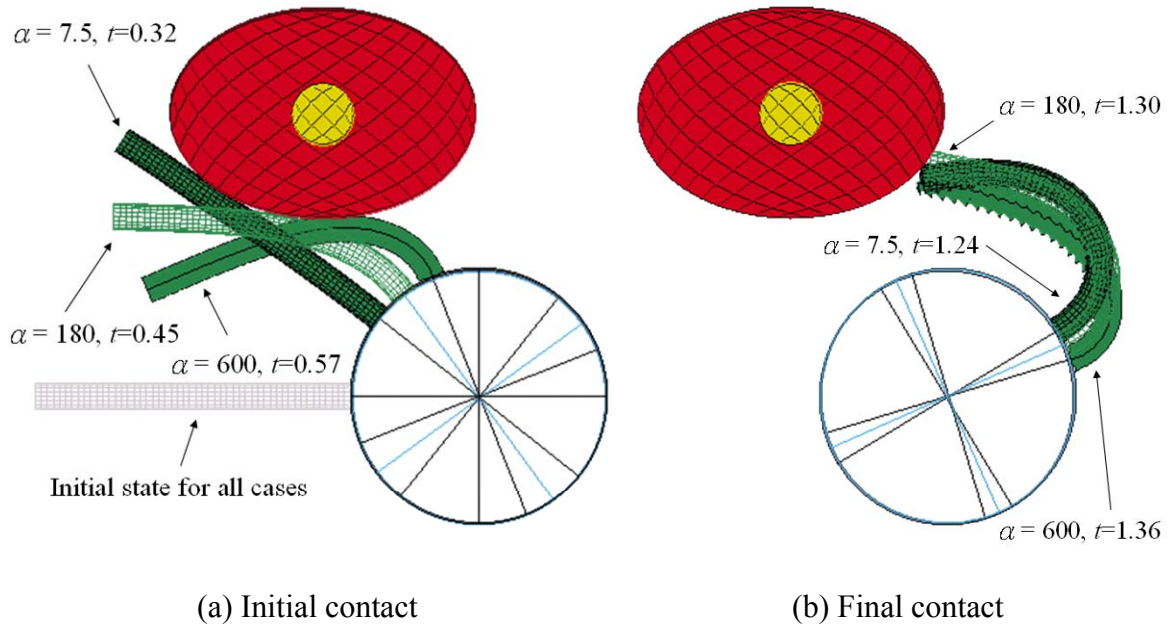


Figure 3-30 Initial and final contact instants for $\alpha = 7.5, 180$ and 600 cases

For the effect of different elastic modulus of finger, the dynamic responses for the maximum finger stress, maximum object stress, and reaction force are given in Figure 3-31, Figure 3-32, and Figure 3-33 respectively showing that the higher finger elastic modulus can lead to higher finger stress, object stress, and reaction force.

For the effect of different elastic modulus of object, the dynamic responses for the maximum finger stress, maximum object stress, and reaction force are given in Figure 3-34, Figure 3-35, and Figure 3-36 respectively. As summarized in Table 3-7, the higher elastic modulus of the object leads to higher maximum object stress, while the maximum finger stress and reaction force increase slightly. Figure 3-22 shows the contact location between finger and object when the object with different elastic modulus. Because of the finger compliance, the deformation is from the finger and the contact locations are close for both cases.

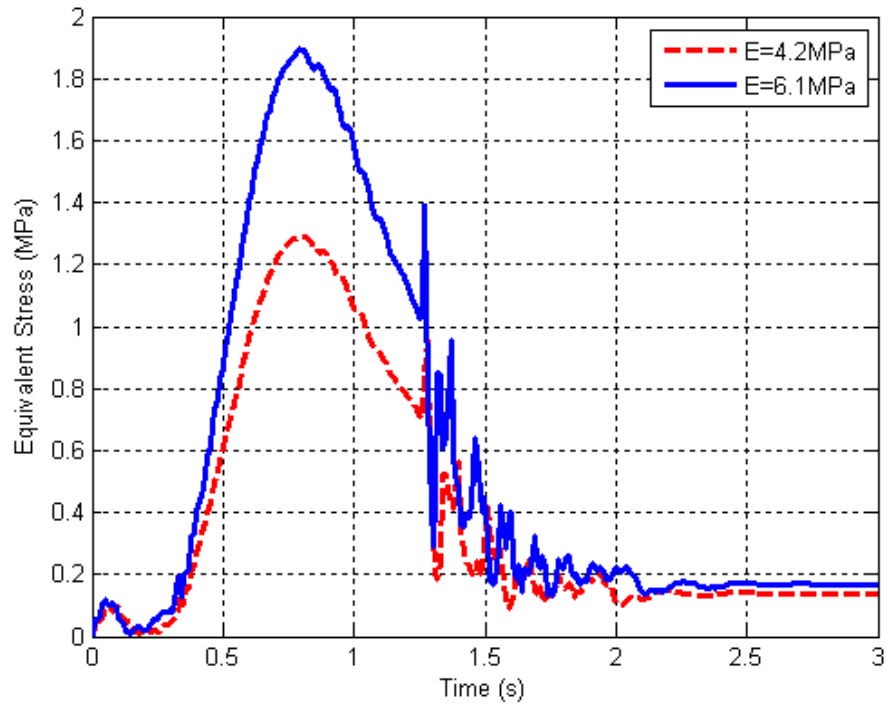


Figure 3-31 Effect of finger elastic modulus on maximum finger stress

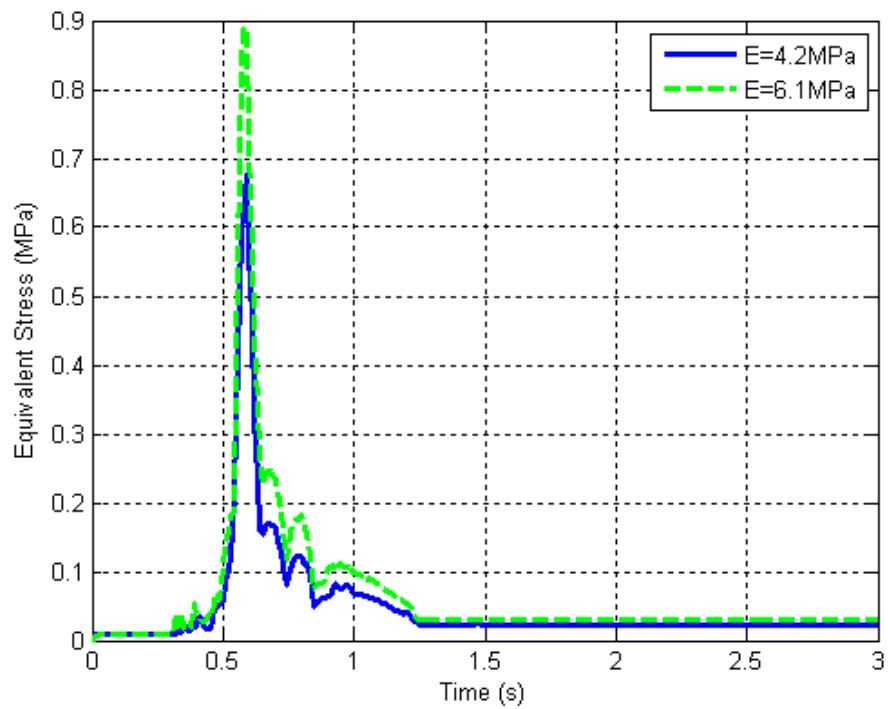


Figure 3-32 Effect of finger elastic modulus on maximum object stress

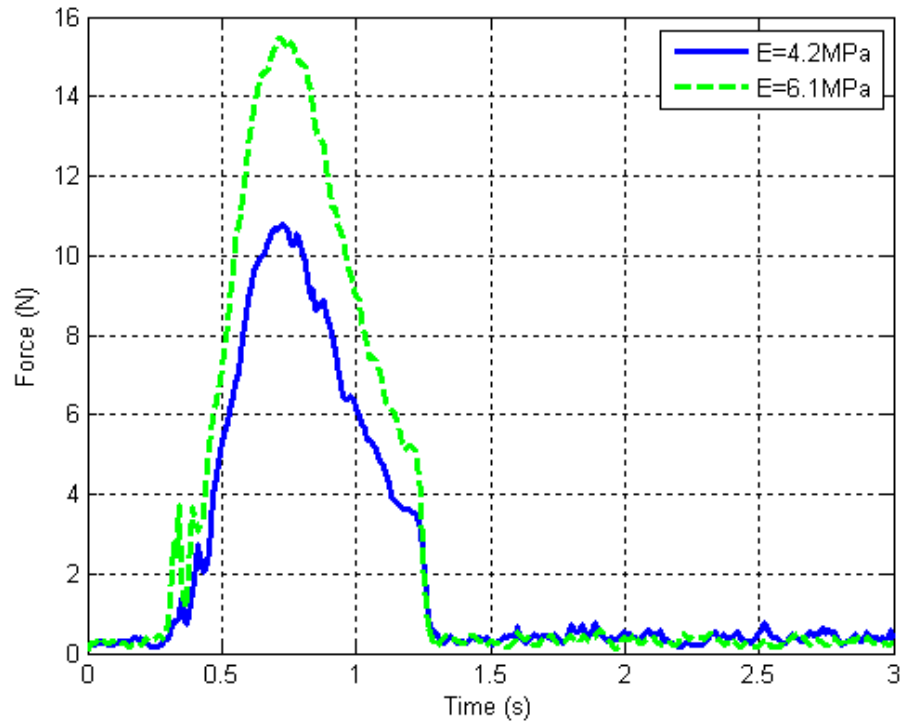


Figure 3-33 Effect of finger elastic modulus on reaction force

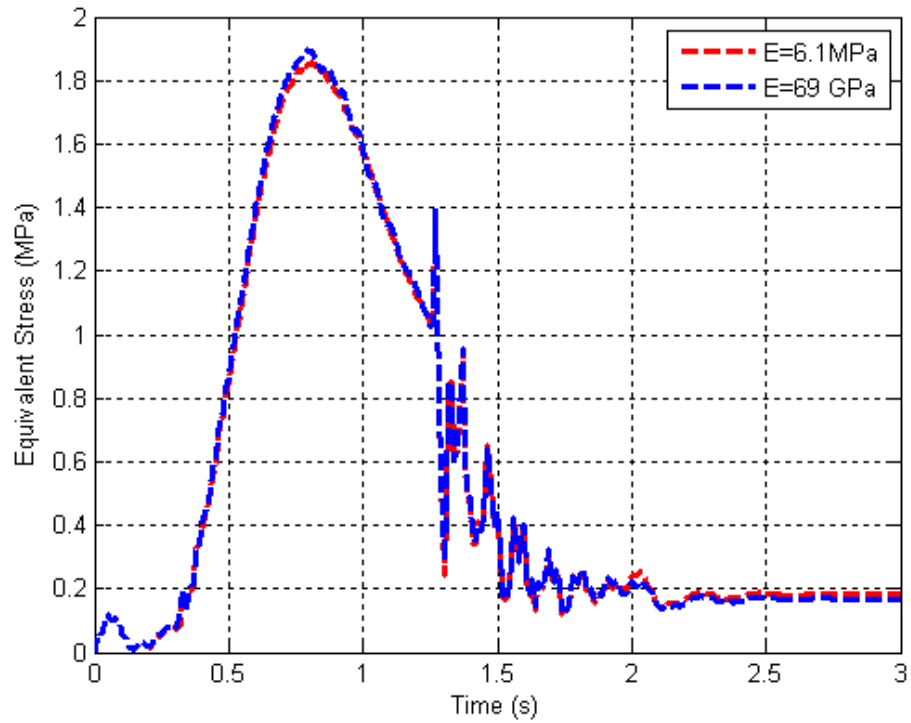


Figure 3-34 Effect of object elastic modulus on maximum finger stress

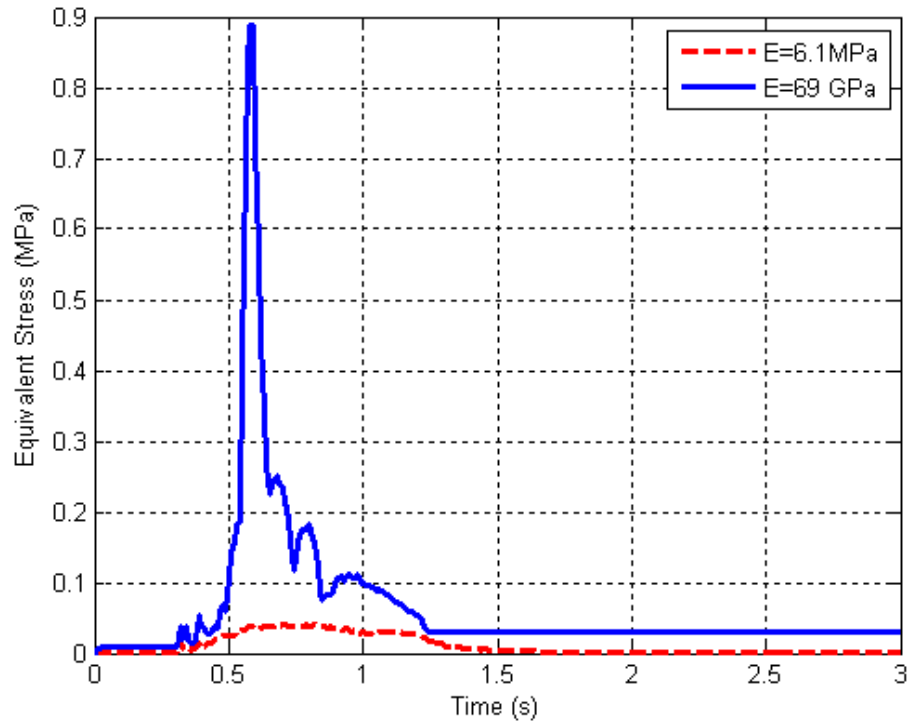


Figure 3-35 Effect of object elastic modulus on maximum object stress

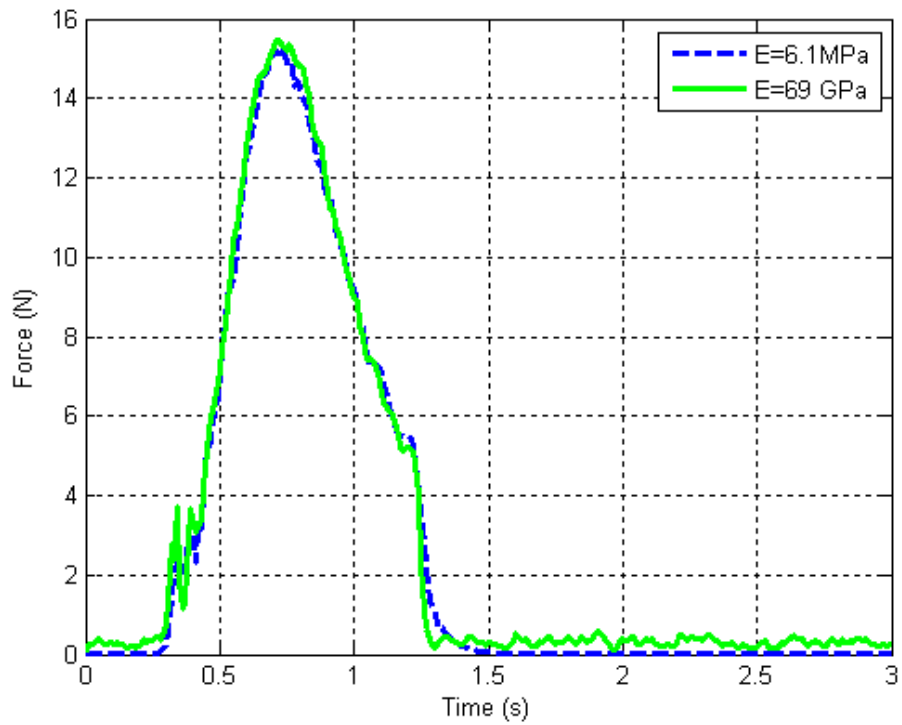


Figure 3-36 Effect of object elastic modulus on reaction force

3.6 Twist Deformation of Compliant Finger

Previous dynamic simulations and experiments focus on bending deformation of the compliant fingers. In this section, we evaluate the twist deformation and compare the simulation against experimental data. The simplified hexa-meshed 4.5-inch finger model and the corresponding boundary conditions are given in Figure 3-37. The 4.5-inch finger is fixed at one end and the force F (showing in Figure 3-37) is one pound (4.45 N) in this simulation. The finger model for this analysis is the same as Case (A) described in Section 3.3.

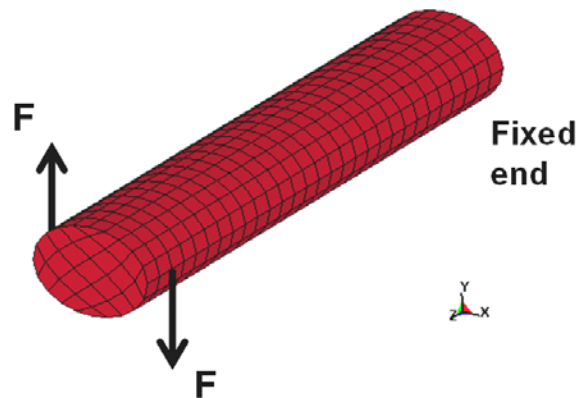
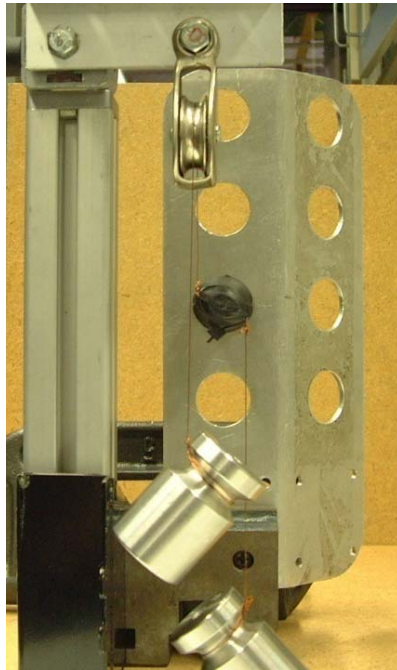
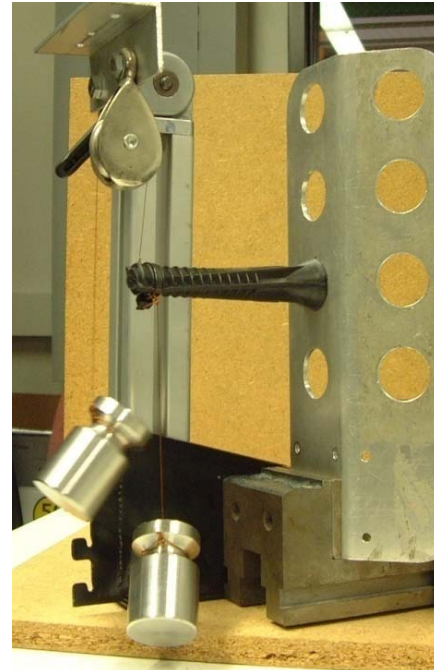


Figure 3-37 Finite element model for finger-twist simulation

The experimental setup for the torsion test can be seen in Figure 3-38. The 4.5-inch finger is fixed at the finger bracket, and two one-pound weights are used for creating the torque (static loading) for twisting the compliant finger. A pulley and the corresponding frame set are used for change the loading direction. The relative equipments for the torsion test are summarized in Table 3-8.



(a) View 1



(b) View 2

Figure 3-38 Experimental setup of finger-twist test

Table 3-8 Equipment for the torsion test

Equipment	Number	Purpose
4.5-inch finger	1	Torsion test specimen
Finger bracket	1	Fix the finger
Fixture	1	Fix the finger bracket
One-pound weight	2	Twist loading
Wire	2	Connect finger and weights
Cable tie	1	Bind at the finger's tip for the connection of the wire
Pulley	1	Change the direction of loading
Frame set	1	Hook the pulley

The simulation and experimental results are compared in Figure 3-39 showing the twist deformation before and after the static loading. The maximum twist angle from the simulation is 25.5 degree at time 5.7ms, and the maximum twist angle from the experiment is 25 degree. From simulation, the dynamic responses at the loading points on the finger are given in Figure 3-40. The dynamic response for the twist angle versus time is given in Figure 3-41.

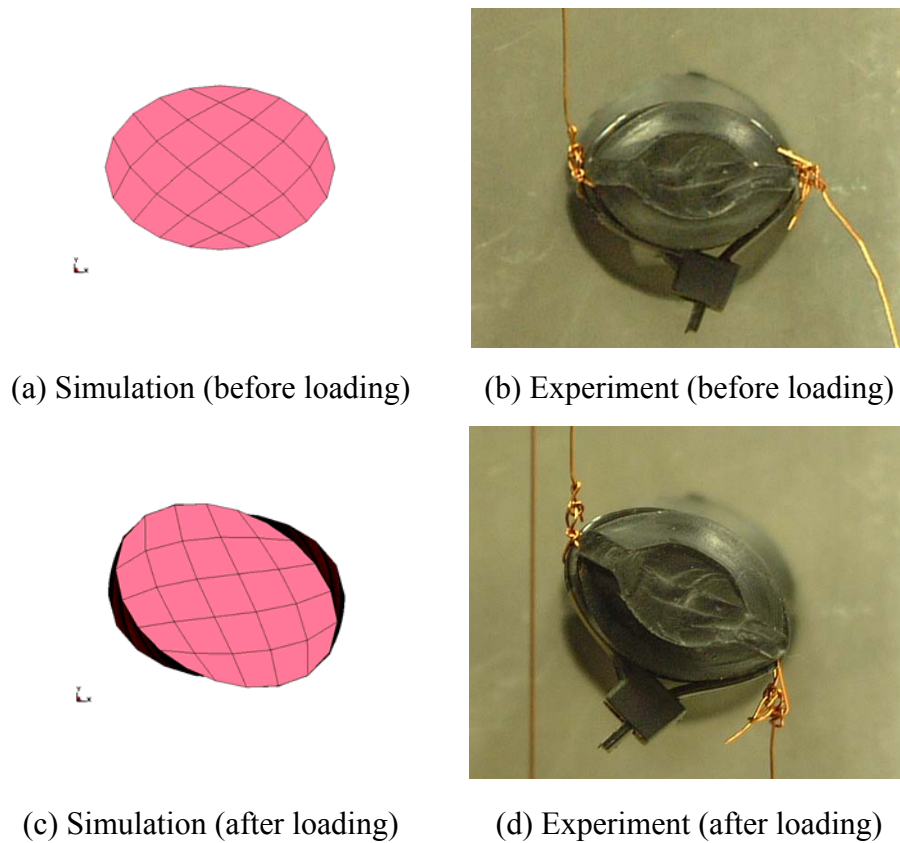


Figure 3-39 Comparison of simulation and experimental results of the twist angle

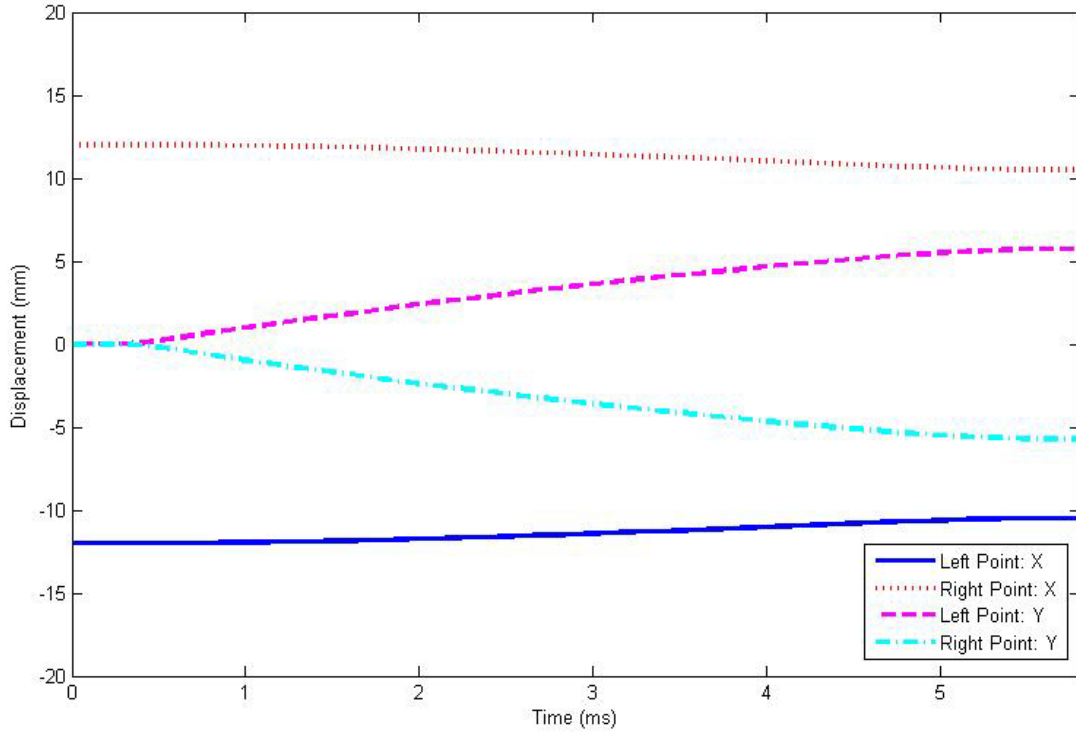


Figure 3-40 Dynamic responses of the loading points

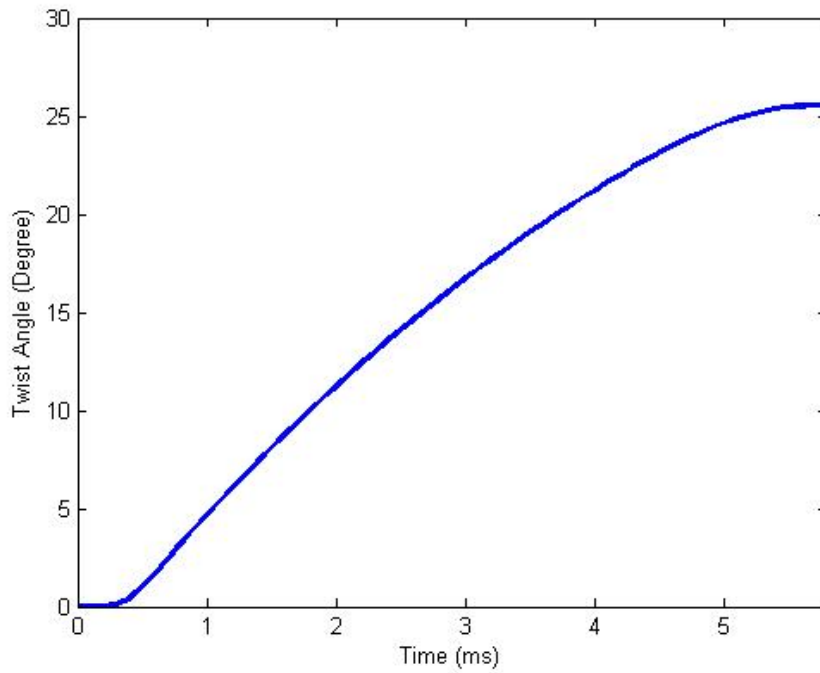


Figure 3-41 Twist angle versus time

3.7 Summary

A highly damped compliant finger has been analyzed. The modal analysis shows that the mass proportional damping assumption is valid for this application. Four different finger-modeling cases (with different element types and sizes) are discussed showing that the simplified hexa meshed finger (Case A) is a reasonable model for a conservative analysis, and then used in the following dynamic simulation to identify the mass proportional damping coefficients by the computational/experimental coupled identification technique. For an underdamped system, the damping ratio can be determined experimentally by the log decrement method. For an overdamped system, the experimentally obtained impulse response provides a basis to numerically search for a trial damping coefficient to match the experimental response. The method is validated by comparing the simulated response of a rotating finger (acting on an elliptical object) against published experimental data, which agrees well. The effect of damping coefficient and elastic modulus on the contact response are investigated. Further, the twist deformation of the compliant finger is also simulated and compared against the experimental result. The maximum twist angle is around 25 degree both from the simulation and experiment.

CHAPTER 4

GRASPING DYNAMIC ANALYSIS OF ELLIPSOIDAL OBJECTS

4.1 Introduction

In Chapter 3, the dynamic model of compliant finger has been presented. This chapter discusses a robotic hand with multiple high-damped compliant fingers for grasping applications. To reduce the number of live chickens to be tested in the development of the live-bird transfer system, the ellipsoidal objects (which are similar to the chicken's body) are used in this study so that factors related to mechanical designs can be isolated.

Two examples are considered in this chapter. In the first example, a moving football and the compliant fingers form a multibody system. The fingers are continuously deformed when the football passing through the rotating hands. The effects of several operating parameters are investigated against the published experimental data [Yin, 2003]. In the second example, the dynamic response of an ellipsoidal object is simulated as the object flips under the control of the compliant hands. These simulations offer insight into the development of an automated transfer system.

4.2 Grasping Dynamic Analysis of a Football

Figure 4-1 describes a prototype of an automated transfer system where a pair of

compliant robotic hands grasps a football as it moves on the conveyor. Both drums rotate in the x-z plane at the same speed but in opposite direction. The grasper consists of a pair of rotating drums, each with five compliant fingers. The finger configurations based on [Yin and Lee, 2002] along with the material and finite element modeling are summarized in Table 4-1 and Table 4-2 respectively.


These fingers are the simplified hexa-meshed models with the same elliptical cross section as described in Chapter 3. As defined in Figure 4-1b and Table 4-1, each finger has its specified orientation (R_x and R_z) in its local coordinate. Fingers A and B are placed at the upper level of the drum where the radius (r_{drum}) is equal to 3.25-inch. Fingers C, D, and E are placed at the lower level where the radius is equal to 4.25-inch. The origin of the global coordinate is at the center of the bottom area of the drum. The initial angle (θ_f) of Finger D is defined as zero degree as shown in Figure 4-1a. The height of finger (h_f) is measured from the fixed end of the finger along the y-coordinate. The damping coefficients (mass proportional) are based on results in Chapter 3. The corresponding boundary conditions are summarized in Table 4-3.

The simulation here relaxes the quasi-static assumption that commonly assumed in previous studies, and the effect of relative displacement (between the football and pallet) can be investigated more realistically. The following assumptions are made in this study:

- The football moves along the center line between two drums and a half symmetric model is used.
- The football is assumed to be a homogeneous solid with its density calculated from the raw weight (0.425 kg) divided by the volume.

- The static and dynamic friction coefficients are assumed to be 0.4 and 0.3 respectively [Yin and Lee, 2002].

Table 4-1 Finger set configuration

Parameters	Values					
Finger #						
Major semi-axis, a	12 mm					
Minor semi-axis, b	8.45 mm					
Length mm (inch)	114.3 (4.5)	114.3 (4.5)	76.2 (3.0)	76.2 (3.0)	76.2 (3.0)	
Height mm (inch) h_f	76.2 (3.0)	76.2 (3.0)	25.4 (1.0)	19 (0.75)	25.4 (1.0)	
Initial angle θ_f	-11.25°	11.25°	-22.5°	0°	22.5°	
Drum radius mm (inch) r_{drum}	82.6 (3.25)	82.6 (3.25)	108 (4.25)	108 (4.25)	108 (4.25)	
Orientation R_x	45°	-45°	-45°	0°	45°	
Orientation R_z	10°	10°	-2.5°	-10°	-2.5°	
Damping coefficient (1/s) α	180	180	600	600	600	

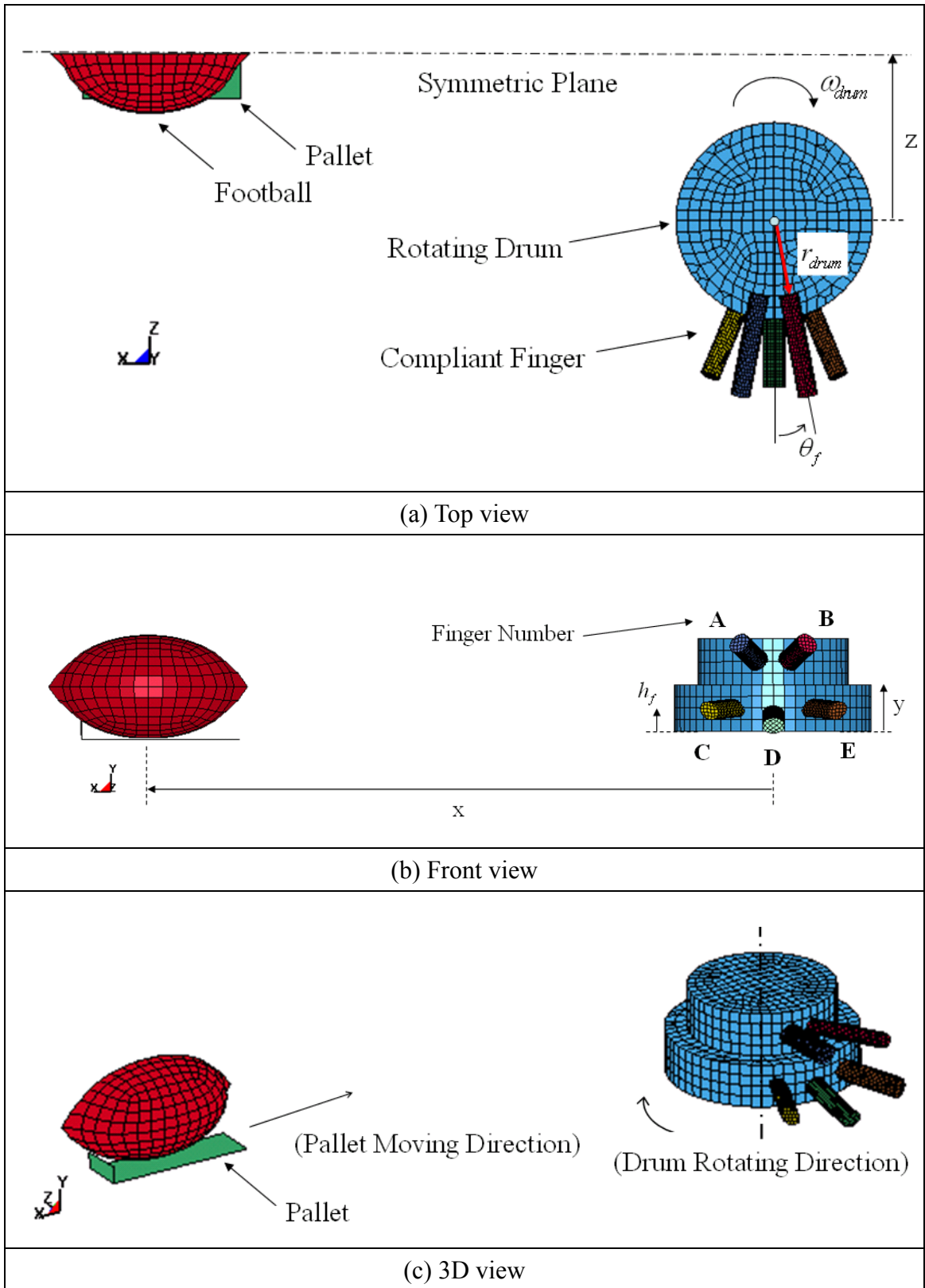


Figure 4-1 Finite element (half symmetric) model for football grasping

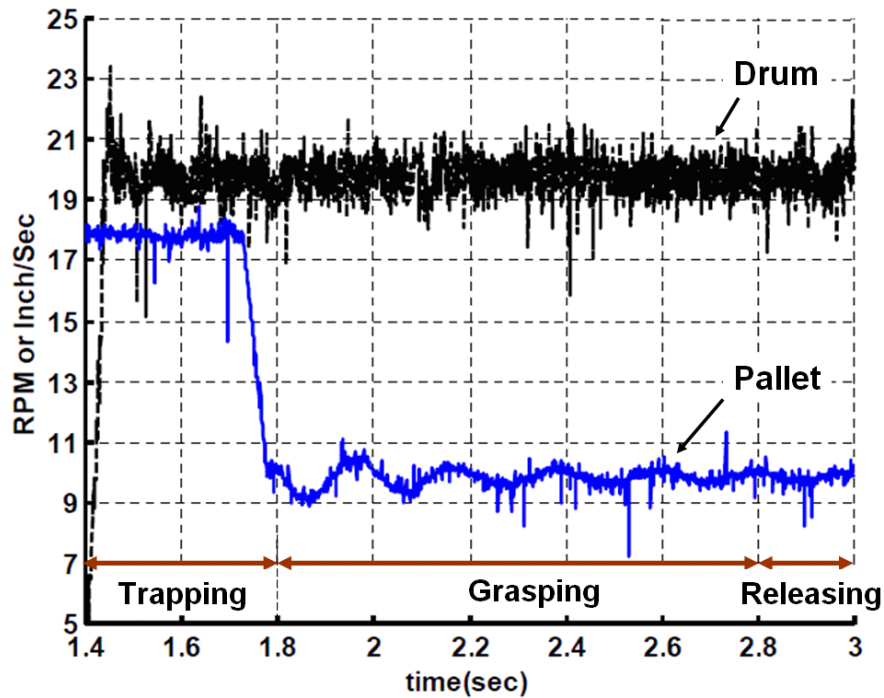
Table 4-2 Material and finite element modeling of the football grasping analysis

Part Name	Material	E (GPa)	ν	ρ (kg/m ³)	Element Type	Element #	Node #
Football	Rubber	0.0061	0.49	275	Solid 164	512	677
Drum	AL6061	69	0.33	2700	Shell 163	1271	1212
Fingers A and B	Rubber	0.0061	0.49	1000	Solid 164	725	1080
Fingers C, D, and E	Rubber	0.0061	0.49	1000	Solid 164	500	756
Pallet	Steel	210	0.28	7700	Shell 163	2	6
sum	-	-	-	-	-	4735	6323

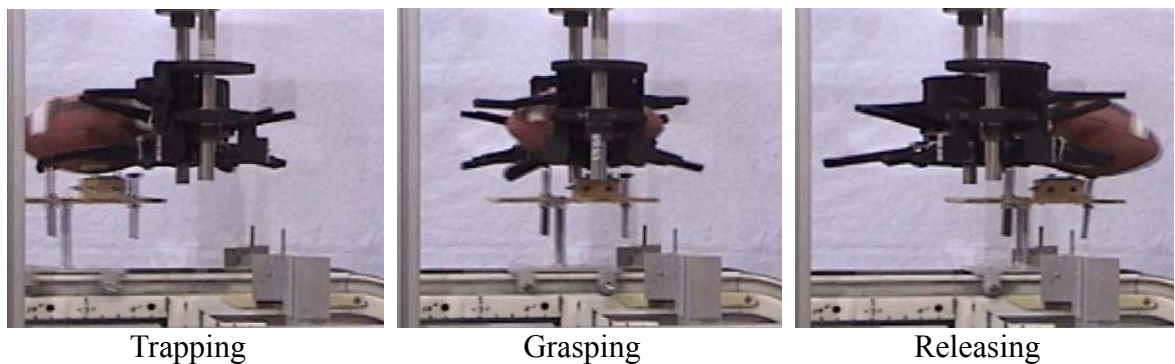
Table 4-3 Boundary conditions

Parameters	Values
Football initial position	(x, y, z) = (685.5, 50.8, 184) mm Football dimension: 244/132/132 mm (max. length)
Conveyor (pallet) speed	0-1.19s 0.457 m/s (18 inch/s) 1.19-3s 0.254 m/s (10 inch/s) Pallet dimension: length: 200 mm, width: 50 mm
Angular velocity of drum	2.0944 rad/s (20 rpm), operating time: 3s
Static/Dynamic friction	0.4/0.3
Gravity	9.81 m/s ²
Constraints	Drum DOF UY =0, Drum center line all DOF=0 Ellipsoid symmetric plane DOF UZ=0
Simulation time	3s

Figure 4-2a shows the specified velocity profiles of the drum (rpm) and the conveyor (inch/s) obtained from the encoder readings of the motors [Yin, 2003]. The motion trajectory of the football is extracted from the video recording of a 30 fps video camera. Figure 4-2b illustrates the three phase of the grasping process: trapping, grasping, and releasing respectively.



(a) Experimental specified drum and conveyor velocity profiles



(b) Experimental snapshots of football grasping process

Figure 4-2 Experiment of football grasping [Yin, 2003]

The simulation and experimental results for the y-axis trajectory of the football are given in Figure 4-3, which qualitatively agrees with the experiment. The maximum displacement obtained from simulation is slightly larger than the experiment, and the difference is 2mm at time between 1.80-1.85 sec. Figure 4-4 shows the football and pallet remain a constant relative distance around 8mm (football behind pallet) while the pallet starts to move forward. The relative distance increases initially during the grasping process then decreases due to the predefined pallet speed is slow down and the fingers push the football forward during the releasing process. Figure 4-5 shows the dynamic response from simulation at some specific time.

From above, the overall trend of the simulation closely follows the experiment. The difference may be contributed by the following causes: 1) The simplified FE model, which neglects the rigs and the taper fixed-end cross section, tends to predict a larger deflection and higher stresses. 2) The experimental specified conveyor and drum velocities are oscillated (as shown in Figure 4-2a) while these specified velocities are ideal step response in the simulation.

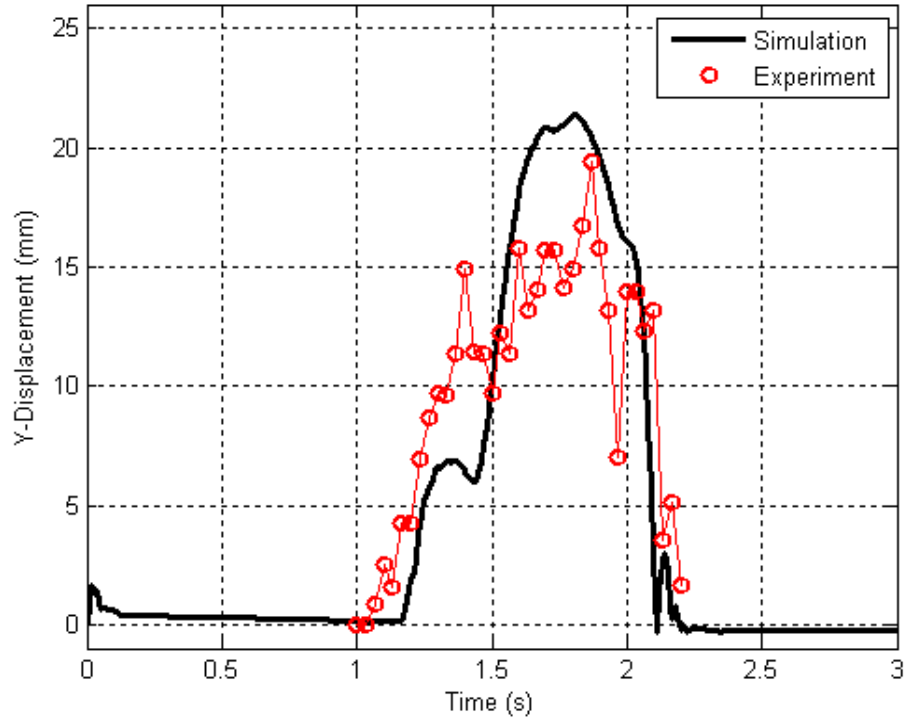


Figure 4-3 Football y-axis trajectory

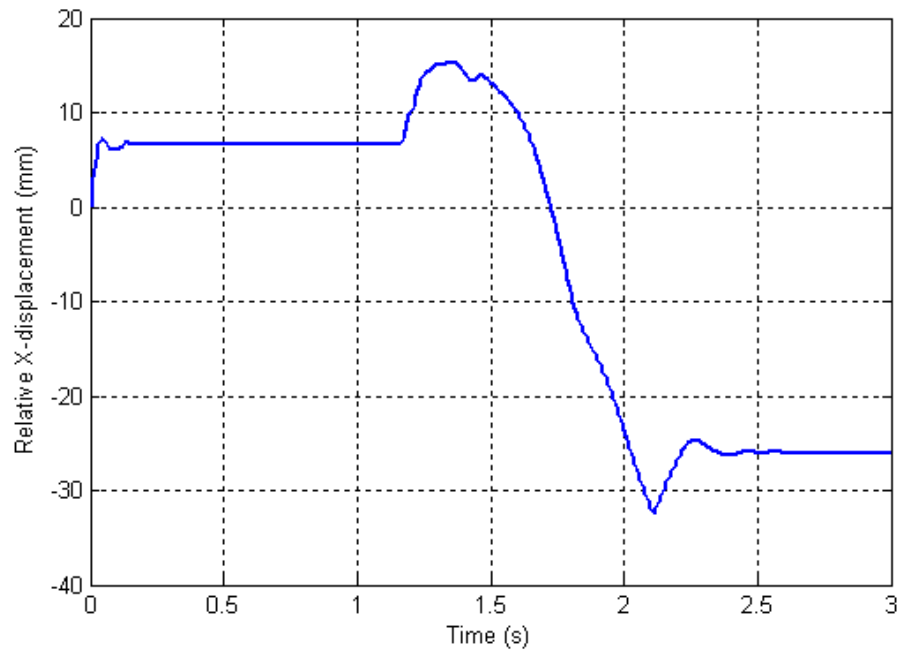


Figure 4-4 Relative X-displacement between the football and pallet

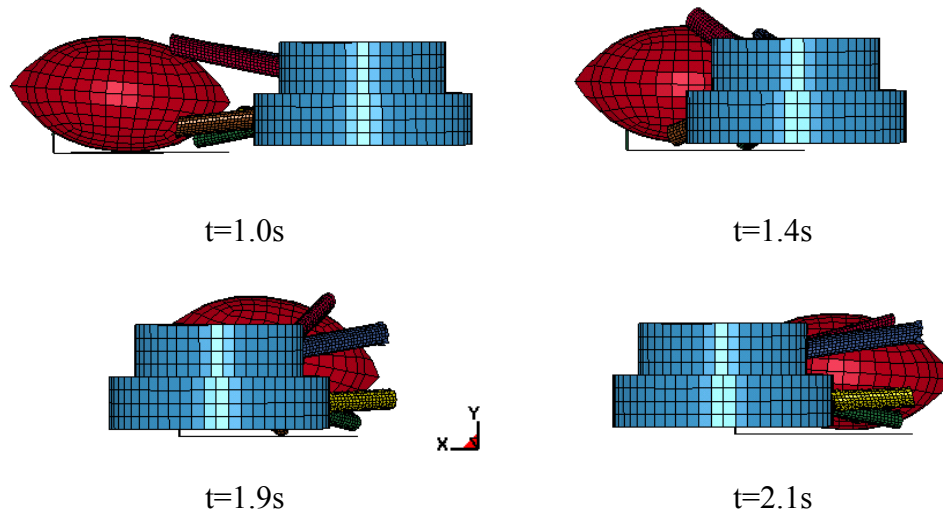


Figure 4-5 Dynamic response from simulation

4.3 Effects of Operating Parameters

In previous section, different speeds were used to control the pallet while the drum rotates at a constant speed (20 rpm) for the entire cycle time. The conveyor speed decreases from 0.457 m/s (18 inch/s) to 0.254 m/s (10 inch/s) when the relative distance between football and drum is 0.142m (5.6 inch). The interest here is to investigate the sensitivity of the conveyor speed and timing parameters on the trajectory of the multibody motion. Several cases are simulated and summarized in Table 4-4 where Case 4 is the operating condition in previous section. Case 1 uses constant conveyor speed for the entire cycle, while other cases use the non-constant speeds to regulate the relative distance between the football and drum. Simulated maximum y displacements and maximum equivalent stresses acting on the football for these four cases are summarized in Table 4-4.

Table 4-4 Design analysis for conveyor (pallet) speed and timing

Case	Conveyor speed (m/s)	Timing (s)	Football/drum distance when speed changed (m)	Max. y-axis displacement (mm)	Max. stress on football (MPa)
1	0.457 (18 inch/s)	0-3	-	24.6	0.042
2*	0.457 (18 inch/s)	0-1.38 1.38-3	0.055	17.6	0.035
3		0-1.28 1.28-3	0.1	21.6	0.054
4 [^]		0-1.19 1.19-3	0.142	21.4	0.072
5		0-1.06 1.06-3	0.2	23.2	0.065

* optimal result; [^] operating condition in previous football experiment

The dynamic responses of the football in the x and y directions are given in Figure 4-6 and Figure 4-7 respectively. The center of the football is initially at 0.6855 m (in the x-direction) relative to the drum center. Figure 4-8 shows the maximum equivalent stress acting on the football during the automated transfer process. The simulation result shows that Case 2 (non-constant conveyor speed) obtains the minimum y displacement and stress on the football. Since the unnecessary large oscillation and stress acting on the object are avoided during the process, Case 2 condition is referred as the preferred operating parameters for controlling the automated step. The dynamic responses for Case 2 are given in Figure 4-9, which shows the multibody motion at some specific time. The corresponding contact location between the football and compliant fingers is given in Figure 4-10, where A, B, C, D and E represent the finger number defined in Figure 4-1b. Among which, fingers A and C are relatively less interactions with the football. Figure

4-11 shows the finger-tip responses, which imply the contact time between fingers and football. The maximum deflection occurs at Finger B at time 1.68 second.

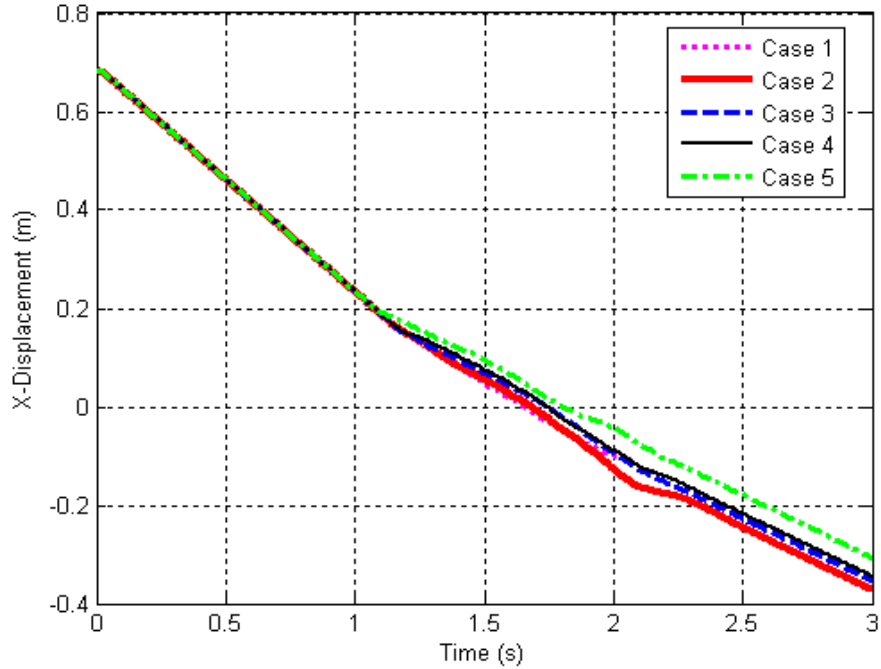


Figure 4-6 X-direction response of the football

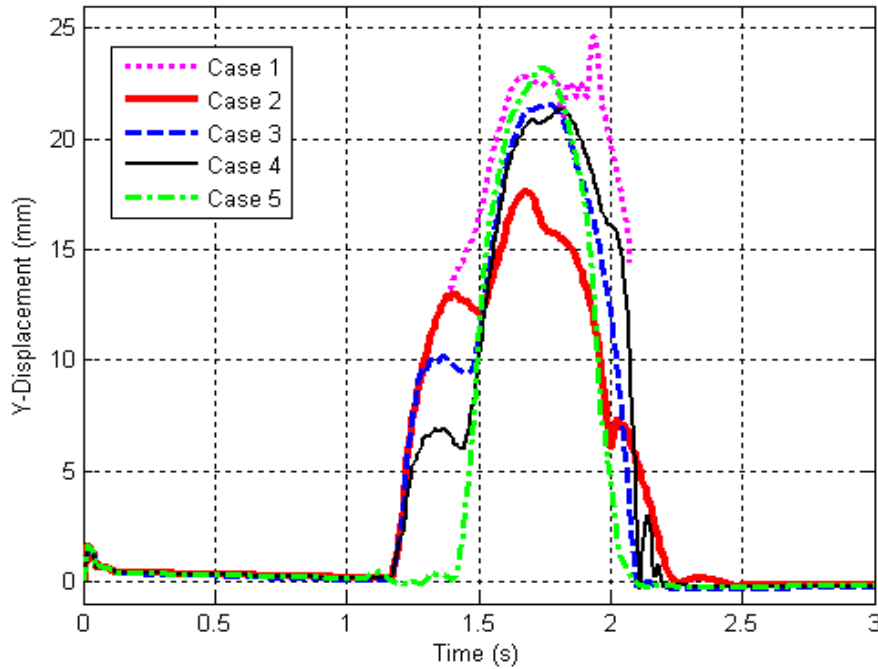


Figure 4-7 Y-direction response of the football

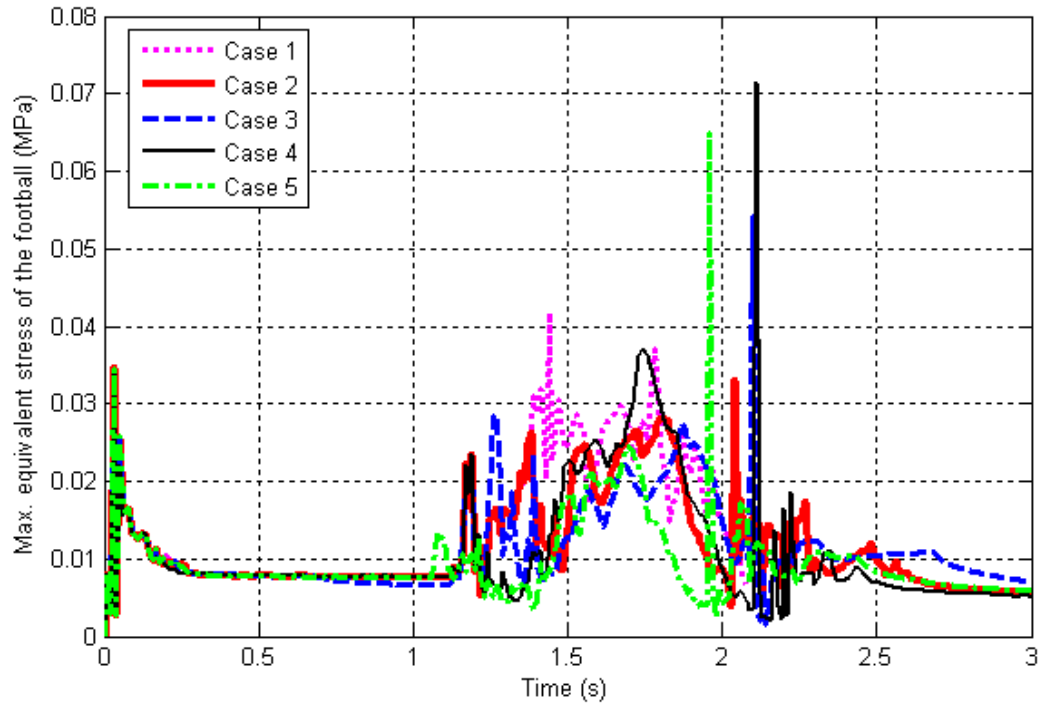


Figure 4-8 Maximum equivalent stress on football

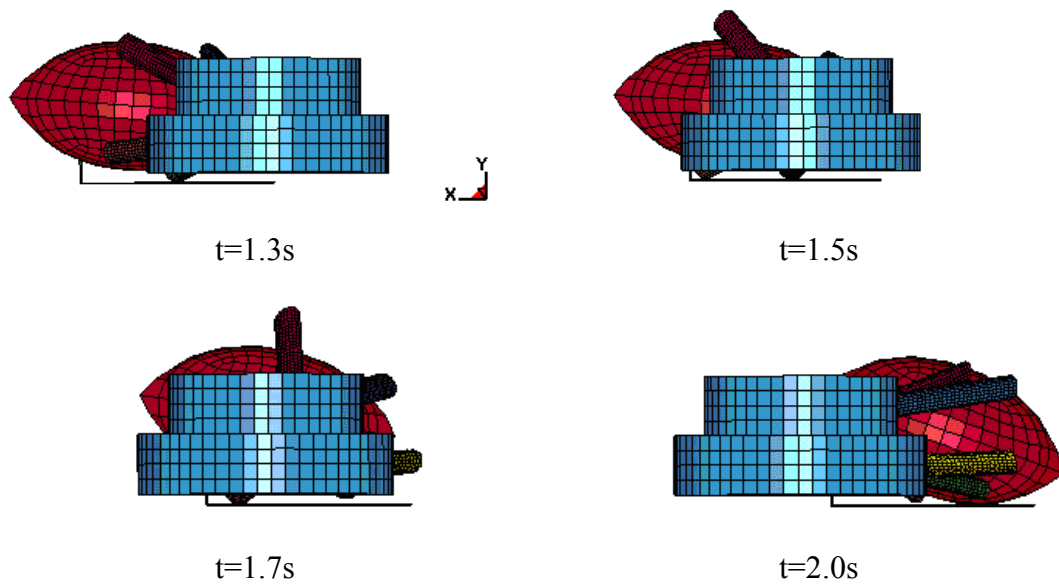


Figure 4-9 Dynamic response under the optimal operating parameters (case 2)

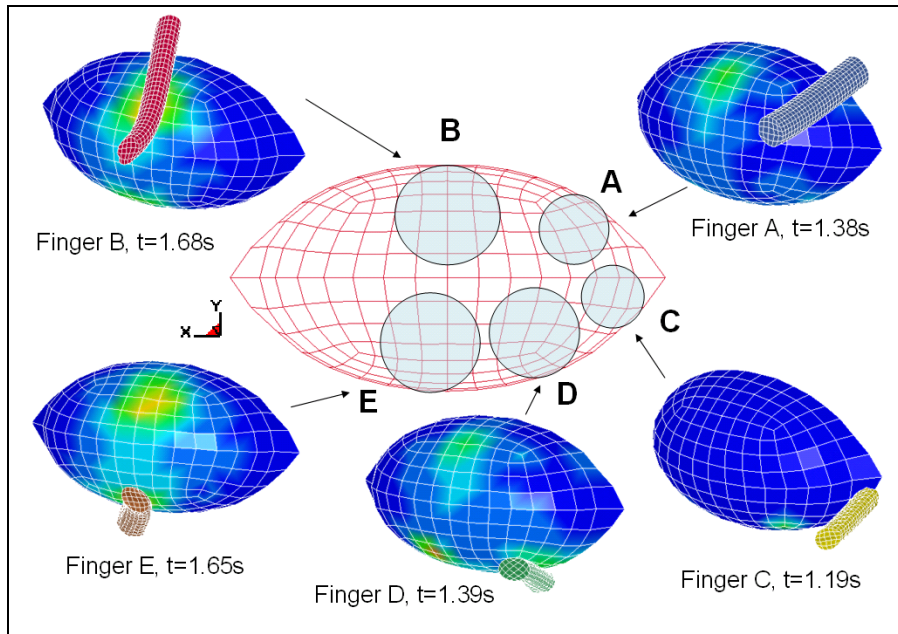


Figure 4-10 Contact location between the fingers and football (Case 2)

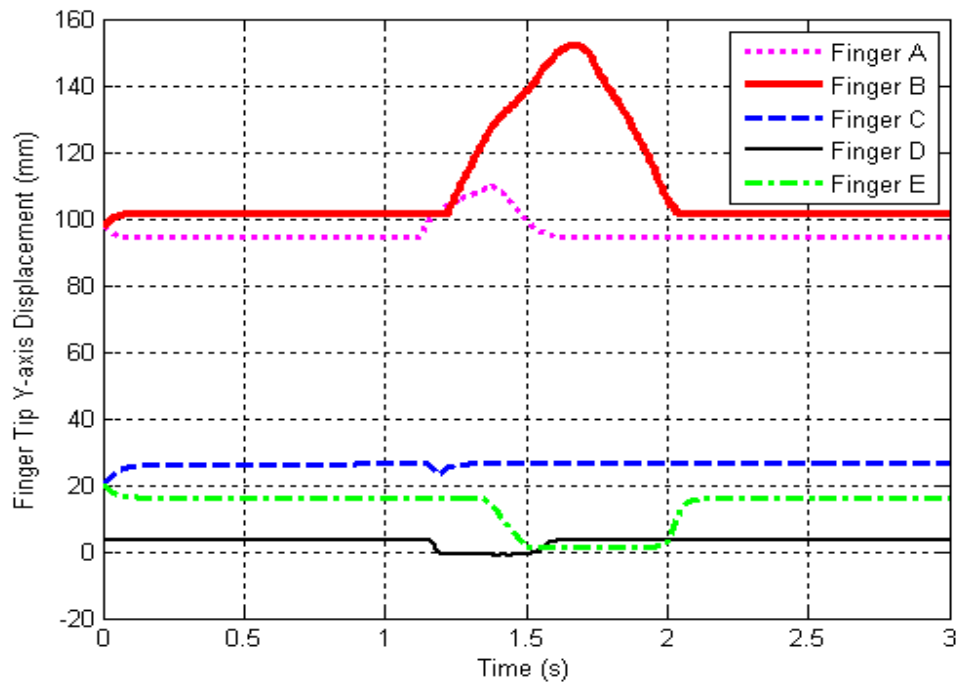


Figure 4-11 Finger-tip response (y-axis)

4.4 Grasping and Flipping Dynamic Analysis of an Ellipsoid

In developing the automated transfer system, a flipping step of the compliant hands after the fingers grasp the object is considered as a possible process. An ellipsoid is assumed as the target object in this section and the dynamic model is performed to predict the dynamic response of the multibody system. The configurations of the compliant hands (rotating drum and fingers) are the same as Section 4.3. The full geometry model can be seen in Figure 4-12 and a half symmetric model is used as described in previous section. The target object is changed from the football to an ellipsoid with a relative heavier mass (1.53 kg). The semi-axes of the ellipsoid are 97, 66, and 57 mm. The density is 1000 kg/m^3 .

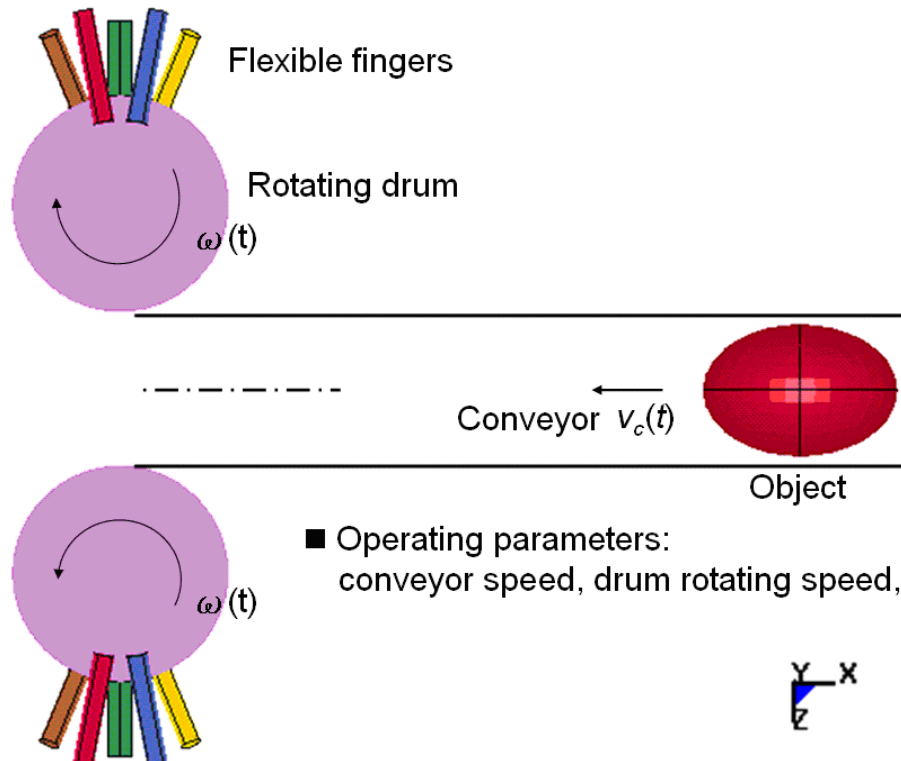


Figure 4-12 Top view of the transfer system for the grasping/flipping analysis

The dynamic simulation consists of two steps: grasping and flipping. In order to investigate if the ellipsoid can be held well by the compliant hands during the flipping process, an ideal grasping of the object is performed first (no relative displacement between the object and conveyor) so the factors other than the flipping process (for example, not grasp the object well before flip) can be isolated. Thus, the result from the grasping step provides the initial condition of the flipping process.

In the grasping step, the conveyor (ellipsoid) moves toward to the negative x direction and stops at the drum-center while the drum rotates about y axis in the x-z plane as shown in Figure 4-12. After the rotating hand grasps the ellipsoid, the drum flips about the z axis and stops when the rotating angle equals to 135 degree (which is referred to here the flipping process).

The boundary conditions for the grasping step are summarized in Table 4-5, and the simulation results can be seen in Figure 4-13, which shows the dynamic response during grasping at some specific time. The drum rotating angle θ_y is initially at 0° and it stops rotate after grasping the ellipsoidal object when the rotating angle θ_y equal to 180° at time 1.5 sec. The total simulation time is 2 sec. Figure 4-14 is the symmetry expansion when the compliant hands grasp the ellipsoidal object. Figure 4-15 shows the finger tip response during grasping where A, B, C, D and E are the finger-number defined in Figure 4-1b. The maximum deformation is happened on finger A in this case which is about 34 mm at time 1.5 sec. Figure 4-16a is the contour plot for y-axis deformation at time 1.5 sec, while Figure 4-16b is the equivalent stress contour. The simulation results show that the maximum stress occurs at Finger A with the value about 0.69 MPa at $t=1.48$ sec, which is lower than the yield stress of rubber (around 9 MPa).

Table 4-5 Boundary conditions for grasping dynamic analysis

Parameters	Values
Object initial position	0.69m (x), 0.184m (z) relative to drum center
Angular velocity of drum	2.0944 rad/s (20 rpm), operation time: 1.5s
Conveyor speed	0.457 m/s (18 in/s), conveyor speed=object speed
Static/Dynamic friction	0.4/0.3 [Yin and Lee, 2002]
Constraints	Drum DOF UY =0, Drum center line all DOF=0 Ellipsoid symmetric plane DOF UZ=0
Simulation time	2s, object arrives drum center at 1.5s

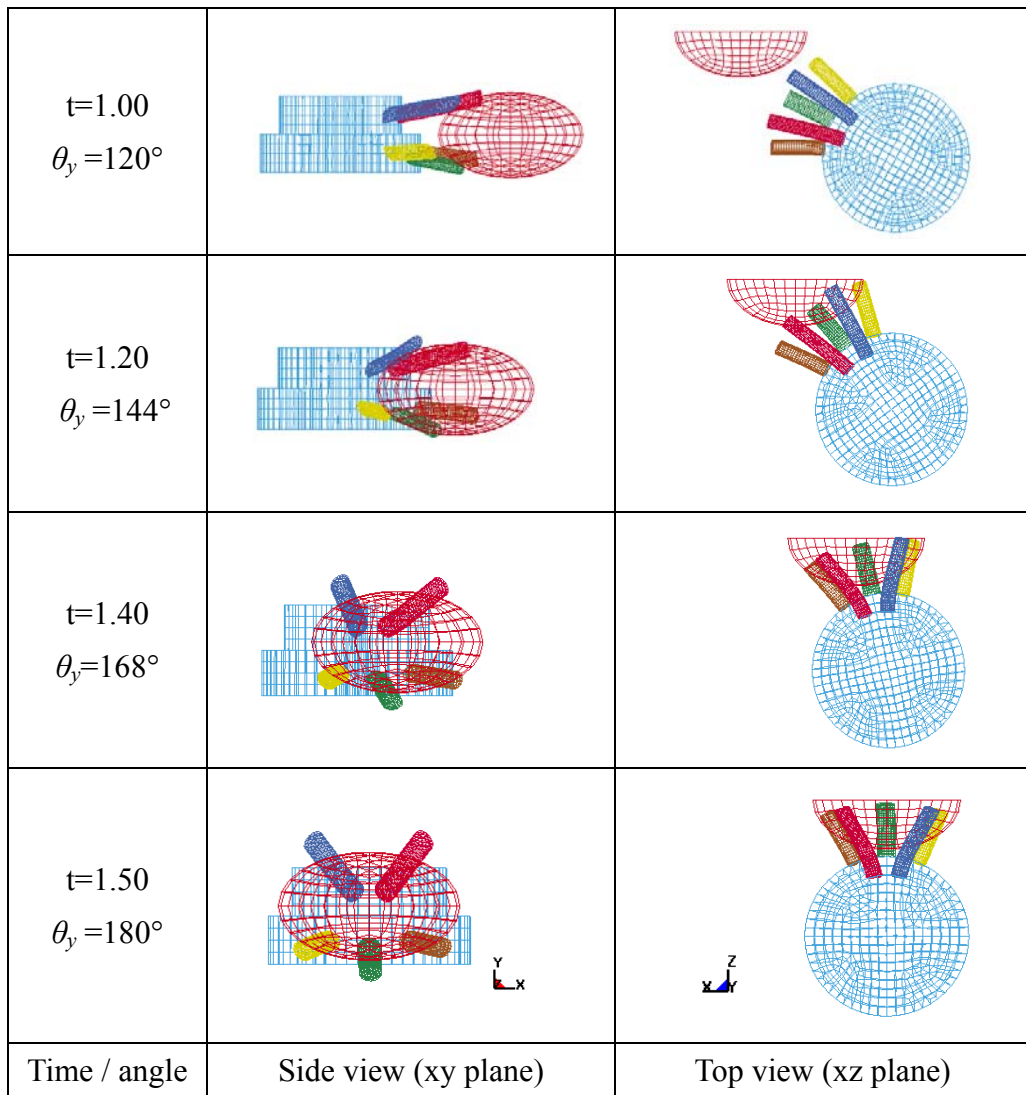


Figure 4-13 Grasping dynamic analysis results

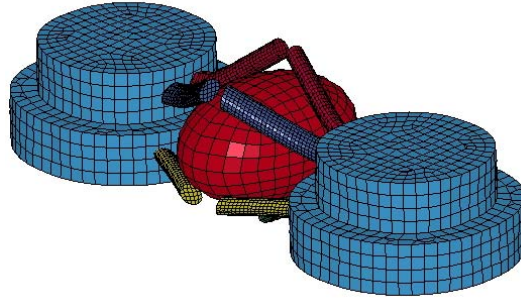


Figure 4-14 Symmetry expansion of grasping dynamic analysis result

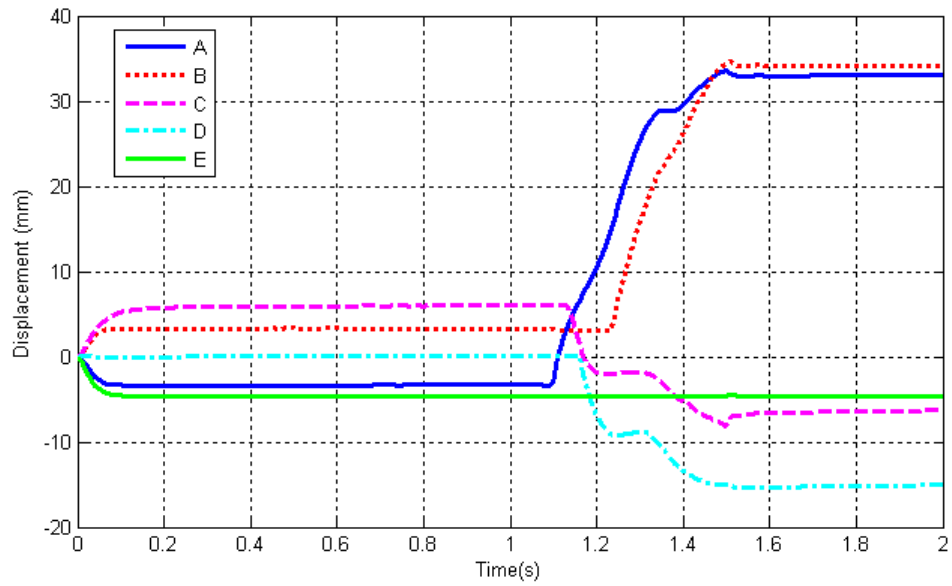
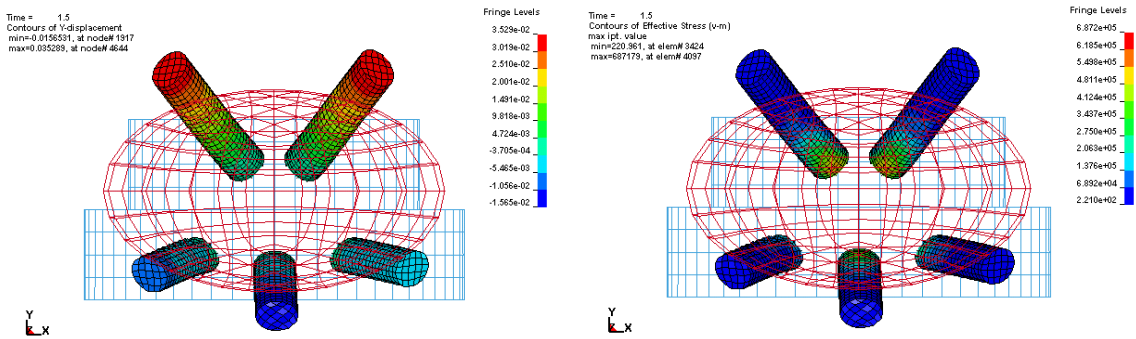


Figure 4-15 Finger tip response (y-axis)



(a) y-displacement contour

(b) stress contour

Figure 4-16 Y-axis deformation and stress contour of the compliant fingers

After the object is grasped, a flipping process is considered as the next step for the automated transfer procedure. The boundary conditions are summarized in Table 4-6. The initial conditions (such as object location and finger deformation) are based on previous grasping dynamic analysis results. The flipping angle θ_z starts from 0° and stops at 135° when the time from 0 to 0.5 sec. The rotating speed (ω_z) is 4.71 rad/s (45 rpm). The total simulation time is 1.0 sec.

Table 4-6 Boundary conditions for flipping dynamic analysis

Parameters	Values
Object initial position	Based on the grasping dynamic analysis result
Flipping velocity of drum	4.71 rad/s (45 rpm), operating time: 0.5s
Gravity	9.81m/s ²
Static/Dynamic friction	0.4/0.3 [Yin and Lee, 2002]
Constraints	Drum bottom center line: all DOF=0 Ellipsoid symmetric plane DOF UZ=0
Simulation time	1s

Figure 4-17 shows the flipping dynamic response at some specific time. Figure 4-18 shows the trajectory of the ellipsoid and drum (all measured from the center point) during the flipping process. The simulation result shows that the robotic hand cannot hold the object well during the flipping process since the object slips, which implies the constrained force from the compliant hand is not large enough.

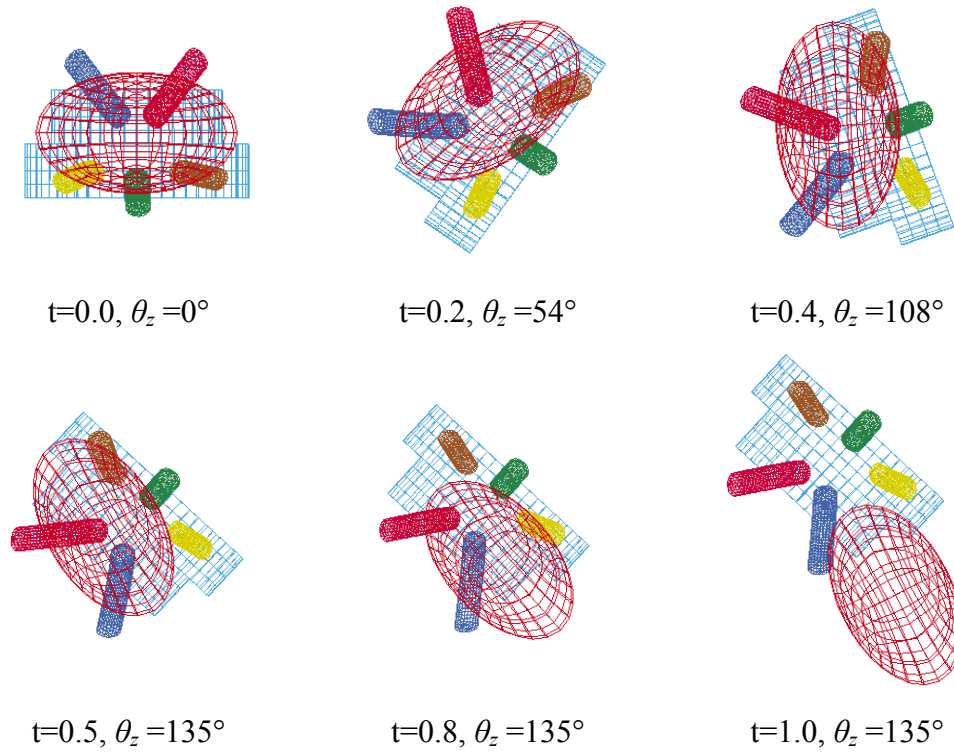


Figure 4-17 Flipping dynamic analysis result

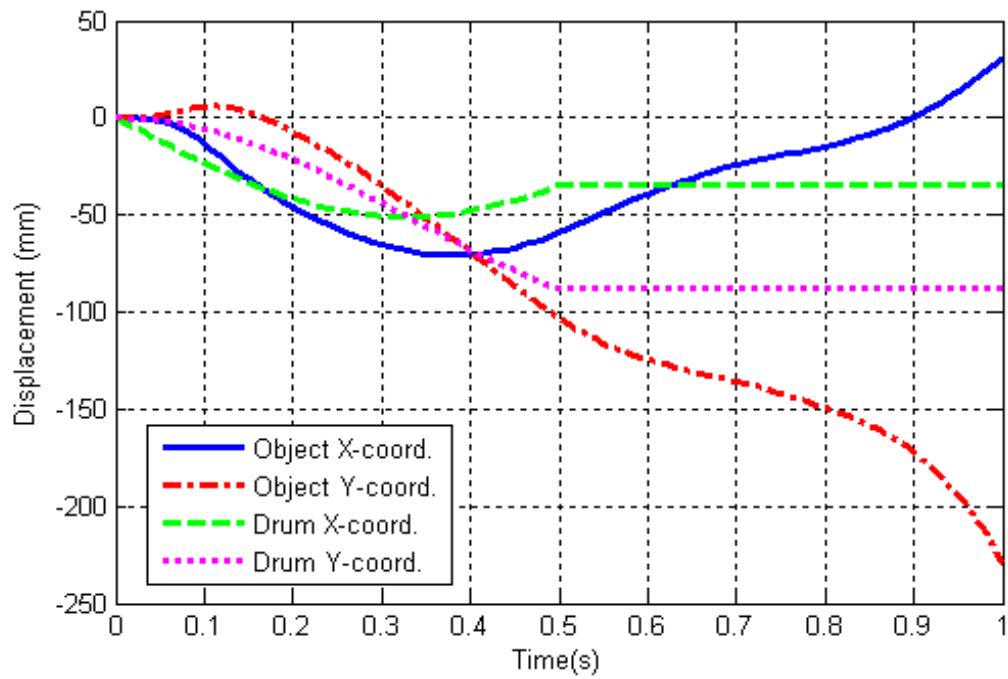


Figure 4-18 Trajectory of the ellipsoid object and drum center

4.5 Summary

Two examples of grasping ellipsoidal objects are illustrated. The highly damped compliant fingers discussed in Chapter 3 are applied in the robotic hand design for grasping. For the first example, the dynamic response of the football passing through the compliant hands is simulated. A half symmetric model is used for the dynamic model, and the overall trend of the simulation agrees with the experimental data. Several different operating parameters are investigated to examine the sensitivity of the conveyor speed and timing parameters on the maximum y-axis displacement and stress acting on the football. The parametric study shows that non-constant conveyor speeds can be used to improve the handling performance.

The second example is to predict if the ellipsoid can be held well as the compliant hands flip. The simulation consists of two steps; grasping and flipping. A grasping analysis simulates the compliant hand grasp the ellipsoid, which provides the initial condition for the flipping analysis. The simulation shows the ellipsoid slips during the flipping process.

CHAPTER 5

GRASPING DYNAMIC ANALYSIS OF LIVE OBJECTS

5.1 Introduction

This chapter applies the models of highly damped compliant fingers discussed in previous chapters to design a live-bird automated transfer system consisting of three processes; body-grasping, leg-gripping, and shackle-rotating/inverting. A more detailed chicken model including its legs and head has been developed to provide a better understanding of the shackling motion during transfer.

The following assumptions are made to reduce the problem to a more tractable form:

- 1 The cycle time is very short that the live chicken has negligible time to react. In other words, the chicken is modeled as a passive dummy.
- 2 The chicken, mechanical structures and associated boundary conditions are symmetric about the x-y plane (Figure 2-3). Thus, a half model is used to simulate the body-grasping and leg-gripping processes.
- 3 The mechanical properties of the chicken cannot be measured. The chicken is modeled with linear, homogeneous, and isotropic material properties similar to rubber with density calculated from the average measured weight divided by the volume of the CAD modeled chicken. In addition, the effect of the chicken feather is ignored.

- 4 As described in [Lee, 1999] and verified in Chapter 3, the compliant finger dominates the contact deformation. The damping modeling is only considered for the compliant fingers.
- 5 The chicken grips on the perch during the body-grasping and leg-gripping processes. The chicken-paw and perch are assumed to be coupled and move simultaneously.
- 6 During the shackle-rotating and inverting processes, the chicken is initially shackled at the desired point.
- 7 The chicken is modeled as a compliant mechanism where the joints between two adjacent limbs are modeled as the rotational compliant joints (Figures 5-1 and 5-2).

This chapter begins with the geometrical modeling of the passive chicken and the shackle mechanism designed using topology optimization. The key operating parameters are then discussed for investigating the grasping dynamic performance. The interest here is to understand the effect of the operating drum speeds and corresponding timing on the overall grasping performance by comparing several design analysis cases. The automated transfer processes including body-grasping, leg-gripping, and shackle-rotating/inverting are simulated.

5.2 Geometry Modeling and Optimization

A realistic prediction requires a good geometric model. To achieve this goal, the geometrical model of the chicken and the design of a shackle mechanism are described.

5.2.1 Geometry Modeling for Body-Grasping and Leg-Gripping

Figure 5-1 shows the half symmetric model for simulating the body-grasping and

leg-gripping, where the chicken is modeled as a half ellipsoid with compliant joints. The characteristic dimensions are defined with respect to the geometric center of the ellipsoid as in Figure 5-2, where L_i is the length of the i^{th} limb; J_i and θ_i are the i^{th} joint and i^{th} angle between two limbs respectively; and L is the length of the chicken (250 mm). The leg model is connected with the ellipsoidal body at joint 4. The dimensions based on averaged chicken size [Lee, 2001] are summarized in Table 5-1. An engineering drawing with more detailed dimensions of the chicken model can be found in Appendix F.

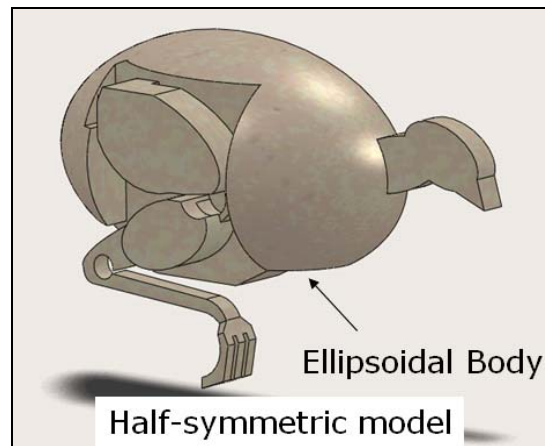


Figure 5-1 Geometry modeling of the live object (chicken)

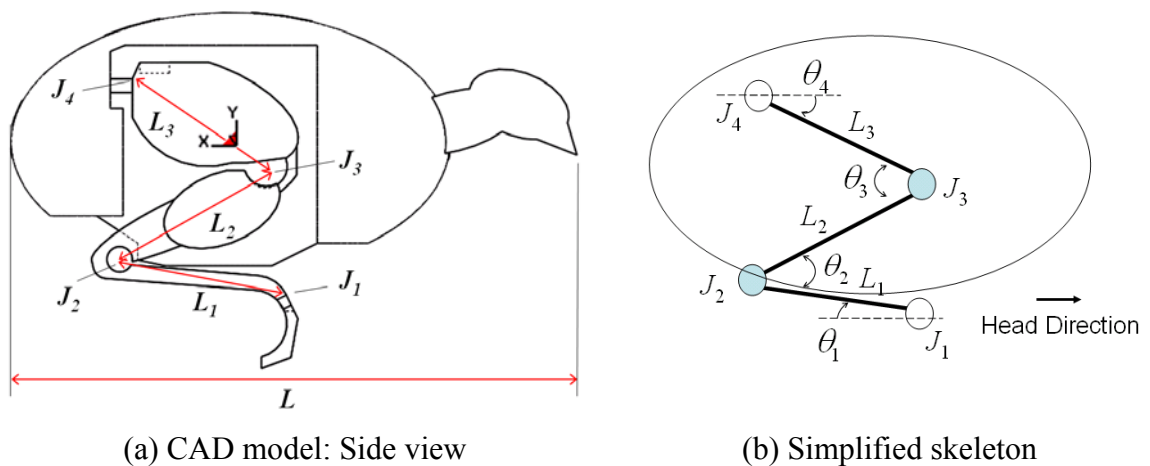
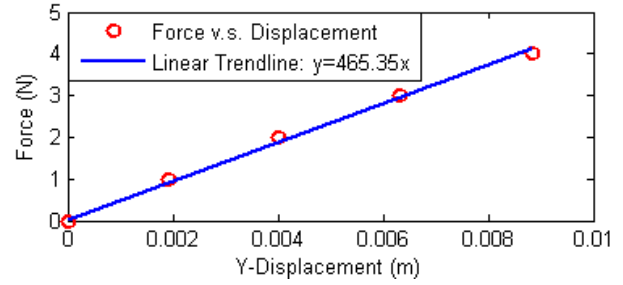
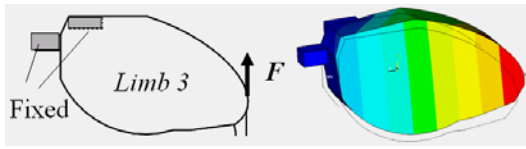


Figure 5-2 Live object (chicken) model and simplified skeleton

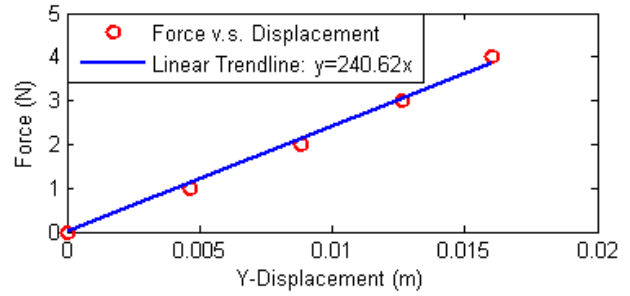
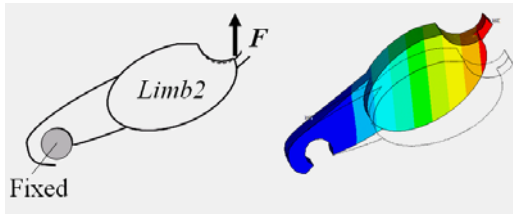
Table 5-1 Geometry model of the live object (chicken)

Compliant Joint	Location (x, y, z) (mm)	Type/Dimension (mm)
J_1	(-24.72, -67.3, 40)	fixed with the perch
J_2	(49, -51.6, 40)	circular hole radius=5.7, thickness=10
J_3	(-15.74, -10.74, 40)	circular hole radius=10, thickness=10
J_4	(43.37, 27.89, 35)	brick (length, height, thickness) (9.85, 7.52, 5.93); (13, 4.76, 5)
Limb	Limb length (mm)	Limb thickness (mm)
L_1	75	20
L_2	77	20 (upper limb) 10 (lower limb)
L_3	71	10
Initial Angle (°) between limbs	$\theta_1=10, \theta_2=40, \theta_3=65, \theta_4=35$	
Body	Ellipsoid with semi-axes 97, 66, and 57 mm [Yin and Lee, 2002] The origin is at the geometric center of the ellipsoid.	

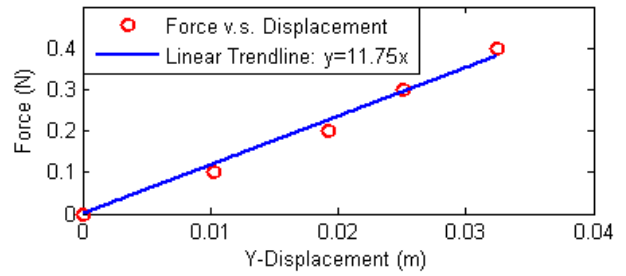
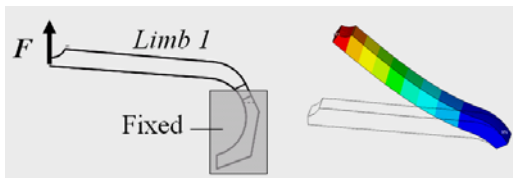
The force-displacement relationships of each leg segment are computed using the nonlinear static FEA meshed with the 10-Node tetrahedral element (Solid 92 in ANSYS). In simulation, the limb is fixed at one end joint and a known force is applied at the other end as illustrated in Figure 5-3. The FE model and the corresponding analysis results are summarized in Table 5-5 where the displacements are measured from the loading points. Based on these simulation results, the equivalent stiffness of each limb can be obtained.



(a) Limb 3



(b) Limb 2



(c) Limb 1

Figure 5-3 Analysis of the force-displacement relationship of each limb

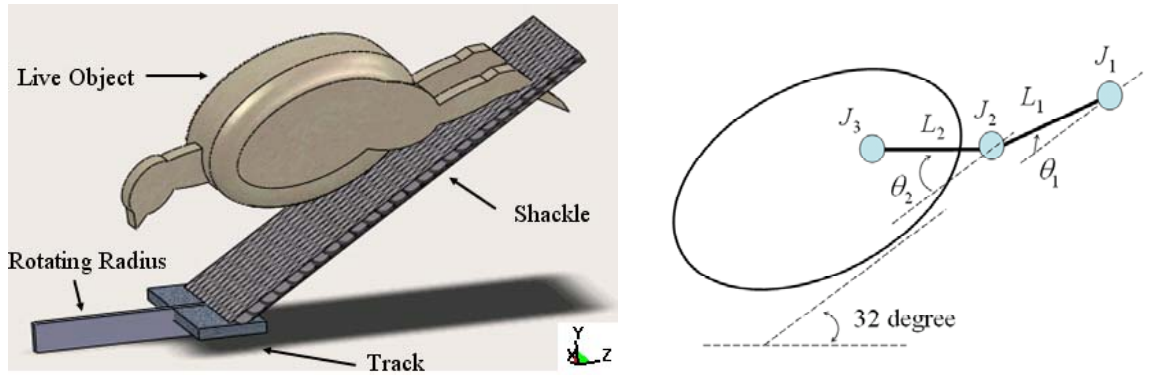
Table 5-2 FE model and force-displacement relationship of each limb

Case	Element Type	Element#	Node#	Force Load (N)	Displacement (m)	Stiffness (N/m)
Limb 1	Solid 92	11753	18425	0.1	0.01026	11.75
				0.2	0.01930	
				0.3	0.02517	
				0.4	0.03240	
Limb 2	Solid 92	8609	13591	1	0.00465	240.62
				2	0.00885	
				3	0.01265	
				4	0.01604	
Limb 3	Solid 92	16328	24579	1	0.00193	465.35
				2	0.00402	
				3	0.00632	
				4	0.00886	

(Material properties: $E=6.1\text{MPa}$, $\nu=0.49$, and $\rho=1270\text{ kg/m}^3$)

5.2.2 Geometry Modeling for Shackle-Rotating/Inverting

Figure 5-4 illustrates the key geometrical parameters involved in the shackle-rotating/inverting processes. A full model is used in the simulation since it involves non-symmetric motion. The shackle mechanism rotates and moves along a separate track, on which the legs of the chicken are inserted into a pair of grippers; thus J_1 is fixed in this simulation. Figure 5-4a shows the initial design domain of the shackle before applying topology optimization. Only two limbs (L_1 and L_2) are modeled since L_3 (Figure 5-2) does not change significantly during the rotating and inverting processes. The geometrical dimensions are summarized in Table 5-3.



(a) CAD model

(b) Simplified skeleton

Figure 5-4 Geometry modeling for shackle-rotating/inverting

Table 5-3 Geometry model for shackle-rotating/inverting

Limb	Limb length (mm)	Limb thickness (mm)
L_1	75	30
L_2	70	30
Initial Angle (°) between limbs	$\theta_1=14, \theta_2=35$	
Part	Dimension (length/width/thickness) (mm)	
Shackle	381/180/10 ; initial inclination= 32° Shackling point (J_1) :330 (from the fixed end of the shackle)	
Track	60/200/10	
Rotating radius	152.4/25.4/10	
Chicken	length: 371.5 semi-axis of elliptical body: 97, 57 (width: 130)	

5.2.3 Topology Optimization of the Shackle Mechanism

The live object sways sideway during the shackle-rotating process [Wang, 2009] and a pair of side holders is added to the shackle to restrict its motion. The shackle mechanism then consists of two parts; shackle-body (which holds the chicken against the

base frame and side holders) and a pair of compliant grippers (that grip both legs of the chicken). Both parts are assumed to be made of steel (the material properties can be found in Table 5-5). Topology optimization using the OC approach is used to design both of these parts (meshed by the 8-node Shell 93 element in ANSYS).

Topology Optimization of the Shackle-Body

The half symmetric FE model is meshed with totally 9669 nodes and 3141 elements. The corresponding boundary conditions are illustrated in Figure 5-5a. The analysis domain is an L-shape plate with two equal sides of plates (0.3×0.08 m). The circular hole at the bottom part represents the shackling point.

The boundary conditions are specified as follows. The nodal DOF are subjected to the constraints of Equations (5-1) and (5-2) for the fixed end and symmetric plane respectively:

$$U_x = U_y = U_z = 0 \quad \text{at } (Y, Z) = (0, 0.3) \text{ m} \quad (5-1)$$

$$U_x = 0 \quad \text{at } (X, Y) = (0, 0) \quad (5-2)$$

The side plate is under a force loading in the negative x direction due to the force acting from the chicken-body center. Similarly a force loading acts at the bottom plate with a 32 degree angle (the shackle initial inclination). Four forces are acting around the circular hole since it's the shackling location. These forces (with a magnitude of 20N) represent possible loading conditions are given in Equations (5-3) to (5-8):

$$(F_x, F_y, F_z) = (0, -17, 10.6) \text{ at } (X, Y, Z) = (-0.05, 0, 0.06) \text{ m} \quad (5-3)$$

$$(F_x, F_y, F_z) = (20, 0, 0) \text{ at } (X, Y, Z) = (-0.04, 0, 0.05) \text{ m} \quad (5-4)$$

$$(F_x, F_y, F_z) = (-20, 0, 0) \text{ at } (X, Y, Z) = (-0.06, 0, 0.05) \text{ m} \quad (5-5)$$

$$(F_x, F_y, F_z) = (0, 0, -20) \text{ at } (X, Y, Z) = (-0.05, 0, 0.04) \text{ m} \quad (5-6)$$

$$(F_x, F_y, F_z) = (0, -17, 10.6) \text{ at } (X, Y, Z) = (0, 0, 0.2) \text{ m} \quad (5-7)$$

$$(F_x, F_y, F_z) = (-20, 0, 0) \text{ at } (X, Y, Z) = (-0.08, 0.079, 0.22) \text{ m} \quad (5-8)$$

Several values of the volume reduction constraint defined in Equation (2-52) are given in Equation (5-9):

$$\int_{\Omega} \rho(x) dx \leq Vol \quad \text{where } Vol=70\%, 80\%, \text{ and } 90\% \text{ respectively} \quad (5-9)$$

The optimization results are displayed in Figure 5-5b-d. The outline of the side holder design can be found based on the topology optimization result.

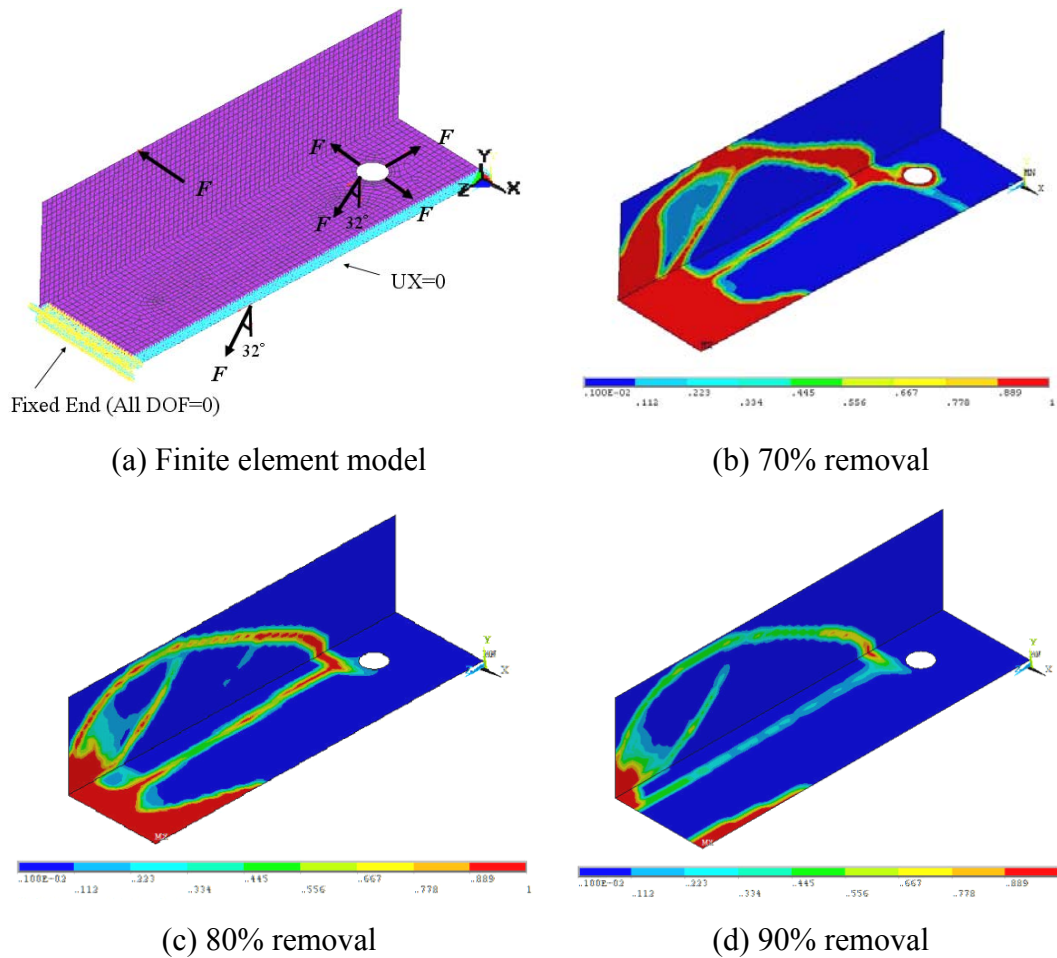


Figure 5-5 Topology optimization of the shackle-body (half model)

Topology Optimization of the Gripper

The FE model (with 3901 nodes and 1250 elements) and its corresponding boundary conditions are shown in Figure 5-6a. The initial design domain is $0.05\text{m} \times 0.1\text{m}$. The right corner is fixed:

$$U_x = U_y = U_z = 0 \quad \text{at } (X, Y, Z) = (0.045 \sim 0.050, 0, 0) \text{ m} \quad (5-10)$$

The loading conditions (N) are given in Equations (5-11) to (5-13):

$$(F_x, F_y, F_z) = (-16.2, -6.5, -5.3) \quad \text{at } (X, Y, Z) = (0.01, 0.09, 0) \text{ m} \quad (5-11)$$

$$(F_x, F_y, F_z) = (-38, -11.5, -1) \quad \text{at } (X, Y, Z) = (0.015, 0.084, 0) \text{ m} \quad (5-12)$$

$$(F_x, F_y, F_z) = (-50.6, -55.3, -22.6) \quad \text{at } (X, Y, Z) = (0.02, 0.078, 0) \text{ m} \quad (5-13)$$

Two values of the volume reduction constraint are defined in Equation (5-14):

$$\int_{\Omega} \rho(x) dx \leq Vol \quad \text{where } Vol = 85\% \text{ and } 90\% \text{ respectively} \quad (5-14)$$

The corresponding optimization results are given in Figure 5-6b and c.

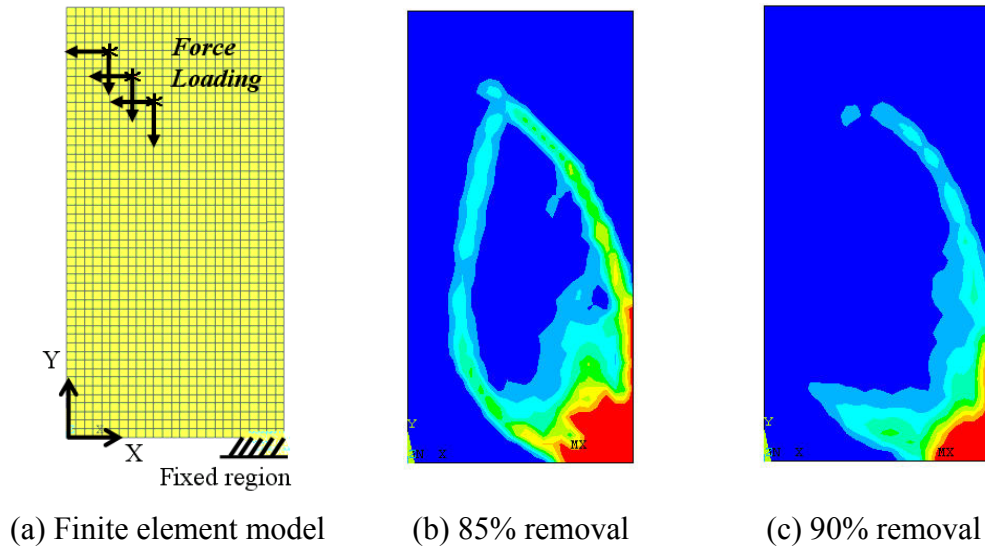


Figure 5-6 Topology optimization of the gripper (compliant part)

The optimal shackle concept design is obtained as shown in Figure 5-7. The side holder and compliant gripper designs are based on the 90% removal results. Some rollers are added in the design at the landing area for the chicken body.

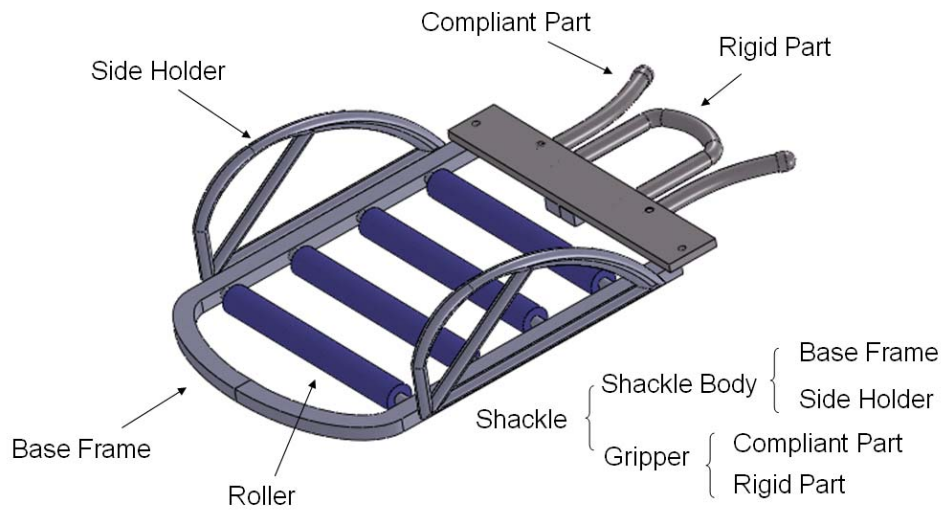


Figure 5-7 Optimal shackle concept design

5.3 Operating Parameters

As shown in Figure 5-8, the simulation begins with an incoming chicken sits on the perch (build-in with the conveyor) such that the conveyor and the perch move at the same speed $V_{conveyor}$. The body-grasping and leg-gripping processes take place when the chicken passes through the compliant robotic hands, where the shackle initially at a 32 degree inclination $\theta_{shackle}$ grips both legs of the chicken.

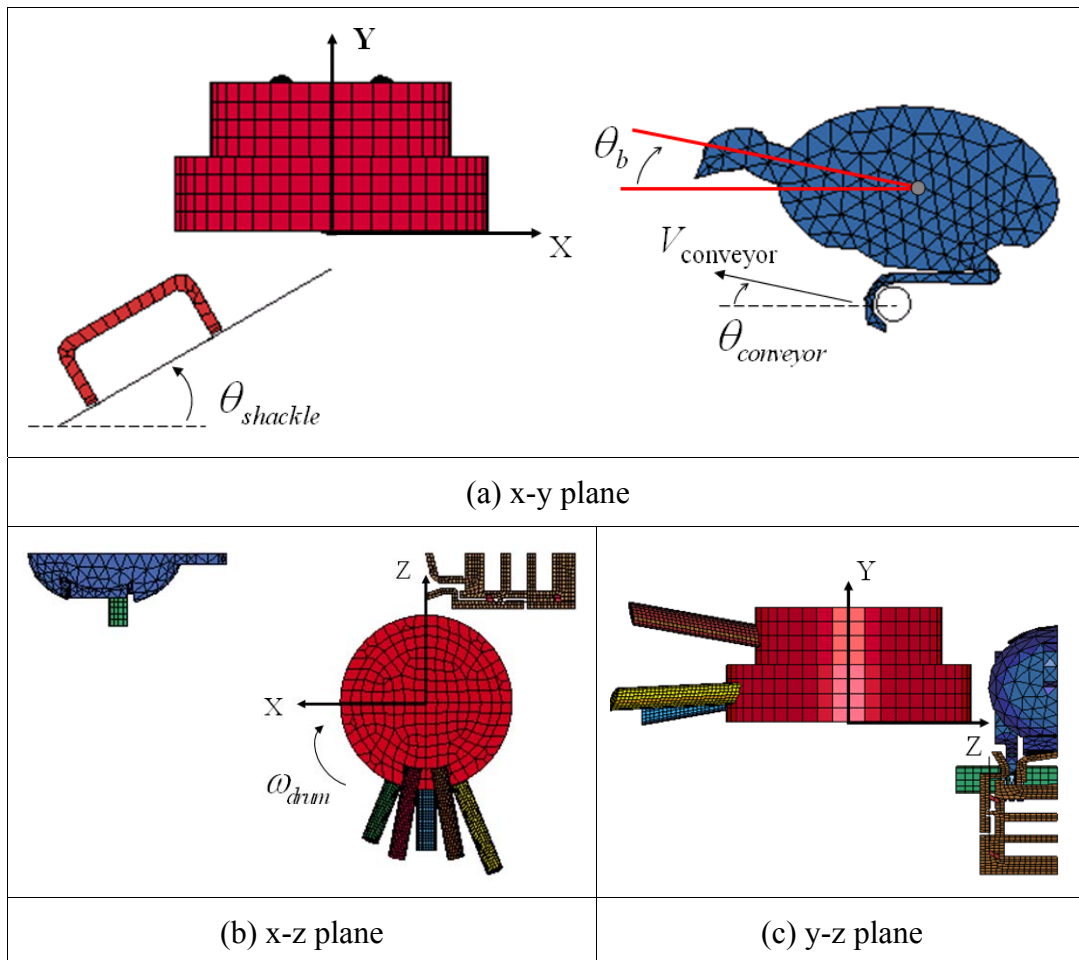


Figure 5-8 FE model for body-grasping and leg-gripping

The input operating parameters are defined in Figure 5-9 showing the desired trajectory of chicken centroid, where t_{peak} is the time instant when the perch arrives the highest point of the conveyor path; $t_{shackling}$ is the time instant that the shackle grips the chicken's leg; and t_{end} is the time instant that the chicken is released on the shackle (thus finishes the leg-gripping process). To explore the effect of different non-constant drum speeds on the success of grasp the body of the chicken, we introduce two additional timing parameters $t_{drum 1}$ and $t_{drum 2}$, which are the time instants when the drum changes its speed. The time instant $t_{drum 1}$ is to temporarily slow down the compliant hand to trap the chicken body, while $t_{drum 2}$ is to increase the drum speed to push the chicken body onto the shackle.

The initial desired trajectory of chicken centroid before t_{peak} is a straight line parallel to the initial conveyor path. After grasp the chicken body from t_{peak} to $t_{shackling}$, the desired trajectory is a straight line parallel to the X axis since we assume the chicken body is temporarily constrained by the compliant fingers. From $t_{shackling}$ to t_{end} , the desired trajectory is an arc since its body is released onto the shackle while its legs are constrained by a pairs of grippers.

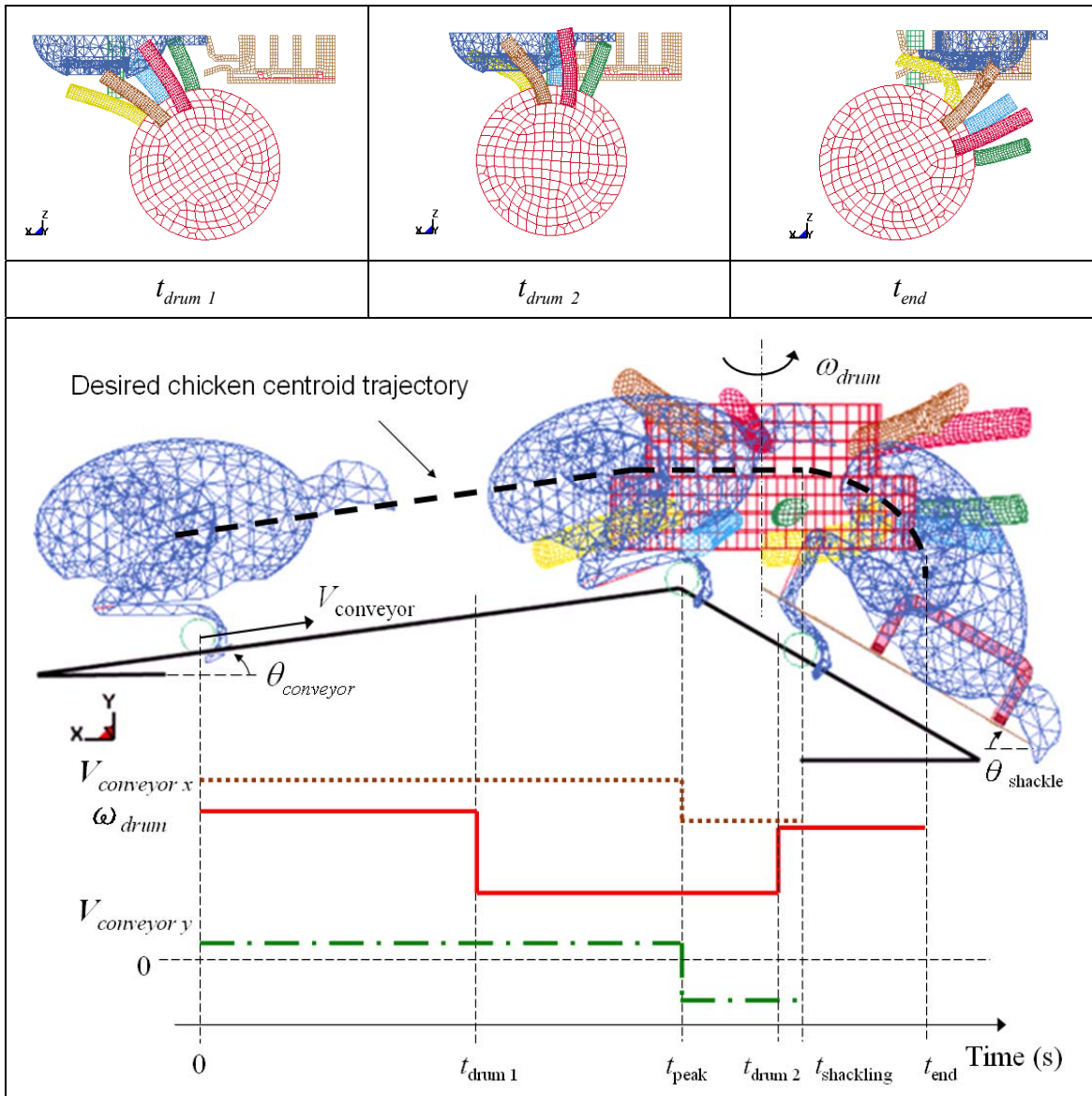


Figure 5-9 Trajectory of the input operating parameters

Five different operating parameters are given in Table 5-4. The first three cases operate at a constant drum speed while the other two cases use non-constant speeds. The corresponding timing specifications for controlling the drum speed are also summarized in Table 5-4. If the interaction between the compliant fingers and the object are neglected, the centroid of the chicken should arrive to the center between two drums when they

rotate at the constant speed. However, the analysis here involves contact deformation of a flexible multibody system with complex geometries and highly damped dynamic response; the grasping dynamics must be analyzed. The conveyor inclination $\theta_{conveyor}$ also makes the problem more complex since it changes the object position in y-axis as well as the x and y-component speeds $V_{conveyor\ x}$ and $V_{conveyor\ y}$ while the compliant hand rotates at the x-z plane (ω_{drum}). So the non-constant drum speed is considered for this application.

Table 5-4 Design analysis cases for different operating parameters

Drum speed & Timing (s)	Case	Drum speed (ω_{drum}) (rpm)
Constant $0 < t < 1.1$	1	35
	2	40
	3	45
Non-constant $0.00 < t < 0.55$ $0.55 < t < 0.85$ $0.85 < t < 1.10$	4*	45
		20
		40
	5	45
		19
		45

* optimal result

The operating parameters of the transfer processes from body-grasping to leg-gripping are evaluated by comparing the sensitivity of the drum rotating speed ω_{drum} and timing parameters on the multibody motion. The FE models for body-grasping and leg-gripping are shown in Figure 5-8, where θ_b is the orientation measured from the bird's head to its body-center (7.8 degree initially). The compliant hand including the rotating drum and fingers defined in Tables 4-1 and 4-2 is used here except that the length of finger E (Figure 4-1b) is 4.5-inch instead of 3-inch. The material properties and FE model with element types given in Appendix A are summarized in Table 5-5. The boundary conditions are summarized in Table 5-6.

Table 5-5 Material and FE model for body-grasping and leg-gripping

Part Name	Material	<i>E</i> (GPa)	<i>v</i>	ρ (kg/m³)	Element Type	Element#	Node#
Chicken	-	0.0061	0.49	1270	Solid 168	2233	4328
Perch	AL6061	69	0.33	2700	Shell 163	144	156
Shackle	Steel	210	0.28	7700	Shell 163	405	537
Side Holder	Steel	210	0.28	7700	Shell 163	27	52
Fingers & Drum	Same as Table 4-1 and Table 4-2, except finger E is 4.5-inch						
sum	-	-	-	-	-	7255	11037

Table 5-6 Boundary conditions

Parameters	Values
Origin of the global coordinate	Drum bottom center (as shown in Figure 5-8)
Chicken centroid initial position	$x, y, z = 0.402, 0.032, 0.184$ (m); $\theta_b = 7.8$ degree
Perch initial position	$x, y, z = 0.387, -0.039, 0.184$ (m) (top-center point)
Shackle initial position	Gripper: $x, y, z = 0, -0.026, 0.130$ (m) Fixed end: $x, y, z = -0.187, -0.135, 0.116 \sim 0.184$ (m) Initial angle ($\theta_{shackle}$): 32 degree
Drum speed (ω_{drum})*	0.00-0.55 s : 45 rpm (4.7124 rad/s) 0.55-0.85 s : 20 rpm (2.0944 rad/s) 0.85-1.10 s : 40 rpm (4.1888 rad/s)
Conveyor angle ($\theta_{conveyor}$)	5 degree inclination, 30 degree declination acme: 2-inch from drum center
Conveyor speed ($V_{conveyor}$)	0.4741 m/s (18.67 inch/s) 0.0-0.7s : 0.4723 m/s (x), 0.04132 m/s (y) 0.7-0.9s : 0.4105 m/s (x), 0.23705 m/s (y)
Bird initial velocity	0.4723 m/s (x), 0.04132 m/s (y)
Shackling time	$t=0.9$ s, perch arrives shackling point
Gravity	9.81 m/s^2 from $t=0.9$ s (shackling time)
Static/Dynamic friction	0.4/0.3 [Yin and Lee, 2002]
Damping coefficient	3-inch finger: 600 s^{-1} (based on Table 3-3) 4.5-inch finger: 180 s^{-1}
Simulation time	1.10s

* optimal result

5.4 Simulation Results

The simulation results for the body-grasping, leg-gripping, and shackle-rotating/inverting processes are discussed as follows.

5.4.1 Body-Grasping and Leg-Gripping

The simulated snapshots at two time instants, 0.7 and 1.1 seconds, for different cases (defined in Table 5-4) are compared in Figure 5-10, which correspond to specified time instants at which the chicken body is grasped and released on the shackle respectively. Figure 5-10 shows that the drum speed for Cases 1 and 2 (constant speed, 35 and 40 rpm respectively) are not fast enough to grasp the chicken body but the fingers hit it instead. On the other hand, Case 3 (constant speed, 45 rpm) is too fast. These lead to the consideration of using non-constant drum speeds (in Case 4 and 5) since the conveyor moves at different speeds in x and y direction immediately after the perch arrive the highest point (as shown in Figure 5-9) at the time instant $t=0.7$ second (t_{peak}). Figure 5-10 shows that the operating parameters for both Case 4 (non-constant drum speed, 45/20/40 rpm) and Case 5 (non-constant drum speed, 45/19/45 rpm) can grasp the chicken body well by reducing the drum speed at the time instant 0.55 second ($t_{drum 1}$). The perch arrives the shackling location at the time instant 0.9 second ($t_{shackling}$). However, the chicken can be released on the shackle at time 1.1 second (t_{end}) only in Case 4 (which minimize the cycle time) while other cases need some additional time.

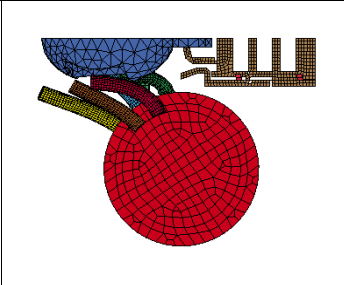
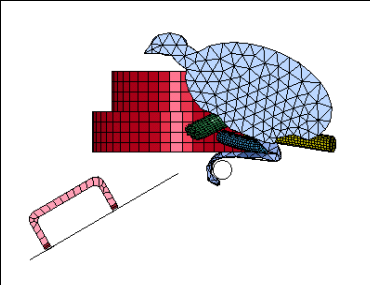
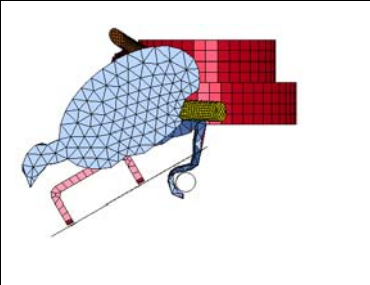
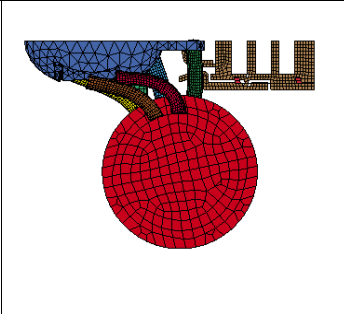
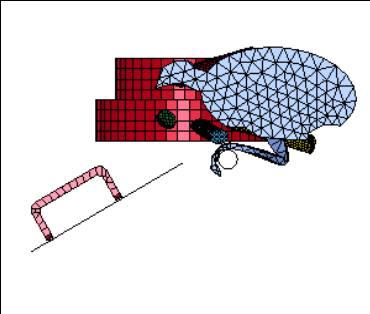
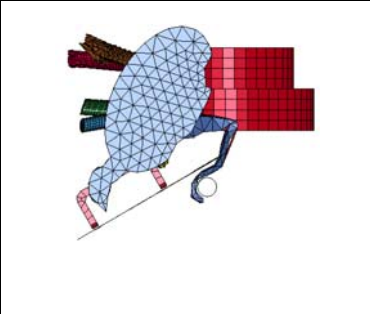
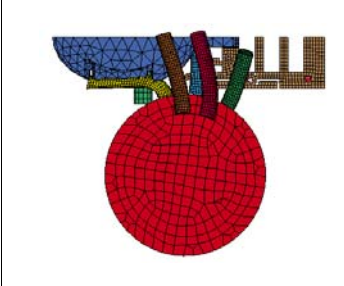
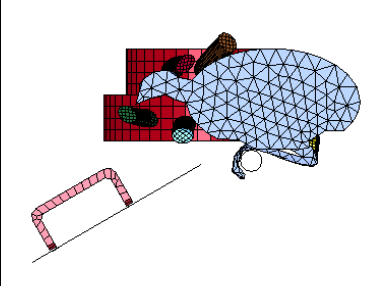
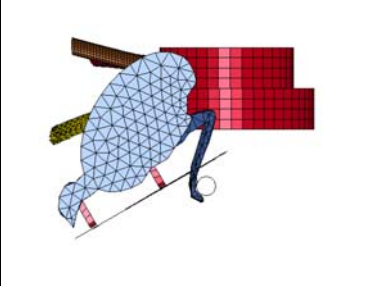
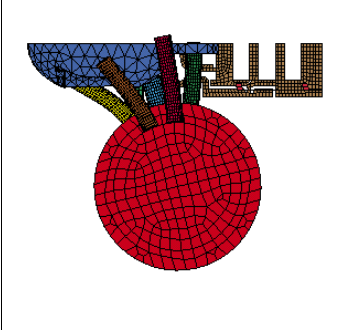
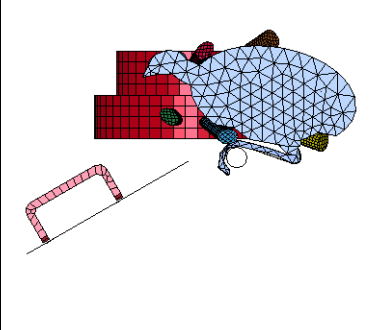
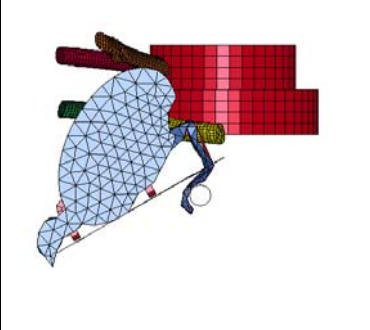
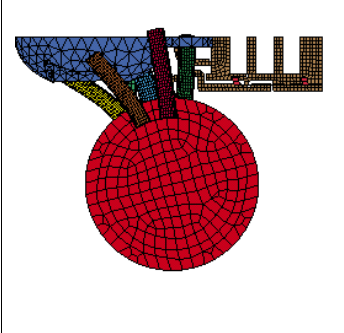
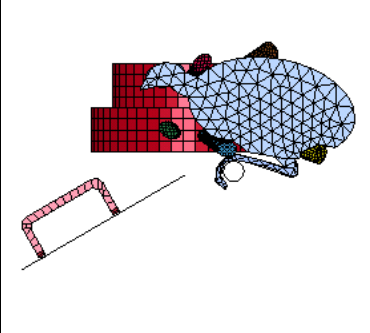
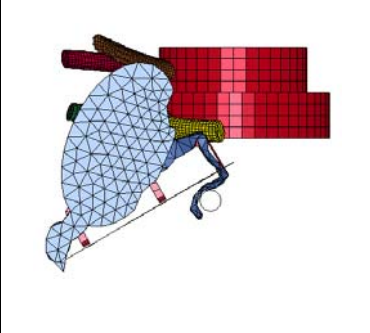
1			
2			
3			
4			
5			
Case	Top view (time 0.7s)	Side view (time 0.7s)	Side view (time 1.1s)

Figure 5-10 Comparison of the dynamic responses for different cases

The trajectories of the live object (body-center) and the perch (top-center point) for different cases are given in Figure 5-11, showing that Cases 1, 2, and 3 result in large oscillations (the fingers hit the chicken's body instead of grasp). The trajectories for Cases 4 and 5 are similar but Case 4 minimizes the relative distance between the live object and the conveyor. As unnecessary extra movement may increase the time for the live object to react or struggle. Case 4 condition (non-constant drum speed, 45/20/40 rpm) is identified as the optimal operating parameters for the automated transfer process.

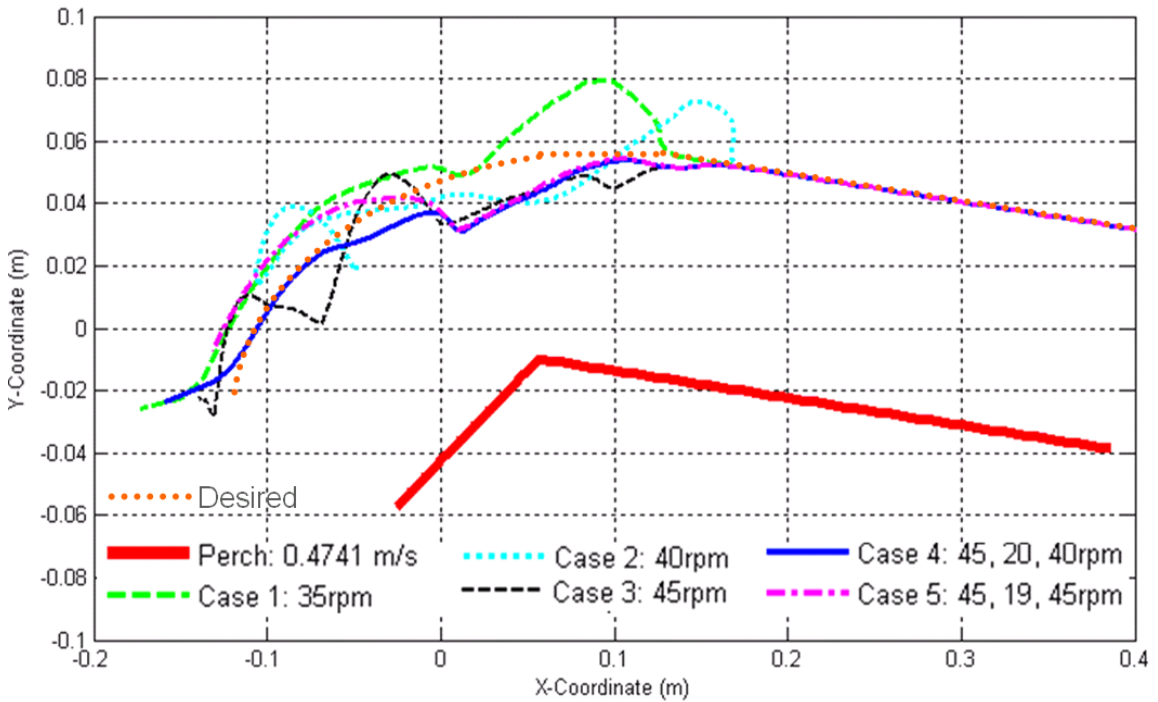


Figure 5-11 Trajectory of the live object under different cases

Figure 5-12 shows the snapshots of Case 4 at some specific time instants. At $t=0.7$ second, the perch reaches the highest point of the conveyor path. At $t=0.9$ second, the perch arrives the desired shackling point. The trajectories of the output parameters are given in Figure 5-13 including the locations and orientation of the bird and the trajectories of the perch and drum. The maximum orientation angles (defined in Figure 5-8a) of the bird are 24.5° and -60° at time 0.88 and 1.1 seconds respectively. Figure 5-14 shows the finger-tip response at y direction (where A, B, C, D, E are the finger numbers defined in Table 4-1), which implies the contact time between fingers and object. The maximum deformation and maximum equivalent stress are happened at finger E, which are 70.3 mm at time 0.94 second and 2.85 MPa at time 0.97 second respectively. The yield stress of rubber is about 9 MPa, so the maximum stress is lower than the yield stress, and the deformation is still under the elastic region. Figure 5-15 shows the finger-stress contour when maximum finger-stress happened.

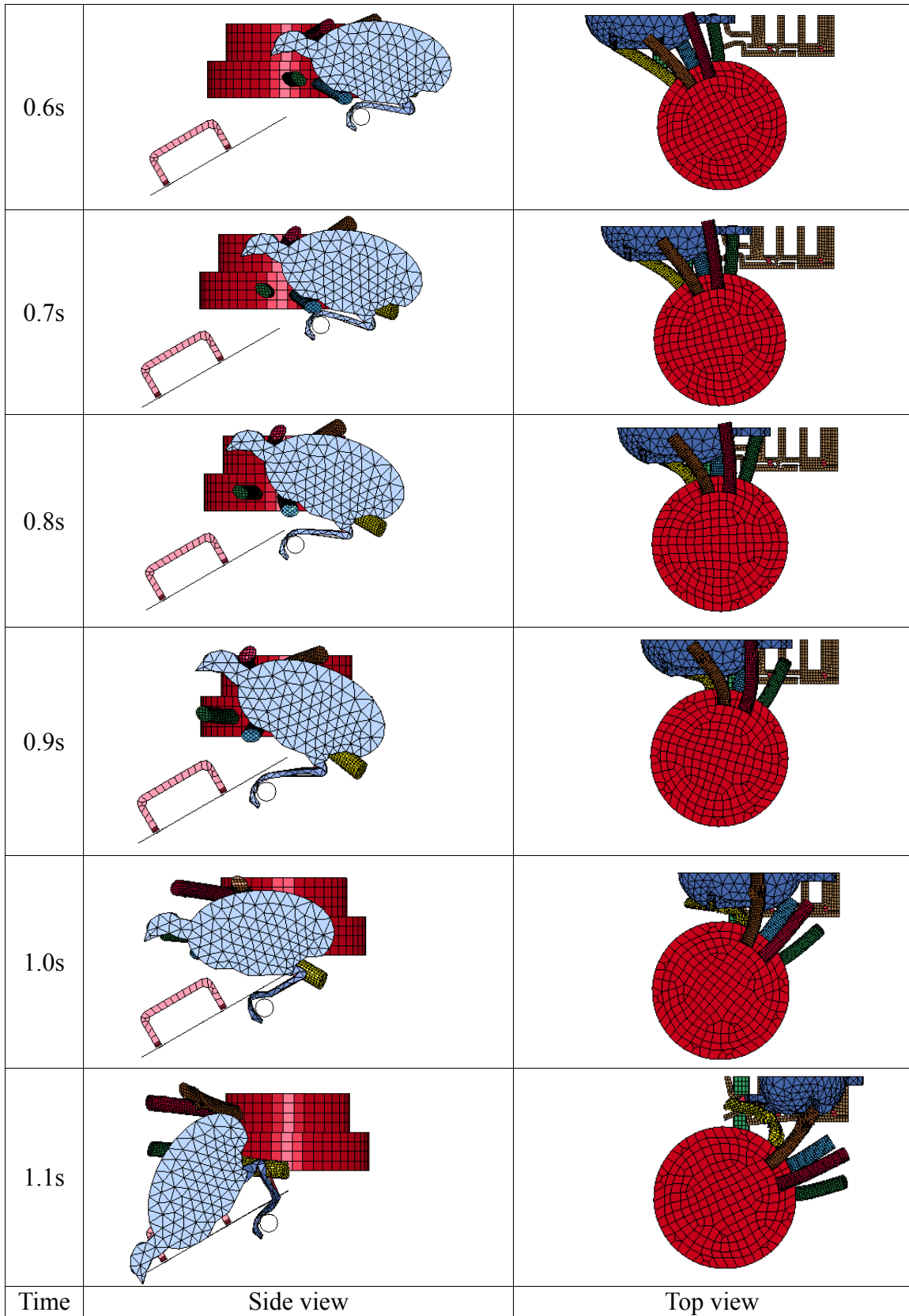


Figure 5-12 Dynamic response under the optimal operating parameters (Case 4)

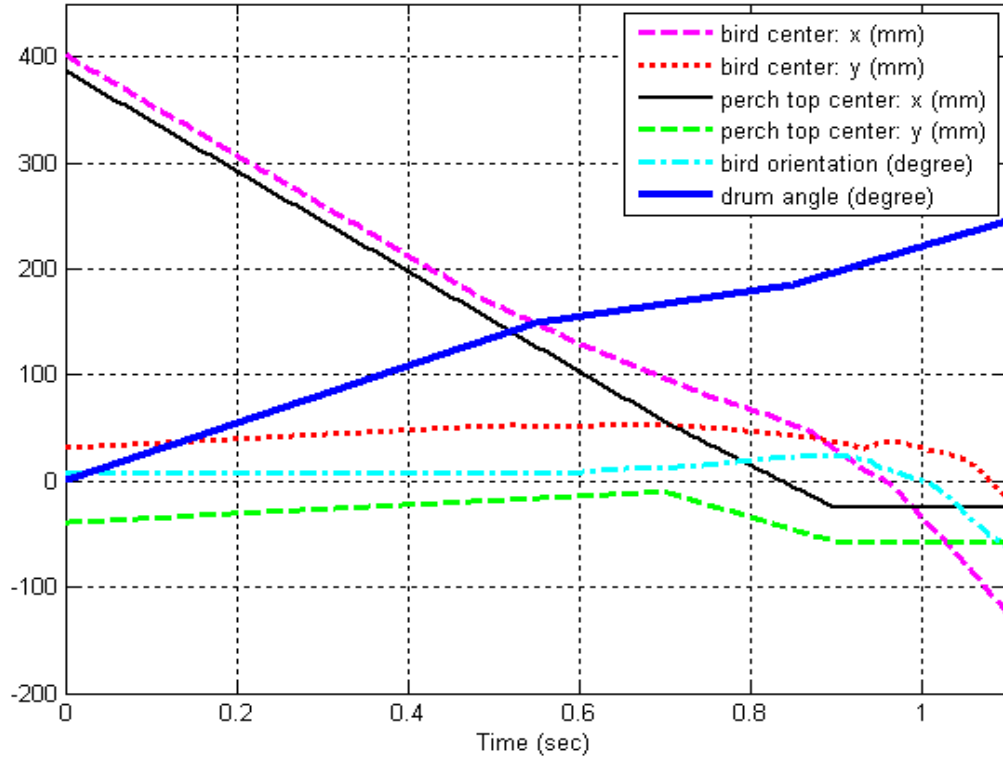


Figure 5-13 Trajectories of the output parameters (optimal case)

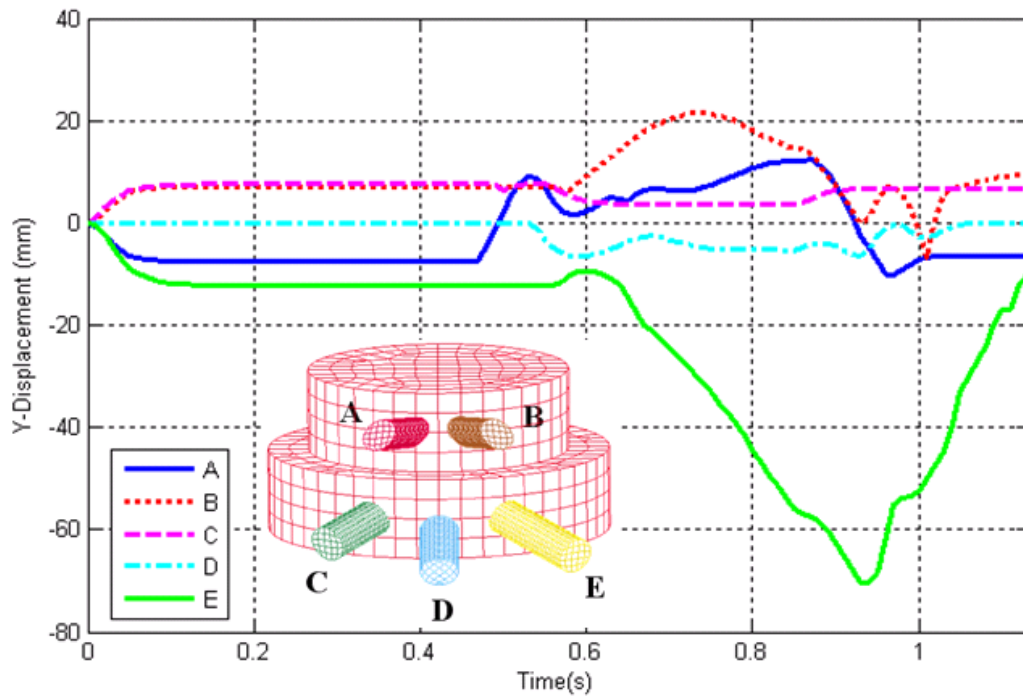


Figure 5-14 Finger-tip response

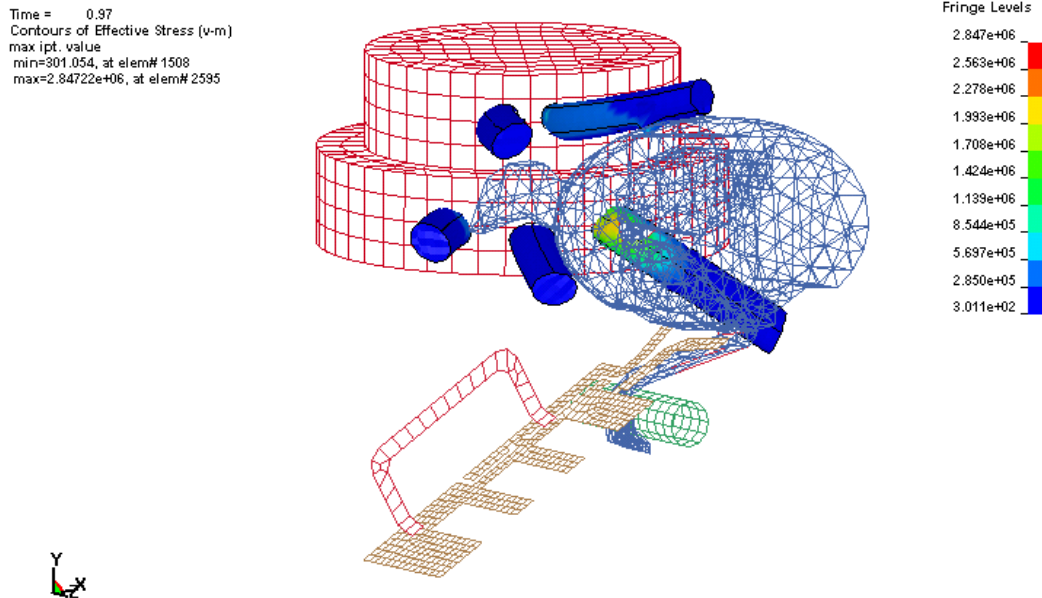


Figure 5-15 Simulation result when maximum finger-stress happened (t=0.97s)

Figure 5-16 and Figure 5-17 provide the displacement contour for the body-grasping (at time 0.7 second) and leg-gripping (at time 1.1 second). Figure 5-16 shows the instant when the body of the object is constrained by four of these compliant fingers (A, B, D, and E). A key factor for this step is that the chicken leg is restrained between fingers D and E, and its neck is under constraint of the finger A. Then the chicken body is pushed toward to the inclined shackle mechanism and its legs are guided into the compliant gripper as in Figure 5-17. Figure 5-18 shows the schemes of the live-bird transfer system from the initial state to body-grasping, leg-gripping, and shackle rotating/inverting processes. The simulation results of the shackle rotating/inverting processes are discussed in the following section.

Time = 0.7
Contours of Resultant Displacement
min=0, at node# 20
max=0.436015, at node# 2982

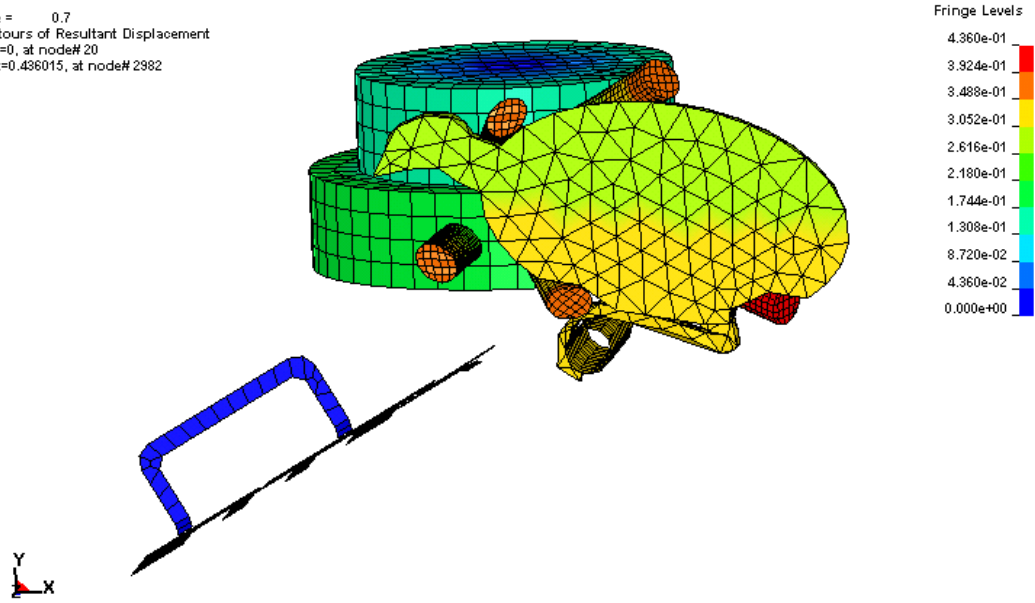


Figure 5-16 Simulation result of the body-grasping (t=0.7s)

Time = 1.1
Contours of Y-displacement
min=-0.190498, at node# 7645
max=0.0572297, at node# 6159

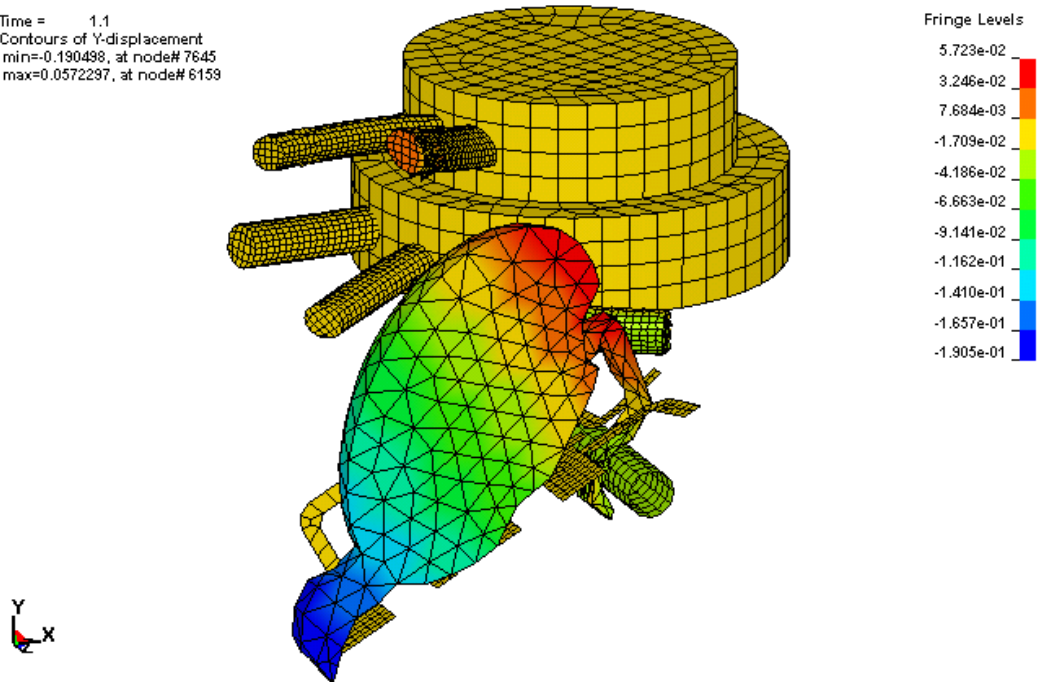


Figure 5-17 Simulation result of the leg-gripping (t=1.1s)

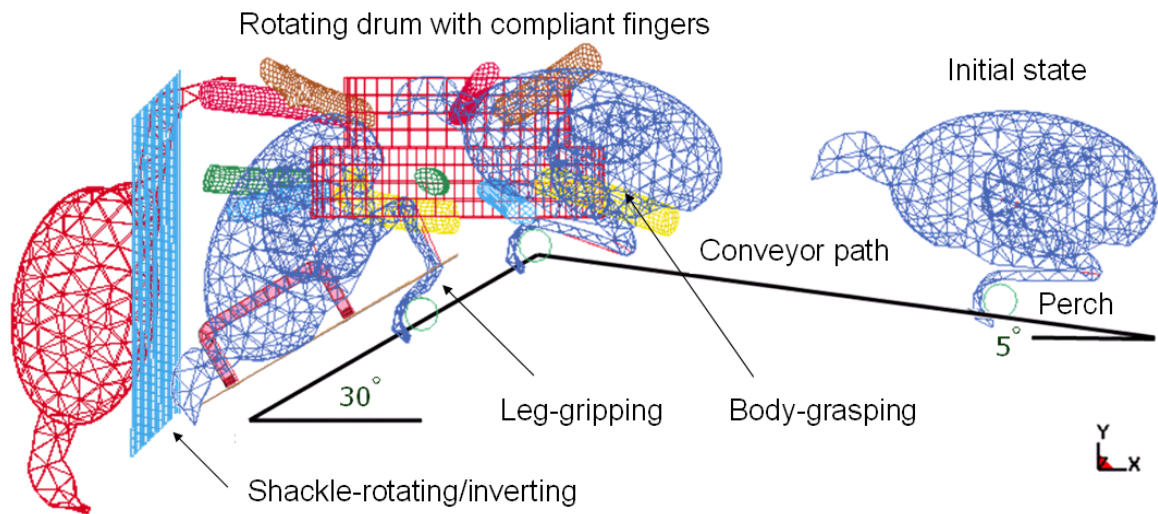


Figure 5-18 Schemes of the live-bird transfer system

5.4.2 Shackle-Rotating/Inverting

As previous described in Section 2.2 as well as in Figure 5-18, the shackle-rotating/inverting processes are the next step followed by the body-grasping and leg-gripping procedures. The FE model for shackle-rotating/inverting is shown in Figure 5-19. The corresponding material properties and FE model are summarized in Table 5-7. The densities for the chicken models for both cases (body-grasping and leg-gripping; shackle-rotating/inverting) are different since we want to remain the same weight (1.69 kg) for the chicken model while the volumes of the CAD models are different.

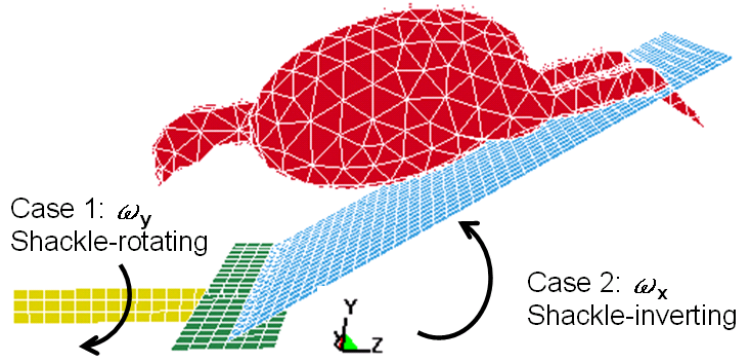


Figure 5-19 FE model for shackle-rotating/inverting

Table 5-7 Material and FE model for shackle-rotating/inverting

Part Name	Material	E (GPa)	ν	ρ (kg/m ³)	Element Type	Element#	Node#
Shackle	Steel	210	0.28	7700	Shell 163	702	760
Chicken	-	0.0061	0.49	680	Solid 168	3948	6507
Track	Steel	210	0.28	7700	Shell 163	120	147
Rotating Radius	Steel	210	0.28	7700	Shell 163	48	68
sum	-	-	-	-	-	4818	7482

As defined in Figure 5-19, there are two analysis cases in this section: Case (1) is the shackle-rotating process, where the rotating radius rotates about y axis while the shackle remains 32 degree; Case (2) is the shackle-inverting process, where the shackle rotates about x axis from 32 degree to 90 degree. The corresponding parameters for both cases are summarized in Table 5-8. The dynamic responses from FEA will be compared against the results solved by Lagrange Dynamics [Wang, 2009].

Table 5-8 Parameters for shackle-rotating/inverting simulation

Parameters	Shackle-Rotating	Shackle-Inverting
Rotation speed	$\omega_y = 4.71$ rad/s (45 rpm)	$\omega_x = 8.73$ rad/s (83 rpm)
Operation time	0.116 sec	0.116 sec
Shackle inclination	32 degree (θ_x)	32 degree (θ_x)
Rotation angle	30 degree (θ_y)	58 degree (θ_x)
Static/Dynamic friction	0.4/0.3	0.4/0.3
Damping coefficient	100 1/s (chicken)	100 1/s (chicken)
Gravity	9.81 m/s ²	9.81 m/s ²
Simulation time	0.5 sec	0.5 sec

Shackle-Rotating Simulation

For the shackle-rotating simulation, Figure 5-20 shows the resultant displacement of the chicken and shackle (measuring from the center point) during the shackle-rotating process. The maximum relative displacement is about 9.5 cm at time 0.12 sec. Figure 5-21 shows the dynamic response (contour plot for the resultant displacement) at some specific time. The simulation shows that the chicken sways sideways, and the maximum equivalent stress on the shackle is about 25 MPa, which is lower than the yield stress of steel (around 248 MPa).

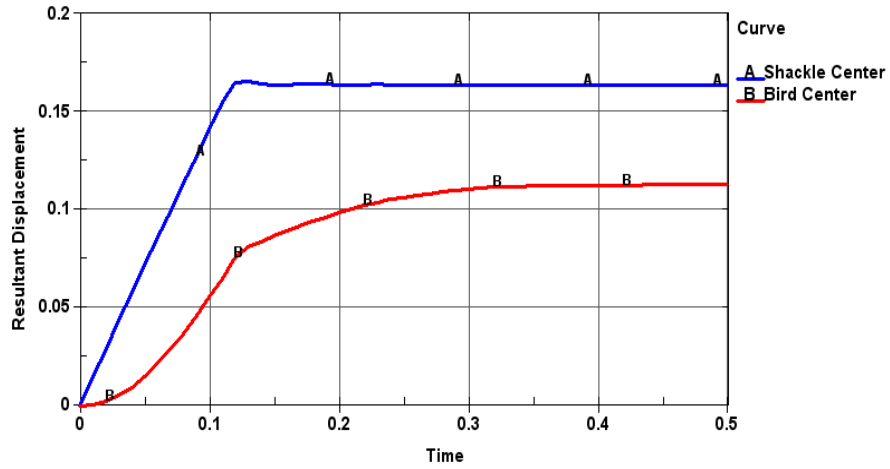


Figure 5-20 Resultant displacement (m) of chicken and shackle

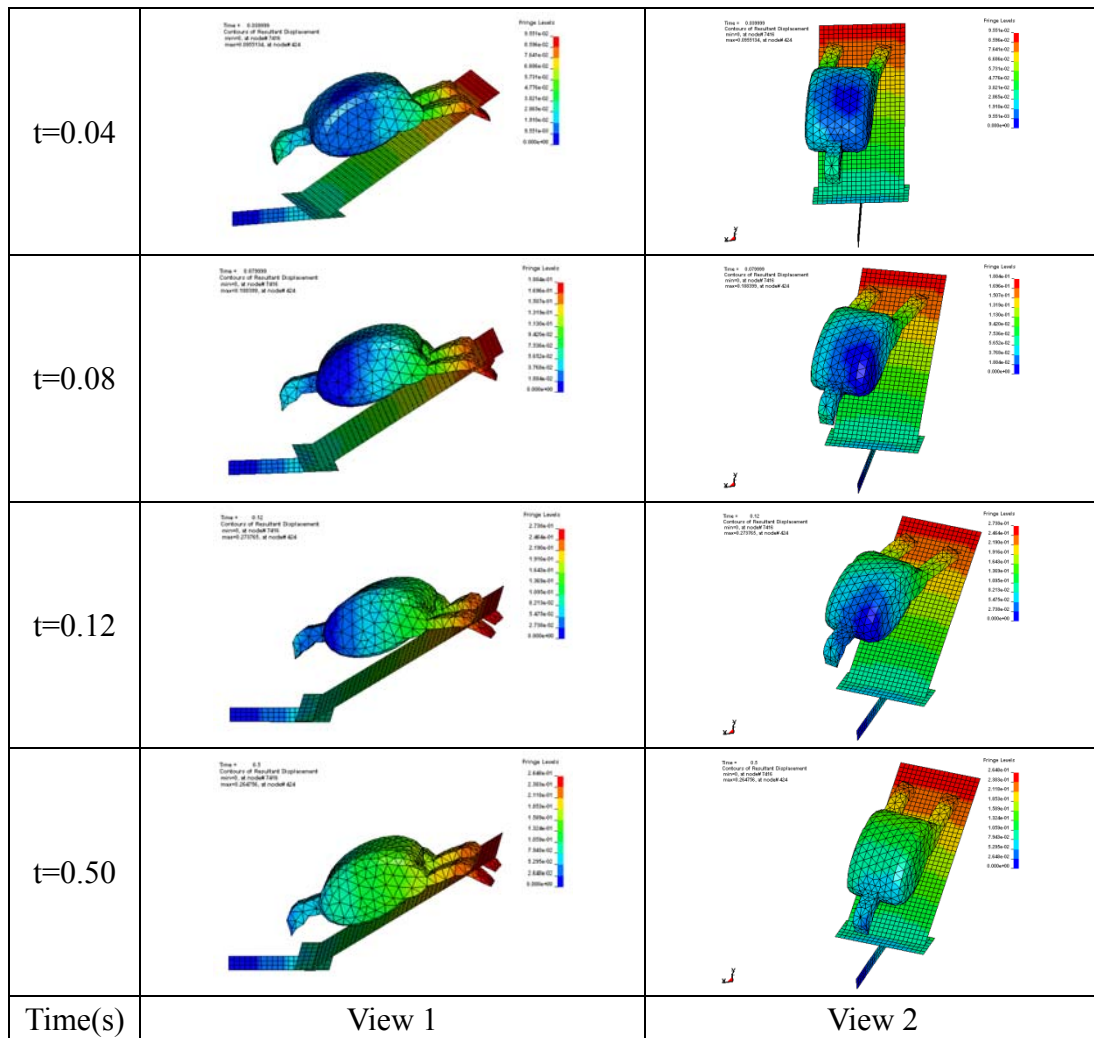


Figure 5-21 Dynamic analysis results of the shackle-rotating process

Shackle-Inverting Simulation

Figure 5-22 shows the dynamic response (contour plot for the resultant displacement) at some specific time. The simulation results show that the chicken can be handled well (with small relative displacement between the chicken and shackle) during the shackle-inverting process. The maximum stress on the shackle is about 78.5 MPa which is lower than the yielding stress of steel (around 248 MPa).

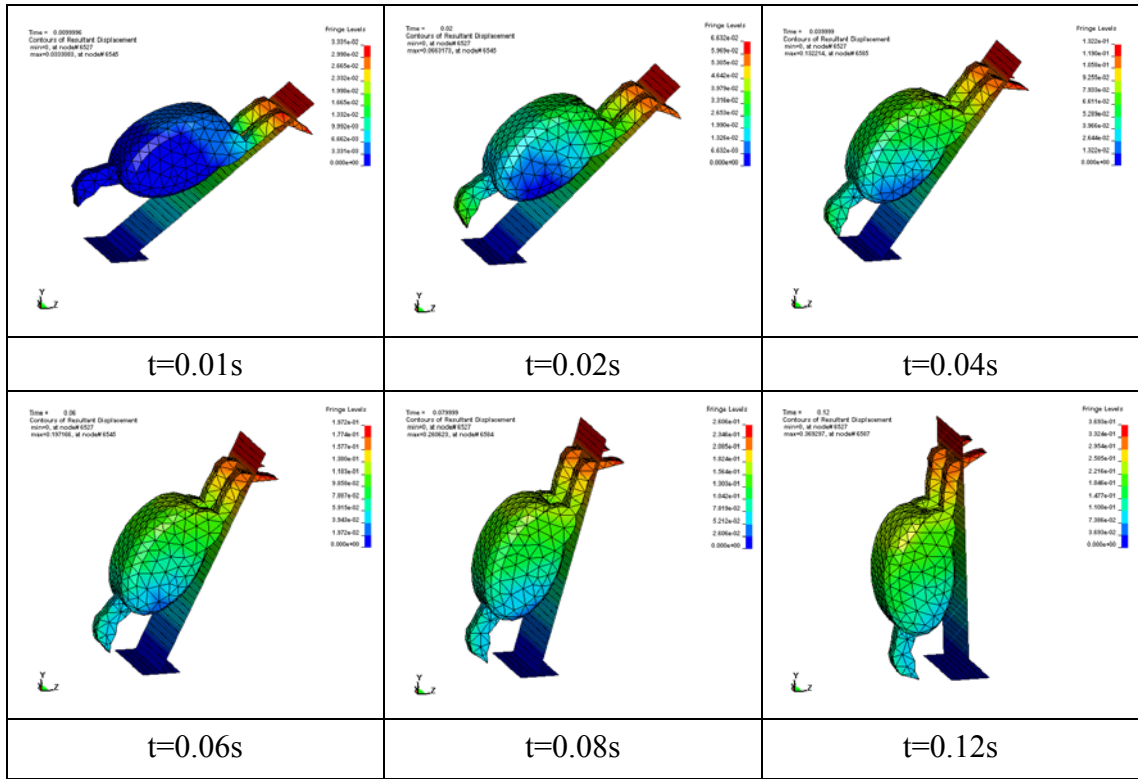


Figure 5-22 Dynamic analysis results of the shackle-inverting process

Comparison with the Lagrange Dynamics

The dynamic simulation for the shackle-rotating/inverting processes are compared against the result (as shown in Figure 5-23) solved by Lagrange dynamics [Wang, 2009]. The comparisons of the body-center response are given in Figure 5-24 (shackle-rotating) and Figure 5-25 (shackle-inverting). The simulation from Lagrange dynamics obtains a

relatively larger response compared to the result from explicit dynamic FEA. The difference may be from it simplifies the shackle-rotating/inverting processes into a two-dimensional, lumped-parameter rigid body problem, which makes its motion larger than the deformable and distributed mass FE model. In addition, to decide what values to assign for the spring constants is another critical issue of applying Lagrange dynamics for the simulation. It can be applied for a quick calculation but a three-dimensional FE model is necessary to obtain a more realistic prediction.

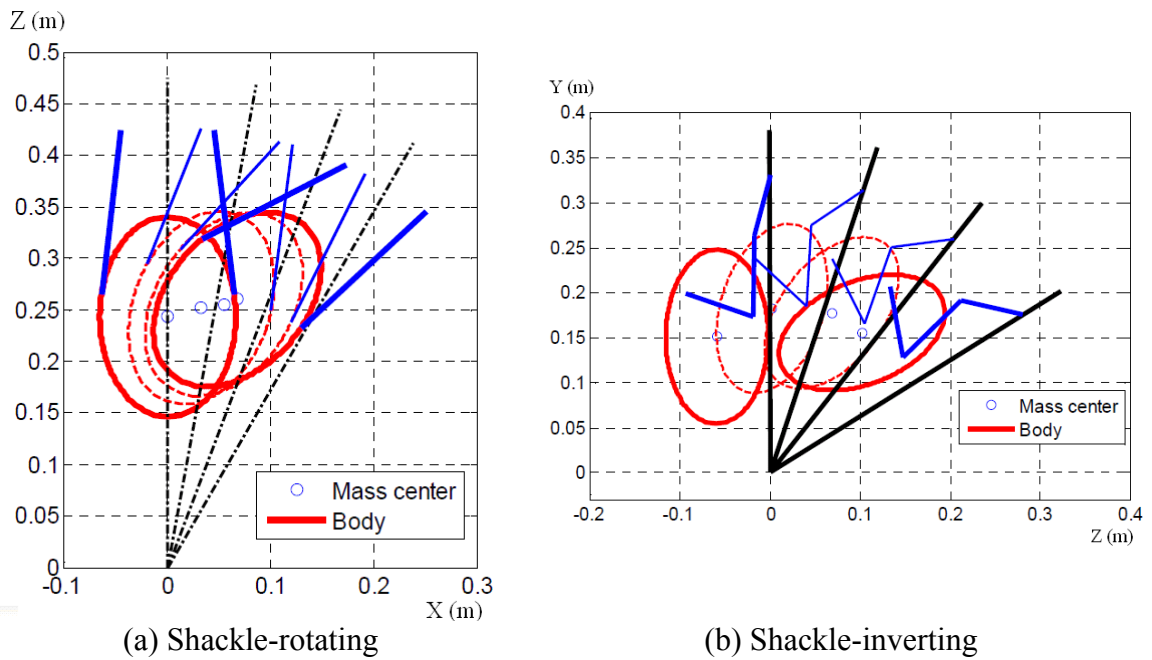


Figure 5-23 Simulation snapshots by Lagrange dynamics [Wang, 2009]

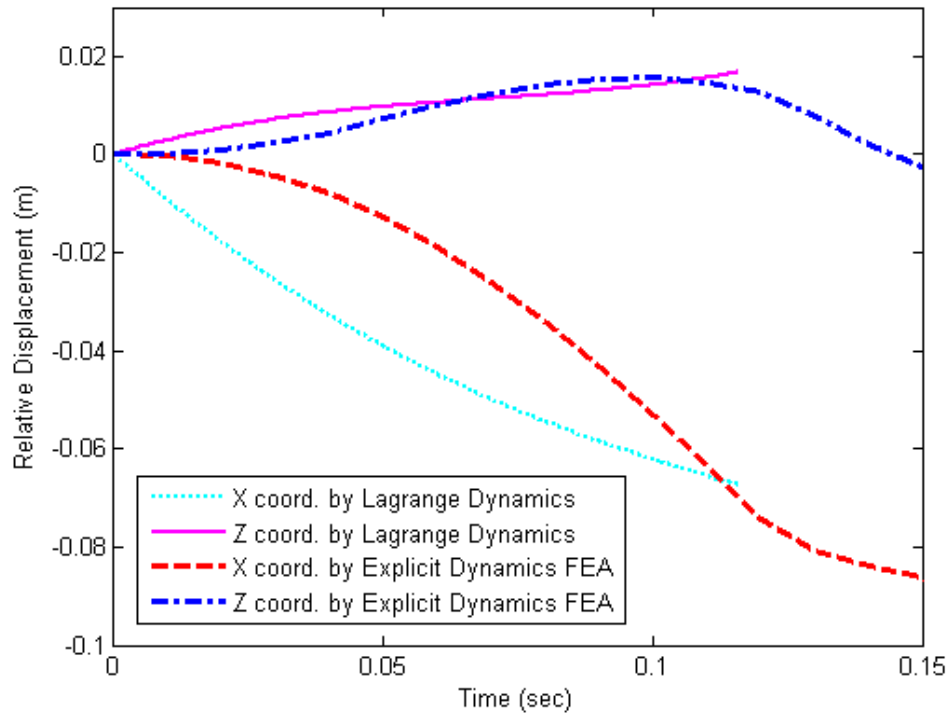


Figure 5-24 Comparison of the body-center response (shackle-rotating)

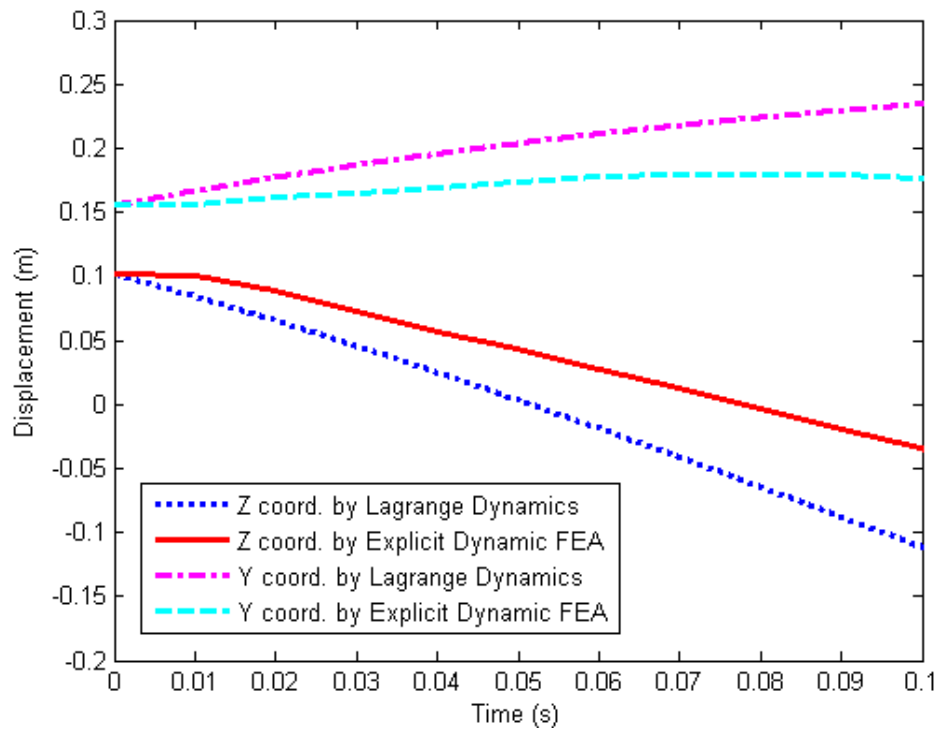


Figure 5-25 Comparison of the body-center response (shackle-inverting)

5.5 Summary

Two application examples, grasping and handling of the live object, are illustrated using the explicit dynamic FEM which relaxes the quasi-static assumption. Unlike Chapter 4 which uses an ellipsoid to represent the live object, the chicken model (modeled as a compliant mechanism) in this chapter including its head and legs has been developed. An optimal shackle mechanism has been developed based on topology optimization technique. The automated transfer processes including body-grasping, leg-gripping, and shackle-rotating/inverting are simulated to investigate the dynamic performance of the multibody system. Several different operating parameters are performed to investigate the effect of the drum rotating speed and timing parameters on the trajectory of the multibody motion. The simulation results show that Case 4 (non-constant drum speed: 45/20/40 rpm), which minimizes the oscillations and relative distance between the live object and perch, is a preferred set of operating parameters for the body-grasping and leg-gripping processes.

The simulation of the shackle-rotating process shows that the live object sways during this process, and topology optimization is applied to obtain an optimal shackle design. The shackle-rotating/inverting processes are simulated and compared against results from Lagrange dynamics [Wang, 2009], which exhibits a relatively larger response compared to the result from explicit dynamic FEA since it simplifies these processes into two-dimensional, lumped-parameter rigid body problems instead of deformable and distributed mass FE model. In addition, to decide suitable values to assign for the spring constants is another critical issue of applying Lagrange dynamics. It

can be applied for a quick calculation but the realistic 3D finite element model is necessary to obtain a more realistic prediction.

The simulation results in this chapter offer a better understanding of the flexible multibody system for improving future designs.

CHAPTER 6

CONCLUSIONS AND FUTURE WORK

6.1 Conclusions

This thesis investigates practical issues related to the development of an automated live-bird transfer system. The findings provide a better understanding on the dynamics of a flexible multibody system incorporating high-damped compliant mechanisms. Two specific contributions of this research are summarized as follows:

1. Dynamic Modeling Method

An explicit FEA-based dynamic modeling method that incorporates topology optimization, modal analysis and damping effect has been developed and validated for design and analysis of a flexible multibody system with large deformation, contact nonlinearity, and complex geometry. The explicit FEA method evaluates both geometric and operating parameters in designing a flexible multibody system for industrial automation. As compared to other methods, this method is more realistic than lump-parameter methods (such as pseudo-rigid-body model which requires estimate suitable spring and damping constants), and more importantly it relaxes the quasi-static assumption made in many prior studies, and thus avoids the drawback of remodeling the geometry models.

Unlike most general damping identification methods, the computational/experimental coupled method obtains the damping coefficient of a general continuum

structure. For mechanisms vibrate at lower modes where the stiffness proportional term is insignificant, the proportional damping assumption greatly reduces the identification problem. It provides an effective means to estimate the damping coefficient of a highly damped continuum structure by a combination of finding critical damping coefficient numerically, and searching an appropriate response to match a set of experimental data. The advantage of this identification technique is its capability to obtain the damping coefficients for FEA, and analyze high-damped continuum structures.

The critical time step is a compromise between numerical stability and computation time. Unlike implicit methods that are stable for linear and many nonlinear problems, explicit methods are only stable when the time step is smaller than a critical value. If the time step is too large, the method loses the numerical stability. If the time step is too small than necessary, the computation would be too expensive. The critical time step has been discussed in terms of material properties (elastic modulus, density, and Poisson ratio), and mesh quality (characteristic length), and has been shown to play an important role in the flexible multibody systems especially for complex geometries. Among the material properties, the critical time step is most sensitive to elastic modulus and density, and relatively insensitive to Poisson ratio. A smaller elastic modulus or larger density can lead to a larger critical time step. Since the characteristic length (determined by element size and shape) is linearly proportional to the critical time step implying that mesh quality must be carefully considered and well planned. As has been shown, a uniform quadrangular and hexahedral mesh is preferred for explicit dynamic FEA.

2. Grasping Dynamic Analysis: A Practical Application of the Developed Method

Motivated by the development of the automated live-bird transfer system, the dynamic modeling method has been applied to investigate the performance of the robotic grasping by multiple highly damped compliant fingers. The FEA begins with a modal analysis to justify the assumption of only mass proportional damping in this application. The effect of FE finger model on the critical time step has been examined. This, along with the damping identification, provides the basis to analyze the contact between a set of rotating fingers and elliptical/ellipsoidal objects. Comparison against the experimental data shows qualitative agreement.

The effectiveness of the dynamic modeling method, which relaxes the quasi-static assumption, has been demonstrated in the analyses of developing an automated transfer system involved grasping and handling objects by the compliant robotic hands. This FE based dynamic model offers a more realistic simulation than prior results based on quasi-static models, and provides a better understanding of the effect of design parameters for improving future designs. Several cases are numerically simulated to analyze the grasping dynamics of the ellipsoidal objects using the highly damped compliant fingers. A more detailed FE model of a chicken dummy (with both legs modeled as compliant mechanisms) has been developed for investigating the effect of several key operating parameters on the trajectory of the multibody motion.

While the immediate application is the development of the automated live-bird transfer system, the proposed method can be applied to a spectrum of engineering applications where flexible multibody dynamics plays a significant role.

6.2 Future Work

Further research on the use of the proposed method for analyzing a flexible multibody system can be extended from the following perspectives.

- (1) In this analysis, the incoming objects are assumed to be symmetric. In addition, the average size and weight of a live chicken are used in modeling. However, the objects may enter the system with different orientations. The effects of non-symmetric geometry and size/weight variations on the system success should be further investigated.
- (2) The material property of the rubber finger is assumed to be linear elastic. For applications involving large strain deformation of rubber material (hyperelastic behavior), the nonlinear Mooney-Rivlin model or Ogden model can be incorporated into the dynamic modeling. Similarly, for components with nonlinear material properties, the nonlinear stress-strain relationship can be applied in the material modeling when necessary.
- (3) The cyclic fatigue behavior of the rubber finger can be further investigated with the aids of Basquin's Law (stress-based approach) and Coffin-Manson relationship (strain-based approach), which will help estimate the fatigue life under a cyclic loading condition. In addition, the fracture and crack propagation phenomenon can be further investigated by defining plastic material properties and failure strain.

APPENDIX A

GENERAL ELEMENT TYPES FOR EXPLICIT DYNAMIC FINITE ELEMENT ANALYSIS

The general elements types for explicit dynamic analysis are summarized in Table A-1, which shows the elements transformation relation between the general-purpose FEA packages; ANSYS and LS-DYNA. It also shows the node number for each specific element, and the degree of freedom (DOF) for each node; where U is displacement, V is velocity, A is acceleration, R is rotation, x, y, z are the directions.

Table A- 1 General element types for explicit dynamic FEA

Element Type ANSYS	Element Type LS-DYNA	Node#	DOF#	DOF Items
BEAM161	Beam Element 1	2	12	U_i, V_i, A_i, R_i
SHELL163	Shell Element 2	4	12	U_i, V_i, A_i, R_i
SOLID164	Solid Element 1	8	9	U_i, V_i, A_i
MASS166	Mass Element	1	9	U_i, V_i, A_i
SOLID168	Solid Element 16	10	3	U_i

(where $i=x, y, z$)

The following description of these elements; BEAM161, SHELL163, SOLID164, MASS166 and SOLID168 are summarized from ANSYS Elements Reference.

BEAM161 (Figure A-1a) is defined by nodes I and J in the global coordinate system. Node K defines a plane (with I and J) containing the element s-axis. The element r-axis runs parallel to the centroidal line of the element and through nodes I and J. Node K is always required to define the element axis system and it must not be colinear with nodes I and J. The location of node K is used only to initially orient the element.

SHELL163 (Figure A-1b) is a 4-node shell element with both bending and membrane capabilities. Both in-plane and normal loads are permitted. The element has 12 degrees of freedom at each node: translations, accelerations, and velocities in the nodal x, y, and z directions and rotations about the nodal x, y, and z-axes.

SOLID164 (Figure A-1c) is a hexahedral element used for the 3-D modeling of solid structures. The element is defined by eight nodes with the following degrees of freedom at each node: translations, velocities, and accelerations in the nodal x, y, and z directions.

MASS166 is defined by a single node with concentrated mass up to nine degrees of freedom: translations, velocities, and accelerations in the nodal x, y, and z directions.

SOLID168 (Figure A-1d) is a higher order 3-D, 10-node tetrahedral element. It has a quadratic displacement behavior and is well suited to modeling irregular meshes such as those produced from various CAD packages. The element is very useful for modeling irregular complex geometry. It is defined by ten nodes having three degrees of freedom at each node: translations in the nodal x, y, and z directions.

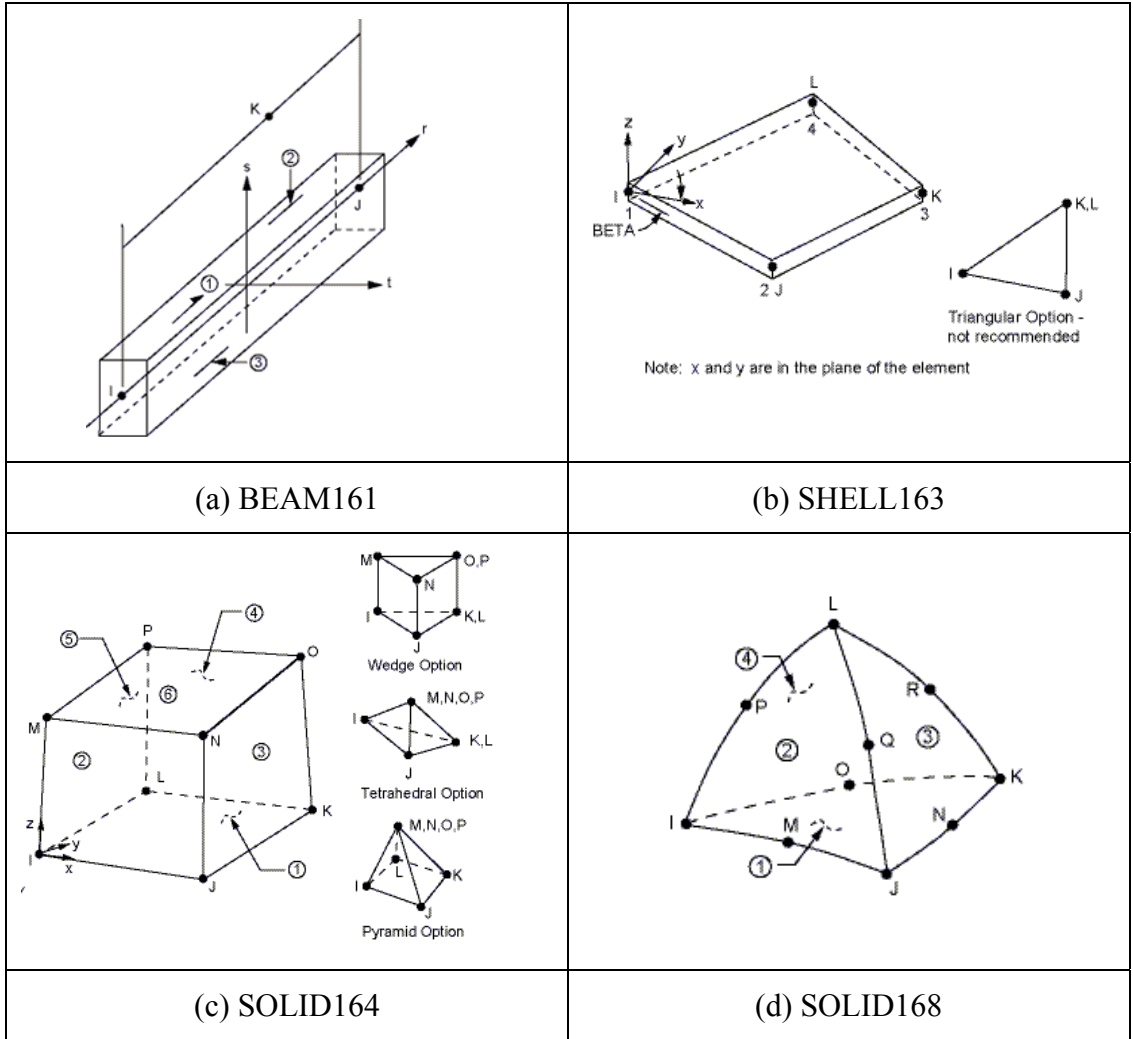


Figure A-1 General element types for explicit dynamic FEA
 [ANSYS Elements Reference]

APPENDIX B

SOME ENGINEERING EXAMPLES GOVERNED BY THE WEAK FORM FORMULATION

Consider the problem of finding the function $u(x)$ that satisfies the second order differential equation:

$$-\frac{d}{dx}(a(x)\frac{du(x)}{dx}) + c(x)u(x) - f(x) = 0, \quad 0 < x < L \quad (\text{B-1})$$

By multiplying the second order governing differential equation (B-1) with the weight function $w(x)$ and integrate over a element from x_a to x_b yields the weak form formulation in Equation (B-2):

$$0 = \int_{x_a}^{x_b} w(x) \left[-\frac{d}{dx}(a(x)\frac{du(x)}{dx}) + c(x)u(x) - f(x) \right] dx \quad (\text{B-2})$$

Where $u(x)$ is the unknown function; $w(x)$ is the weight function; (x_a, x_b) is the domain of an element; $a(x)$, $c(x)$, and $f(x)$ are the known quantities. The physical interpretation of these functions can be found in Table B-1, which shows some engineering examples governed by the weak form formulation.

Table B- 1 Some engineering examples governed by the weak form formulation

[Reddy, 2006]

Field of study	Primary variable u	Problem data			Secondary variable Q
		a	c	f	
Heat transfer	Temperature $T - T_\infty$	Thermal conductance kA	Surface convection $AP\beta$	Heat generation f	Heat Q
Flow through porous medium	Fluid head ϕ	Permeability μ	0	Infiltration f	Point source Q
Flow through pipes	Pressure P	Pipe resistance $1/R$	0	0	Point source Q
Flow of viscous fluids	Velocity v_x	Viscosity μ	0	Pressure gradient $-dP/dx$	Shear stress σ_{xz}
Elastic cables	Displacement u	Tension T	0	Transverse force f	Point force P
Elastic bars	Displacement u	Axial stiffness EA	0	Axial force f	Point force P
Torsion of bars	Angle of twist θ	Shear stiffness GJ	0	0	Torque T
Electrostatics	Electrical potential ϕ	Dielectric constant ϵ	0	Charge density ρ	Electric flux E

* k = thermal conductance; β = convective film conductance; p = perimeter; P = pressure or force; T_∞ = ambient temperature of the surrounding fluid medium; $R = 128\mu h/(\pi d^4)$ with μ being the viscosity, h the length, and d the diameter of the pipe; E = Young's modulus; A = area of cross section; J = polar moment of inertia.

APPENDIX C

NATURAL FREQUENCIES AND MODE SHAPES OF THE PORTAL FRAME STRUCTURE

The first 30 natural frequencies and mode shapes (solved by FEM) of the assembled model (Figure C-1a), missing 1 screw model (Figure C-1b), and missing 2 screws model (Figure C-1c) described in Section 2.4.2 are given in Figure C-2 to Figure C-7.

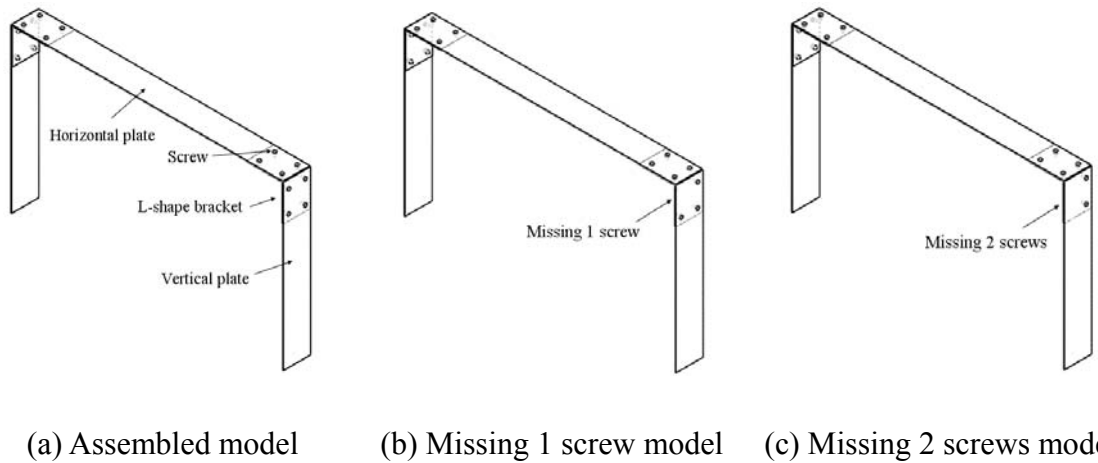


Figure C-1 Simulation models for the study of missing-screw effect

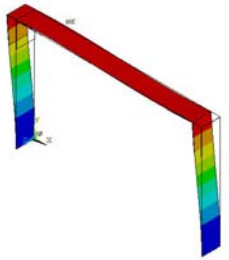
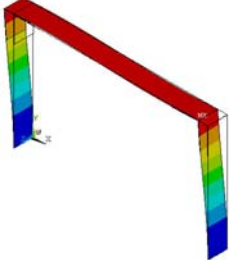
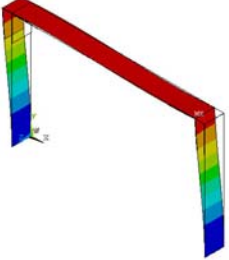
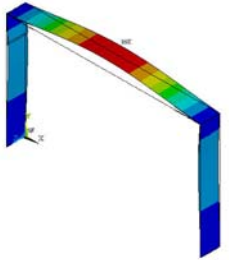

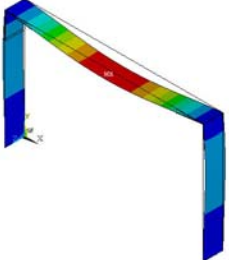
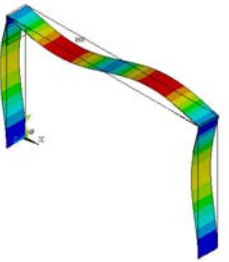


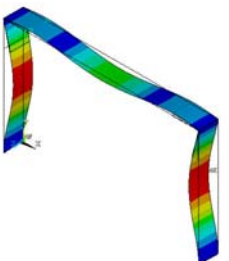
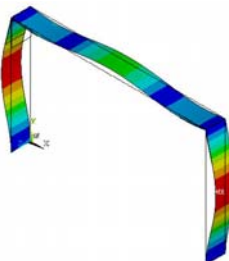
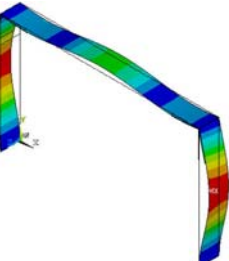
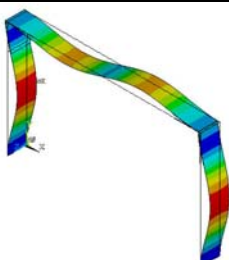
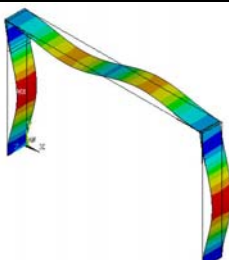
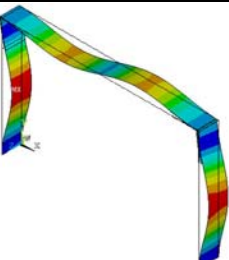
Assembled Model	Missing 1 Screw Model	Missing 2 Screws Model
		
Mode 1 (2.1 Hz)	Mode 1 (2.1 Hz)	Mode 1 (2.1 Hz)
		
Mode 2 (5.5 Hz)	Mode 2 (5.5 Hz)	Mode 2 (5.4 Hz)
		
Mode 3 (13.4 Hz)	Mode 3 (13.4 Hz)	Mode 3 (13.4 Hz)
		
Mode 4 (17.2 Hz)	Mode 4 (17.2 Hz)	Mode 4 (17.1 Hz)
		
Mode 5 (22.3 Hz)	Mode 5 (22.3 Hz)	Mode 5 (22.1 Hz)

Figure C-2 Natural frequencies and mode shapes (modes 1-5)

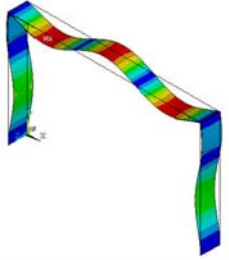
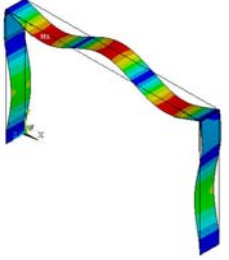
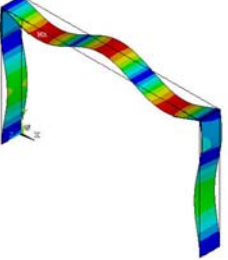

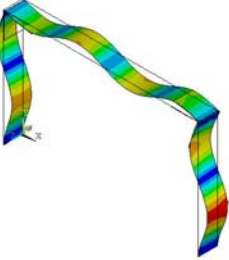
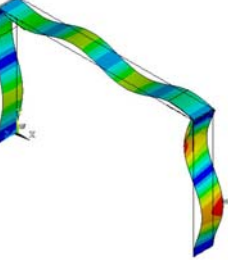
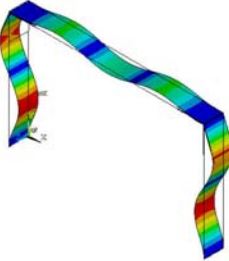
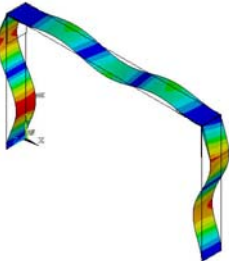
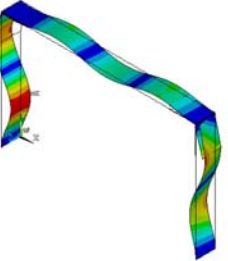
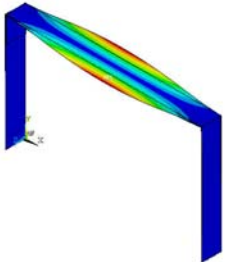
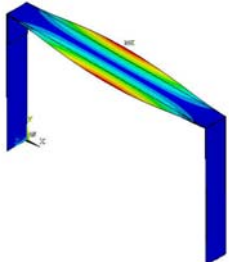
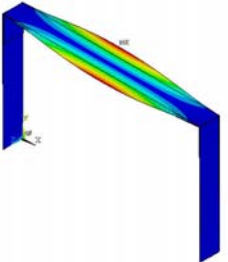
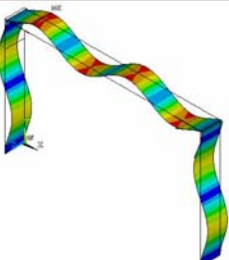
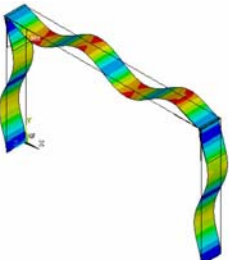
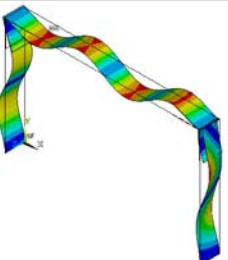
Assembled Model	Missing 1 Screw Model	Missing 2 Screws Model
		
Mode 6 (32.8 Hz)	Mode 6 (32.7 Hz)	Mode 6 (32.6 Hz)
		
Mode 7 (46.6 Hz)	Mode 7 (46.4 Hz)	Mode 7 (46.1 Hz)
		
Mode 8 (49.9 Hz)	Mode 8 (49.7 Hz)	Mode 8 (49.2 Hz)
		
Mode 9 (50.5 Hz)	Mode 9 (50.5 Hz)	Mode 9 (50.4 Hz)
		
Mode 10 (59.2 Hz)	Mode 10 (59.1 Hz)	Mode 10 (58.6 Hz)

Figure C-3 Natural frequencies and mode shapes (modes 6-10)

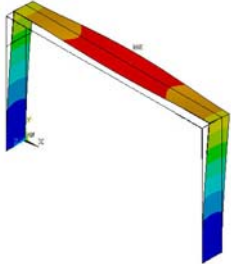
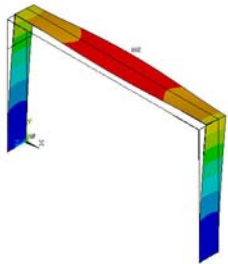
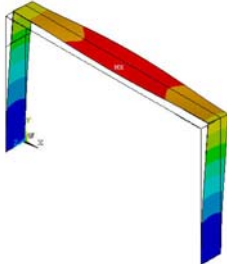
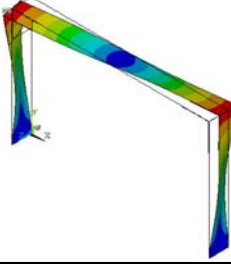
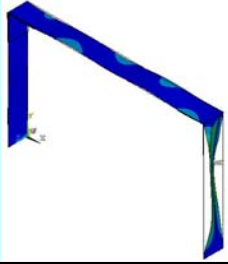


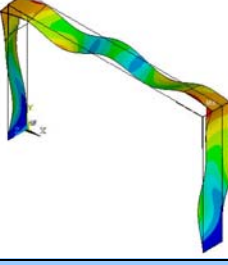
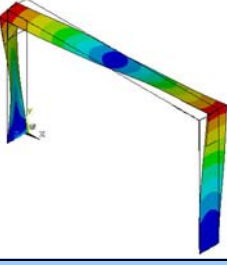
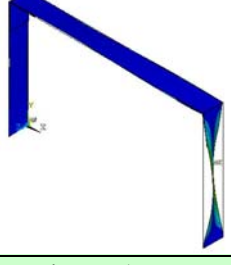
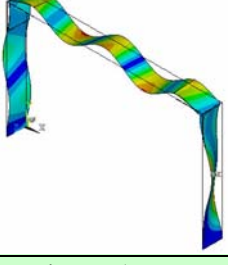

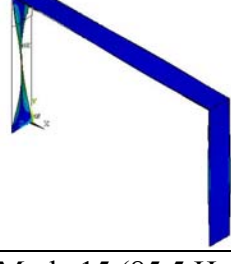
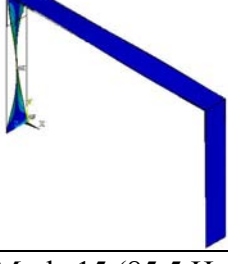
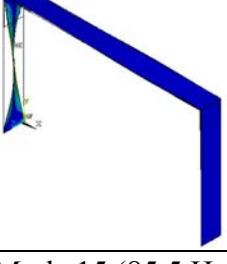
Assembled Model	Missing 1 Screw Model	Missing 2 Screws Model
		
Mode 11 (59.9 Hz)	Mode 11 (59.9 Hz)	Mode 11 (59.8 Hz)
		
Mode 12 (81.1Hz)	Mode 12 (78.6 Hz)	Mode 12 (68.7 Hz)
		
Mode 13 (82.0 Hz)	Mode 13 (81.4 Hz)	Mode 13 (81.1 Hz)
		
Mode 14 (85.3 Hz)	Mode 14 (82.2 Hz)	Mode 14 (81.5 Hz)
		
Mode 15 (85.5 Hz)	Mode 15 (85.5 Hz)	Mode 15 (85.5 Hz)

Figure C-4 Natural frequencies and mode shapes (modes 11-15)

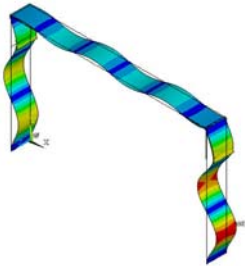
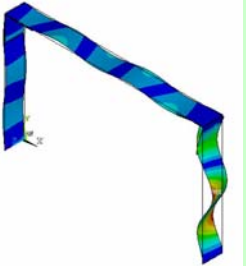
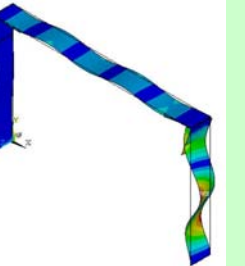
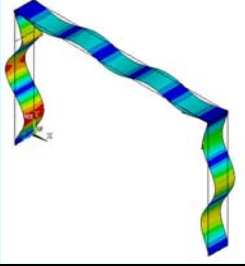
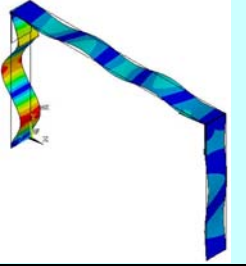
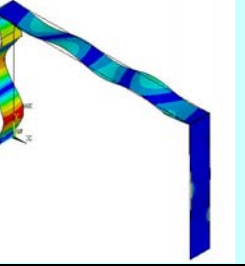
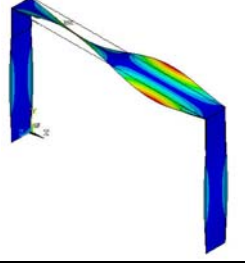
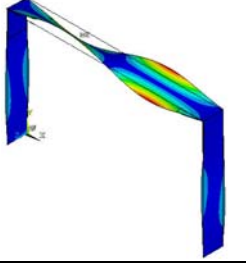
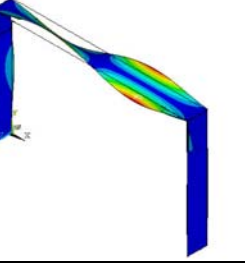
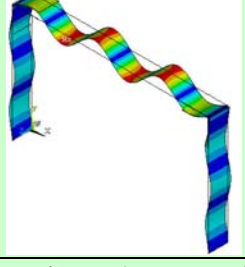
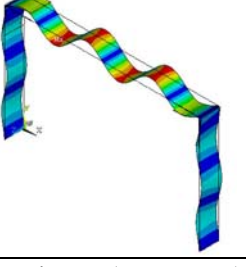
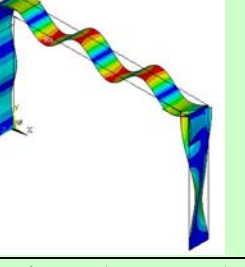
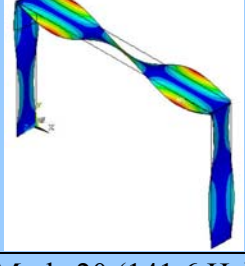
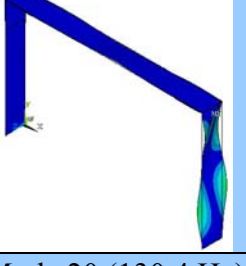
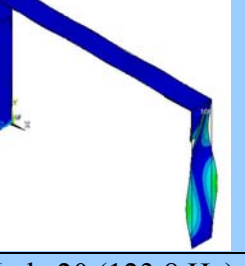
Assembled Model	Missing 1 Screw Model	Missing 2 Screws Model
		
Mode 16 (98.4 Hz)	Mode 16 (97.1 Hz)	Mode 16 (94.8 Hz)
		
Mode 17 (99.3 Hz)	Mode 17 (99.1 Hz)	Mode 17 (99.0 Hz)
		
Mode 18 (99.8 Hz)	Mode 18 (99.8 Hz)	Mode 18 (99.6 Hz)
		
Mode 19 (120.8 Hz)	Mode 19 (120.7 Hz)	Mode 19 (120.1 Hz)
		
Mode 20 (141.6 Hz)	Mode 20 (130.4 Hz)	Mode 20 (123.8 Hz)

Figure C-5 Natural frequencies and mode shapes (modes 16-20)

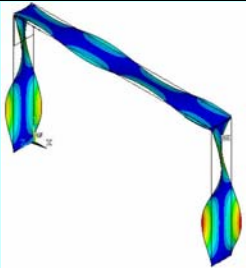


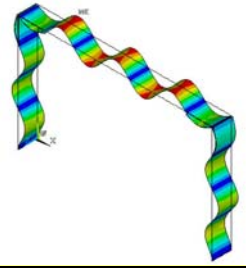
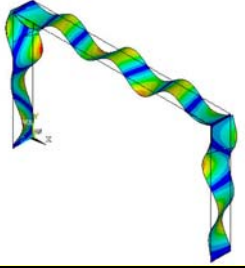
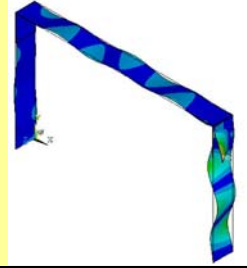
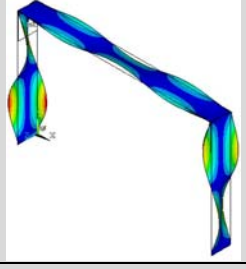
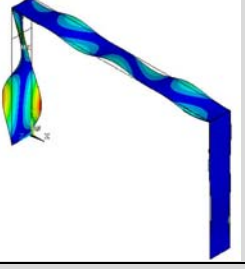
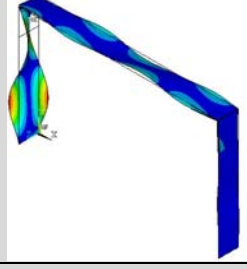
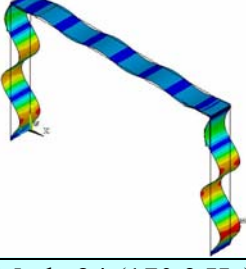
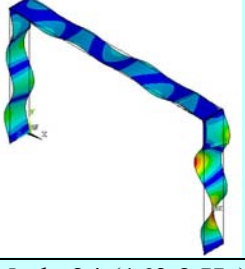
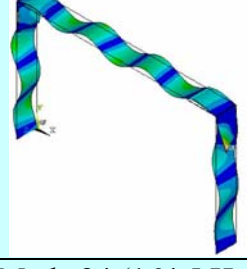
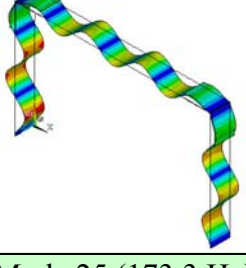
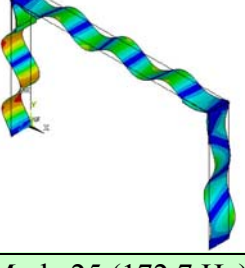
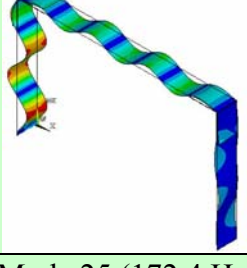
Assembled Model	Missing 1 Screw Model	Missing 2 Screws Model
		
Mode 21 (160.0 Hz)	Mode 21 (143.0 Hz)	Mode 21 (141.6 Hz)
		
Mode 22 (160.9 Hz)	Mode 22 (160.8 Hz)	Mode 22 (154.2 Hz)
		
Mode 23 (163.1Hz)	Mode 23 (161.9Hz)	Mode 23 (161.6 Hz)
		
Mode 24 (170.3 Hz)	Mode 24 (169.2 Hz)	Mode 24 (164.5 Hz)
		
Mode 25 (173.3 Hz)	Mode 25 (172.7 Hz)	Mode 25 (172.4 Hz)

Figure C-6 Natural frequencies and mode shapes (modes 21-25)

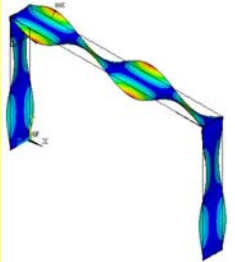
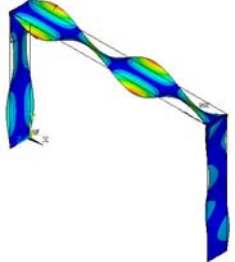
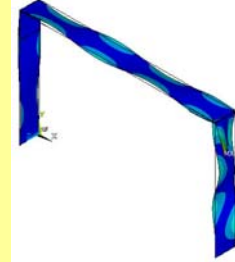
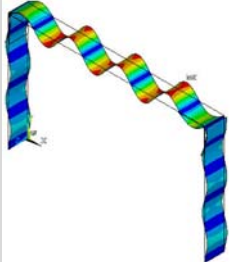
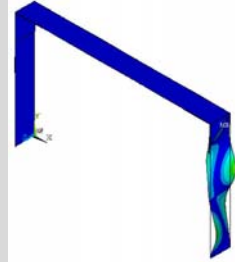
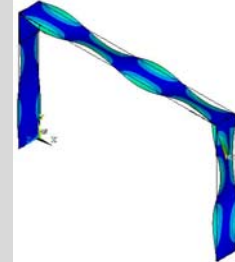
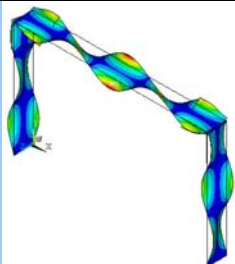
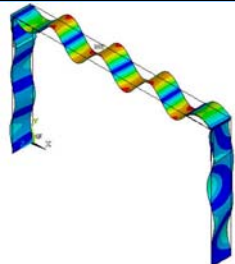
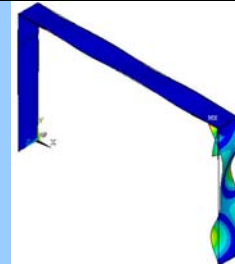
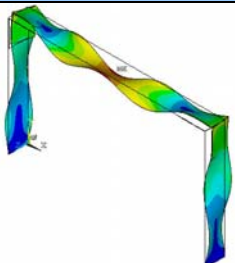
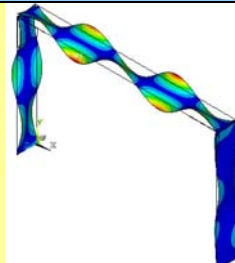
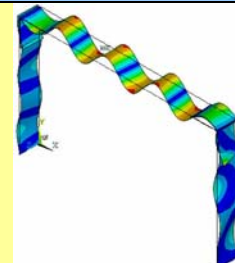
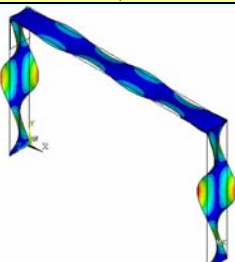
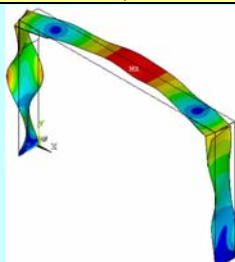
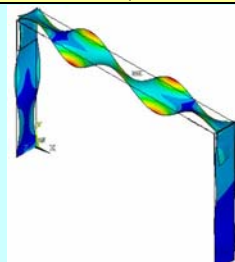
Assembled Model	Missing 1 Screw Model	Missing 2 Screws Model
		
Mode 26 (185.1 Hz)	Mode 26 (184.6 Hz)	Mode 26 (176.4 Hz)
		
Mode 27 (217.2 Hz)	Mode 27 (196.8 Hz)	Mode 27 (188.6 Hz)
		
Mode 28 (223.1 Hz)	Mode 28 (217.2 Hz)	Mode 28 (199.5 Hz)
		
Mode 29 (225.4 Hz)	Mode 29 (224.1 Hz)	Mode 29 (216.8 Hz)
		
Mode 30 (237.4 Hz)	Mode 30 (225.7 Hz)	Mode 30 (224.9 Hz)

Figure C-7 Natural frequencies and mode shapes (modes 26-30)

APPENDIX D

TRADITIONAL DAMPING

IDENTIFICATION METHODS

For dynamic problems, the consideration of damping is important for an accurate prediction of the dynamic response. For illustration, considering a free vibration single DOF system with viscous damping, the dynamic response can be classified into three cases: underdamped, critical damped, and overdamped, which are determined by the values of the damping ratio (or damping factor). For the underdamped case, damping ratio $\zeta < 1$, the motion is oscillatory with decaying amplitude. For the overdamped case, $\zeta > 1$, there is no oscillation. For the critical damped case, $\zeta = 1$, it is a critical point between oscillation and non-oscillation, and the response stabilizes most quickly.

Traditional damping identification methods are used to estimate the damping ratio of the dynamic systems. The measurement of the dynamic response is required in time or frequency domain. The most general methods for identification of damping are the log decrement method and half-power bandwidth method, which are in time domain and frequency domain respectively, and will be discussed as following subsections

D.1 Log Decrement Method (Time Domain)

For an underdamped free vibration response in time domain as in Figure D-1, damping ratio can be obtained from the measured amplitude x_1 and x_n (the 1st and n^{th}

cycle's peak amplitude at time t_1 and t_n respectively), which decays exponentially with time for the viscous damping assumption.

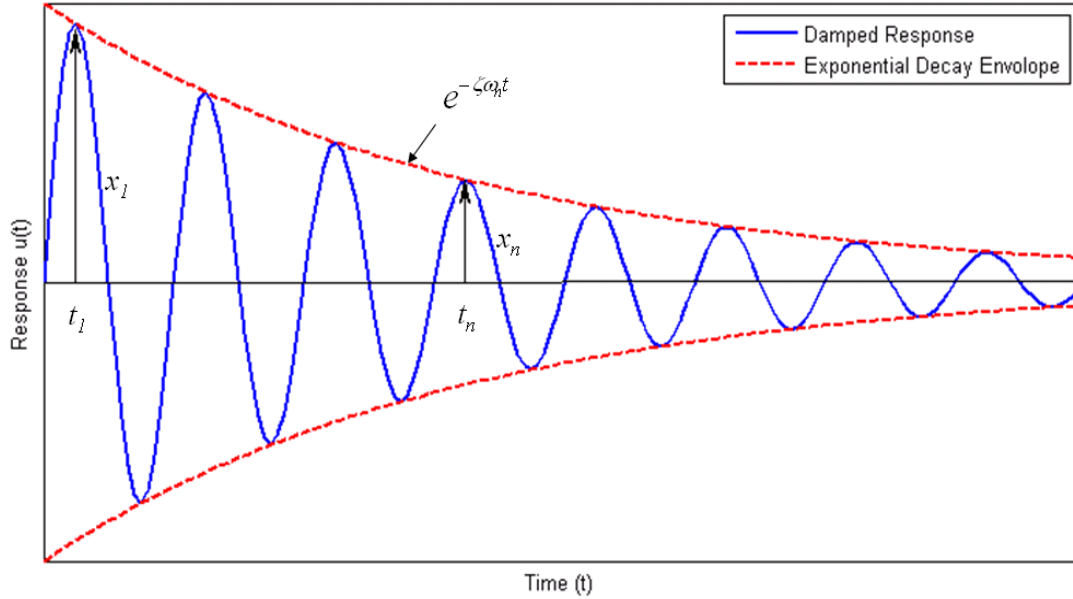


Figure D-1 Underdamped free vibration response

For underdamped case, the ratio of two amplitudes x_1 and x_n can be written as in Equation (D-1):

$$\frac{x_1}{x_n} = \frac{e^{-\zeta\omega_n t_1}}{e^{-\zeta\omega_n [t_1 + (n-1)]T}} = e^{(n-1)\zeta\omega_n T} \quad (\text{D-1})$$

where T is the period, ω_n is the natural frequency, and $t_n = t_1 + (n-1)T$.

The log decrement is the logarithm of the ratio of two amplitudes defined in Equation (D-2) and can be written in terms of damping ratio by the aid of Equation (D-1).

$$\text{Log decrement: } \delta = \frac{1}{n-1} \ln\left(\frac{x_1}{x_n}\right) \quad (\text{D-2})$$

$$= \zeta \omega_n T = \zeta \omega_n \frac{2\pi}{\omega_d} = \frac{2\pi\zeta}{\sqrt{1-\zeta^2}}$$

where the damped frequency: $\omega_d = \omega_n \sqrt{1-\zeta^2}$. By rearranging Equation (D-2), the damping ratio for the underdamped response can be obtained in Equation (D-3):

$$\zeta = \frac{\delta}{\sqrt{(2\pi)^2 + \delta^2}}, \quad \text{where } \delta = \frac{1}{n-1} \ln\left(\frac{x_1}{x_n}\right) \quad (\text{D-3})$$

The above formulation is well known as the log decrement method, which determines damping ratio by the decaying amplitude of the oscillation. It should be noted that log decrement method is for single DOF systems and more effective for light-damped cases. Figure D-2 shows the effect of the damping ratio on free vibration response. When damping ratio is greater than 0.6, there is almost no second cycle appeared which implies the log decrement method is hardly be applied for the high-damped cases.

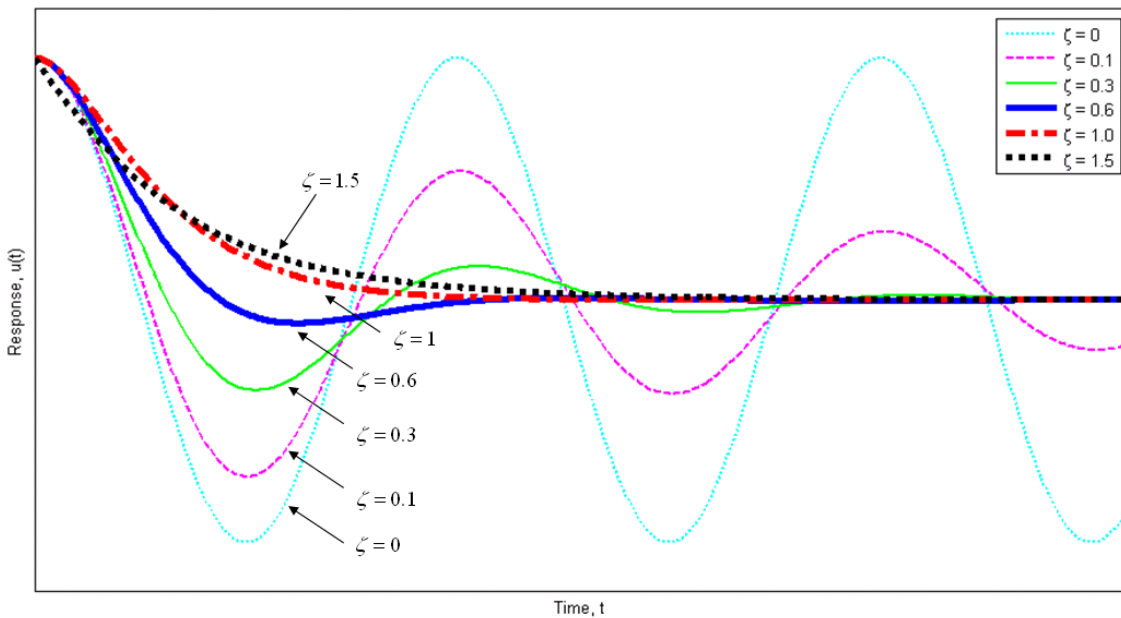


Figure D-2 Damping ratio effect on free vibration response in time domain

D.2 Half-Power Bandwidth Method (Frequency Domain)

The half-power bandwidth method (or half-power method, bandwidth method) is the method for identification of damping in frequency domain. For illustration, considering a single DOF system under harmonic excitation, the equation of motion is:

$$m\ddot{u} + c\dot{u} + ku = p_0 e^{i\omega t} \quad (\text{D-4})$$

where m , c , k are the mass, viscous damping coefficient, and stiffness respectively; p_0 is the amplitude of the excitation force; ω is the force excitation frequency (rad/s).

Assuming $u = Ue^{i\omega t}$, and substituting into above equation, we can get:

$$[(k - m\omega^2) + ic\omega]U = p_0 \quad (\text{D-5})$$

The displacement vs. force relation can be obtained as follows:

$$\frac{U}{p_0} = \frac{1}{(k - m\omega^2) + ic\omega} \quad (\text{D-6})$$

which is one kind of the frequency response function (FRF). The displacement-force relation in Equation (D-6) is also known as Receptance. Mobility and Accelerance are the other forms of FRF, which are defined as velocity and acceleration vs. force respectively.

The magnitude and the phase angle of the FRF in Equation (D-6) are given in Equation (D-7) and (D-8):

$$|H(\omega)| = \frac{1}{[(k - m\omega^2)^2 + (c\omega)^2]^{1/2}} = \frac{1/k}{[(1 - r^2)^2 + (2\zeta r)^2]^{1/2}} \quad (\text{D-7})$$

$$\text{Phase angle } \theta: \quad \tan \theta = \frac{c\omega}{k - m\omega^2} = \frac{2\zeta r}{1 - r^2} \quad (\text{D-8})$$

where $\text{Frequency ratio: } r = \frac{\omega}{\omega_n} \quad (\text{D-9})$

when $r=1$ ($\omega = \omega_n$), resonance occurs, and the magnitude of FRF is given by:

$$|H(\omega)|_{r=1} = \frac{1/k}{2\zeta} \quad (\text{D-10})$$

However, the use of this equation to determine ζ would require the determination of k , which is rarely available for general cases. Therefore, the half-power bandwidth method defines the half-power point (or 3db point) as Equation (D-11):

$$\text{Half-power point: } |H(\omega)|_{r_i} = \frac{1}{\sqrt{2}} |H(\omega)|_{r=1} = \frac{1}{\sqrt{2}} \left(\frac{1/k}{2\zeta} \right) \quad (\text{D-11})$$

Upon squaring above equation:

$$|H(\omega)|_{r_i}^2 = \frac{(1/k)^2}{(1-r_i^2)^2 + (2\zeta r_i)^2} = \frac{1}{2} \left(\frac{1/k}{2\zeta} \right)^2 \quad (\text{D-12})$$

Equation (D-12) can be simplified as:

$$r_i^4 - 2(1-2\zeta^2)r_i^2 + (1-8\zeta^2) = 0 \quad (\text{D-13})$$

The solutions of Equation (D-13) are given by:

$$r_i^2 = (1-2\zeta^2) \pm 2\zeta \sqrt{1+\zeta^2} \quad (\text{D-14})$$

For light-damped case: $\zeta \ll 1$, $\zeta^2 \approx 0$.

$$r_i = (1 \pm 2\zeta)^{1/2} \quad (\text{D-15})$$

Applying Taylor expansion for Equation (D-15) and neglecting high order term, we can get the following relations:

$$r_2 - r_1 = 2\zeta \quad \text{where } r_1 = 1 - \zeta, \quad r_2 = 1 + \zeta \quad (\text{D-16})$$

Finally, the half-power bandwidth formula can be obtained as:

$$\zeta = \frac{1}{2Q} \quad \text{where } Q = \frac{\omega_n}{\Delta\omega} = \frac{f_n}{f_2 - f_1} \quad (\text{D-17})$$

where Q is the quality factor; f_1 and f_2 are the frequencies (Hz) at the half-power points; f_n is the natural frequency (Hz).

Figure D-3 shows a general light-damped response in a FRF magnitude vs. frequency plot. From the half-power bandwidth method, the damping ratio can be determined by the measuring frequencies. The half-power bandwidth method can be applied for the multiple DOF systems; however, it is only valid for light-damped cases based on its assumption.

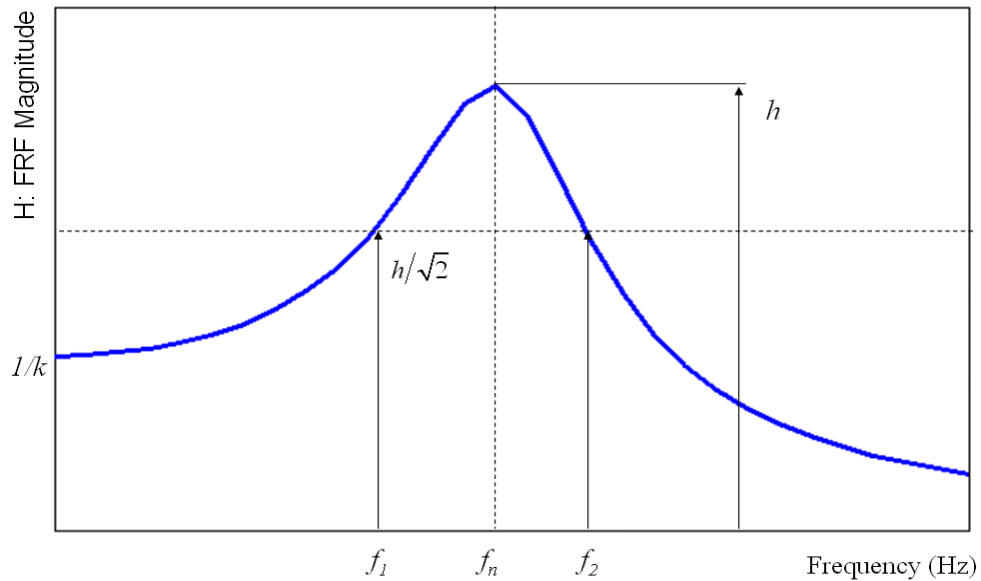


Figure D-3 FRF magnitude vs. frequency: half-power bandwidth method

Figure D-4 shows the damping ratio effect in the magnification factor (D_s) versus frequency ratio (r) plot, where the magnification factor is defined as:

$$D_s = \left| \frac{U}{U_0} \right| = \frac{1}{[(1-r^2)^2 + (2\zeta r)^2]^{1/2}} \quad (\text{D-18})$$

where the static displacement:
$$U_0 = \frac{P_0}{k} \quad (D-19)$$

When resonance occurs, the magnification factor is given by:

$$D_s = \frac{1}{2\zeta} \quad (D-20)$$

From Figure D-4, it shows larger damping ratio can lead to smaller magnification factor. When the damping ratio is greater than 0.7, there is no peak appeared in the frequency domain response, which implies the half-power bandwidth method is not valid for the high-damped cases.

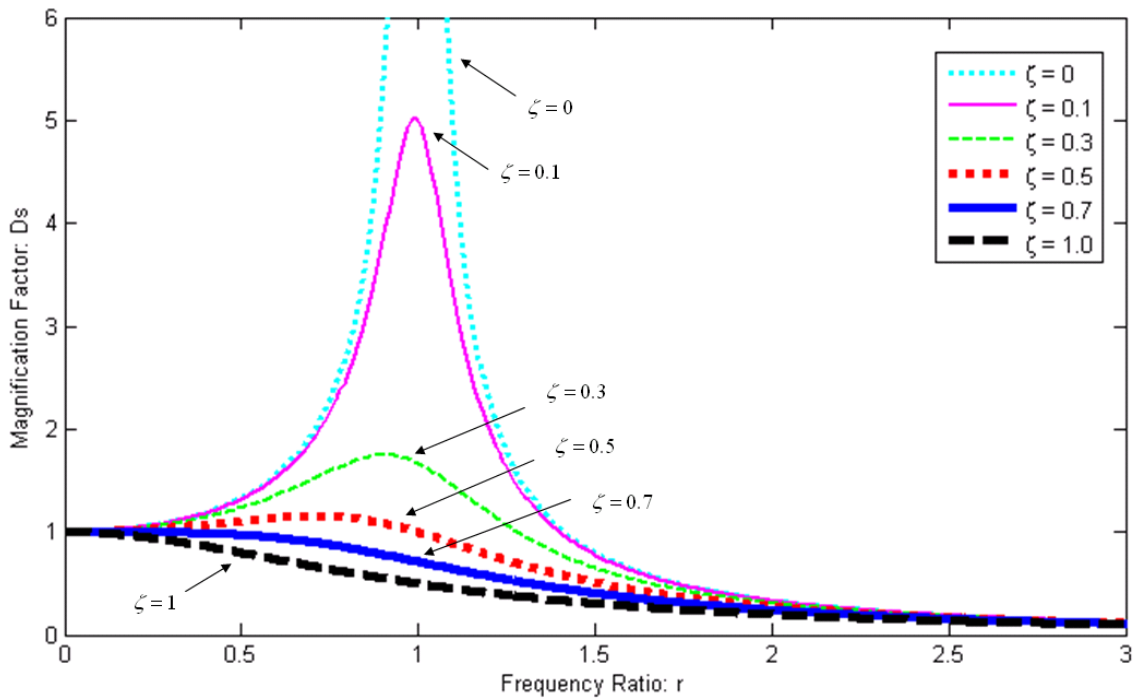


Figure D-4 Damping ratio effect in frequency domain response

APPENDIX E

DUNKERLEY'S METHOD

Dunkerley's equation for the approximate determination of the fundamental natural frequency of an Euler-Bernoulli beam with a tip mass can be written as [Stephen, 1980 and 1991]:

$$\frac{1}{\omega_1^2} \approx \frac{1}{\omega_{11}^2} + \frac{1}{\omega_{22}^2} + \frac{1}{\omega_{33}^2} \quad (\text{E-1})$$

$$\text{and } \omega_{11} = \sqrt{\frac{3EI}{0.243mL^3}}; \quad \omega_{22} = \sqrt{\frac{3EI}{ML^3}}; \quad \omega_{33} = \sqrt{\frac{EI}{JL}} \quad (\text{E-2})$$

where ω_1 is the fundamental natural frequency; ω_{11} is the natural frequency of the cantilever beam without tip mass; ω_{22} is the natural frequency of the mass less cantilever beam with tip mass; ω_{33} is the natural frequency of the mass less cantilever beam carrying tip rotatory inertia; m is the mass of the beam; M is the tip mass; L is the length of the beam; E is the elastic modulus of the beam; I is the moment of inertia; J is the polar moment of inertia.

For a circular cross section, the moment of inertia I and polar moment of inertia J are given in Equation (E-3) and (E-4).

$$I = \frac{\pi d^4}{64} \quad (\text{E-3})$$

$$J = \frac{\pi d^4}{32} \quad (\text{E-4})$$

For general structures, the effect of the tip rotatory inertia term is usually relatively insignificant; by omitting the third term in Equation (E-1), the Dunkerley's formula can be reduced to a more general form as Equation (E-5):

$$\omega_1 = \sqrt{\frac{\omega_{11}^2 \omega_{22}^2}{\omega_{11}^2 + \omega_{22}^2}} \quad (\text{E-5})$$

APPENDIX F

CAD MODEL OF THE LIVE OBJECT

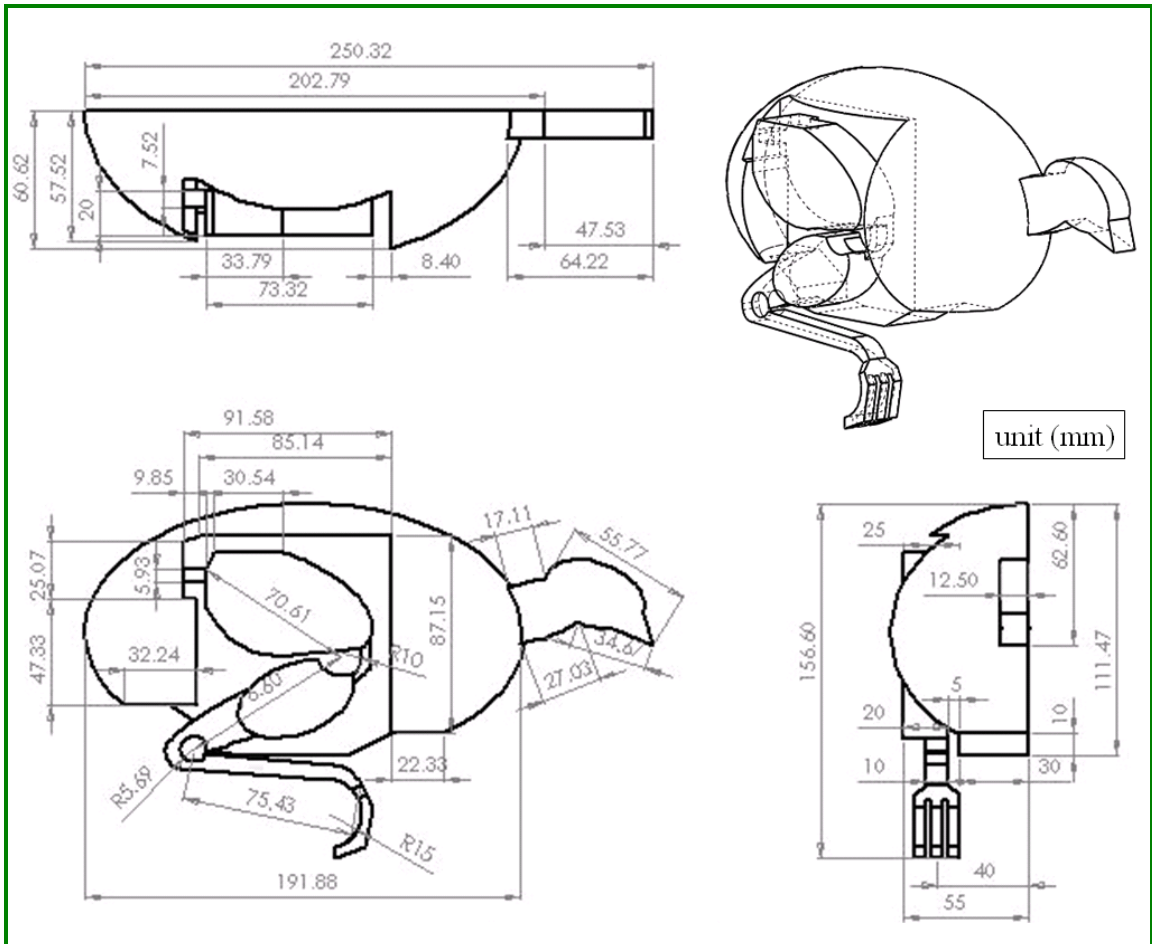


Figure F-1 Engineering drawing of the live object (chicken)

REFERENCES

- [1] Al-Gallaf, E.A., "Multi-Fingered Robot Hand Optimal Task Force Distribution: Neural Inverse Kinematics Approach," *Robotics and Autonomous Systems*, Vol. 54, Issue 1, pp. 34-51, 2006.
- [2] Amirouche, F.M.L., "Computational Methods in Multibody Dynamics," Prentice Hall, 1992.
- [3] Banerjee, A., Bhattacharya, B., and Mallik, A.K., "Forward and Inverse Analyses of Smart Compliant Mechanisms for Path Generation," *Mechanism and Machine Theory*, Vol. 44, Issue 2, pp 369-381, 2009.
- [4] Bauchau, O.A. and Ju, C., "Modeling Friction Phenomena in Flexible Multibody Dynamics," *Computer Methods in Applied Mechanics and Engineering*, Vol. 195, Issues 50-51, pp. 6909-6924, 2006.
- [5] Bauchau, O.A., and Rodriguez, J., "Modeling of Joints with Clearance in Flexible Multibody Systems," *International Journal of Solids and Structures*, Vol. 39, Issue 1, pp41-63, 2002.
- [6] Baumgartner, A., Harzheim, L. and Mattheck, C., "SKO (Soft Kill Option) The Biological Way to find an Optimum Structure Topology," *International Journal of Fatigue*, Vol.14, No.6, pp. 387-393, 1992.
- [7] Belytschko, T., Yen, H.-J., and Mullen, R., "Mixed Methods for Time Integration," *Computer Methods in Applied Mechanics and Engineering*, Vol. 17-18, pp. 259-275, 1979.
- [8] Bendsøe, M.P. and Kikuchi, N., "Generating Optimal Topologies in Structural Design Using a Homogenization Method," *Computer Methods in Applied Mechanics and Engineering*, Vol.71, No.2, pp. 197-224, 1988.
- [9] Boyle, C., Howell, L.L, Magleby, S.P., and Evans, M.S., "Dynamic Modeling of Compliant Constant-Force Compression Mechanisms," *Mechanism and Machine Theory*, Vol. 38, Issue 12, pp 1469-1487, 2003.

- [10] Bruns, T.E., "Topology Optimization of Convection-Dominated, Steady-State Heat Transfer Problems," *International Journal of Heat and Mass Transfer*, Vol. 50, Issues 15-16, pp. 2859-2873, 2007.
- [11] Bruns, T.E., "Topology Optimization by Penalty (TOP) Method," *Computer Methods in Applied Mechanics and Engineering*, Vol. 196, Issues 45-48, pp. 4430-4443, 2007.
- [12] Ceccarelli, M., "Fundamentals of Mechanics of Robotic Manipulation," Springer, 2004.
- [13] Chamberlain, F.W., "Atlas of Avian Anatomy: Osteology-Arthrology-Myology" Michigan State College, 1943.
- [14] Chan, J.C. and Liu, Y., "Dynamic Simulation of Multi-Fingered Robot Hands Based on a Unified Model," *Robotics and Autonomous Systems*, Vol. 32, Issues 2-3, pp. 185-201, 2000.
- [15] Chen, W., "Dynamic Modeling of Multi-Link Flexible Robotic Manipulators," *Computers & Structures*, Vol. 79, Issue 2, pp. 183-195, 2001.
- [16] Cheng, Z.Q., Thacker, J.G., Pilkey, W.D., Hollowell, W.T., Reagan, S.W., and Sieveka, E.M., "Experiences in Reverse-Engineering of a Finite Element Automobile Crash Model," *Finite Elements in Analysis and Design*, Vol. 37, Issue 11, pp. 843-860, 2001.
- [17] Chiandussi, G., Gaviglio, I., and Ibba, A., "Topology Optimisation of an Automotive Component without Final Volume Constraint Specification," *Advances in Engineering Software*, Vol. 35, Issues 10-11,, pp. 609-617, 2004.
- [18] Clough, R.W., "The Finite Element Method in Plane Stress Analysis," *Proceedings of 2nd ASCE Conference on Electronic Computation*, Pittsburgh, PA, 1960.
- [19] Consolazio, G.R., Chung, J.H., and Gurley, K.R., "Impact Simulation and Full Scale Crash Testing of a Low Profile Concrete Work Zone Barrier," *Computers & Structures*, Vol. 81, Issue 13, pp.1359-1374, 2003.

- [20] Cook, R.D., Malkus, D.S., Plesha, M.E., and Witt, R.J., "Concepts and Applications of Finite Element Analysis," 4th Edition, Wiley, 2001.
- [21] Craig, R.R. and Kurdila, A.J., "Fundamentals of Structural Dynamics," 2nd Edition, Wiley, 2006.
- [22] Dede, E.M. and Hulbert, G.M., "Computational Analysis and Design of Lattice Structures with Integral Compliant Mechanisms," *Finite Elements in Analysis and Design*, Vol. 44, Issue 14, pp. 819-830, 2008.
- [23] Diaz, A.R., and Kikuchi, N., "Solutions to Shape and Topology Eigenvalue Optimization Problems Using a Homogenization Method," *International Journal for Numerical Methods in Engineering*, Vol.35, pp.1487-1502, 1992.
- [24] Dowling, N.E., "Mechanical Behavior of Materials," 3rd Edition, Pearson, 2007.
- [25] Drew, S.J. and Stone, B.J., "Torsional Damping of a Back-to-Back Gearbox Rig: Experimental Measurements and Frequency Domain Modeling," *Proceedings of the Institution of Mechanical Engineers Part K: Journal of Multi-Body Dynamics*, Vol. 216, pp. 157-168, 2002.
- [26] Edin, B.B., Ascari, L., Beccai, L., Roccella, S., Cabibihan, J.-J., and Carrozza, M.C., "Bio-Inspired Sensorization of a Biomechatronic Robot Hand for the Grasp-and-Lift Task," *Brain Research Bulletin*, Vol. 75, Issue 6, pp. 785-795, 2008.
- [27] El-Sabbagh, A., Akl, W., and Baz, A., "Topology Optimization of Periodic Mindlin Plates," *Finite Elements in Analysis and Design*, Vol. 44, Issue 8, pp. 439-449, 2008.
- [28] Eschenauer, H.A., Kobolev, V.V., and Schumacher, A., "Bubble Method of Topology and Shape Optimization of Structures," *Structural Optimization*, Vol.8, No.1, pp.42-51, 1994.
- [29] Flanagan, D.P., and Belytschko, T., "Eigenvalues and Stable Time Steps for the Uniform Strain Hexahedron and Quadrilateral," *Journal of Applied Mechanics*, Vol. 51, pp. 35-40, 1984.

- [30] Fleury, C., "Sequential Convex Programming for Structural Optimization Problems. In: G.I.N. Rozvany, Editor, Optimization of Large Structural Systems," Vol. 1, pp. 531-553, 1993.
- [31] Flores, P., "Modeling and Simulation of Wear in Revolute Clearance Joints in Multibody Systems," Mechanism and Machine Theory, Vol. 44, Issue 6, pp. 1211-1222, 2009.
- [32] Geradin, M. and Cardona, A., "Flexible Multibody Dynamics: A Finite Element Approach," Wiley, 2001.
- [33] Hallquist, J.O. (compiled by), "LS-DYNA Theoretical Manual," Livermore Software Technology Corporation, 1998.
- [34] Hanssen, A.G., Girard, Y., Olovsson, L., Berstad, T., and Langseth, M., "A Numerical Model for Bird Strike of Aluminium Foam-Based Sandwich Panels," International Journal of Impact Engineering, Vol. 32, Issue 7, pp. 1127-1144, 2006.
- [35] Harrigan, T.P. and Hamilton, J.J., "Bone Remodeling and Structural Optimization," Journal of Biomechanics, Volume 27, Issue 3, pp.323-328, 1994.
- [36] Hinton, E. and Sienz, J., "Fully Stressed Topological Design of Structures Using an Evolutionary Procedure," Engineering Computations, Vol.12, pp.229-244, 1995.
- [37] Howell, L.L, Midha, A. and Norton, T.W., "Evaluation of Equivalent Spring Stiffness for Use in a Pseudo-Rigid-Body Model of Large-Deflection Compliant Mechanisms," ASME Journal of Mechanical Design, Vol. 118, pp 126-131, 1996.
- [38] Howell, L.L., "Compliant Mechanisms," Wiley, 2001.
- [39] Hughes, T.J.R., Pister, K.S., and Taylor, R.L., "Implicit-Explicit Finite Elements in Nonlinear Transient Analysis," Computer Methods in Applied Mechanics and Engineering, Vol. 17-18, pp. 159-182, 1979.
- [40] Hull, P.V. and Canfield, S., "Optimal Synthesis of Compliant Mechanisms Using Subdivision and Commercial FEA," Journal of Mechanical Design, Vol. 128, Issue 2, pp. 337-348, 2006.

- [41] Jang, G.-W., Kim, K.J., and Kim, Y.Y., "Integrated Topology and Shape Optimization Software for Compliant MEMS Mechanism Design," *Advances in Engineering Software*, Vol. 39, Issue 1, pp. 1-14, 2008.
- [42] Jang, I.G. and Kim, I.Y., "Computational Study of Wolff's Law with Trabecular Architecture in the Human Proximal Femur Using Topology Optimization," *Journal of Biomechanics*, Vol. 41, Issue 11, pp. 2353-2361, 2008.
- [43] Joni, H.J., "Force Analysis of an Automated Live bird Transfer System," Master Thesis, Georgia Institute of Technology, 2000.
- [44] Kazerooni, H. and Foley, C., "A Robotic Mechanism for Grasping Sacks," *IEEE Transactions on Automation Science and Engineering*, Vol. 2, Issue 2, pp. 111-120 2005.
- [45] Khatait, J.P., Mukherjee, S., and Seth, B., "Compliant Design for Flapping Mechanism: A Minimum Torque Approach," *Mechanism and Machine Theory*, Vol. 41, Issue 1, pp. 16, 2006.
- [46] Kim, H.A., Clement, P.J., and Cunningham, J.L., "Investigation of Cancellous Bone Architecture Using Structural Optimization," *Journal of Biomechanics*, Vol. 41, Issue 3, pp. 629-635, 2008.
- [47] Kim, I., Nakazawa, N., and Inooka, H., "Control of a Robot Hand Emulating Human's Hand-Over Motion," *Mechatronics*, Vol. 12, Issue 1, pp. 55-69, 2002.
- [48] Knight, N.F., Jaunky, N., Lawson, R.E., and Ambur, D.R., "Penetration Simulation for Uncontained Engine Debris Impact on Fuselage-Like Panels Using LS-DYNA," *Finite Elements in Analysis and Design*, Vol. 36, Issue 2, pp. 99-133, 2000.
- [49] Koterakos, J.R., and Lehoucq, R.B., "Estimating the Critical Time step in Explicit Dynamics Using the Lanczos Method," *International Journal for Numerical Methods in Engineering*, Vol. 69, Issue 13, pp. 2780-2788, 2007.
- [50] Kwasniewski, L., Bojanowski, C., Siervogel, J., Wekezer, J.W., and Cichocki, K., "Crash and Safety Assessment Program for Paratransit Buses," *International Journal of Impact Engineering*, Vol. 36, Issue 2, pp. 235-242, 2009.

- [51] Lan, C.-C. and Lee, K.-M., "Generalized Shooting Method for Analyzing Compliant Mechanisms with Curved Members," ASME Journal of Mechanical Design, Vol. 128, Issue 4, pp. 765-775, 2006.
- [52] Lan, C.-C., "Computational Models for Design and Analysis of Compliant Mechanisms," Ph.D. Dissertation, Georgia Institute of Technology, 2005.
- [53] Lee, K.-M., "Automated Feet Gripping System for Continuous Transfer of Live Broilers to Shackle," Invention Disclosure, GTRC ID2844, 2003.
- [54] Lee, K.-M., "Design Criteria for Developing an Automated Live bird Transfer System," IEEE Transactions on Robotics and Automation, Vol. 17(4), pp.483 – 490, 2001.
- [55] Lee, K.-M., "On the Development of a Compliant Grasping Mechanism for On-line Handling of Live Objects, Part I: Analytical Model," Int. Conf. on Advanced Intelligent Mechatronics Proc. (AIM'99), Atlanta, GA, pp. 354-359, 1999.
- [56] Lee, K.-M., Foong, S., Liu, C.-H., Pointextor, B. and Webster, B., "Methods of Loading Live Birds from Conveyors to Kill Line Shackles," GTRC ID 4731, Provisional Application (61/147, 219, January 26), 2009.
- [57] Lee, K.-M. and Guo, J., "Biological Joint Kinematic Model for Flexible Deboning Automation," 2008 International Symposium on Flexible Automation, Atlanta, GA, 2008.
- [58] Lee, K.-M., Joni, J., and Yin, X., "Compliant Grasping Force Modeling for Handling of Live Objects," Proceedings of the IEEE ICRA'2001, May 21-26, Seoul, Korea, pp. 1059-1064, 2001.
- [59] Lee, K.-M., Webster, A.B., Joni, J., Yin, X., Cary, R., Lacy, M.P., and Gogate, R., "On the Development of a Compliant Grasping Mechanism for On-line Handling of Live Objects, Part II: Design and experimental investigation," Int. Conf. on Advanced Intelligent Mechatronics Proc. (AIM'99), Atlanta, pp. 360-365, 1999.
- [60] Lee, K.-M. and Yin, X., "Design Algorithm for Automated Dynamic Grasping of Live Birds," IEEE/ASME AIM'01 Proceedings, Como, Italy, pp. 207-212, 2001

- [61] Li, Q. and Lee, K.-M., "An Adaptive Meshless Method for Analyzing Large Mechanical Deformation and Contacts," *Journal of Applied Mechanics*, Vol. 75, Issue 4, 2008.
- [62] Li, Q., "Effects of Adaptive Discretization on Numerical Computation using Meshless Method with Live-Object Handling Applications," Ph.D. Dissertation, Georgia Institute of Technology, 2007.
- [63] Li, Q., Steven, G.P., Xie, Y.M., and Querin, O.M., "Evolutionary Topology Optimization for Temperature Reduction of Heat Conducting Fields," *International Journal of Heat and Mass Transfer*, Vol. 47, Issue 23, pp. 5071-5083, 2004.
- [64] Lin, J.I., "An Element Eigenvalue Theorem and its Application for Stable Time Steps," *Computer Methods in Applied Mechanics and Engineering*, Vol. 73, Issue 3, pp. 283-294, 1989.
- [65] Ling, X. and Cherukuri, H.P., "Stability Analysis of An Explicit Finite Element Scheme for Plane Wave Motions in Elastic Solids," *Computational Mechanics*, Vol. 29, pp. 430-440, 2002.
- [66] Low, K.H., Wang, Y., Hoon, K.H., and Vahdati, N., "Initial Global-Local Analysis for Drop-Impact Effect Study of TV Products," *Advances in Engineering Software*, Vol. 35, Issues 3-4, pp. 179-190, 2004.
- [67] Lu, K.-J. and Kota, S., "Topology and Dimensional Synthesis of Compliant Mechanisms Using Discrete Optimization," *Journal of Mechanical Design*, Vol. 128, Issue 5, pp. 1080-1091, 2006.
- [68] Luharuka, R. and Hesketh, P.J., "Design of Fully Compliant, In-Plane Rotary, Bistable Micromechanisms for MEMS Applications," *Sensors and Actuators A: Physical*, Vol. 134, Issue 1, pp. 231-238, 2007.
- [69] Luo, Z., Yang, J., and Chen, L., "A New Procedure for Aerodynamic Missile Designs Using Topological Optimization Approach of Continuum Structures," *Aerospace Science and Technology*, Vol. 10, Issue 5, pp. 364-373, 2006.

- [70] Ma, Z.D., Kikuchi, N., Pierre, C. and Raju, B., "Multidomain Topology Optimization for Structural and Material Designs," *Journal of Applied Mechanics*, Vol. 73, Issue 4, pp. 565-573, 2006.
- [71] Machado, G. and Trabuco, L., "Some Results in Topology Optimization Applied to Biomechanics," *Computers & Structures*, Volume 82, Issues 17-19, pp. 1389-1397, 2004.
- [72] Mankame, N.D. and Ananthasuresh, G.K., "Topology optimization for synthesis of contact-aided compliant mechanisms using regularized contact modeling," *Computers & Structures*, Vol. 82, Issues 15-16, pp. 1267-1290, 2004.
- [73] Maute, K. and Frangopol, D.M., "Reliability-Based Design of MEMS Mechanisms by Topology Optimization," *Computers & Structures*, Vol. 81, Issues 8-11, pp. 813-824, 2003.
- [74] Midha, A., Howell, L.L., and Norton, T.W., "Limit Positions of Compliant Mechanisms Using the Pseudo-Rigid-Body Model Concept," *Mechanism and Machine Theory*, Vol. 35, pp 99-115, 2000.
- [75] Misra, S., Reed, K.B., Douglas, A.S., Ramesh, K.T., and Okamura, A.M., "Needle-Tissue Interaction Forces for Bevel-Tip Steerable Needles," *Proceedings of the 2nd Biennial IEEE/RAS-EMBS International Conference on Biomedical Robotics and Biomechatronics*, Scottsdale, AZ, 2008.
- [76] Mlejnek, H.P. and Schirrmacher, R., "An Engineer's Approach to Optimal Material Distribution and Shape Finding," *Computer Methods in Applied Mechanics and Engineering*, Vol. 106, pp. 1-26, 1993.
- [77] Moon, Y.-M., "Bio-Mimetic Design of Finger Mechanism with Contact Aided Compliant Mechanism," *Mechanism and Machine Theory*, Vol. 42, Issue 5, pp. 600-611, 2007.
- [78] Mullen, R. and Belytschko, T., "An Analysis of an Unconditionally Stable Explicit Method," *Computers & Structures*, Vol.16, No.6, pp. 691-696, 1983.

- [79] Mullender, M.G., Huiskes, R., and Weinans, H., "A Physiological Approach to the Simulation of Bone Remodeling as a Self-Organizational Control Process," *Journal of Biomechanics*, Vol. 27, No.11, pp.1389-1394, 1994.
- [80] Nomura, T., Nishiwaki, S., Sato, K., and Hirayama, K., "Topology Optimization for the Design of Periodic Microstructures Composed of Electromagnetic Materials," *Finite Elements in Analysis and Design*, Vol. 45, Issue 3, pp. 210-226, 2009.
- [81] Oden, J.T., Belytschko, T., Fish, J., Hughes, T.J.R., Johnson, C., Keyes, D., Laub, A., Petzold, L., Srolovitz, D., and Yip, S., "Simulation-Based Engineering Science - Revolutionizing Engineering through Simulation," Report of the National Science Foundation Blue Ribbon Panel on Simulation-Based Engineering Science, 2006.
- [82] Ogata, K., "System Dynamics," 4th Edition, Prentice Hall, 2003.
- [83] Pagnini, L.C. and Solari, G., "Damping Measurements of Steel Poles and Tubular Towers," *Engineering Structures*, Vol. 23, Issue 9, pp. 1085-1095, 2001.
- [84] Pan, M.-C. and Chen, P.-C., "Drop Simulation/Experimental Verification and Shock Resistance Improvement of TFT-LCD Monitors," *Microelectronics Reliability*, Vol. 47, Issue 12, pp. 2249-2259, 2007.
- [85] Pedersen, C.B.W., Fleck, N.A., and Ananthasuresh, G.K., "Design of a Compliant Mechanism to Modify an Actuator Characteristic to Deliver a Constant Output Force," *Journal of Mechanical Design*, Vol. 128, Issue 5, pp. 1101-1112, 2006.
- [86] Rao, S.S., "Mechanical Vibrations," 3rd Edition, Addison-Wesley Publishing Company, Inc., 1995.
- [87] Reddy, J.N., "An Introduction to the Finite Element Method," 3rd Edition, McGraw-Hill, 2006.
- [88] Rozvany, G.I.N., "Structural Design via Optimal Criteria," Kluwer, Dordrecht, 1989.
- [89] Seepersad, C.C., Allen, J. K., McDowell, D. L. and Mistree, F., "Multifunctional Topology Design of Cellular Material Structures," *Journal of Mechanical Design*, Vol. 130, Issue 3, 031404, 2008.

- [90] Shim, H. and Lee, J., "Acceleration Workspace of Cooperating Multi-Finger Robot Systems," *Journal of Bionic Engineering*, Vol. 5, Issue 2, pp. 103-110, 2008.
- [91] Shuib, S., Ridzwan, M.I.Z., and Kadarman, A.H., "Methodology of Compliant Mechanisms and its Current Developments in Applications: A Review," *American Journal of Applied Sciences*, 4(3): 160-167, 2007.
- [92] Shumway, C.M., "Dynamic Modeling and Analysis of the Body Inversion," Master Thesis, Georgia Institute of Technology, 2002.
- [93] Sigmund, O., "Design of Multiphysics Actuators Using Topology Optimization – Part I: One-Material Structures," *Computer Methods in Applied Mechanics and Engineering*, Vol. 190, Issues 49-50, pp.6577-6604, 2001.
- [94] Sigmund, O., "Design of Multiphysics Actuators Using Topology Optimization – Part II: Two-Material Structures," *Computer Methods in Applied Mechanics and Engineering*, Vol. 190, Issues 49-50, pp. 6605-6627, 2001.
- [95] Simeon, B., "On Lagrange Multipliers in Flexible Multibody Dynamics," *Computer Methods in Applied Mechanics and Engineering*, Vol. 195, Issues 50-51, pp. 6993-7005, 2006.
- [96] Stephen, N.G., "Extended Dunkerley's Method for Additional Flexibility," *Journal of Sound and Vibration*, Vol. 146, Issue 2, pp. 345-352, 1991.
- [97] Stephen, N.G., "Vibration of a Cantilevered Beam Carrying a Tip Heavy Body by Dunkerley's Method," *Journal of Sound and Vibration*, Vol. 70, Issue 3, pp. 463-465, 1980.
- [98] Summer, M.D., "Design Algorithm of a Novel Computer-Controlled Gripper for a Live Bird Transfer System," Master Thesis, Georgia Institute of Technology, 2002.
- [99] Vogel, F., "Topological Optimization of Linear-Elastic Structures with ANSYS 5.4," *NAFEMS Conference on Topological Optimization*, 1997.
- [100] Wagner, M., Morehouse, J., and Melkote, S., "Prediction of Part Orientation Error Tolerance of a Robotic Gripper," *Robotics and Computer-Integrated Manufacturing*, Vol. 25, Issue 2, pp. 449-459, 2009.

- [101] Wang, D., "Dynamic Analysis of Constrained Object Motion for Mechanical Transfer of Live Objects," Master Thesis, Georgia Institute of Technology, 2009.
- [102] Wang, M.Y., Wang, X., and Guo, D., "A Level Set Method for Structural Topology Optimization," *Computer Methods in Applied Mechanics and Engineering*, Vol. 192, Issues 1-2, pp. 227-246, 2003.
- [103] Wang, Y.-L., "Modular Design Process for a Micro Motion Actuator," *Mechatronics*, Vol. 15, Issue 7, pp. 793-806, 2005.
- [104] Weinans, H., Huiskes, R. and Grootenboer, H.J., "The Behavior of Adaptive Bone-Remodeling Simulation Models," *Journal of Biomechanics*, Vol. 25, No. 12, pp. 1425-1441, 1992.
- [105] Wolff, J., "The Law of Bone Remodeling," Berlin Heidelberg New York: Springer, 1986 (translation of the German 1892 edition).
- [106] Xie, M., "Flexible Multibody System Dynamics: Theory and Applications," CRC, 1993.
- [107] Xie, Y.M. and Steven, G.P., "A Simple Approach to Structural Frequency Optimization," *Computers & Structures*, Vol.53, No.6, pp. 1487-1491, 1994.
- [108] Xie, Y.M. and Steven, G.P., "A Simple Evolutionary Procedure for Structural Optimization," *Computers & Structures*, Vol.49, No.5, pp. 885-896, 1993.
- [109] Xie, Y.M. and Steven, G.P., "Optimal Design of Multiple Load Case Structures Using an Evolutionary Procedure," *Engineering Computations*, Vol.11, pp.295-302, 1994.
- [110] Xie, Y.M. and Steven, G.P., *Evolutionary Structural Optimization*, Springer, 1997.
- [111] Xu, J. and Li, Z., "A Kinematic Model of Finger Gaits by Multifingered Hand as Hybrid Automaton," *IEEE Transactions on Automation Science and Engineering*, Vol. 5, Issue 3, pp. 467-479, 2008.
- [112] Yang, R.J., "Multidiscipline Topology Optimization," *Computers & Structures*, Vol.63, No.6, pp. 1205-1212, 1997.

- [113] Yin, X., "Modeling and Analysis of Grasping Dynamics for High Speed Transfer of Live Birds," Ph.D. Dissertation, Georgia Institute of Technology, 2003.
- [114] Yin, X. and Lee, K.-M., "Modeling and Analysis of Grasping Dynamics for High Speed Transfer of Live Birds," Proceedings of the 2nd IFAC Conference on Mechatronic Systems, Berkeley, California, 2002.
- [115] Yin, X., Lee, K.-M., and Lan, C.-C., "Computational Models For Predicting The Deflected Shape Of A Non-Uniform, Flexible Finger," Proc. of the IEEE ICRA2004, New Orleans, LA., 2004.
- [116] Yoo, J. and Hong, H., "A Modified Density Approach for Topology Optimization in Magnetic Fields," International Journal of Solids and Structures, Vol. 41, Issues 9-10, pp. 2461-2477, 2004.
- [117] Yoo, W.-S., Lee, J.-H., Park, S.-J., Sohn, J.-H., Dmitrochenko, O., and Pogorelov, D., "Large Oscillations of a Thin Cantilever Beam: Physical Experiments and Simulation Using the Absolute Nodal Coordinate Formulation," Nonlinear Dynamics, 34, pp. 3–29, 2003.
- [118] Young, R.J. and Chuang, C.H., "Optimal Topology Design Using Linear Programming," Computers & Structures, Vol.52, No.2, pp. 265-275, 1994.
- [119] Zettl, B., Szyszkowski, W., and Zhang, W.J., "Accurate Low DOF Modeling of a Planar Compliant Mechanism with Flexure Hinges: the Equivalent Beam Methodology," Precision Engineering, Vol. 29, Issue 2, pp. 237-245, 2005.
- [120] Zhu, D., Qi, Q., Wang, Y., Lee, K.-M., and Foong, S., "A Prototype Mobile Wireless Sensor Network for Structural Health Monitoring," Proceedings of SPIE, Nondestructive Characterization for Composite Materials, Aerospace Engineering, Civil Infrastructure, and Homeland Security 2009, 7294: San Diego, CA, March, 2009.
- [121] Zhu, X., Gong, H., and Gao, B., "The Application of Topology Optimization on the Quantitative Description of the External Shape of Bone Structure," Journal of Biomechanics, Vol. 38, Issue 8, pp. 1612-1620, 2005.

- [122] Zhu, Z.H. and Meguid, S.A., “Nonlinear FE-Based Investigation of Flexural Damping of Slacking Wire Cables,” *International Journal of Solids and Structures*, Vol. 44, Issue 16, pp. 5122-5132, 2007.
- [123] Zollo, L., Roccella, S., Guglielmelli, E., Carrozza, M.C., and Dario, P., “Biomechatronic Design and Control of an Anthropomorphic Artificial Hand for Prosthetic and Robotic Applications,” *IEEE/ASME Transactions on Mechatronics*, Vol. 12, No. 4, pp. 418-429, 2007.